

Aggregation Aptitude in Rigid and Flexible Molecular Systems: Comparative Photophysical and Analytical Studies

A Dissertation

*Submitted in partial fulfillment for the degree of
Doctor of Philosophy*



Sagnik De

(Roll No. 186122032)

Thesis Supervisor: Prof. Gopal Das

Department of Chemistry

Indian Institute of Technology Guwahati

Assam -781039, India

Aggregation Aptitude in Rigid and Flexible Molecular Systems: Comparative Photophysical and Analytical Studies

A Dissertation

*Submitted in partial fulfillment for the degree of
Doctor of Philosophy*



Sagnik De

(Roll No. 186122032)

Thesis Supervisor: Prof. Gopal Das

Department of Chemistry

Indian Institute of Technology Guwahati

Assam-781039, India

*Dedicated to the loving
memory of my grandfather...*

and

To my family and friends...





INDIAN INSTITUTE OF TECHNOLOGY GUWAHATI

Department of Chemistry

STATEMENT

I do hereby declare that the matter embodied in this thesis is the result of investigations carried out by me in the Department of Chemistry, Indian Institute of Technology Guwahati, Assam – 781039, India, under the supervision of Dr. Gopal Das, Professor, Department of Chemistry, Indian Institute of Technology Guwahati, Assam – 781039, India. In keeping with the general practice of reporting scientific observations, due acknowledgements have been made wherever this work is based on the findings of other investigators.

Date: June 2023

(Sagnik De)

Place: IIT Guwahati





INDIAN INSTITUTE OF TECHNOLOGY GUWAHATI

Department of Chemistry

CERTIFICATE

This is to certify that **Mr. Sagnik De** (Roll No. 186122032) has been working under my supervision since July, 2018 as a regular registered Ph. D. student. His thesis entitled **“Aggregation aptitude in rigid and flexible molecular systems: Comparative Photophysical and analytical studies”** is an authentic record of the results obtained from the research work carried out under my supervision in the Department of Chemistry, Indian Institute of Technology Guwahati, Assam - 781039, India. I am forwarding his thesis to submit for the award of degree of Doctor of Philosophy, from this institute. I hereby certify that he has fulfilled all the requirements, according to the rules of this institute regarding the investigations embodied in his thesis and this work has not been submitted elsewhere for a degree.

Dr. Gopal Das

(Thesis Supervisor)

Professor, Department of Chemistry

IIT Guwahati, Assam - 781039, India

Acknowledgment

"all which we behold is full of blessings.."- William Wordsworth, Tintern Abbey

I am overbrimming with my emotions while penning down this section. When we have the finest company, the journey to the destination is delightful.

At the very outset, I cherish the unconditional support and strength bestowed on me by my parents, Mr. Pradipta De and Mrs. Gopa De for being there through thick and thin. I am gratified to my aunt Prof. Swati De, who is an academic icon for me on this exciting journey. My uncle (Prof. Sudipta De) along with my aunt not only provided moral support but also necessary academic guidance. I remember my 'Dadai' Late Syama Prasad De, who would have burst into happiness on this occasion of my thesis writing. I want to thank my grandma (Mrs. Anjali De) and the rest of my family for their unwavering support of my every accomplishment.

At this final stage of a truly memorable journey toward my intellectual destination, I would like to thank my supervisor Professor Gopal Das. The chief reason this journey has been so exceptional is his endless support and his calm and composed nature, which I want to imbibe in my personality. As an avid fanboy of supramolecular chemistry, I cherish the pleasure of working in this unique domain. During the challenges of experimenting, examining, and writing my thesis, he gave me the moral boost and freedom I needed to continue. The members of the thesis committee Prof. Lal Mohan Kundu, Dr. Dipankar Srimani, and Dr. Akshai Kumar A. S. for being my most important advisors and source of valuable scientific input. I am also grateful to the heads of our department (during my doctoral studies) Prof. T. Punniyamurthy Prof. G. Das, and Prof. A.N. Panda all faculty, research staff, technical and non-technical staff in the Department of Chemistry, IIT Guwahati. My sincere thanks to all the staff and instrument users of Central Instrumentation Facility IIT Guwahati who provided all necessary instrumentation during my research. I am grateful to Govt. of India, the Department of Science Technology, and the Department of Biotechnology for providing us with the necessary funds to execute my research projects.

Lab CHL-201 was a nice place to work with these people Nilotpal Da, Utsab Da, Biswajit Da, Rupinder Bhaiya, Bishu Da, Arnab Da, Jayakrishnan Bhaiya, Senjuti Di, Deepa Di, Asesh Da,

Megha Di, Debojit da, Debolina, Pampi, Oiyao, Rubi, Neha, Bikram, and Sulekha. Thank you to everyone at the lab for many years of tea, snacks, pranks, birthdays, parties, movies, outings, and fun while working on the thesis! I am grateful to Barlina ba from the Biosciences and Bioengineering department for her unconditional help, as well as cooperative juniors like Subhrajyoti, Abhijit, and Srijan from SP Biswas sir's Laboratory at IIT Guwahati.

Now, it is time to thank all my IIT Guwahati friends whose contribution is worth mentioning. Of course, nothing would function properly without the beloved friends and batchmates: Debjyoti, Sandeep, Samir, Tanumoy, Tirupati, Vinay, Chang, Pran, Monu, Bikoshita, Rinki, Bittu, Sabina, and Priyanka. From gossiping in the hostel corridor to hanging out on the weekends, reveling in the fests, and looting one another at birthday/success parties, I will surely miss all of them and treasure the love and laughter we shared. A special group of friends is not revealed yet, because they deserve their part, thanks to Aritra, Arin, Anindya, and Anjishnu. From secret crimes, movies, and shindig to staycations we relished every bit. Without them all, my IITG experience would not have been as reassuring and unforgettable. I sincerely wish them the best in their future.

I extend my feelings to my teachers to whom I owe the debt for their blessings and teachings; Avik Sir, Lopamudra Maam, Sohini Maam, M.B Maam, Manisha Maam, Anwasha Maam, S.G. Sir, and many others from my school, college, and university who gave me the academic guidance and encouragement to move forward in this field. I am sorry that many names are missing whose guidance is worth mentioning.

I would like to acknowledge IIT Guwahati for the fellowship, the Microsoft Corporation for presenting MS Word and Excel as well as Adobe Corporation for AI software.

Finally, I bow down to the Lord Almighty for his grace and blessings from the beginning of my academic life up to this doctoral level.

Sagnik



The contents of this thesis entitled “**Aggregation aptitude in rigid and flexible molecular systems: Comparative Photophysical and analytical Studies.**” has been divided into six chapters based on the results of experimental work performed during the research period.

Chapter 1: Introduction

Supramolecular chemistry, commonly referred to as "chemistry beyond the molecule," focuses on the research of molecular recognition and high-order ensembles created by noncovalent interactions. This is in its forte for the last 50 years, already been widely investigated in several fields, including molecular sensors, molecular machines, analytical tools, nanoreactors, gas absorption, chemical catalysis, and drug delivery. It is a branch of chemistry that encompasses multiple fields, including, organic chemistry, physical chemistry, coordination chemistry, analytical science polymer chemistry, biological science, materials science, and many more. Supramolecular assemblies or self-assemblies often exhibit stimuli-responsiveness due to their dynamic characteristics, which can be useful in a variety of analytical contexts.¹⁻²

Nature accomplishes complex processes through vast molecular arrangements, which are impossible to execute through monomeric versions. Molecular self-assembly is described as the spontaneous organizing of molecules into structurally well-ordered and stable configurations through non-covalent interactions. Self-assembly is characterized by a high level of integration, which allows for the creation of unique and complex structures from relatively simple building components. Chemical tuning on the molecular framework can control the self-assembly and disassembly behavior.³⁻⁵

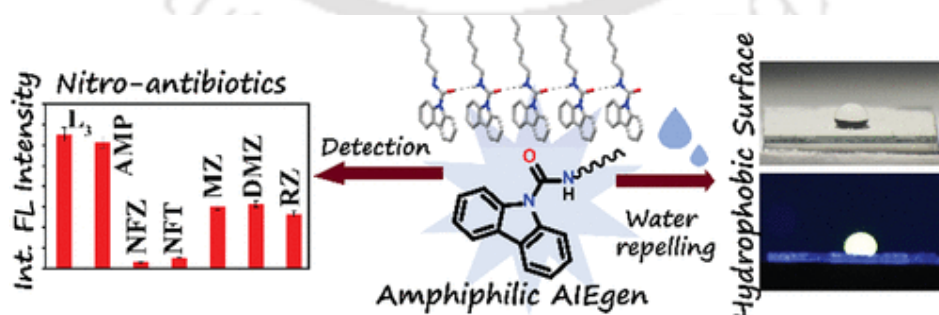
Supramolecular entities involving a variety of functional fluorophores are receiving special attention because they not only provide an in-depth understanding of the photophysical properties and progressive development of the assemblies, but they also lend themselves to advanced applications in bio-analytical, physical, biochemical, and technological fields. Fluorophores, capable of forming supramolecular aggregates, have fascinated scientists for years due to their remarkable visual/optical properties.⁶⁻⁷ The structure and environment impact the spectral features of fluorescent compounds. Individual fluorophores have been characterized in multitudes, but aggregates of them have their own set of characteristics. Controlling fluorophore self-assembly thus gives a way to access unusual photophysical properties. Molecular self-assembly is a potent phenomenon obtained from nature that scientists have used to create unique supramolecular designs. It has evolved as a significant method for the creation of soft functional materials with broad implications in materials

science and biology. From studying biophysical interaction to the detection of toxic analytes, these supramolecular entities are effective.⁸ Among these advancements, Prof. B. Z. Tang discovered “Aggregation-Induced Emission” (AIE) in 2001, an unusual occurrence in certain strategically designed molecules. Significant progresses in designing AIE active building blocks for molecular self-assemblies to create molecular superstructures with distinctive morphologies have caught the interest of researchers all over the world. The principles of AIE and AIEE were unusual discoveries in the domain of organic luminophores since they challenged the common perception that aggregation-caused quenching (ACQ) suppresses luminescence. Despite the importance of AIEgens, developing a new methodological approach that can build AIEgenic systems from common ACQphores is a difficult task.⁹⁻¹⁰ Herein, we specifically aim for the synthesis of different types of flexible and rigid molecular frameworks and features of their aggregation performance, morphological changes, and resultant applicability. We attempt to contribute an account of amphiphiles and quinoxaline scaffolds which have been designed to undergo spontaneous aggregation/disaggregation in response to environmental and chemical stimuli along with their photophysical aspects.

Chapter 2: Experimental methods and characterization

This chapter is a thorough report of the various reagents used in the synthesis of the probes, their synthetic pathways, photophysical studies, crystallization details, detection limits, binding study, and specifications of analytical instruments employed in the characterization of probes and their respective analytes of interest.

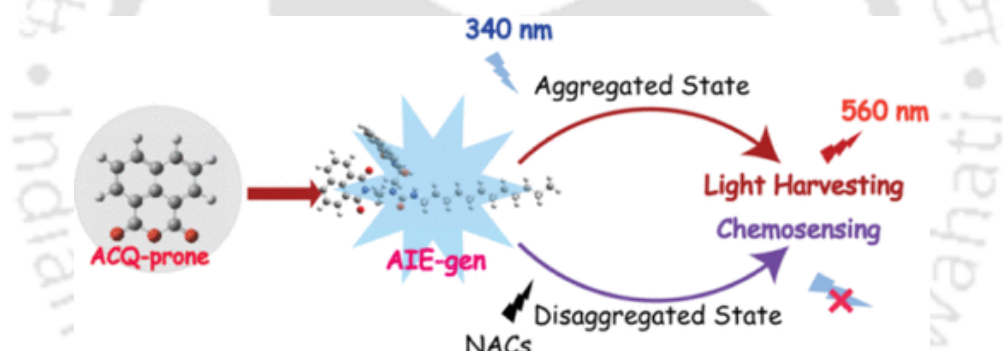
Chapter 3: Carbazole-adhered Amphiphilic AIEgen: Detection of Nitro-Antibiotics and Hydrophobic Surfaces (*Langmuir* 2023, 39, 6, 2444–2449)



We have designed three amphiphilic compounds with varying chain lengths. The amphiphile bears carbazole at one end, adhered by a substituted urea linkage. These hydrophobic amphiphiles displayed aggregation-induced emission on solvent switching. A binary solvent

(THF-water) system was considered for this optical study through fluorescence spectroscopy. The aggregates were further detailed by microscopy viz; FESEM and AFM. These fluorescent amphiphiles were coated on glass slides to create water-repelling surfaces utilizing their hydrophobic nature. These AIEgen has been applied in the detection of nitro antibiotics. The high emission intensity was quenched by nitro-antibiotics and the mechanism of quenching was analyzed to be a photoinduced electron transfer process. DFT calculations were run on both amphiphiles and targeted analytes to derive the HOMO-LUMO energy level and probe the mechanism. The analytical usefulness of the AIEgens is being demonstrated concerning the detection of nitro antibiotics in biofluids (Simulated Body Fluid and Simulated Gastric Fluid). Our current work is intended to contribute to both photophysical research and analytical utility.

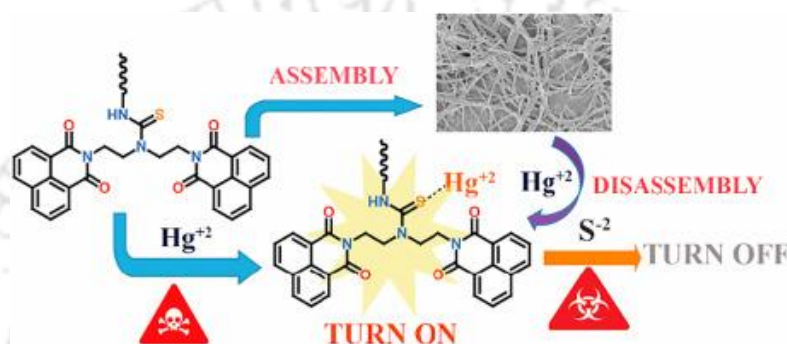
Chapter 4A: Insights into the Aggregation performance and Light-Harvesting facet of Naphthalimide-based Amphiphile and Non-amphiphile AIEgen (*Langmuir* 2022, 38, 19, 6158–6163)



In chapter 4A, we report a comparative study of two Naphthalimide-tethered amphiphiles and non-amphiphiles with their aggregation-induced emission properties. The amphiphiles are tripodal where two heads bear the Naphthalimide unit and the rest arm is attached via urea-amide linkage. The unit phthalimide is prone to aggregation-caused quenching. A synthetic tuning on the molecular framework repressed the ACQ-phoric fluorophore to an AIEgen. **L4** & **L5** remain in the dispersed form in DMF and exhibit aggregation and intense emission signals in aqueous media. Microscopy images of the aggregating species have been analyzed. Not only the AIEgens are emissive in water but also, they are emissive in the solid state. The natural light-harvesting process is mimicked by the aggregated state, establishing an energy transfer process between **L4** and commercial dye, Rhodamine B. The light-harvesting process which stems from the photophysical occurrence FRET is probed by fluorescence spectroscopy as well as fluorescence lifetime measurements.

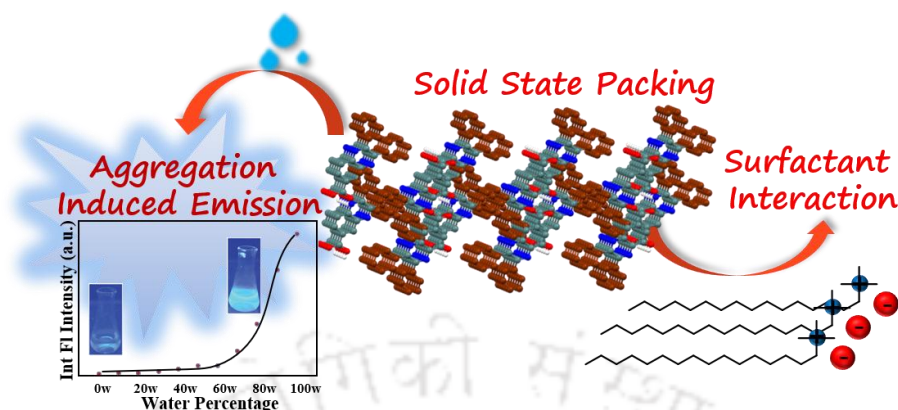
Disaggregation of the AIEgen has also been utilized in the detection of nitroaromatics. Picric acid, a toxic as well as explosive analyte has been targeted. The mechanism was proved to be PET via DFT calculations. The limit of Detection for picric is also calculated to be 5.12 μM . Detection of PA in solid support and environmentally relevant water samples is also demonstrated. We intend our present work contributes to both photo-physical research and analytical applicability.

Chapter 4B: Turn-ON mercury detection in water by tripodal synthetic amphiphile chemosensors via self-assembly and desulfurization (*Dyes Pigm.* 2021, **195**, 109659)



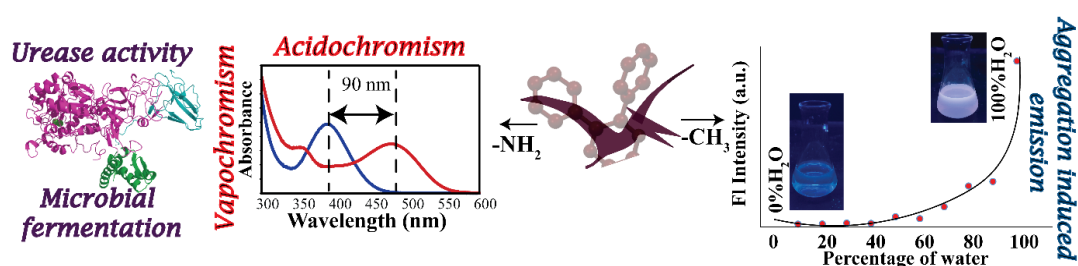
In this chapter functionalization of the previously synthesized tripodal is done. A comparative study between the urea and thiourea is laid out. In this case, water-soluble substituted thiourea amphiphile detects mercury with a Turn-On emission signal. The urea counterpart acts as a control to this occurrence. Desulfurization-mediated mercury sensing in water has been resolved with spectral studies. The amphiphile shows appreciable selectivity and sensitivity among other cations and heavy metals. Binding constant, stoichiometric binding along with the limit of detection is determined by emission spectroscopy considering probe-analyte interaction. Critical aggregation constant (CAC) is determined for both urea and thiourea amphiphiles in water via emission spectroscopy. The asymmetric tripodal can self-assemble into ribbon-like morphology in aqueous media, which has been outlined by microscopic analysis. Microscopy studies and DLS details the self-aggregated morphology and hydrodynamic size of the reported probe. The analytical utility of the tripodal has been probed through real water samples and soil testing. The disaggregation process initiates the addition of the self-assembled structures, outlined by FESEM and DLS. Besides, the Hg-ensemble selectively recognizes H_2S viz; sulfide ion in water and rendering a substantially low detection limit of 0.5 ppm. Realistically, paper strips are set for the fluorimetric visualization of both analytes.

Chapter 5: Disaggregation of Quinoxaline derived AIEgen by Surfactants: Aggregation Propensity in Solid and Solution States (*Soft Matter*, 2023,19, 6116-6121)



This chapter deals with aggregation in a rigid system unlike demonstrated in the previous chapters. The aggregating aptitude is shown in both solution and solid-state packing. Herein, we designed five propellor-shaped molecules based on the quinoxaline scaffold with a functional group variation. They exhibit aggregation-induced emission and responses of these congeners concerning good solvent and the poor solvent is conducted both spectroscopically and microscopically. THF and Water are considered as the binary mixture of good and poor solvents respectively. The differences in the aggregation profile are described. Solid as well as solution state parallel analysis on the aggregation facet is laid out. Notably, $-\text{COOH}$ bearing counterpart interacts specifically with a cationic surfactant, unlike other congeners where the mechanism goes via disaggregation. From real water sample analysis to the selectivity of surfactants, it holds analytical and environmental significance.

Chapter 6: The aggregation and optical properties of a Quinoxaline scaffold as an acidochromic and solvatochromic urease tracker (*J. Photochem. Photobiol. A*, 2023, 443, 114884)



This chapter describes the dependence of aggregation and optical capability on synthetic modulation in the molecular framework. We have synthesized quinoxaline-based motifs

bearing variation in the functional group. **L12** exhibited the highest emission in the water against binary solvent switching, proving itself to be an AIEgen. On the other hand, **L14** exhibited several optical properties. It displayed positive solvatochromism with increasing solvent polarity. Vapochromism i.e., this probe changed its color on exposure to acidic vapor confirmed by absorption spectroscopy. This acid labile behavior of **L14** or acidochromic property is examined through absorption and emission spectroscopy via several applications and real sample analysis. The hydrolysis of urea into ammonia and carbon dioxide is carried out by the Nickel-dependent urease enzyme. Protonated **L14** can track the pH changes in solution due to urea and urease, thus proving itself to be a urease tracker. The proposed scheme was utilized to monitor the formation of biogenic amines from the putrefaction of food and assess the freshness of food after these encouraging results. The prepared protonated **L14**-loaded paper strips were then used as an indicator to monitor food freshness under optimal conditions. We affirm that this piece of work adds to future research on photophysical and aggregation studies along with applications in analytical fields.

Conclusion and Future Perspective

In summary, this thesis contributes to the field of supramolecular chemistry encompassing synthetic, photophysical, material, and analytical prospects. Experimentation on aggregation-induced emission on amphiphiles, tripodal amphiphiles, as well as rigid quinoxaline scaffolds, is carried out both spectroscopically and microscopically. Their disaggregation processes in presence of toxic (picric acid, Hg^{+2}) and important analytes (nitro antibiotics, surfactants) are demonstrated. In **L1**, **L7-12** we were able to demonstrate their solid-state packing. Hydrophobicity in amphiphiles is wielded in creating water-repelling surfaces. Photophysical phenomena like FRET, and PET, are also outlined considering their analytical value. Hopefully, this thesis will contribute to further delving deep into photophysical characteristics along with analytical utility with these types of molecular frameworks.

References

1. F. Huang and E. V. Anslyn, Introduction: Supramolecular Chemistry, *Chem. Rev.* 2015, **115**, 15, 6999–7000.
2. J. M. Lehn, Supramolecular chemistry: Where from? Where to?, *Chem. Soc. Rev.*, 2017, **46**, 2378.
3. M. Grzelczak, L. M. Liz-Marzán and R. Klajn, Stimuli-responsive self-assembly of nanoparticles, *Chem. Soc. Rev.*, 2019, **48**, 1342-1361.
4. C. Rest, R. Kandanellia and G. Fernández, Strategies to create hierarchical self-assembled structures

- via cooperative non-covalent interactions, *Chem. Soc. Rev.*, 2015,44, 2543-2572.
5. M. Hecht and F. Würthner, Supramolecularly Engineered J-Aggregates Based on Perylene Bisimide Dyes, *Acc. Chem. Res.*, 2021, **54** , 642 —653.
 6. S. Pratihar, A. Bhattacharyya and E. Prasad, Achieving ACQ-AIE modulation using isostructural organic fluorophores, *J. Photochem. Photobiol. A.*, 2020, **396**, 112458.
 7. C. Xu, Wu, D. Tian; Yanmei Zhou, A naphthalimide-derived hypochlorite fluorescent probe from ACQ to AIE effect transformation, *Chem. Commun.* 2021, **57**, 11366– 11369.
 8. V. Viji, V. Bhalla, and M. Kumar, Hexaarylbenzene: Evolution of Properties and Applications of Multitalented Scaffold, *Chem. Rev.* 2016, 116, 16, 9565–9627.
 9. P. Li, D. Zhang, Y. Zhang, W. Lu, J. Zhang, W. Wang, Q. He, P. Theato, T. Chen, Aggregation-Caused Quenching-Type Naphthalimide Fluorophores Grafted and Ionized in a 3D Polymeric Hydrogel Network for Highly Fluorescent and Locally Tunable Emission, *ACS Macro Lett.* 2019, **8**, 937– 942.
 10. J. Mei, N. L. C. Leung, R. T. K. Kwok, J. W. Y. Lam and B. Z. Tang, Aggregation-Induced Emission: Together We Shine, United We Soar! *Chem. Rev.* 2015, 115, 21, 11718–11940.





Contents

CHAPTER 1: Introduction	Page No.
1.1 Supramolecular Self-assembly: A Brief Introduction	1
1.2 Aggregation Induced Emission (AIE): The unique case of Self-assembly	3
1.3 Detection of Analytes: Aggregation/ Disaggregation Approach	10
1.4 Advantages of fluorescence-based methods for detection of analyte/guest	17
1.5 Concluding Remarks and objective of the Thesis	18
References	18
CHAPTER 2: Experimental Details and Characterization	
2.1 General Information and Materials	22
2.2 Synthetic procedure of the probes (L₁-L₁₄)	
2.2.1 Synthesis of L₁ [N-hexyl-9H-carbazole-9-carboxamide]	22
2.2.2 Synthesis of L₂ [N-dodecyl-9H-carbazole-9-carboxamide]	23
2.2.3 Synthesis of L₃ [N-octadecyl-9H-carbazole-9-carboxamide]	23
2.2.4 Synthesis of L₄ [1,1-bis(2-(1,3-dioxo-1H-benzo[de]isoquinolin-2(3H)-yl) ethyl)-3-dodecylurea]	24
2.2.5 Synthesis of L₅ [N, N-bis(2-(1,3-dioxo-1H-benzo[de]isoquinolin-2(3H)-yl) ethyl) acetamide]	24
2.2.6 Synthesis of L₆ [1,1-bis(2-(1,3-dioxo-1H-benzo[de]isoquinolin-2(3H)-yl) ethyl)-3-octylthiourea]	25
2.2.7 Synthesis of L₇ [2,3-diphenylquinoxaline]	25
2.2.8 Synthesis of L₈ [2,3-diphenylquinoxaline-6-carboxylic acid]	25
2.2.9 Synthesis of L₉ [ethyl 2,3-diphenylquinoxaline-6-carboxylate]	26
2.2.10 Synthesis of L₁₀ [(2,3-diphenylquinoxalin-6-yl) methanol]	26
2.2.11 Synthesis of L₁₁ [(2,3-diphenylquinoxalin-6-yl) (phenyl)methanone]	27
2.2.12 Synthesis of L₁₂ [6-methyl-2,3-diphenylquinoxaline]	28
2.2.13 Synthesis of L₁₃ [6-nitro-2,3-diphenylquinoxaline]	28
2.2.14 Synthesis of L₁₄ [2,3-diphenylquinoxalin-6-amine]	29

2.3 UVvis and Fluorescence Studies	29
2.4 Estimation of Apparent Binding Constant	29
2.5 Detection Limit (LOD)	29
2.6 Field emission scanning electron microscopy (FE-SEM)	29
2.7 Atomic force microscopy (AFM)	29
2.8 Dynamic light scattering (DLS)	31
2.9 Fluorescence lifetime	31
2.10 Density-functional theory (DFT)	31
2.11 References	31
2.12 Appendix 2	32

CHAPTER 3: Carbazole-adhered Amphiphilic AIEgen: Detection of Nitro-Antibiotics and Hydrophobic Surfaces

3.1 Background and focus of the chapter	55
3.2 Crystallographic evidences	55
3.3 Photophysical Studies	56
3.4 Hydrophobicity and water repelling properties	59
3.5 Interactions with Nitro-antibiotics	60
3.6 Conclusion	62
References	62
Appendix chapter 3	63

CHAPTER 4A: Insights into the Aggregation performance and Light-Harvesting facet of Naphthalimide-based Amphiphile and Non-amphiphile AIEgen

4A.1 Background and focus of the chapter	72
4A.2 Studies on photophysical behaviour	72
4A.3 Light Harvesting	76
4A.4 Interactions with Nitroaromatics	75
4A.5 Conclusion	78
References	79
Appendix chapter 4A	80

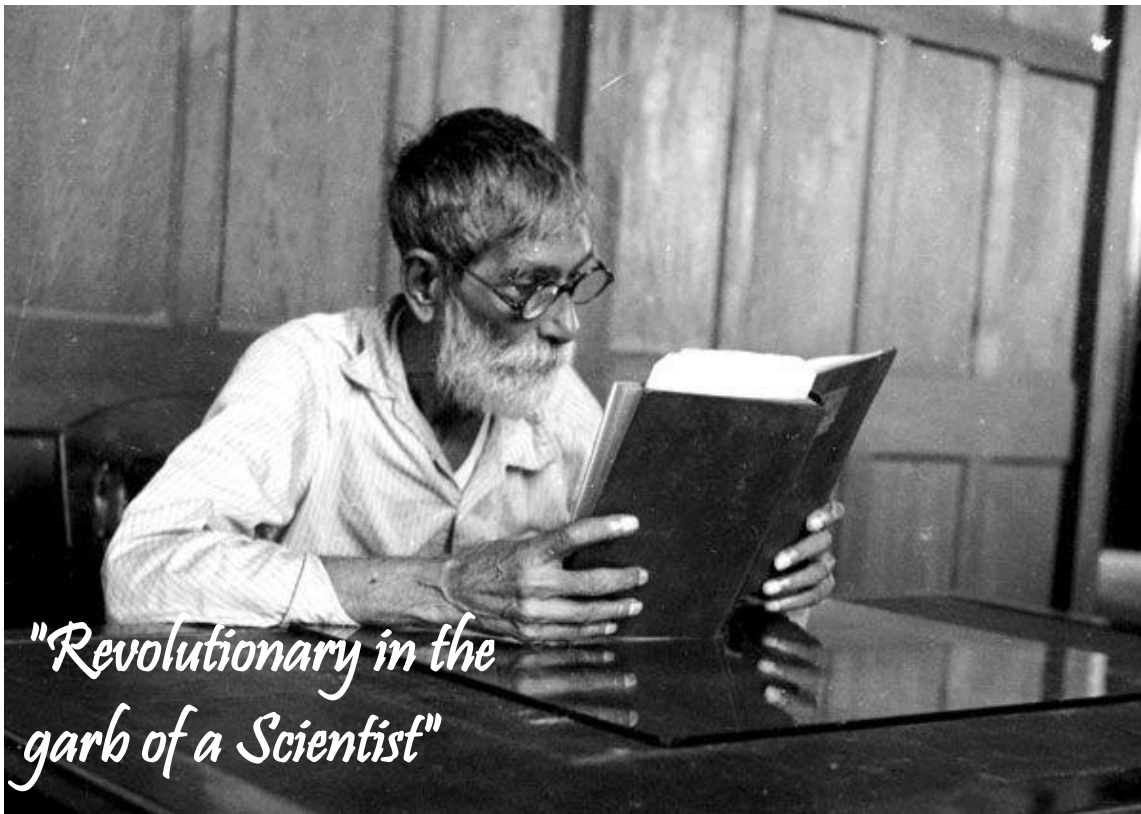
CHAPTER 4B: Turn-ON mercury detection in water by tripodal synthetic amphiphile chemosensors via self-assembly and desulfurization

4B.1 Background and focus of the chapter	83
--	----

4B.2 Explore the self-aggregation potential	84
4B.3 Response of metal ions on the probe: Selective Interaction with Mercury	85
4B.4 Analyte and self-aggregated state	87
4B.5 Probing the mechanism of sensing	88
4B.6 Investigation in real samples	89
4B.7 Effects of anion towards Hg(II)-ensemble	91
4B.8 Conclusion	92
References	94
Appendix chapter 4B	94
CHAPTER 5: Disaggregation of Quinoxaline derived AIEgen by Surfactants: Aggregation Propensity in Solid and Solution States	
5.1 Background and focus of the chapter	100
5.2 Crystallographic description	100
5.3 Photophysical studies	101
5.4 Surfactant interaction	103
5.5 Conclusion	106
References	106
Appendix chapter 5	107
CHAPTER 6: The aggregation and optical properties of a Quinoxaline scaffold as an acidochromic and solvatochromic urease tracker	
6.1 Background and focus of the chapter	111
6.2 Crystallographic evidences	111
6.3 Photophysical studies	111
6.4 pH sensitivity and other applications	115
6.5 Urease activity and microbial fermentation	117
6.6 Conclusion	119
References	119
Appendix chapter 5	121
Conclusion and Future Perspective	124
Curriculum Vitae	



Introduction



Institute of Technology Gu

Introduction

1.1 Supramolecular Self-assembly: A Brief Introduction

We are motivated to discover Nature from our surroundings which is an endless source of inspiration. Since nature has evolved sophisticated machinery that primarily consists of supramolecular assemblies of bio macromolecules and performs complex biological tasks in all organisms, researchers are all interested in uncovering the mysterious veil of nature (such as living organisms, especially cells) at molecular levels. The effective assembly of sizable supramolecular structures implies a precise balance between stereochemical properties (chirality), conformational flexibility, and noncovalent interactions. Building macromolecules from two or more chemical building blocks with noncovalent intramolecular forces is known as supramolecular chemistry. In the 1970s, Jean-Marie Lehn was the first to coin the phrase supramolecular chemistry. The mechanisms of some important interactions, including host-guest, self-assembly, and molecular recognition in representative applications from material science to biological chemistry, are identified by these weaker interactions (2-250 kJ/mol) than covalent bonds (100-400 kJ/mol), which include the π -interaction, H-bonding, electrostatic interaction, hydrophobic interaction, and Van der Waals forces. These interactions play a remarkable function in promoting the self-assembly of the molecular components by aligning them in an ordered form.

Nature achieves complex processes through vast molecular frameworks, which are impossible to accomplish through monomeric versions. A supramolecular chemist's objective is to create the most basic molecular building blocks capable of assembling into supramolecular assemblies with unique functionalities that cannot be performed by a single molecule or group of molecules. These molecular architectures can serve a variety of purposes, including catalysis, molecular recognition, transport mechanisms, and unique magnetic and optical properties.^{1.1-1.4}

Supramolecular self-assembly has rapidly grown into an interdisciplinary field as a result of the different approaches used by chemists. Nature provides us with many inspiring examples of self-assembled nanostructures which are quite vital in the sustenance and maintenance of life, i.e., folding of polypeptide-based chains, formation of cell membranes by aggregation of phospholipid bilayers, nucleic acids, polymer, metalloproteins, dendrimer etc. The DNA double helix structure is one of the most prominent examples; it consists of two polymeric intertwined strands that are held together by π -stacking and H-bonding between their complementary base pairs.^{1.5-1.10}

One of the finest supramolecular assembly studied is tubular protein structures in the tobacco mosaic virus (TMV) capsid. Beijerinck discovered the TMV virus in the late nineteenth century after identifying an infectious agent as the cause of disease in tobacco plants. Rosalind Franklin proposed its general structure in the 1950s, and it consists of a helical coat structure enveloping a single stranded RNA molecule. The TMV helical coat structure consists of 2130 identical coat

particles (CP), which self-assemble into a right-handed helix; 300 nm in length, 18 nm in diameter with a 4 nm inner channel. It is supposed that assembly begins when a two-layered disk (named 20S disk after its sedimentation coefficient) contained of two rings of 17 CPs each recognises an RNA sequence. This recognition order enables a hydrogen-bonding pattern between the RNA bases and the RNA base binding sites of the 20S aggregate causing the RNA loop to fold. The RNA loop is then pulled through the TMV coat particle as additional short helix aggregates stack on top of the nucleation disc (Figure 1.1). TMV has a significantly robust structure, exhibiting stability at high temperatures as 90 °C, also stable at a pH range of 3.0–9.0 and it shows resilience to organic solvents such as acetone, ethanol, and water containing DMSO and THF. Remarkably, the TMV species are capable of aggregating into larger units, such as fibers, which can be caused in vitro by increasing the particle or / and ion concentration.^{1,11}

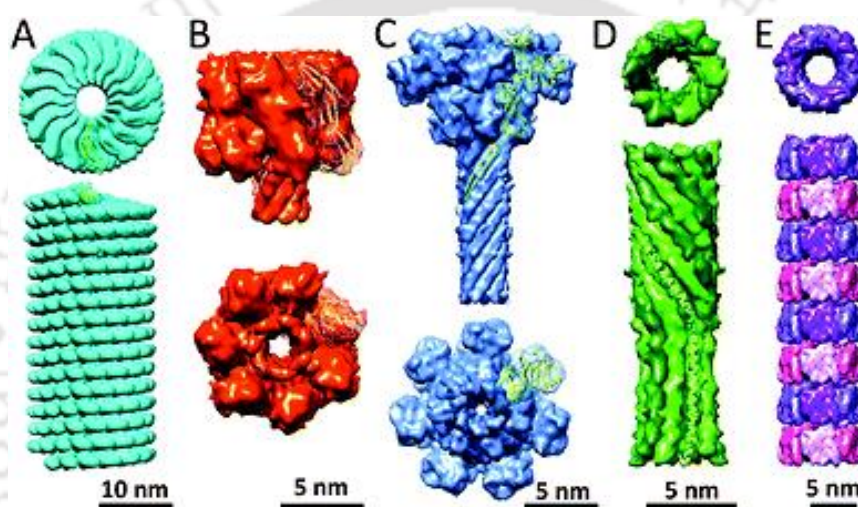


Figure 1.1: Tubular protein assemblies: (A) TMV (PDB: 4UDV). The side view only displays part of the length of the helical TMV assembly; (B) α -hemolysin pore complex (PDB: 7AHL); (C) antrax protective antigen pore (PDB: 3J9C); (D) PhiX174 bacteriophage tail (PDB: 4JPP); (E) Hcp1 from *P. aeruginosa* (*Chem. Soc. Rev.*, **2016**,*45*, 24-39)

Another example of supramolecular architecture is chaperones. Chaperonins are cylindrically structured protein assemblies that belong to the molecular chaperones protein family. They, like other members of this family, help in proper protein folding and proteome maintenance. Chaperonins are classified into two groups: group I, which includes the cylinder and a removable cap, is present in bacteria (GroEL-GroES) alongside endosymbiotic organelles including mitochondria and chloroplasts (HSP60-HSP10). Archaea and eukaryotic cell cytosol contain Group II chaperonins, which have a built-in lid. Both chaperonin groups are made up of two stacked rings that are placed back-to-back. The two rings of group II are more complicated eight- or nine-membered heteromultimeric assemblies, in contrast to group I's heptameric rings, which are made up of identical 60 kDa subunits. The bacterial GroEL–GroES complex (Mw \approx 1 MDa) is focused by researchers and its very fascinating mechanism of action has been elucidated. The

open internal cavities of the two rings are 5 nm in diameter and are enclosed by a hydrophobic surface (Figure 1.2). The rings are prepared to engulf polypeptides with exposed hydrophobic surfaces in this configuration. On ATP binding, the GroEL ring draws a GroES cap, a protein ring comprising seven identical 10 kDa subunits. As a result, the open cavity transforms into an enclosed chamber with a hydrophilic lining, starting a drastic structural shift. Folding of the protein can happen in this protected environment, subsequently the chamber is re-opened to release the protein.^{1,11}

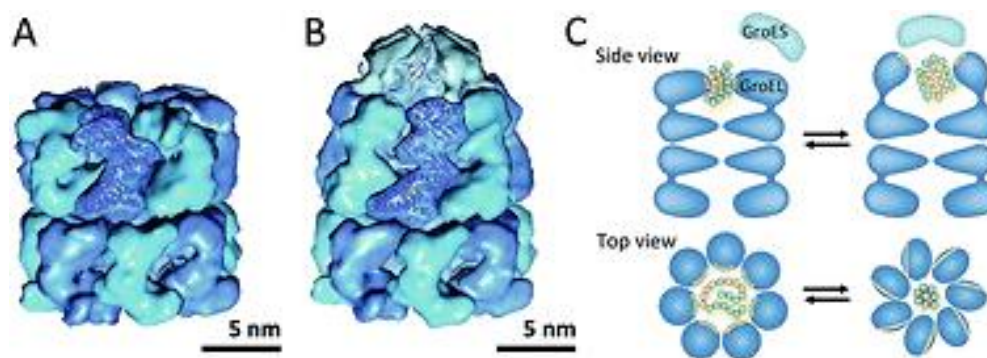


Figure 1.2: Chaperonin group I: (A) uncapped GroEL (PDB: 1OEL); (B) GroEL–GroES complex (PDB: 1SVT); (C) schematic overview of structural changes during GroEL-assisted protein folding in which the hydrophobic surfaces and residues are shown in yellow and the polar residues are displayed in green. Reprinted by permission from Macmillan Publishers Ltd: Nature Review Molecular Cell Biology, Saibil45 © 2013. (*Chem. Soc. Rev.*, **2016**,45, 24–39)

1.2 Aggregation Induced Emission (AIE): the special case of supramolecular aggregates

Aggregation-induced emission (AIE) is a photophysical phenomenon whereby the process of molecular aggregation leads to an enhanced emission from an ensemble than individual molecules. AIE research has achieved significant advances in material development, mechanistic investigation, and high-tech applications over the last 20 years. The accomplishments of AIE research show that molecular aggregates have numerous traits and functions that molecular species do not have. We summarise the advances in the field of AIE and related fields in this review. We concentrate on the novel features of materials achieved by molecular aggregates that go beyond the tiny molecular level. We believe that this review will spur further research into molecular ensembles at and beyond the meso level, resulting in important advances in material and biological science. Aggregation-induced emission (AIE) is a photophysical occurrence associated with luminophore aggregation. The aggregate formation in the AIE mechanism causes non-emissive luminophore /luminogens to emit. The luminogens with AIE characteristics are known as AIEgens.^{1,12-1.17}

B. Z. Tang et. a. reported a new AIE luminogen comprising two units of tetraphenylethene (BTPE) and it emits more efficiently than that with one tetraphenylethene unit in the solid state (Figure

1.3). The four phenyl rings in TPE are subject to an active intramolecular rotations (IMR) process in the solution state, which causes the emission intensity to decrease. However, the aggregation slowed down the IMR process by obstructing the non-radiative decay pathway, making TPE emissive. The emission spectra of BTPE in the THF solution exhibit a flat line parallel to the abscissa, demonstrating that it is not fluorescent. Later on, it began exhibiting distinct peaks in THF/water mixtures with large water fractions ($f_w=70\%$). Since water is a poor solvent for BTPE, the molecules must have aggregated in the THF-aqueous mixtures with high f_w ratios. The BTPE molecules self-assemble to form crystalline microfibrils that glow with 100% efficiency, producing aggregation-induced emission. These fibres can further assemble into thicker rods, as shown by the optical image. When photo-excited, the luminescent microwires emit a bright blue light. It is promising for a variety of technical applications due to its simple self-assembly and good EL performance.^{1.18}

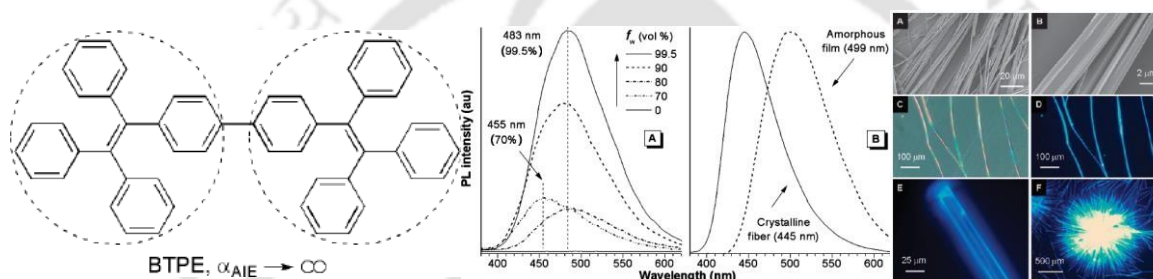


Figure 1.3: Left-Chemical structures. Middle-Emission spectra of (A) THF solution of BTPE (10 mM) and its aggregates suspended in THF/water mixtures with different fractions of water (f_w 70–99.5 vol%) and (B) its amorphous film and crystalline fibre in the solid state. Right-(A, B) SEM, (C) optical and (D–F) fluorescent images of the microfibrils of BTPE obtained by slow evaporation of its THF/ethanol solutions. (Reproduced with permission from ref. 1.57 Copyright 2010 RSC).

A series of AIEE active V-shaped naphthalimide derivatives are synthesized by Iyer and co-workers. In aqueous conditions, regardless of concentration or surface, 8-hydroxyquinoline (-NQ) functionalized naphthalimide derivative can spontaneously produce extremely fluorescent "nanoribbon"-like structures (Figure 1.4). The single crystal X-ray investigation indicated the classical head-to-tail - stacking as the primary driving factor for the J-type aggregation with distinctive self-aggregating behaviour.^{1.19}

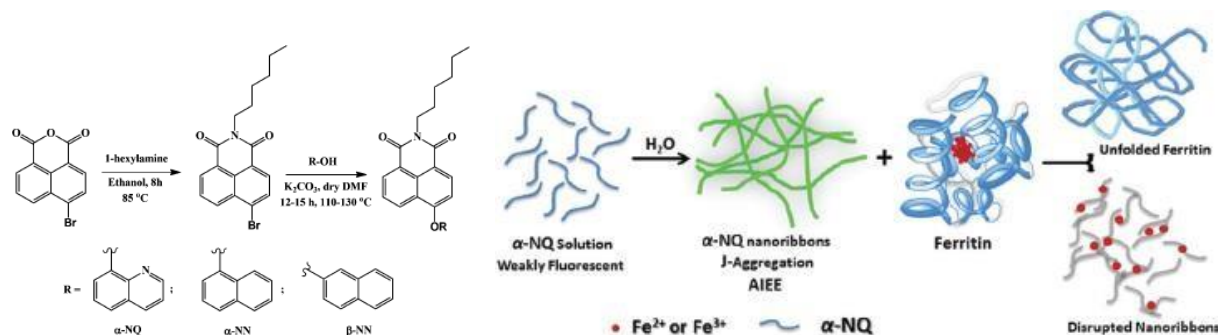


Figure 1.4: compounds α -NQ, α -NN and β -NN and illustration of the mechanism of protein unfolding and nanoribbon disruption using a fluorescent probe under physiological conditions with AIEE characteristics (Reproduced with permission from ref. 1.77 Copyright 2016 RSC).

Gunnlaugsson et. al synthesized a 4-amino-1,8- naphthalimide Troger's base functionalized with phenyl terpyridine and analysed its AIE properties. This synthesized molecule shows emission intensity in a higher percentage of water in aqueous-DMSO content. The FESEM analysis proves the formation of amorphous aggregates with the presence of an irregular distribution of spherical particles. This was further utilized as a fluorescent sensor for the chemo sensing of π -electron-deficient nitroaromatic. The highest fluorescence quenching was observed with picric acid.^{1.20}

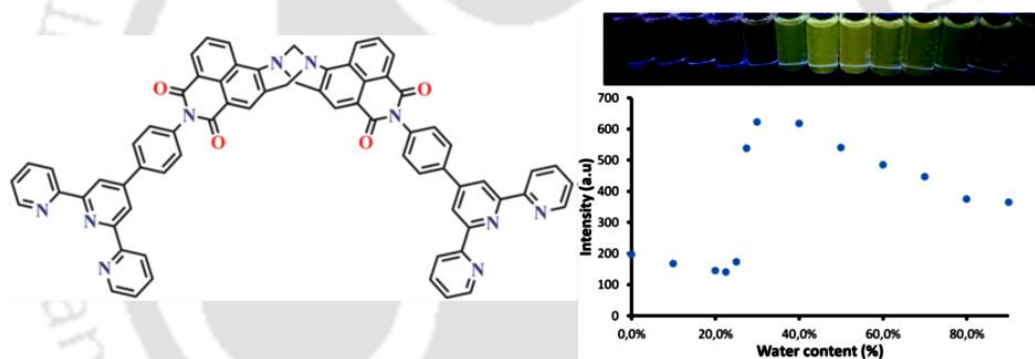


Figure 1.5: Structure of TBNap-TPy fluorophore studied and Intensity plot of TBNap-TPy ($c = 4.6 \times 10^{-6}$ M) in DMSO upon addition of water. Inset: Visible colour changes observed under UV lamp (ex. 360 nm). (*Chem. Commun.*, **2020**, 56, 2562).

Hou and co-workers designed a series of 4-N, N-dimethylamino aniline salicylaldehyde Schiff-base (DAS). Not only they showed distinctive aggregation Induced emission properties with various emissions intensities from green to red but also high fluorescence quantum yields in an

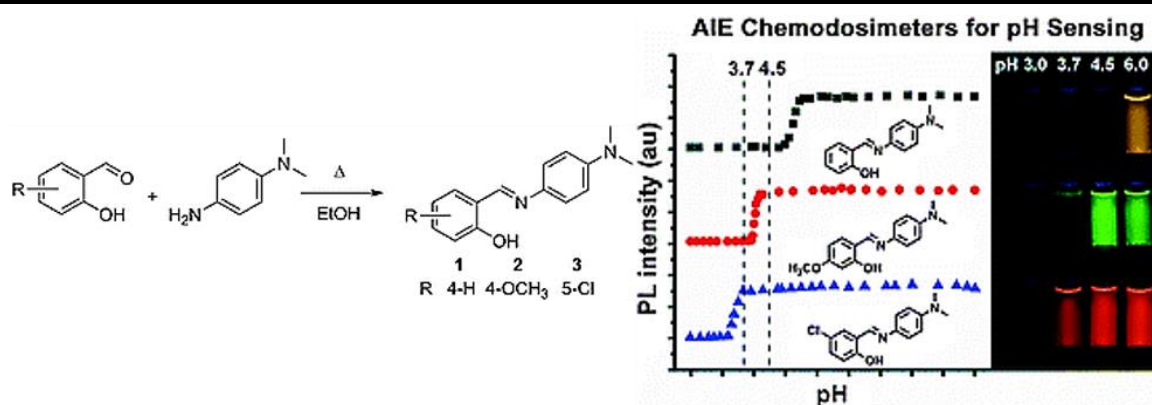


Figure 1.6: Synthesis of DAS the compounds. Fluorescence emission peak intensities of 1–3 as a function of pH value. (B) Fluorescence photographs of 1–3 in 99% water/EtOH (v/v) at different pH values. Conditions: the concentrations of compounds are 50 mmol L⁻¹. The excitation/emission wavelengths of 1–3 is 333/542, 338/513, and 356/580 nm, respectively. The photographs were taken under an irradiation of 365 nm UV light.

aggregated state. DAS compounds show pH-dependent optical characteristics. The luminous DAS compounds get hydrolyzed under acid conditions, resulting in a nonluminous mixture of 4-N, N-dimethylamino aniline and the corresponding salicylaldehyde derivatives. The varying substituent groups in the salicylaldehyde motif result in the difference in titration jump pH, which ensures their potential application prospects in pH sensing. Their work provides a new direction for rising pH chemo dosimeters based on AIE gens.^{1,21}

Mahapatra and group synthesized and designed an unsubstituted naphthalimide-based dipeptide to deduce its photophysical properties in the solid and self-assembled state. It was noticeable that the structurally simple luminogen displays J-type aggregation in the gel, solid, and solution states. A discussion has been laid out on the different structural facets of this naphthalimide derivative in the solid state. The amide-based hydrogen bonding interaction leads the arrangement in the J-type fashion. J-type aggregation was ascertained by different spectroscopic techniques in gel and solution states. The aggregation-induced emission property in the aqueous solution was employed in live cell imaging. They suggested that these naphthalimide units can be easily tuned by chemical synthesis to enhance additional functionality for the right fluorescence and self-assembly properties.^{1,22}

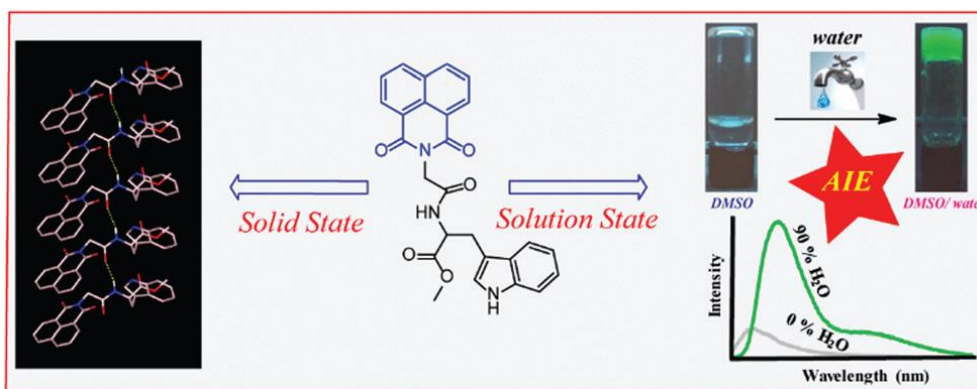


Figure 1.7: Chemical structure of the studied naphthalimide derivative (NMI-GW-OMe) and its supramolecular assemblies in the solid and solution state. (*Mater. Adv.*, 2020, 1, 3532).

Mukherjee and group reported star-shaped donor-acceptor (D-A) type conjugated molecules containing triphenylamine end-capped arms. The photophysical properties of these compounds were analysed systematically through spectroscopic and theoretical methods. Several photophysical properties were deduced eg; high extinction coefficient, large Stokes shift, and distinct solvatochromic effect. A binary solvent mixture of THF-water was used to show aggregation-induced emission in these systems. The aggregation was assured by electron microscopy viz; TEM, SEM and dynamic light scattering experiments. They demonstrated by tuning the acceptor motif colours can be controlled from blue to yellow as well as by modulating the ratios between these two compounds almost pure white light can be achieved. Their experimental outcomes and findings have the possibility for the growth of radiating materials for applications in lighting and display devices.^{1,23}

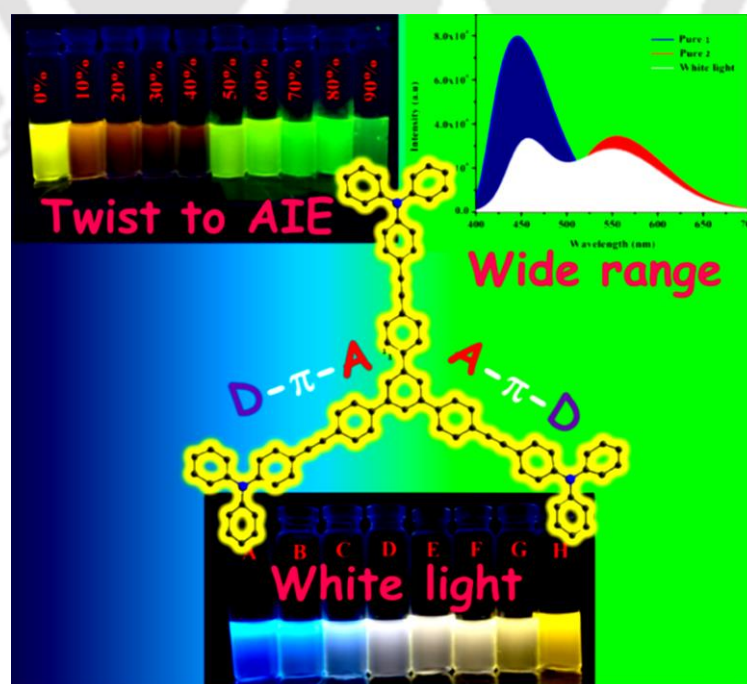


Figure 1.8: Schematic representation of the work. (*ACS Omega* 2018, 3, 13757–13771).

Thilagar and co-worker have synthesized four “V” shaped 1,8-naphthalimides and calculated their fluorescence quantum yields correlated to their molecular flexibility. Among the four congeners, one of them proved to be an AIEGen via the formation of fluorescent nanoaggregates. They reported THF-water binary system for assessing the AIE behaviour. The thiol-containing AIEGen was utilized as a chemodosimeter for detecting Hg (II) ions in solution. This selective chemodosimeter showed an 8.7 times enhancement in fluorescence intensity upon the addition of Hg (II).^{1,24}

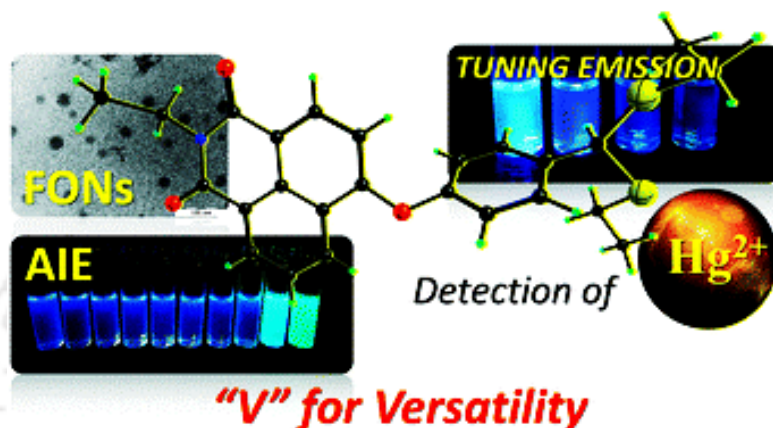


Figure 1.9: Schematic representation of the work. (*Chem. Commun.*, 2013,49, 7292-7294).

Yakali reported synthesized propeller-shaped as well as nonconjugated-chiral molecules which were examined by SC-X-ray crystallography, and theoretical and photophysical studies. Moreover, their electrochemical properties and thermal analysis were done using cyclic voltammetry and thermal gravimetric analysis, respectively. The molecule showed aggregation-induced enhanced

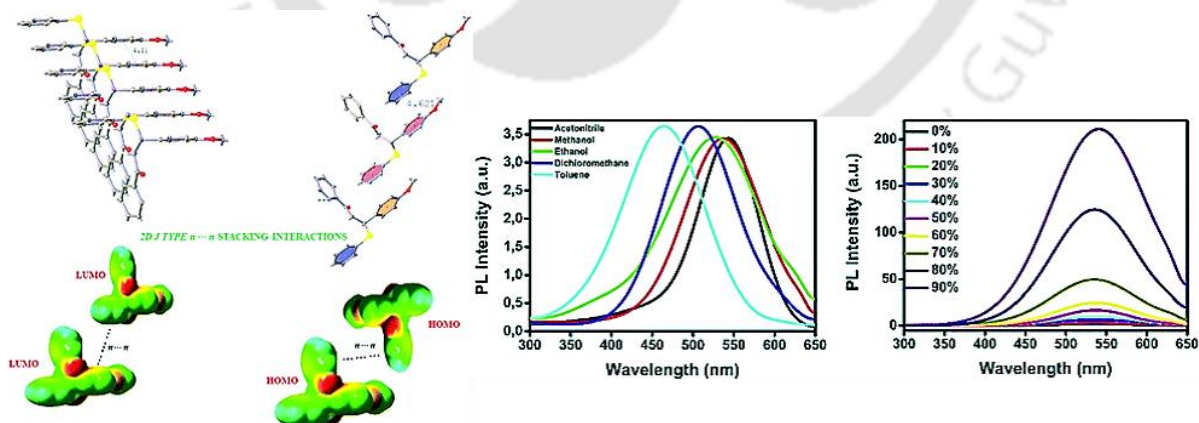


Figure 1.10: The views of the π - π stacking interactions of the molecule with the molecular orbital density. Fluorescence spectra of the compound in different solvents (2×10^{-5} M) and different concentrations. (*Phys. Chem. Chem. Phys.*, 2021, 23, 11388).

blue emission in the single crystal phase and this observation is attributed to strong J-type stacking and restricted intramolecular rotation (RIR) between the phenyl rings in the molecule's crystal

phase. The solvent polarity-caused emission also confirmed the AIEE occurrence. The uniqueness lies in the development of nonconjugated-chiral molecules showing strong blue emission in the solid phase because designing deep blue organic emitters has been most challenging owing to their low emission efficiency and low stability. The importance of non-conjugation and chirality in the synthesised molecule lead to a new, unique AIEE material and paved the way for the design of a nonconjugated chiral fluorescent compound for optoelectronic material.^{1,25}

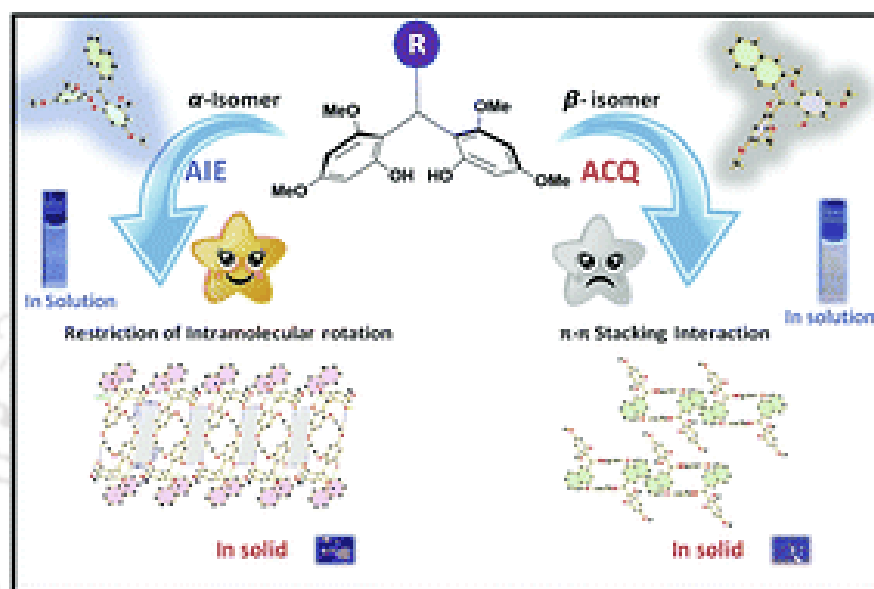


Figure 1.11: Schematic representation of the work. (*New J. Chem.*, **2022**, 46, 7212).

Saha and his group have achieved modulating photophysical properties by a slight structural change in triaryl methane (TAM) derivatives rendering their distinguished and wide applications in the medicinal and dye industries along with the progress of organic functional materials. They reported two isomeric TAM derivatives, which display fair differences in fluorescence properties in the solid state. The common (ACQ) ‘aggregation caused quenching’ is repressed by a change in the substitution position of the naphthalene derivatives, leading to unusual and desired ‘aggregation induced emission’ (AIE). Apart from photophysical properties, both isomers show the same antimicrobial activity.^{1,26}

Das et. al reported two fluorogenic Schiff base molecules pyrene and anthracene derivatized having both donor and acceptor moieties, respectively. It triggered the AIE activity examined through spectroscopic and microscopic analysis. A Binary solvent system; CAN-water was chosen for the AIE activity analysis. Photophysical results suggested probable aggregation-activated fluorescence enhancement through Restriction of Intramolecular Motion. The aggregated turned out to be an efficient hydrazine sensor via fluorescence Turn-On signal. The detection limits (LODs) for hydrazine were experimented to be 0.5 ppb and 0.4 ppb for pyrene and anthracene

derivatives, respectively. The sensing process can be ascribed to the hydrogen bonding-induced disaggregation occurrence of AIEgen aggregates. This sensing aptitude was also used in the fluorescence imaging experiment to examine hydrazine in plant roots and mammalian cells.^{1,27}

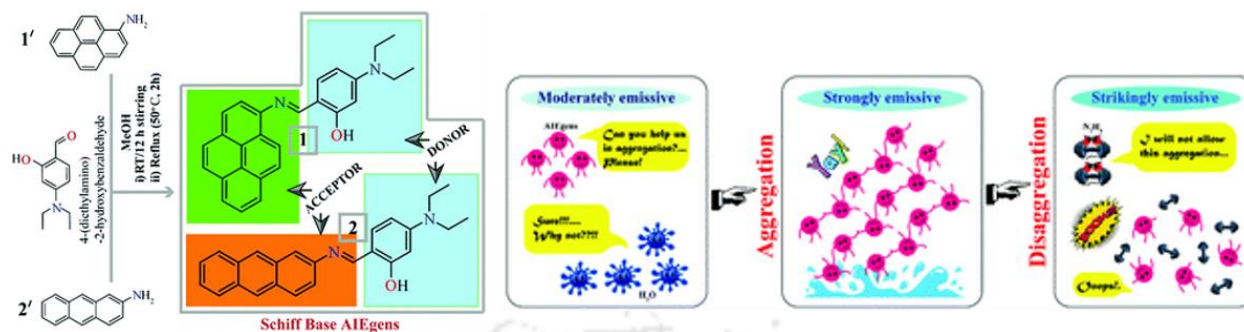


Figure 1.12: Schematic representation of the work. (*J. Mater. Chem. C*, 2021,9, 8596-8605).

1.3 Detection of analytes: aggregation/disaggregation approach

The necessity to recognise and detect environmentally and biologically essential species has resulted in significant attempts to build suitable sensors and probes. Compared with conventional analytical approaches [i.e., liquid-chromatography, gas-chromatography and mass spectrometry] probes bear distinct advantages, such as straightforward signal amplification, technical simplicity, fast processing time and low costs, which all add up to their tremendously huge impact on the sensing field. Despite the significant number of probes synthesized each year, their sensing mechanisms are limited to only a few, including photo-induced electron transfer, intramolecular charge transfer, resonance energy transfer, and aggregation-induced emission (AIE). By varying their recognising, reporting, or motifs, these sensing systems are used repeatedly in the sophisticated development of novel probes. The investigation of a novel sensing mechanism is comparatively underdeveloped in comparison to the efforts put forth in developing innovative probes. The demand for a unique sensing mechanism opens up new possibilities for probe design. Herein, we dealt with rising sensing mechanism based on signal on-off caused by disaggregation from aggregated probes. Though a few research papers have been published using this process to produce novel probes, the importance of "disaggregation" in probe development requires thorough examination.^{1,28-1.30}

Aggregation denotes the formation of clusters of particle groups from their singular individual ones (monomers). Aggregation of probes at a high concentration is a frequently observed phenomenon, especially in aqueous solutions, due to their non-covalent interactions like hydrophobicity or intermolecular van der Waals-like attractive forces among the molecules. While the solution may appear homogeneous, the compounds are "dispersed" in the solvent rather than "dissolved".

Sakurai *et al.* synthesized a sumanene derivative functionalized with triphenyl benzene units which were found to display aggregation-induced emission enhancement (AIEE). It showed strong yellow light emission. A disaggregation process was observed and initiated after the addition of caesium cations (Cs^+). The disaggregation manifested as a turn-off fluorescent signal. The driving force for the disaggregation behaviour was due to the formation of the sandwich complex between Cs^+ and two sumanene molecules. This interaction is caused by the site-selective π -cation interaction that occurs following insertion in the concave side of sumanene. Also, the Cs^+ detection process was found to be selective, as no differences in the emission intensities between the samples after addition with Cs^+ only or with Cs^+ in the presence of other relevant cations.^{1.31}

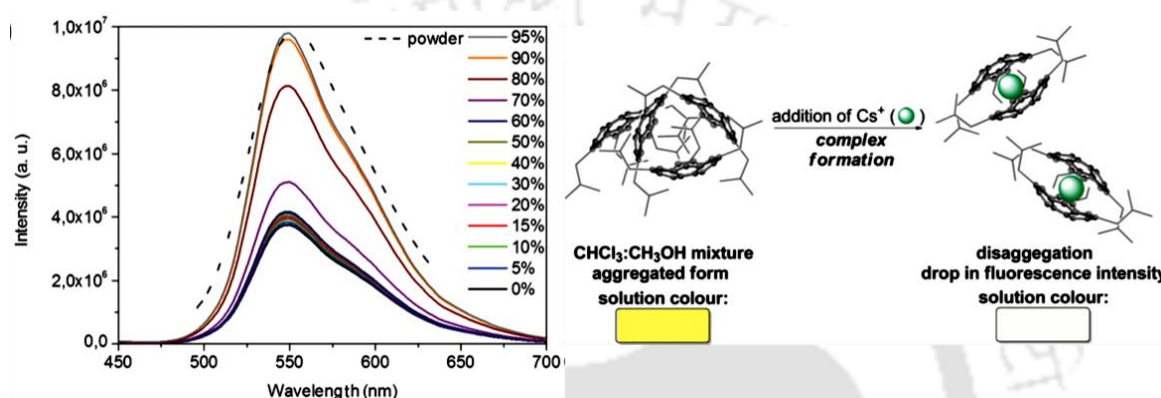


Figure 1.13: Emission spectra of sumanene derivative ($\lambda_{\text{ex}} = 360 \text{ nm}$) measured in different CHCl_3 – CH_3OH compositions and Graphical representation of the proposed recognition process. (*Chem. Commun.*, **2021**, 57, 343).

Thayumanavan and co-workers developed a coumarin-labelled unimer for protein binding-induced supramolecular disassembly strategy with the ratio of excimer and monomer fluorescence as the tool for protein sensing and quantification. They synthesized a dendritic molecule which was modified with a phenyl sulfonamide ligand and 7-diethyl aminocoumarin. The coumarin motif was combined into the hydrophobic part of the amphiphile, which in turn encapsulates this functionality into the hydrophobic core of the amphiphilic nano-assembly, rendering an excimer fluorescence. The incorporation of phenyl sulfonamide in the hydrophilic face of the amphiphile allows the ligand to be in the solvent-exposed shell of the nano assembly, assuring accessibility to protein binding. Based on lock and key strategy the binding of the probe displays appreciable selectivity and quantification accuracy to the protein. This work features the output signal as the monomer and excimer emission intensity ratio instead of fluorescence intensity, rendering better results for interferences, such as from metal quenching. The selective sensing and precise quantification relied on protein binding-induced supramolecular disassembly.^{1.32}

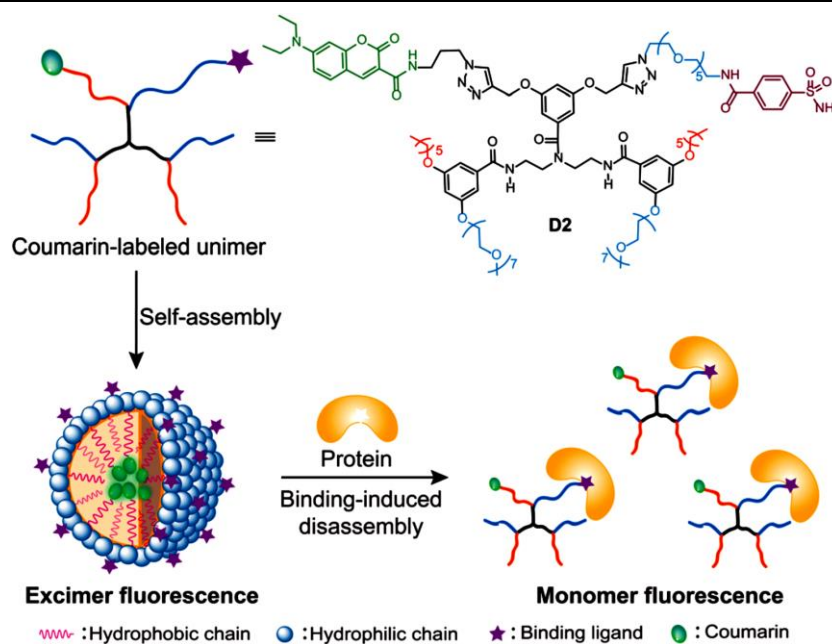


Figure 1.14: Schematic representative of protein binding-induced disassembly using excimer–monomer transformation. (*Chem. Commun.*, **2021**, 57, 9776).

Prasad and co-workers developed and stabilized spherical, urchin, flower, and polydispersed AuNPs via pomegranate (*Punica granatum*) peel extract. Upon addition of Fe (III) ions, the interaction between the Fe(III) and capping agent causes the AuNPs to aggregate, with a visual colour change. The AuNP–Fe system disaggregates in the presence of As(III) ions only, leading to colour change in the visible region. Apart from the chemo sensing of Fe(III) via colour change, the adsorbed Fe(III) ions also form an alloy along with core-shell nano-systems with the AuNPs. They suggested from a literature review that a strong interaction is probable between As(III) and α -Fe₂O₃. The chemosensing via the disaggregation process results in a colour change. The detection limit for As(III) by the naked eye was calculated to be 10⁻⁴ M. The outcomes summed together show that the presence of pomegranate peel extract is important for the detection of metal ions, due to its rich content of functional groups.^{1.33}

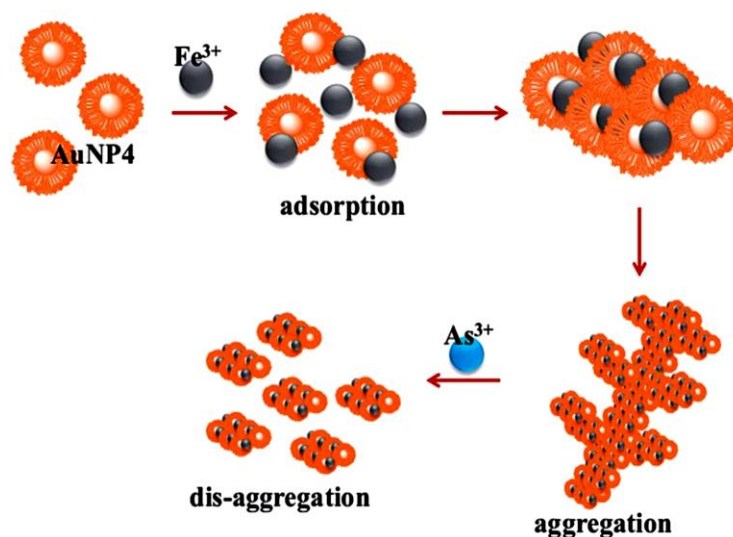


Figure 1.15: Proposed mechanism for the aggregation and disaggregation of AuNP₄ with the addition of Fe³⁺ and As³⁺ ions. (*Anal. Methods*, 2015, 7, 168–174).

Sessler et. al reported a new approach to sensing anion that involves excimer disaggregation-induced emission (EDIE). It comprises the anion-facilitated disaggregation of the excimer formed out of a cationic macrocycle via increment in fluorescence intensity. The proposed strategy was used in fluorescence “turn-on” solution-phase detection of the HP₂O₇³⁻ and H₂PO₄⁻ oxoanions. The anions are effective in disintegrating these aggregated species and leading to the production of fluorescent monomeric anion complexes whose structure prevents efficient aggregation. They affirm that disaggregation-based approaches concerning excited-state species play a role in the design of new sensor systems.^{1,34}

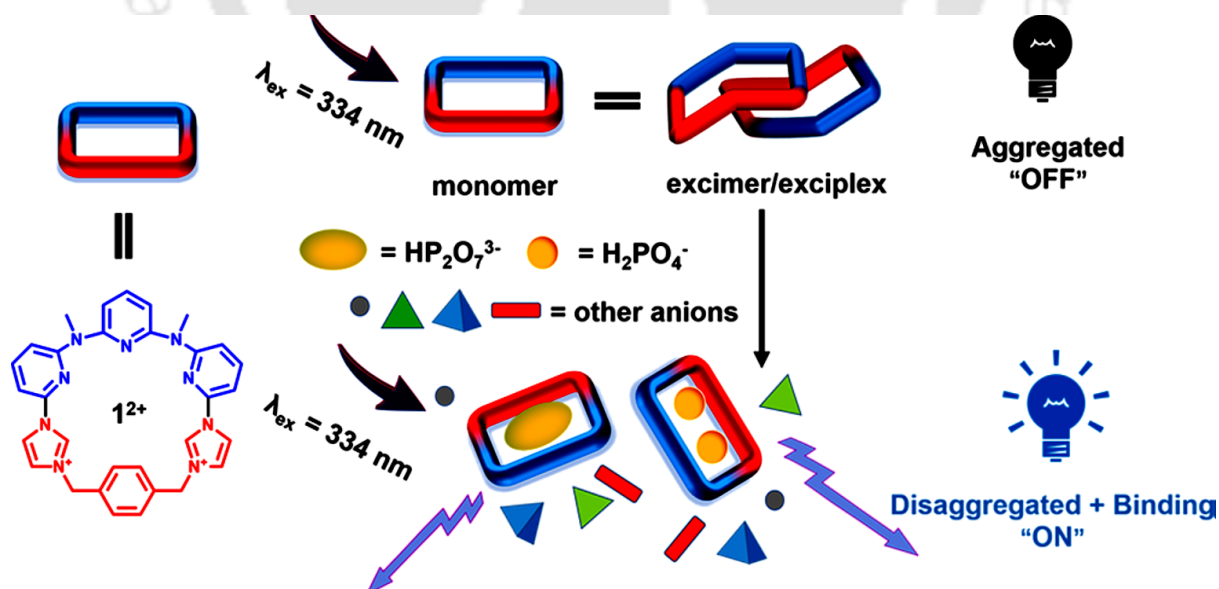


Figure 1.16: Schematic representation of the work. (*J. Am. Chem. Soc.* 2019, 141, 4597–4612).

Gour and her group synthesized a self-assembling acyl-thiourea-based sensor N-((6-methoxypyridine-2-yl) carbamothioyl}benzamide (NG1) with fluorescent panchromatic fibres and its two-fold sensing properties for the successive detection of Cu^{2+} ions and lactic acid. These

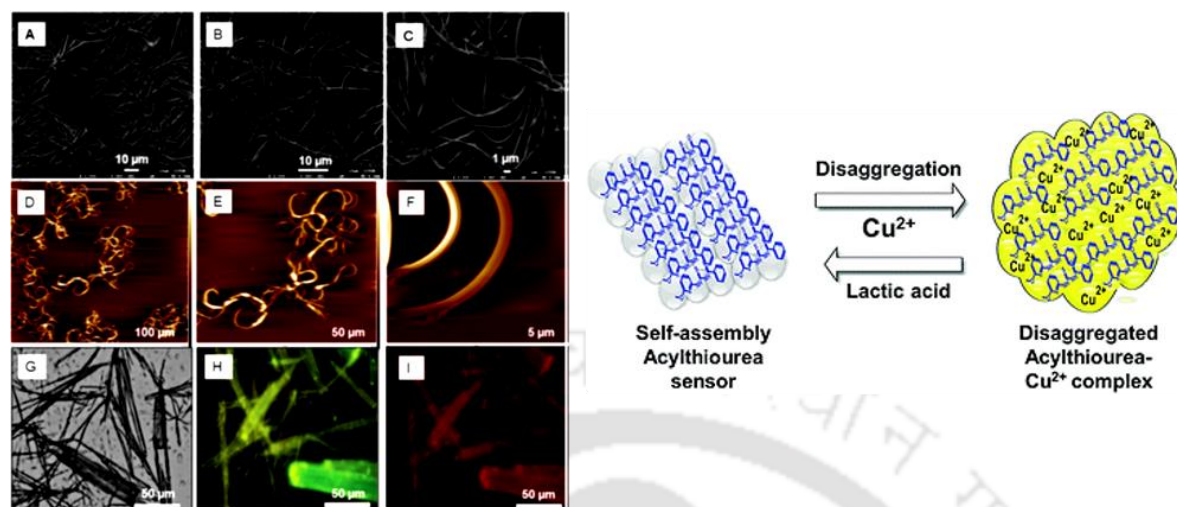


Figure 1.17: Microscopy images of self-assembled structures of NG1 (1 mM) in 70% aqueous methanol. (A) SEM at 10 mm scale; (B) SEM at 5 mm scale; (C) SEM at 1 mm scale; (D) AFM at 100 mm scale; (E) AFM at 50 mm scale bar; and (F) AFM at 5 mm scale; (G) bright field images of the fibres of NG1, (H) under the green filter, and (I) under the red filter. Graphical representation of the work. (*Soft Matter*, **2021**, *17*, 4304–4316).

panchromatic fibres from NG1 were disrupted in addition to Cu^{2+} ions and this was observed by a visual colour change i.e., colourless to yellow. Further addition of lactic acid to the NG1 + Cu^{2+} solution, causes induced re-aggregation to fibrillar structures and the colour of the solution restores colourless. The specificity and sensitivity of NG1 for sensing Cu^{2+} ions are examined using various spectroscopic and biophysical analyses. The layout of the experimental and theoretical outcomes along with cell studies provides a fair understanding of the mechanism of the probe as well as proper practical utility for future applications.^{1,35}

Kumar and his group synthesized 1-(p-Terphenyl)-benzimidazolium (TRIPDTP) molecules actively self-assemble to form rodlike structures in the aqueous medium. Upon gradual addition of picric acid (PA) to these aggregates causes aggregation/disaggregation process to complex morphological structures (10^{-12} – 10^{-10} M PA) and spherical aggregates (10^{-9} – 10^{-8} M PA). Visible fluorescence quenching is observed. The other Nitroaromatics Compounds, including 2,4-Dinitrophenol, TrinitroToluene, and Chloro-Dintrobenzene, also caused efficient fluorescence quenching but only at higher concentrations. The proposed study provides a new perception of the design of self-assembled molecular probes for the recognition of nitro-aromatic explosives.^{1,36}

Montalti and coworkers developed fluorogenic nanoparticles (NPs) capable of sensing varying physiological environments and responding with disaggregation and fluorescence switching OFF/ON. Thus emerging as powerful tools in nanomedicine as they can merge

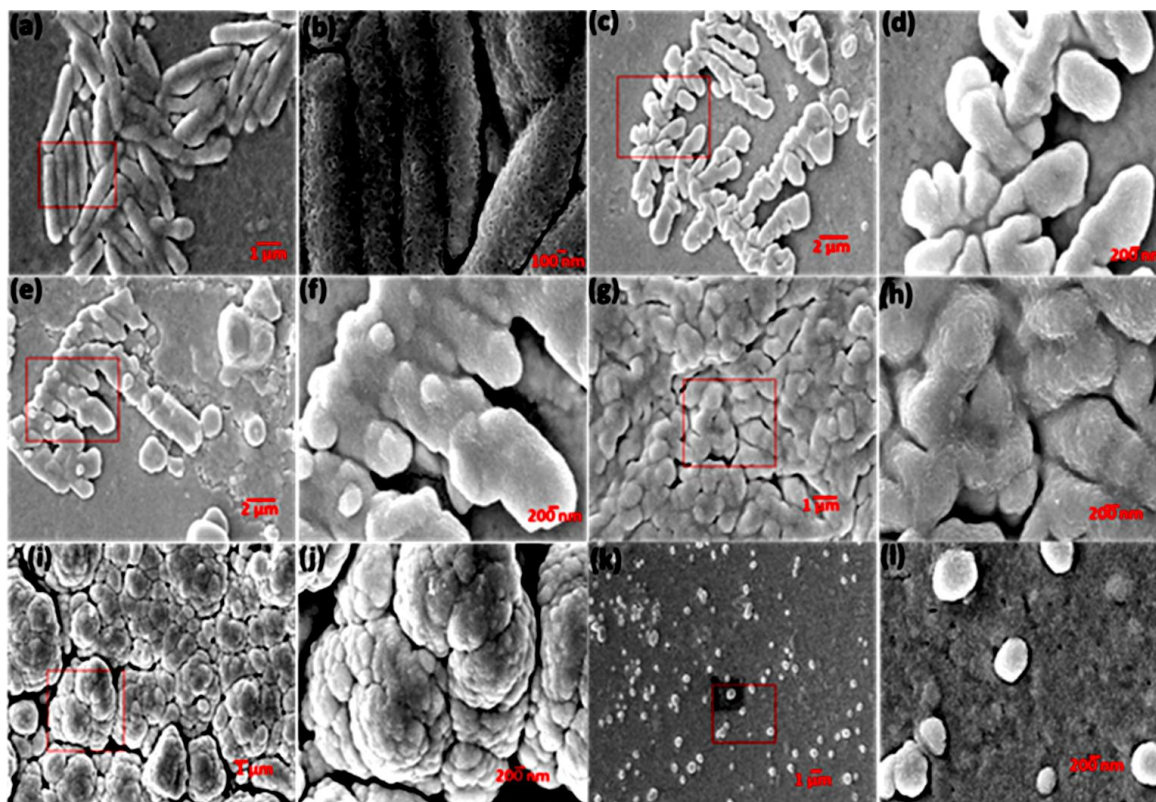


Figure 1.18: Morphological changes in TRIPOD-TP upon the addition of various amounts of picric acid. (a) [PA] = 0 M; (b) magnified view of selected area in (a); (c) [PA] = 10^{-12} M; (d) magnified view of selected area in (c); (e) [PA] = 5×10^{-11} M; (f) magnified view of selected area in (e); (g) [PA] = 10^{-9} M; (h) magnified view of selected area in (g); (i) [PA] = 5×10^{-8} M; (j) magnified view of selected area in (i); (k) [PA] = 2×10^{-7} M; (l) magnified view of selected area in (k). (*ACS Appl. Mater. Interfaces* **2015**, *7*, 10491–10500).

diagnostics with therapeutic action. They demonstrated that polymerization, which is mainly interesting as it allows the direct polymerization of functional monomers, can be applied to produce pH-responsive fluorogenic micelles. These micelles are stable at physiological pH, they quickly disaggregate at pH 5 leading to a rise in fluorescence “switch ON”. The change was confirmed with in vitro experiments with a model cancer cell line, in which the drop in the pH and the endolysosomal pathway give rise to green fluorescence. This is an important synthetic base in which therapeutics can be simply incorporated through direct polymerization allowing the advance of novel nano-theranostic agents in which fluorescence activation is followed by drug release at the targeted site.^{1.37}

Koner and his group presented the self-assembly and simultaneous disassembly of a pyrene-based system in the addition of aliphatic biogenic di- and polyamines in the solution. This work demonstrates how biogenic amines govern the transient assembly and disassembly of a pyrene dianhydride-based motif through the nucleophilic reaction. The progress of the transient assembly using ground-state pre-association and disassembly was confirmed by detailed spectroscopic and microscopic studies. They showed that selective conjugates, which were present in the lysosomal

1.4 Advantages of fluorescence-based methods for detection of analyte/guest

Detection of various analytes via specific molecular receptors relies on the fact that the recognition of the analyte should produce some readable responses, which can be optical (change of fluorescence or colour), an electrochemical or sol-gel transition, that can confirm the presence along with the concentration of the analyte. However, out of these several sensing techniques, optical sensors-based recognition of analyte is broadly favoured for their ease to handle, simplicity, reasonable, fast response time, and steady signal understanding capacity,^{1.39- 1.40} where either molecular interactions or a chemical reaction cause changes the optical outputs. Predominantly optical sensors are categorized into two parts (1) absorbance-based or colorimetric sensors and (2) fluorescence-based or luminescent sensors. The host or receptor molecule (the recognition site) is connected with a chromophore and/or fluorophore/ luminophore termed as the signalling unit, which can respond to the recognition process through perceptible as well as measurable colorimetric or fluorometric indication.^{1.41} Thus, out of available detection tools for an analyte, fluorescence-based detection of an analyte has a suitable signal-to-noise ratio, fast response, adaptability in nature, extensive stability, low-cost, hassle-free sample preparation and fairly simple handling.

To act as a fluorescence sensor, the emission features (e.g., enhancement or quenching of fluorescence intensity) regarding the detection of analytes must undergo perceptible change via certain mechanistic pathways. The fluorescence emission characteristics are governed by various fluorescence mechanisms involved in the detection and measurement of the chemical species that are being subjected. The parent molecule and the formed products display different electronic charge distributions in their different energy states. The following changes in the electronic charge distribution of the probe upon binding with guest analytes can be attributed to certain mechanisms. Among them, aggregation-induced emission (AIE), photoinduced electron transfer (PET), fluorescence resonance energy transfer (FRET), intramolecular charge transfer (ICT), chelation induced enhanced fluorescence (CHEF), twisted intramolecular charge transfer (TICT), C=N isomerization, electronic energy transfer (EET), excimer/excimer formation and are the most significant process associated with photophysical studies.^{1.42, 1.44} Where ICT, ESIPT, and FRET mechanisms generally shift the position of the wavelength in emission spectra (ratiometric phenomena).

The importance and popularity of the chemosensors, especially the optical (chromogenic and fluorogenic) chemosensors have attracted the attention of analytical chemists at large all over the world. There remains a demand for developing new sensing probes is laid on their extensive advantages and their applications. It is no longer sufficient to simply form a system that is selective to a single target analyte. Multiple other factors like stability and solubility of the probe, ratiometric

or switch-on-off response, countable stokes shift and extinction coefficient, regarding cytotoxicity, cell permeability etc. have become similarly important to be introspected. Several mechanisms, including fluorescence resonance energy transfer (FRET), photoinduced electron transfer (PET), intramolecular charge transfer (ICT), twisted intramolecular charge transfer (TICT), metal–ligand charge transfer (MLCT), and, electronic energy transfer (EET), and excimer/exciple formation have been used extensively to design fluorescent sensors. However fluorescent probes synthesized by these tactics often meet drawbacks like aggregation-caused quenching effect, which limits them from being used at high concentrations and hence causes decreased fluorescence and compromised sensitivity.

1.5 Concluding Remarks and Objective of Thesis

- Our concern is to devise molecular frameworks with varying flexibility which can aggregate when subjected to certain environmental conditions. Also, to monitor and compare these aggregating species via an optical output and microscopy. The aggregation must not lead to commonly occurring aggregation-caused quenching but rather to repress the common phenomenon by synthetic tuning to an unusual and useful property i.e., aggregation induced emission. Furthermore, to employ these aggregation molecules in analytical, photophysical and synthesis of materials. In a nutshell, objective of my thesis work is,
- To synthesize the fluorogenic and chromogenic probes, for the optical detection of target analytes via simple steps.
- To examine the aggregation features of amphiphile/ non-amphiphile molecules in aqueous/mixed aqueous medium.
- To probe the photophysical changes and mechanism occurring in the aggregating and chemo sensing processes.
- Application of these synthesized compound ds in real samples for analytical and environmental benefits.

References:

1. Chen, S.; Costil, R.; King-Chi Leung, F. and Feringa, B. L. Self-Assembly of Photoresponsive Molecular Amphiphiles in Aqueous Media, *Angew. Chem. Int. Ed.* **2021**, *60*, 2–26.
2. Tu, Y.; Peng, F.; Adawy, A.; Men, Y.; Abdelmohsen, L. K. E. A. and Wilson, D. A. Mimicking the Cell: Bio-Inspired Functions of Supramolecular Assemblies, *Chem. Rev.* **2016**, *116*, 2023–2078.
3. Wang, C.; Chen, Q.; Xu, H.; Wang, Z. and Zhang, X. Photoresponsive Supramolecular Amphiphiles for Controlled Self-Assembly of Nanofibers and Vesicles, *Adv. Mater.* **2010**, *22*, 2553–2555.

4. Das, K.; Gabrielli, L. and J. Prins, L. Chemically Fueled Self-Assembly in Biology and Chemistry, *Angew. Chem. Int. Ed.* **2021**, *60*, 2–26.
5. Song, S.; Song, A. and Hao, J. Self-assembled structures of amphiphiles regulated via implanting external stimuli, *RSC Adv.*, **2014**, *4*, 41864.
6. Syamala, P. P. N.; Soberats, B.; Górral, D., Gekle, S. and Würthner, F.; Thermodynamic insights into the entropically driven self-assembly of amphiphilic dyes in water, *Chem. Sci.*, **2019**, *10*, 9358.
7. Boyle, B. M.; Collins, J. L.; Mensch, T. E.; Ryan, M.D.; Newell, B. S.; and Miyake, G. M.; Impact of backbone composition on homopolymer dynamics and brush block copolymer self-assembly, *Polym. Chem.*, **2020**, *11*, 7147.
8. Kundu, N.; Banik, D. and Sarkar, N.; Self-Assembly of Amphiphiles into Vesicles and Fibrils: Investigation of Structure and Dynamics Using Spectroscopy and Microscopy Techniques, *Langmuir* **2018**, *34*, 11637–11654.
9. Zhang, J.; Liu, K.; Müller, K. and Yin, M.; Self-assemblies of amphiphilic homopolymers: synthesis, morphology studies and biomedical applications, *Chem. Commun.*, **2015**, *51*, 11541.
10. Wang, C.; Wang, Z. and Zhang, X. Amphiphilic Building Blocks for Self-Assembly: From Amphiphiles to Supra-amphiphiles, *Acc. Chem. Res.* **2012**, *45*, 608–618.
11. Pieters, B. J. G. E.; van Eldijk, M. B.; Nolte, J. M. R. and Mecerovc, J.; Natural supramolecular protein assemblies, *Chem. Soc. Rev.*, **2016**, *45*, 24.
12. Zhao, Z.; Zhang, H.; Lam, J. W. Y. and Tang, B. Z. Aggregation-Induced Emission: New Vistas at the Aggregate Level, *Angew. Chem. Int. Ed.* **2020**, *59*, 9888–9907.
13. Nabara, M.; Yamamoto, S.; Nishiyama, Y. and Nagatani, H. Aggregation-Induced Emission of Water-Soluble Tetraphenylethene Derivatives at Polarized Liquid-Liquid Interfaces, *Langmuir* **2020**, *36*, 10597–10605.
14. Jana, P. and Kanvah, S. Aggregation-Induced Emission and Organogels with Chiral and Racemic Pyrene-Substituted Cyanostyrenes, *Langmuir* **2020**, *36*, 2720–2728.
15. Meher, N. and Iyer, P. K. Functional group engineering in naphthalimides: a conceptual insight to fine-tune the supramolecular self-assembly and condensed state luminescence, *Nanoscale*, **2019**, *11*, 13233–13242.
16. Prakash, K. T.; Singh, N. and Venkatesh, V. Synthesis of novel luminescent copper nanoclusters with substituent driven self-assembly and aggregation induced emission (AIE), *Chem. Commun.*, **2019**, *55*, 322–325.
17. Externbrink, M.; Riebe, S.; Schmuck, C. and Voskuhl, J. A dual pH-responsive supramolecular gelator with aggregation-induced emission properties, *Soft Matter*, **2018**, *14*, 6166–6170.
18. Zhao, Z.; Chen, S.; Shen, X.; Mahtab, F.; Yu, Y.; Lu, P.; Lam, J. W. Y.; Kwok, H.S. and Tang, B.Z. Aggregation-induced emission, self-assembly, and electroluminescence of 4,4'-bis(1,2,2-triphenylvinyl) biphenyl, *Chem. Commun.*, **2010**, *46*, 686–688.
19. Meher, N.; Roy Chowdhury, S. and Iyer, P.K. Aggregation induced emission enhancement and growth of naphthalimide nanoribbons via J-aggregation: insight into disaggregation induced unfolding and detection of ferritin at the nanomolar level, *J. Mater. Chem. B*, **2016**, *4*, 6023–6031.
20. Delente, J. M.; Umadevi, D.; Shanmugaraju, S.; Kotova, O.; Watson, G. W. and Gunnlaugsson, T. Aggregation induced emission (AIE) active 4-amino-1,8-naphthalimide-Troger's base for the selective sensing of chemical explosives in competitive aqueous media, *Chem. Commun.*, **2020**, *56*, 2562.
21. Feng, Q.; Li, Y.; Wang, L.; Li, C.; Wang, J.; Liu, Y.; Li, K. and Hou, H. Multiple-color aggregation-induced emission (AIE) molecules as chemodosimeters for pH sensing, *Chem. Commun.*, **2016**, *52*, 3123.
22. Misra, S.; Singh, P.; Das, A.; Branda, P.; Sahoo, P.; Sepay, N.; Bhattacharjee, G.; Datta, P.; Mahapatra, A. K.; Satpati, B. and Nanda, J. Supramolecular assemblies of a 1,8-naphthalimide conjugate and its aggregation-induced emission property, *Mater. Adv.*, **2020**, *1*, 3532.

23. Das, P.; Kumar, A.; Aniket Chowdhury, and Partha Sarathi Mukherjee, Aggregation-Induced Emission and White Luminescence from a Combination of π -Conjugated Donor–Acceptor Organic Luminogens, *ACS Omega* **2018**, *3*, 13757–13771.
24. Mukherjee, S. and Thilagar, P. Molecular flexibility tuned emission in “V” shaped naphthalimides: Hg(II) detection and aggregation induced emission enhancement (AIEE), *Chem. Commun.*, **2013**, *49*, 7292.
25. Yakalı, G., Examination of aggregation-induced enhanced emission in a propeller-shaped chiral non conjugated blue emitter from restricted intramolecular rotation and J-type $\pi\cdots\pi$ stacking interactions, *Phys. Chem. Chem. Phys.*, **2021**, *23*, 11388.
26. Singh, S.; Verma, A. and Saha, S. Achieving AIE from ACQ in positional isomeric triarylmethanes, *New J. Chem.*, **2022**, *46*, 7212.
27. Halder, S., Nayak, B., Bhattacharjee, B.; Ramesh, A. and Das, G. Insight into the aggregation prospective of Schiff base AIEgens enabling an efficient hydrazine sensor in their aggregated state, *J. Mater. Chem. C*, **2021**, *9*, 8596-8605.
28. Zhai, D.; Xu, W.; Zhang, L. and Chang, Y.T. The role of “disaggregation” in optical probe development, *Chem. Soc. Rev.*, **2014**, *43*, 2402-2411.
29. Beatty, M. A.; González, J. B.; Sinclair, N. J.; Pye, A. T. and Hof, F. Analyte-Driven Disassembly and Turn-On Fluorescent Sensing in Competitive Biological Media, *J. Am. Chem. Soc.* **2018**, *140*, *10*, 3500–3504.
30. Ishihara, S.; Azzarelli, J. M.; Krikorian, M. and Swager, T. M. Ultratrace Detection of Toxic Chemicals: Triggered Disassembly of Supramolecular Nanotube Wrappers, *J. Am. Chem. Soc.* **2016**, *138*, *26*, 8221–8227.
31. Kasprzak, A. and Sakurai, H. Disaggregation of a sumanene-containing fluorescent probe towards highly sensitive and specific detection of caesium cations, *Chem. Commun.*, **2021**, *57*, 343.
32. Liu, H.; Westley, J. and Thayumanavan, S. Excimer–monomer fluorescence changes by supramolecular disassembly for protein sensing and quantification, *Chem. Commun.*, **2021**, *57*, 9776.
33. Kaviya, S. and Prasad, E. Sequential detection of Fe³⁺ and As³⁺ ions by naked eye through aggregation and disaggregation of biogenic gold nanoparticles, *Anal. Methods*, **2015**, *7*, 168.
34. Yang, J.; Dong, C.C.; Chen, X.L.; Sun, X.; Wei, J.Y.; Xiang, J.F.; Sessler, J. L. and Gong, H.Y. Excimer Disaggregation Enhanced Emission: A Fluorescence “Turn- On” Approach to Oxoanion Recognition, *J. Am. Chem. Soc.* **2019**, *141*, 4597–4612.
35. Battistelli, G.; Proetto, M.; Mavridi-Printezi, A.; Calvaresi, M.; Danielli, A.; Constantini, P. E.; Battistella, C.; Gianneschi, N. C. and Montalt, M. Sequential and cellular detection of copper and lactic acid by disaggregation and reaggregation of the fluorescent panchromatic fibres of an acylthiourea based sensor, *Soft Matter*, **2021**, *17*, 4304.
36. Sandhu, S.; Kumar, R.; Singh, P.; Mahajan, A.; Kaur, M. and Kumar, S. Ultratrace Detection of Nitroaromatics: Picric Acid Responsive Aggregation /Disaggregation of Self-Assembled p-Terphenylbenzimidazolium-Based Molecular Baskets, *ACS Appl. Mater. Interfaces* **2015**, *7*, 10491–10500.
37. Battistelli, G.; Proetto, M.; Mavridi-Printezi, A.; Calvaresi, M.; Danielli, A.; Emidio Constantini, P.; Battistella, C.; Gianneschi, N. C. and Montalti, M. Local detection of pH-induced disaggregation of biocompatible micelles by fluorescence switch ON, *Chem. Sci.*, **2022**, *13*, 4884.
38. Roy, R.; Pramanik, A.; Dutta, T.; Sharma, V. and Koner, A. L. Harnessing solution and solid-state emissive materials from aliphatic biogenic amine-induced transient assembly and spontaneous disassembly, *Mater. Chem. Front.*, **2022**, *6*, 3489.
39. Molecular Probes, Chemosensors, and Nanosensors for Optical Detection of Biorelevant Molecules and Ions in Aqueous Media and Biofluids, *Chem. Rev.* **2022**, *122*, *3*, 3459–3636.
40. Wu, D.; Sedgwick, A. C.; Gunnlaugsson, T.; Akkaya, E. U.; Yoon, J. and James, T. D.; Fluorescent chemosensors: the past, present and future, *Chem.Soc.Rev.*, **2017**, *46*, 7105.

41. Mako, T. L.; Racicot, J. M. and Levine, M.; Supramolecular Luminescent Sensors, *Chem. Rev.* **2019**, *119*, *1*, 322–477.
42. Cao, D.; Liu, Z.; Verwilt, P.; Koo, S.; Jangjili, P.; Kim, J. S. and Lin, W. Coumarin-Based Small-Molecule Fluorescent Chemosensors, *Chem.Rev.* **2019**, *119*, 10403–10519.
43. Kwon, N.; Hu, Y. and Yoon, J. Fluorescent Chemosensors for Various Analytes Including Reactive Oxygen Species, Biothiol, Metal Ions, and Toxic Gases, *ACS Omega* **2018**, *3*, 13731–13751.
44. Dongare, P. R. and Gore, A. H. Recent Advances in Colorimetric and Fluorescent Chemosensors for Ionic Species: Design, Principle and Optical Signalling Mechanism, *ChemistrySelect* **2021**, *6*, 5657-5669.



Experimental Details and Characterization



2. Experimental Details and Characterization

This chapter provides thorough descriptions of the various materials and procedures used in the synthesis and characterisation of the involved probes (**L1-L14**). It also outlines the specifications of the analytical tools utilised, as well as the various experimental setups and computations needed to observe the analytes' aggregation, disaggregation, photophysical facets, materialistic properties and interactions with other neutral analytes.

2.1 General Information and Materials

All the reagents, starting materials, solvents, fine chemicals and different metal salts; were procured from commercial sources and were used as received. All were of reagent grade. The solvents used were HPLC grade. For NMR analyses, deuterated solvent [(CD₃)₂SO and CDCl₃] was purchased from Sigma-Aldrich. The UV-Visible or absorption spectra were recorded on a Perkin-Elmer Lambda-750 UV-Vis spectrophotometer using 10 mm path length quartz cuvettes in 250-700 nm wavelengths. Baseline correction was applied for all spectra. Fluorescence emission spectra were recorded on a Horiba Fluoromax-4 spectrofluorometer using a 1 cm path length of quartz cuvettes having a slit width of 3 nm at 298 K. High-resolution mass spectrometry of all probes were carried out on a Waters Q-ToF Premier mass spectrometer. The solution-phase ¹H and ¹³C Nuclear Magnetic Resonance spectra were recorded using Bruker Advances 600 MHz, 500 MHz and 400 MHz NMR instruments. The chemical shifts were reported in parts per million (ppm) with the deuterated solvents. The following abbreviations are used to delineate spin multiplicities in ¹H NMR spectra: s = singlet; d = doublet; t = triplet; q = quartet, m = multiplet.

2.2 Synthetic procedure and characterization of the probes

2.2.1 Synthesis of **L1** [*N-hexyl-9H-carbazole-9-carboxamide*]

Commercially available carbazole was taken and dissolved in DCM. Hexyl isocyanate was added to the solution in a 1:1 equivalent. The resulting solution was refluxed for 24 hr and evaporated to dryness. The dried mass was worked up with DCM water. The organic layer was dried with anhydrous Na₂SO₄ and evaporated to dryness. The obtained product was taken for characterization and analysis without further purification. **L1** (**Scheme 3.1, Chapter 3**).

L1: ¹H NMR (600 MHz, CDCl₃) δ 8.06 (dd, *J* = 17.4, 8.0 Hz, 1H), 7.51 (t, *J* = 7.8 Hz, 1H), 7.37 (t, *J* = 7.5 Hz, 1H), 5.76 (t, *J* = 5.7 Hz, 0H), 3.60 (q, *J* = 6.8 Hz, 1H), 1.76 (p, *J* = 7.5 Hz, 1H), 1.49 (t, *J* = 7.6 Hz, 1H), 1.40 (dd, *J* = 8.1, 4.3 Hz, 1H), 0.98 – 0.91 (m, 1H).

^{13}C NMR (151 MHz, CDCl_3) δ 152.79, 138.38, 126.92, 125.05, 122.17, 120.22, 113.43, 41.09, 31.49, 29.76, 26.73, 22.58, 14.03. ESI-MS (positive mode, m/z): calculated for $\text{C}_{19}\text{H}_{22}\text{N}_2\text{O}$: 294.17. Found: 294.18 $[\text{M} + \text{H}]^+$. Yield (%); 48.

Empirical formula: $\text{C}_{19}\text{H}_{22}\text{N}_2\text{O}$, Mw: 294.38, T= 298 K, Monoclinic, space group: $P 21/n$, $a= 10.599(3)$ Å, $b= 5.0443(7)$ Å, $c= 30.32(3)$ Å, $\alpha= 90$, $\beta= 92.41(4)$, $\gamma=90$, $V= 1619.4(16)$ Å³, $Z= 4$, $D_x(\text{g/cm}^3)= 1.207$, $F(000)= 632.0$, total no. of reflections/ no. of independent reflections / no. of observed reflections = 4957/ 2815/ 1578, R_1 , $I > 2\sigma(I)= 0.0613(1578)$, wR_2 , $I > 2\sigma(I)= 0.1757$, $\text{GOF}(F_2)= 0.865$.

2.2.2 Synthesis of L_2 [*N-dodecyl-9H-carbazole-9-carboxamide*]

Commercially available carbazole was taken and dissolved in DCM. Dodecyl isocyanate was added to the solution in a 1:1 equivalent. The resulting solution was refluxed for 24 hr and evaporated to dryness. The dried mass was worked up with DCM water. The organic layer was dried with anhydrous Na_2SO_4 and evaporated to dryness. The obtained product was taken for characterization and analysis without further purification. L_1 (Scheme 3.1, Chapter 3).

L_2 : ^1H NMR (500 MHz, CDCl_3) δ 8.03 (dd, $J = 14.4, 8.0$ Hz, 4H), 7.48 (t, $J = 7.7$ Hz, 2H), 7.34 (t, $J = 7.5$ Hz, 2H), 5.72 (s, 1H), 3.57 (q, $J = 6.8$ Hz, 2H), 1.72 (q, $J = 7.4$ Hz, 2H), 1.49 – 1.42 (m, 2H), 1.38 (t, $J = 7.2$ Hz, 2H), 1.28 (d, $J = 17.0$ Hz, 14H), 0.88 (t, $J = 6.8$ Hz, 3H). ^{13}C NMR (126 MHz, CDCl_3) δ 152.78, 138.39, 126.90, 125.05, 122.15, 120.20, 113.43, 41.09, 31.91, 29.78, 29.65, 29.63, 29.58, 29.54, 29.34, 29.30, 27.06, 22.68, 14.10.

ESI-MS (positive mode, m/z): calculated for $\text{C}_{25}\text{H}_{34}\text{N}_2\text{O}$: 378.27. Found: 379.27 $[\text{M} + \text{H}]^+$, Yield (%); 42.

2.2.3 Synthesis of L_3 [*N-octadecyl-9H-carbazole-9-carboxamide*]

Commercially available carbazole was taken and dissolved in DCM. Octadodecyl isocyanate was added to the solution in a 1:1 equivalent. The resulting solution was refluxed for 24 hr and evaporated to dryness. The dried mass was worked up with DCM water. The organic layer was dried with anhydrous Na_2SO_4 and evaporated to dryness. The obtained product was taken for characterization and analysis without further purification. L_1 (Scheme 3.1, Chapter 3).

L_3 : ^1H NMR (600 MHz, CDCl_3) δ 8.05 (dd, $J = 17.9, 8.0$ Hz, 4H), 7.59 – 7.47 (m, 2H), 7.37 (t, $J = 7.5$ Hz, 2H), 5.75 (t, $J = 5.7$ Hz, 1H), 3.84 – 3.43 (m, 2H), 1.80 – 1.72 (m, 2H), 1.48 (p, $J = 7.2$ Hz, 2H), 1.41 (p, $J = 6.7$ Hz, 2H), 1.28 (m, 26H), 0.90 (t, $J = 6.9$ Hz, 3H).

^{13}C NMR (126 MHz, CDCl_3) δ 152.78, 138.39, 126.90, 125.05, 122.15, 120.19, 113.43, 41.08, 31.93, 29.78, 29.70, 29.68, 29.66, 29.58, 29.55, 29.36, 29.30, 27.06, 22.69, 14.11.

ESI-MS (positive mode, m/z): calculated for $\text{C}_{31}\text{H}_{46}\text{N}_2\text{O}$: 462.36. Found: 436.36 $[\text{M} + \text{H}]^+$, Yield (%); 41.

2.2.4 Synthesis of **L4** [*1,1-bis(2-(1,3-dioxo-1H-benzo[de]isoquinolin-2(3H)-yl) ethyl)-3-dodecylurea*]

Compound **L** was synthesized following the reported procedure^{2.1}. In the second step, Compound **L** (200 mg; 0.432 mmol) was dissolved in DCM and Dodecyl isocyanate (91.26 mg; 0.432 mmol) were added. After 24 h of reflux, the colorless solution was evaporated and followed by workup with DCM/ H_2O /brine water afforded **L4** (Scheme 4A.1, Chapter 4A) and which was considered for characterization without additional purification.

L4: ^1H NMR (500 MHz, CDCl_3) δ 8.54 (d, $J = 7.3$ Hz, 4H), 8.15 (d, $J = 8.2$ Hz, 4H), 7.69 (t, $J = 7.8$ Hz, 4H), 5.86 (d, $J = 5.4$ Hz, 1H), 4.33 (t, $J = 7.0$ Hz, 4H), 3.63 (t, $J = 7.1$ Hz, 4H), 2.95 (q, $J = 6.6$ Hz, 2H), 1.19 (d, $J = 7.1$ Hz, 20H), 0.81 (t, $J = 6.6$ Hz, 3H).

^{13}C NMR (150 MHz, CDCl_3) δ 164.41, 157.91, 134.10, 131.62, 131.37, 128.27, 126.92, 122.49, 44.90, 40.91, 38.35, 31.94, 29.91, 29.74, 29.71, 29.66, 29.40, 29.36, 26.83, 22.70, 14.14. HRMS: Calculated for $\text{C}_{41}\text{H}_{46}\text{N}_4\text{O}_5$: 674.35 $[\text{M}]^+$, Found 675.36 $[\text{M}+1]^+$, Yield (%); 45.

2.2.5 Synthesis of **L5** [*N, N-bis(2-(1,3-dioxo-1H-benzo[de]isoquinolin-2(3H)-yl) ethyl) acetamide*]

Compound **L** was synthesized following the reported procedure^{2.1}. In the second step, Compound **L** (200 mg; 0.432 mmol) was dissolved in DCM and Dodecyl isocyanate (91.26 mg; 0.432 mmol) were added. After 24 h of reflux, the colorless solution was evaporated and followed by workup with DCM/ H_2O /brine water afforded **L4** (Scheme 4A.1, Chapter 4A) and which was considered for characterization without additional purification.

L5: ^1H NMR (600 MHz, CDCl_3) δ 8.62 (dd, $J = 11.5, 7.2, 1.2$ Hz, 1H), 8.24 (dd, $J = 37.3, 8.3, 1.2$ Hz, 1H), 7.96 – 7.67 (m, 1H), 4.57 – 4.29 (m, 1H), 4.05 – 3.67 (m, 1H), 2.08 (s, 1H).

^{13}C NMR (150 MHz, CDCl_3) δ 171.54, 164.48, 164.18, 134.41, 133.93, 131.70, 131.67, 131.54, 131.19, 128.36, 128.21, 127.08, 126.87, 122.60, 122.22, 45.77, 43.49, 38.08, 38.01, 21.00. ESI-MS (positive mode, m/z): calculated for $\text{C}_{30}\text{H}_{23}\text{N}_3\text{O}_5$: 505.1638. Found: 506.1750 $[\text{M} + \text{H}]^+$. Yield (%); 43.

2.2.6 Synthesis of **L₆** [*1,1-bis(2-(1,3-dioxo-1H-benzo[de]isoquinolin-2(3H)-yl) ethyl)-3-octylthiourea*]

Compound **L** was synthesized following the reported procedure [34]. In the second step, Compound **L** (200 mg; 0.432 mmol) was dissolved in DCM and corresponding 1-isothiocyanatooctane (73.97 mg; 0.432 mmol) were added. After 24 h of reflux, the colourless solution was evaporated and followed by workup with DCM/H₂O/brine water afforded **L₆** which was considered for characterization without additional purification (**Scheme 4B.1, Chapter 4B**).

L₆: ¹H NMR (500 MHz, CDCl₃) δ 8.60 (dd, J = 7.2, 1.1 Hz, 4H), 8.24–8.21 (m, 4H), 7.76 (t, J = 7.7 Hz, 4H), 7.33 (t, J = 4.9 Hz, 1H), 4.46 (t, J = 7.1 Hz, 4H), 4.13 (s, 4H), 3.55 (td, J = 7.2, 4.7 Hz, 2H), 1.35–1.23 (m, 12H), 0.88 (t, J = 6.7 Hz, 3H). ¹³C NMR (125 MHz, CDCl₃) δ 182.18, 164.54, 134.24, 131.67, 131.39, 128.33, 126.93, 122.48, 46.78, 37.28, 31.93, 29.41, 29.31, 28.82, 26.98, 22.70, 14.13. HRMS: Calculated for C₃₇H₃₈N₄O₄S: 634.26, Found 635.26 [M+1]⁺. Yield (%); 40.

2.2.7 Synthesis of **L₇** [*2,3-diphenylquinoxaline*]

Benzil (200 mg; 0.95 millimoles) and 1,2-Diaminobenzene (102.69 mg; 0.95 millimoles) substituted were taken in glacial acetic acid and refluxed under stirring condition for 3-4 hrs. The reaction mixture was cooled to room temperature and filtered. To remove any traces of acetic acid, the formed mass was washed several times with distilled water. 2, 3-diphenyl quinoxaline (**L₇**) were considered for characterization without additional purification (**Scheme 5.1, Chapter 5**).

L₇: ¹H NMR (500 MHz, CDCl₃) δ 8.18 (dd, J = 6.4, 3.5 Hz, 2H), 7.78 (dd, J = 6.4, 3.4 Hz, 2H), 7.56 – 7.48 (m, 4H), 7.39 – 7.29 (m, 6H).

¹³C NMR (125 MHz, CDCl₃) δ 153.50, 141.26, 139.11, 129.97, 129.86, 129.23, 128.81, 128.28.

ESI-MS (positive mode, m/z): calculated for C₂₀H₁₄N₂: 282.11. Found: 283.12 [M + H]⁺.

Empirical formula: C₂₀H₁₄N₂, Mw: 282.12, T= 298 K, Orthorhombic, space group: *P c a 2*₁, a= 31.380(2) Å, b= 5.8076(4) Å, c= 16.7198(11) Å, α= 90, β= 90, γ= 90, V= 3047.1(3) Å³, Z= 8, D_x(g/cm³)= 1.231, F(000)= 1184.0, total no. of reflections/ no. of independent reflections / no. of observed reflections = 58512/5320/ 4182, R₁, I > 2σ(I)= 0.0882(4182), wR₂, I > 2σ(I)= 0.2137(5320), GOF (F₂)= 1.397. CCDC number: 2248347.

2.2.8 Synthesis of **L₈** [*2,3-diphenylquinoxaline-6-carboxylic acid*]

Benzil (200 mg; 0.95 millimoles) and 1,2-Diaminobenzene: 3,4-aminobenzoic acid (144.45 mg; 0.95 millimoles) substituted were taken in glacial acetic acid and refluxed under stirring condition for 3-4 hrs. The reaction mixture was cooled to room temperature and filtered. To remove any traces of acetic acid, the formed mass was washed several times with distilled water. 2,3-

diphenylquinoxaline-6-carboxylic acid (**L8**) were considered for characterization and further reaction without additional purification (**Scheme 5.1, Chapter 5**).

L8: ^1H NMR (500 MHz, DMSO- d_6) δ 13.51 (s, 1H), 8.67 (s, 1H), 8.33 (dd, $J = 8.7, 1.9$ Hz, 1H), 8.25 (d, $J = 8.7$ Hz, 1H), 7.52 (d, $J = 7.4$ Hz, 4H), 7.41 (dd, $J = 15.1, 7.1$ Hz, 6H).

^{13}C NMR (125 MHz, DMSO- d_6) δ 167.06, 155.30, 154.67, 142.84, 140.22, 138.91, 132.64, 131.20, 130.22, 130.19, 130.03, 129.78, 129.62, 129.51, 128.58. ESI-MS: calculated for $\text{C}_{21}\text{H}_{14}\text{N}_2\text{O}_2$: 326.10. Found: 327.11 $[\text{M} + \text{H}]^+$, Yield (%); 59.07.

Empirical formula: $\text{C}_{21}\text{H}_{14}\text{N}_2\text{O}_2$, Mw: 326.11, T= 298 K, Triclinic, space group: $P-1$, $a = 6.4465(10)$ Å, $b = 10.691(2)$ Å, $c = 12.369(2)$ Å, $\alpha = 100.887(17)$, $\beta = 93.957(16)$, $\gamma = 98.408(15)$, $V = 824.0(2)$ Å 3 , $Z = 2$, $D_x(\text{g}/\text{cm}^3) = 1.315$, $F(000) = 340.0$, total no. of reflections/ no. of independent reflections / no. of observed reflections = 6370/ 3715/ 1455, R_1 , $I > 2\sigma(I) = 0.0778(1455)$, wR_2 , $I > 2\sigma(I) = 0.2537(3715)$, GOF (F_2) = 0.987. CCDC number: 2248337.

2.2.9 Synthesis of **L9** [*ethyl 2,3-diphenylquinoxaline-6-carboxylate*]

L8 (100 mg; 0.31 millimoles) was suspended over ethanol and 2-3 drops of conc. H_2SO_4 was added to it. It was refluxed overnight and evaporated to dryness. It was dissolved in DCM and the organic layer was washed with water. The organic layer was dried on anhydrous Na_2SO_4 and evaporated. The dried mass obtained is ethyl 2,3-diphenyl quinoxaline-6-carboxylate (**L9**) which was considered for characterization and further reaction without additional purification (**Scheme 5.1, Chapter 5**).

L9: ^1H NMR (500 MHz, CDCl_3) δ 8.91 (d, $J = 1.8$ Hz, 1H), 8.37 (dd, $J = 8.7, 1.8$ Hz, 1H), 8.21 (d, $J = 8.6$ Hz, 1H), 7.63 – 7.50 (m, 5H), 7.37 (dt, $J = 14.1, 6.8$ Hz, 7H), 4.48 (q, $J = 7.1$ Hz, 2H), 1.46 (t, $J = 7.1$ Hz, 3H).

^{13}C NMR (125 MHz, CDCl_3) δ 165.87, 155.11, 154.44, 143.18, 140.44, 138.69, 138.67, 131.82, 131.61, 129.90, 129.83, 129.53, 129.36, 129.26, 129.13, 128.35, 61.57, 14.33.

ESI-MS: calculated for $\text{C}_{23}\text{H}_{18}\text{N}_2\text{O}_2$: 354.13. Found: 355.14 $[\text{M} + \text{H}]^+$.

Empirical formula: $\text{C}_{23}\text{H}_{18}\text{N}_2\text{O}_2$, Mw: 354.14, T= 298 K, Monoclinic, space group: $P 21/n$, $a = 15.072(2)$ Å, $b = 5.7457(13)$ Å, $c = 22.182(4)$ Å, $\alpha = 90$, $\beta = 106.626(18)$, $\gamma = 90$, $V = 1840.6(6)$ Å 3 , $Z = 4$, $D_x(\text{g}/\text{cm}^3) = 1.275$, $F(000) = 744.0$, total no. of reflections/ no. of independent reflections / no. of observed reflections = 7817/ 4174/ 1634, R_1 , $I > 2\sigma(I) = 0.0713(1634)$, wR_2 , $I > 2\sigma(I) = 0.2232(4174)$, GOF (F_2) = 0.967. CCDC number: 2248342.

2.2.10 Synthesis of **L10** [(*2,3-diphenylquinoxalin-6-yl*) methanol]

L₉ (100 mg; 0.28 millimoles) was dissolved in dry DCM and cooled to -78°C, with the gradual addition of DIBAL-H. The reaction was stirred at -78 °C for 4-5 hrs. until its completion. After completion, it was quenched with water and stirred overnight at room temperature. Evaporation of the brownish-colored solution and workup with DCM/H₂O, yields (2,3-diphenylquinoxalin-6-yl) methanol (**L₁₀**). It was taken for further characterization without further purification (**Scheme 5.1, Chapter 5**).

L₁₀: ¹H NMR (500 MHz, CDCl₃) δ 8.17 (dd, *J* = 1.8 Hz, 1H), 8.15 (dd, *J* = 4.4 Hz, 1H), 7.77 (dd, *J* = 8.7, 1.9 Hz, 1H), 7.55 – 7.48 (m, 4H), 7.40 – 7.30 (m, 6H), 4.95 (s, 2H).

¹³C NMR (125 MHz, CDCl₃) δ 153.66, 153.36, 143.12, 141.18, 140.73, 139.05, 129.86, 129.41, 129.00, 128.86, 128.83, 128.28, 126.16, 64.86. ESI-MS: calculated for C₂₁H₁₆N₂O: 312.12. Found: 313.13 [M + H]⁺, Yield (%); 20.01.

Empirical formula: C₂₁H₁₆N₂O, Mw: 312.13, T= 298 K, Monoclinic, space group: *P* 21/*n*, a= 11.9011(9) Å, b= 6.2428(4) Å, c= 22.2023(16) Å, α= 90, β= 102.180(8), γ= 90, V= 1612.4(2) Å³, Z= 4, D_x(g/cm³) = 1.283, F(000)= 652.0, total no. of reflections/ no. of independent reflections / no. of observed reflections = 5669/ 2843/ 2184, R₁, I > 2σ(I)= 0.0591(2184), wR₂, I > 2σ(I)= 0.1758(2843), GOF (F₂)= 1.063. CCDC number: 2248343.

2.2.11 Synthesis of **L₁₁** [(2,3-diphenylquinoxalin-6-yl) (phenyl)methanone]

Benzil (200 mg; 0.95 millimoles) and (3,4-aminophenyl) (phenyl)methanone (201.48 mg; 0.95 millimoles) substituted were taken in glacial acetic acid and refluxed under stirring condition for 3-4 hrs. The reaction mixture was cooled to room temperature and filtered. To remove any traces of acetic acid, the formed mass was washed several times with distilled water. (2,3-diphenylquinoxalin-6-yl) (phenyl)methanone (**L₁₁**) were considered for characterization without additional purification (**Scheme 5.1, Chapter 5**).

L₁₁: ¹H NMR (500 MHz, Chloroform-*d*) δ 8.54 (s, 1H), 8.29 (t, *J* = 6.8 Hz, 2H), 7.91 (d, *J* = 7.6 Hz, 2H), 7.64 (t, *J* = 7.5 Hz, 1H), 7.58 – 7.50 (m, 7H), 7.37 (m, 7.0 Hz, 7H).

¹³C NMR (125 MHz, CDCl₃) δ 195.80, 155.17, 154.63, 143.01, 140.23, 138.68, 138.65, 138.36, 137.25, 132.81, 132.45, 130.13, 129.91, 129.85, 129.79, 129.73, 129.30, 129.16, 128.53, 128.37. ESI-MS: calculated for C₂₇H₁₈N₂O: 386.14. Found: 387.14 [M + H]⁺, Yield (%); 56.88.

Empirical formula: C₂₇H₁₈N₂O, Mw: 386.14, T= 298 K, Monoclinic, space group: *P* 21/*n*, a= 14.8045(12) Å, b= 6.1470(5) Å, c= 22.9263(19) Å, α= 90, β= 107.231(2), γ= 90, V= 1992.7(3)

\AA^3 , $Z=4$, $D_x(\text{g/cm}^3) = 1.288$, $F(000)=808.0$, total no. of reflections/ no. of independent reflections / no. of observed reflections = 49877/ 3509/ 2257, $R_1, I > 2\sigma(I) = 0.0711(2257)$, $wR_2, I > 2\sigma(I) = 0.2118(3509)$, $\text{GOF}(F_2) = 1.256$. CCDC number: 2248344.

2.2.12 Synthesis of **L₁₂** [6-methyl-2,3-diphenylquinoxaline]

Benzil (200 mg; 0.95 millimoles) and 1,2-Diaminobenzene: 4-methylbenzene-1,2-diamine (116.26 mg; 0.95 millimoles) were taken in glacial acetic acid and refluxed under stirring condition for 3-4 hrs. The reaction mixture was cooled to room temperature and filtered. To remove any traces of acetic acid, the formed mass was washed several times with distilled water. 6-methyl-2,3-diphenyl quinoxaline (**L₁₂**) was considered for characterization without additional purification (**Scheme 6.1, Chapter 6**).

L₁₂: $^1\text{H NMR}$ (500 MHz, CDCl_3) δ 8.07 (d, $J = 8.6$ Hz, 1H), 7.95 (s, 1H), 7.61 (dd, $J = 8.7, 2.0$ Hz, 1H), 7.53 – 7.48 (m, 5H), 7.33 (d, $J = 7.3$ Hz, 5H), 2.62 (s, 3H).

$^{13}\text{C NMR}$ (125 MHz, CDCl_3) δ 153.35, 152.60, 141.32, 140.51, 139.73, 139.25, 134.89, 132.32, 129.93, 129.86, 129.84, 129.03, 128.72, 128.70, 128.64, 128.23, 128.04, 21.92.

ESI-MS (positive mode, m/z): calculated for $\text{C}_{21}\text{H}_{16}\text{N}_2$: 296.13. Found: 297.20 $[\text{M} + \text{H}]^+$, Yield (%); 50.12.

Empirical formula: $\text{C}_{21}\text{H}_{16}\text{N}_2$, Mw: 296.13, $T = 298$ K, Monoclinic, space group: $P 21/c$, $a = 9.8006(17)$ \AA , $b = 9.825(4)$ \AA , $c = 17.40200$ \AA , $\alpha = 90$, $\beta = 103.3800$, $\gamma = 90$, $V = 1630.2(7)$ \AA^3 , $Z = 4$, $D_x(\text{g/cm}^3) = 1.207$, $F(000) = 624.0$, total no. of reflections/ no. of independent reflections / no. of observed reflections = 5739/ 2870/ 1280, $R_1, I > 2\sigma(I) = 0.0661(1280)$, $wR_2, I > 2\sigma(I) = 0.2397(2870)$, $\text{GOF}(F_2) = 0.943$. CCDC number: 2240165.

2.2.13 Synthesis of **L₁₃** [6-nitro-2,3-diphenylquinoxaline]

Benzil (200 mg; 0.95 millimoles) and 4-nitrobenzene-1,2-diamine (145.76 mg; 0.95 millimoles) was taken in glacial acetic acid and refluxed under stirring condition for 3-4 hrs. The reaction mixture was cooled to room temperature and filtered. To remove any traces of acetic acid, the formed mass was washed several times with distilled water. 6-nitro-2,3-diphenyl quinoxaline (**L₁₃**) was considered for characterization and further reaction without additional purification (**Scheme 6.1, Chapter 6**).

L₁₃: $^1\text{H NMR}$ (500 MHz, CDCl_3) δ 9.08 (d, $J = 2.5$ Hz, 1H), 8.53 (dd, $J = 9.3, 2.5$ Hz, 1H), 8.30 (d, $J = 9.2$ Hz, 1H), 7.59 – 7.53 (m, 5H), 7.43 (t, $J = 7.3$ Hz, 3H), 7.37 (t, $J = 7.4$ Hz, 5H).

$^{13}\text{C NMR}$ (125 MHz, CDCl_3) δ 156.33, 155.71, 147.94, 143.60, 140.01, 138.14, 138.07, 130.77, 129.91, 129.84, 129.77, 129.63, 128.46, 125.64, 123.30.

ESI-MS (positive mode, m/z): calculated for $C_{20}H_{13}N_3O_2$: 327.34. Found: 328.10 $[M + H]^+$, Yield (%); 59.

2.2.14 Synthesis of **L14** [2,3-diphenylquinoxalin-6-amine]

L13 (100 mg; 0.30 millimoles) was suspended over ethanol and hydrazine hydrate (76 μ L; 1.52 millimoles) along with a pinch of Pd/C was added to it. It was refluxed overnight and filtered through Whatman filter paper. The filtrate was collected and evaporated. The dried mass obtained is 2,3-diphenyl quinoxaline-6-amine (**L14**). It was taken for further characterization without additional purification (**Scheme 6.1, Chapter 6**).

L14: 1H NMR (500 MHz, DMSO- d_6) δ 7.96 (d, $J = 8.9$ Hz, 1H), 7.50 – 7.43 (m, 4H), 7.31 (t, $J = 6.5$ Hz, 6H), 7.24 (d, $J = 2.4$ Hz, 1H), 7.19 (dd, $J = 8.9, 2.5$ Hz, 1H), 4.20 (s, 2H).

^{13}C NMR (125 MHz, $CDCl_3$) δ 153.49, 149.65, 148.05, 143.12, 139.55, 139.52, 136.36, 130.26, 129.83, 129.77, 128.51, 128.18, 128.14, 122.06, 108.09.

ESI-MS (positive mode, m/z): calculated for $C_{20}H_{15}N_3$: 297.35. Found: 298.13 $[M + H]^+$. Yield (%); 48.

2.3 UV-Vis and Fluorescence Spectral Studies

Stock solutions of different analytes (antibiotics, nitroaromatics, metals, $50 \times 10^{-3} \text{ mol L}^{-1}$) were prepared preferably in water or MeOH/ DMSO depending on solubility. Stock solution of probes **L1-14** ($5 \times 10^{-3} \text{ mol L}^{-1}$) were prepared in DMSO. For fluorescence selectivity experiments, the solution of probes was then diluted to $10 \times 10^{-6} \text{ mol L}^{-1}$ with Millipore water by taking only 4 μ L of stock solution and making the final volume 2 mL. In fluorescence titration experiments, a quartz optical cell of 10 mm pathlength was filled with a 2.0 mL solution of respective probes to which various analytes were gradually added using a micropipette. For the competitive selectivity experiment, fluorescence emission of the 'chemosensor-sensed guest' ensemble was recorded in the absence and presence of the excess (50 equiv.) competitive analytes. For fluorescence measurements, **L1-3** was excited at 280 nm, and emission was procured from 300 nm to 500 nm whereas **L4-6** was excited at 320nm, and emission was procured from 340 nm to 600 nm. **L7-14** was excited at 350 nm, and emission was recorded from 370 nm to 600nm.

2.4 Estimation of the Apparent Binding Constant

Probes **L6** with a sufficient concentration of 10 μ M in water was titrated with varying analyte concentrations. Thus, the apparent binding constant for forming the Probe -analyte complex was assessed utilizing the Benesi–Hildebrand (B–H) plot (Equation 1).

$$1/(I-I_0) = 1/\{K(I_{\max}-I_0) C\} + 1/(I_{\max}-I_0) \quad \dots (1)$$

I_0 is the emission intensity of probes at maximum (λ_{\max}), and I is the recorded emission intensity at that particular wavelength in the presence of a specific concentration of the analyte (C). I_{\max} is the maximum emission intensity value obtained at λ_{\max} during titration with varying analyte concentrations. K is the apparent binding constant (M^{-1}) and was determined from the linear plot's slope.

2.5 Detection limit (LOD)

The detection limit (**L1-14**) was evaluated based on the fluorescence titration changes. The fluorescence emission spectrum of respective probe was computed ten times, and the standard deviation of the blank measurement was obtained. The fluorescence emission at λ_{\max} was plotted as a concentration of added analyte to gain the slope. The detection limits were calculated using the following equation:

$$\text{Detection limit} = 3\sigma/k \quad \dots (2)$$

where σ is the standard deviation of blank measurement, and k is the slope between the fluorescence emission intensity versus [analyte]. The conversion to ppm/ppb unit was done considering molecular weight of analytes.

2.6 Field Emission Scanning Electron Microscope (FESEM) Studies

Size and Morphology of **L1-L14** were imaged separately using Gemini 300 FESEM (Carl Zeiss) or Sigma 300 FESEM (Zeiss) instrument. Images of disaggregated samples under different conditions were obtained using same instrument. The samples were prepared by drop-casting (~1mM), the Water/DMSO mixture in respective solvents on Al-foil covered coverslip, then coated with gold and dried under vacuum before the imaging.

2.7 Atomic Force Microscopy

Transformations in morphology, shapes and sizes of **L1-L6** and **L12** due to solvent switching were observed from a drop-cast solution of mentioned compounds (10 μ M) in a THF-water medium using Asylum Research Cypher (Oxford Instruments).

2.8 Dynamic light scattering measurement

Dynamic light scattering (DLS) experiments were carried out in Malvern Zetasizer Nano ZS instrument equipped with a 4.0 mW He–Ne laser running at a wavelength of 633 nm. The samples and the background were measured at room temperature (25 °C) at a scattering angle of 173°. DLS experiments were executed with optically clear solutions of respective probes (**L1-L14**) (10 µM) in water as well as in presence and absence of with 50 equivalents of analytes in different solvents. The solution was equilibrated for 120 minutes before taking the measurements.

2.9 Measurement of fluorescence lifetime

Fluorescence lifetimes were assessed using the time-correlated single-photon counting (TCSPC) method in the Edinburgh Instrument Life-Spec II spectrometer. The samples (**L1-L5**) and commercial dye rhodamine B were excited at respective excitation wavelengths or required experimental conditions, keeping the emission wavelength fixed as mentioned earlier using a pulsed diode laser. The fluorescence decays were surveyed by the re-convolution method using the FAST software provided by Edinburgh Instruments.

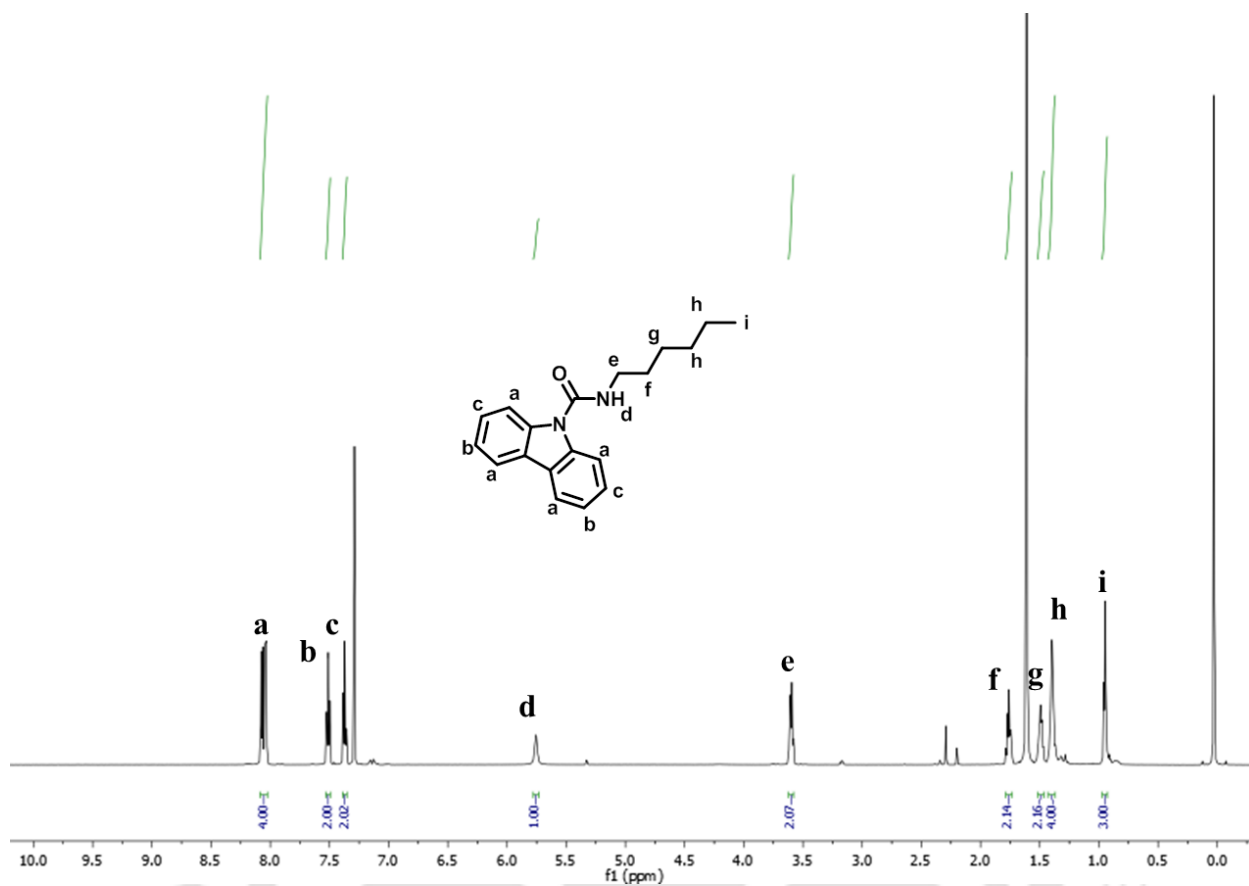
2.10 Theoretical investigations (DFT study)

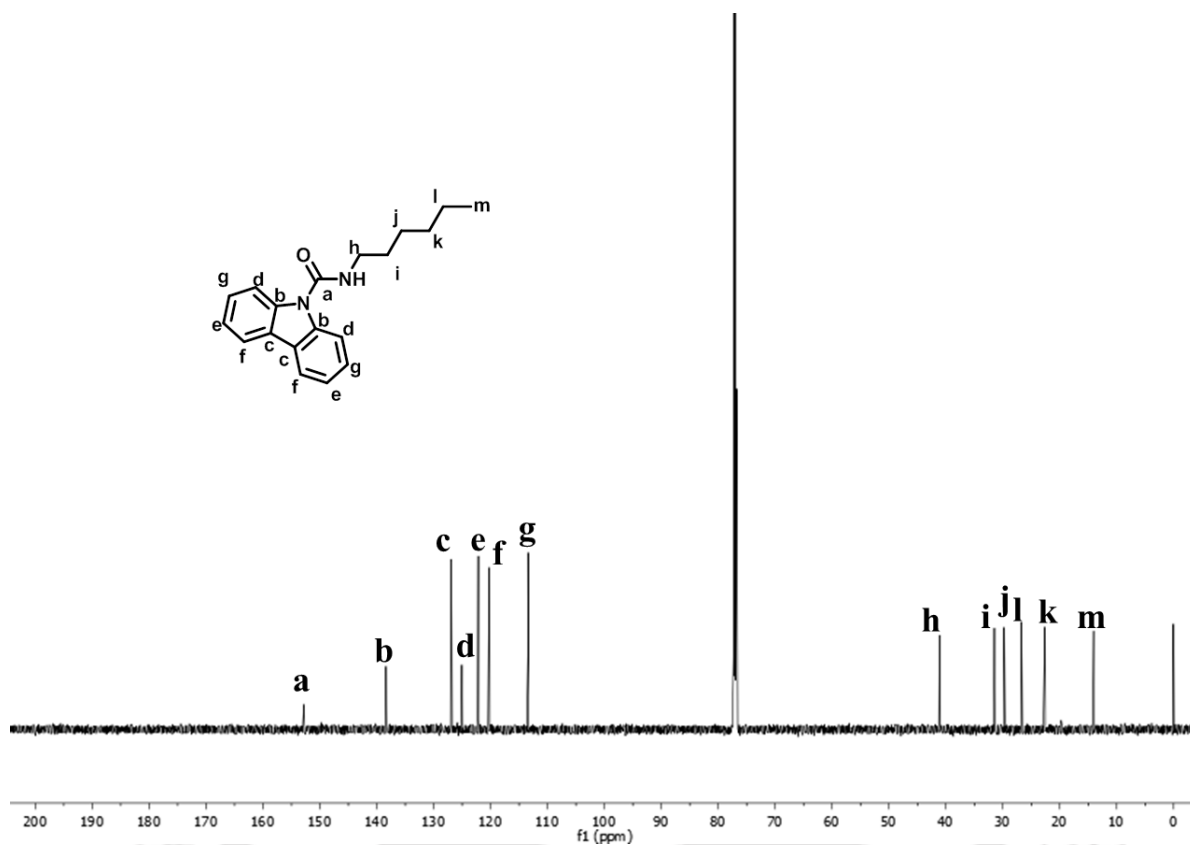
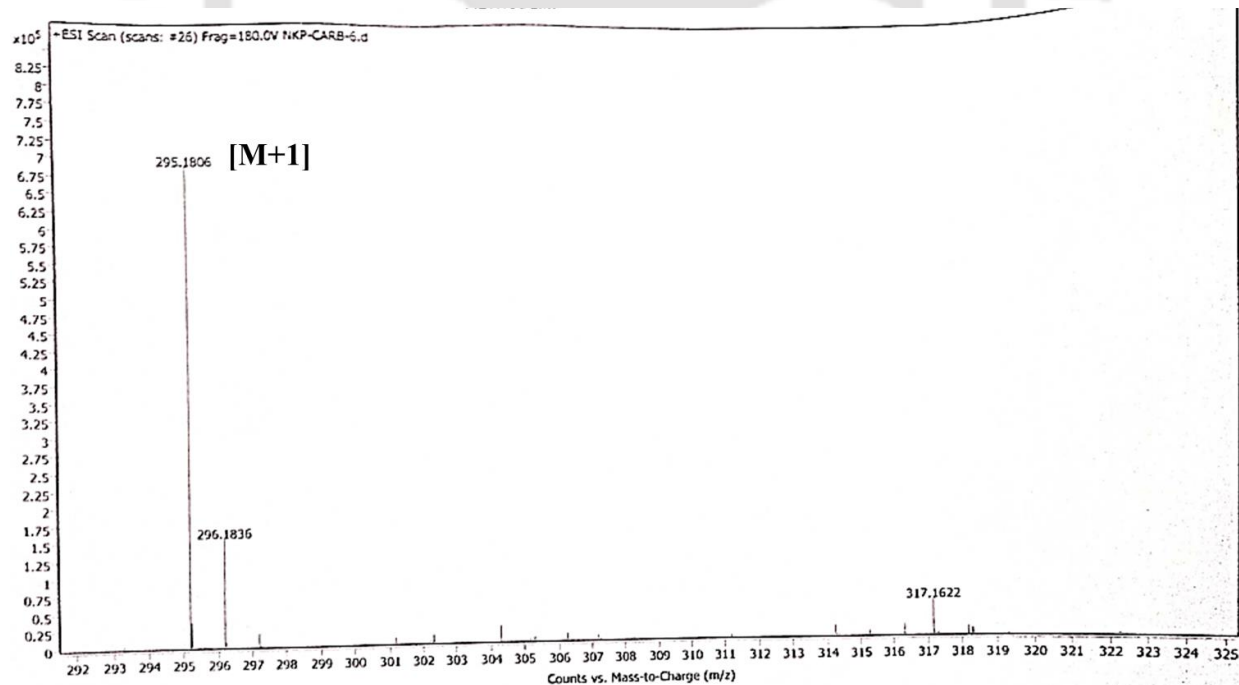
DFT optimizations of **L1-L14** and analytes interaction were accomplished with the exchange correlation function B3LYP and the basis set 6-31G (d,p) incorporating in the Gaussian 09 package. For several calculation water was implemented as solvent system using CPCM model.^{2,2-2.5}

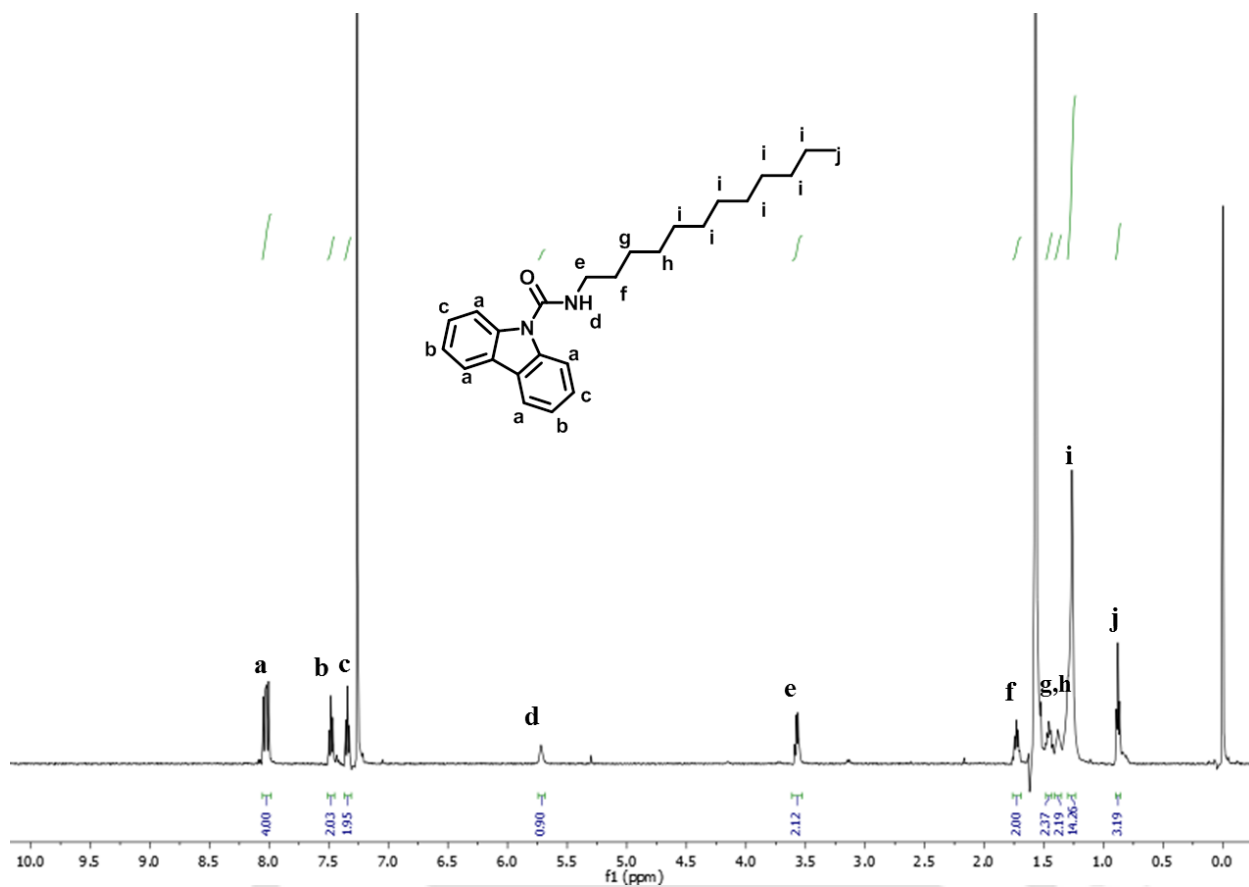
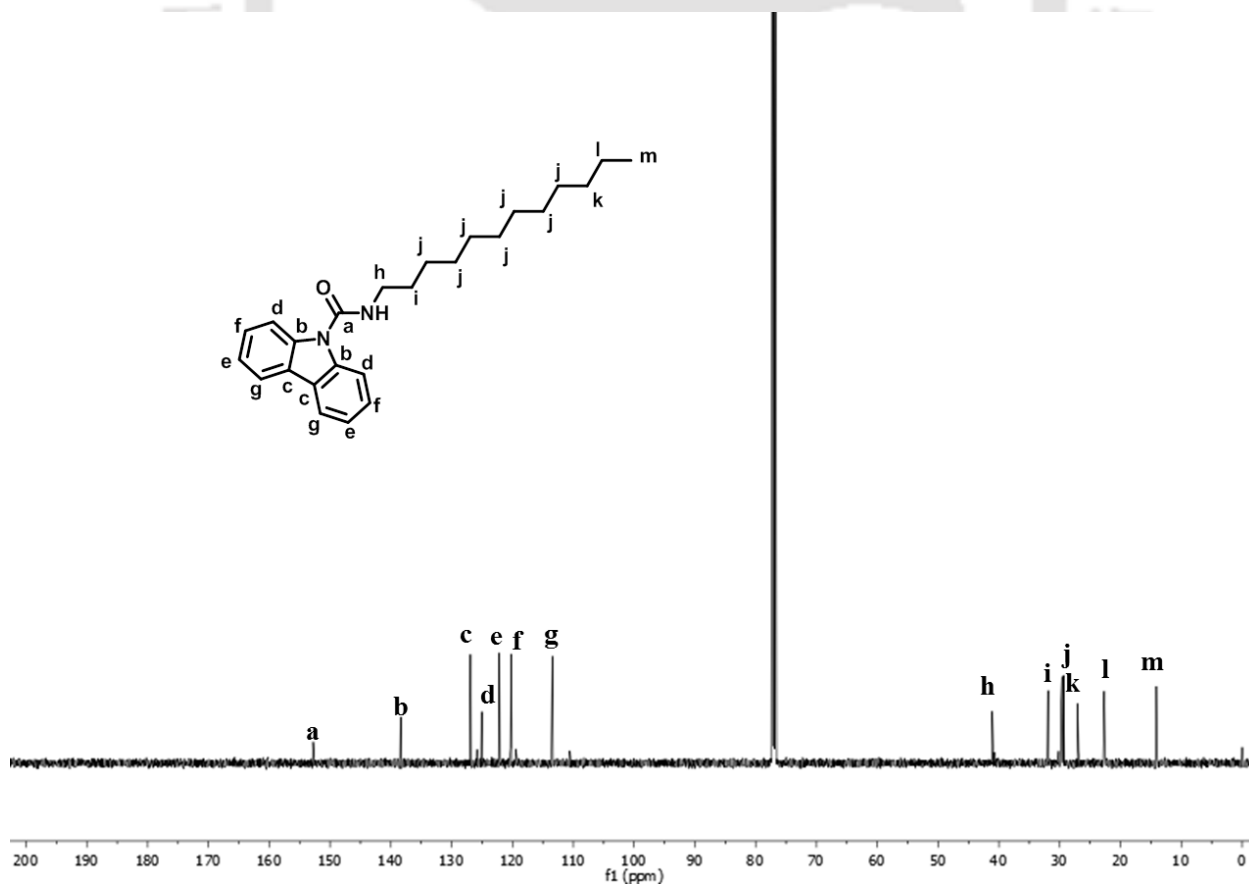
References

- 2.1 Saini, A.; Kaur, M.; Mayank, Kuwar, A.; Kaur, N. and Singh, N. Hybrid nanoparticle-based fluorescence switch for recognition of ketoprofen in aqueous media, *Mol. Syst. Des. Eng.*, **2020**,5, 1428.
- 2.2 J. P. Nandre, S. R. Patil, S. K. Sahoo, C. P. Pradeep, A. Churakov, F. Yu, L. Chen, C. Redshaw, A. A. Patil and U. D. Patil, *Dalton Trans.*, 2017, 46, 14201–14209.
- 2.3 2.3 M. Fisch, G. Trucks, H. Schlegel, G. Scuseria, M. Robb, J. Cheeseman, G. Scalmani, V. Barone, B. Mennucci and G. Petersson, *Gaussian 09 (Revision A. 02)*, Wallingford, CT, 2009.
- 2.4 J. Tomasi, B. Mennucci and E. Cance, *THEOCHEM*, 1999, 464, 211.
- 2.5 A. D. Becke, *J Chem Phys* 1993, 98, 5648-5652.

Appendix - Chapter 2

Figure A2.1: ^1H NMR of L1.

Figure A2.2: ^{13}C NMR of L₁.Figure A2.3: Mass spectrum of L₁.

Figure A2.4: ^1H NMR of L_2 .Figure A2.5: ^{13}C NMR of L_2 .

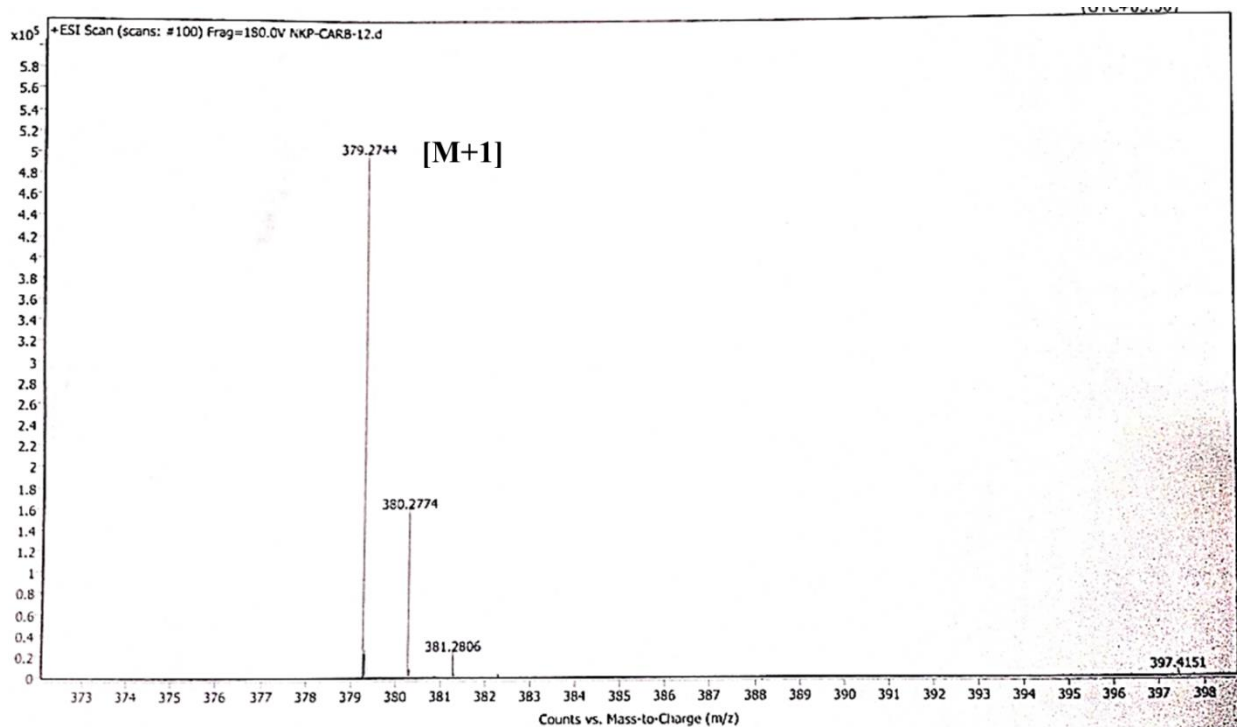
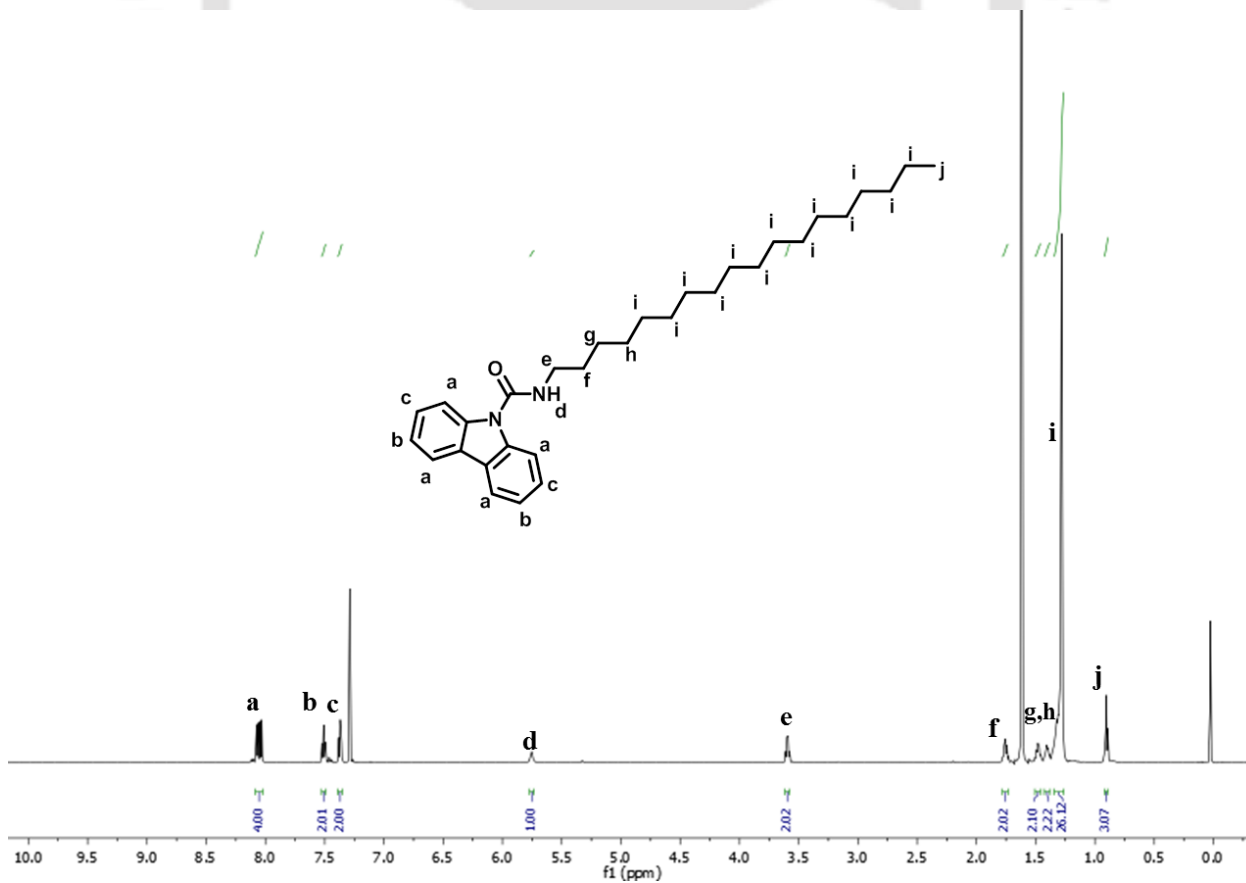


Figure A2.6: Mass spectrum of L2.

Figure A2.7: ¹H NMR of L3.

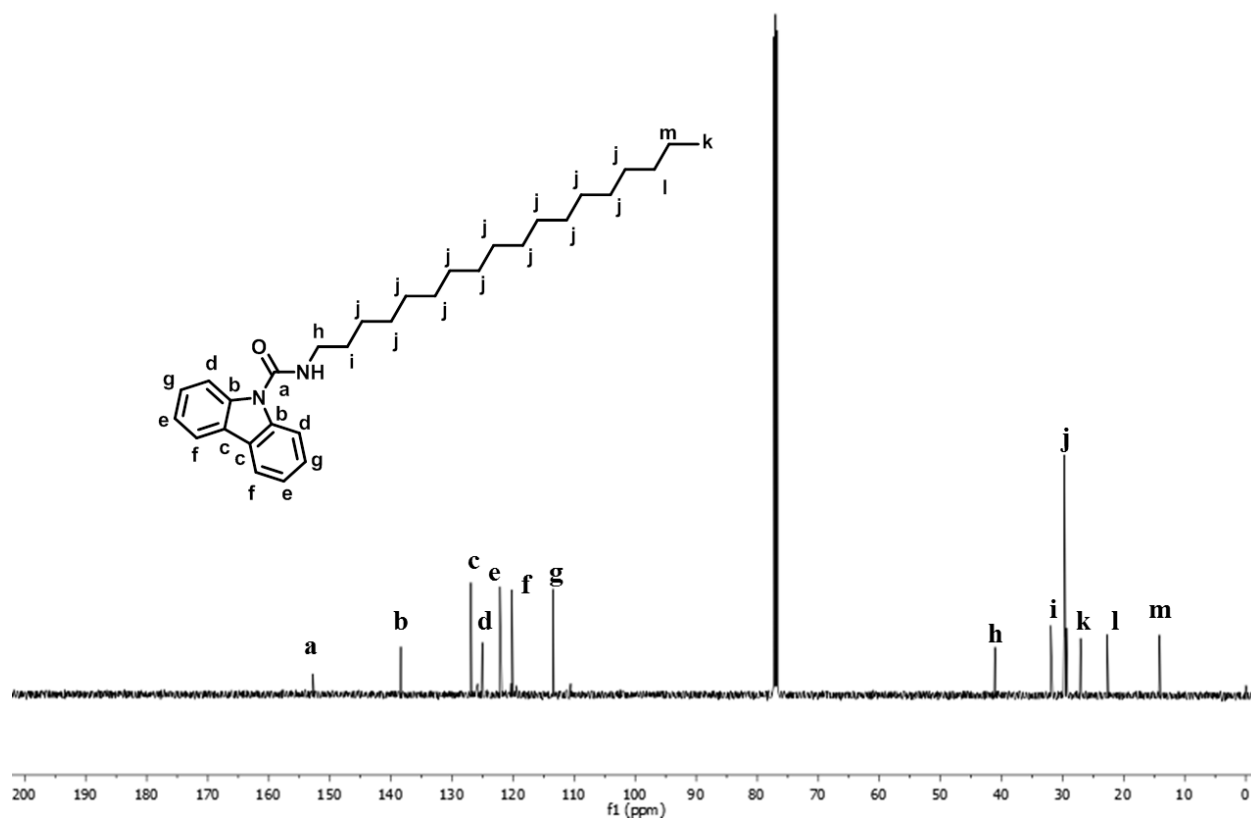
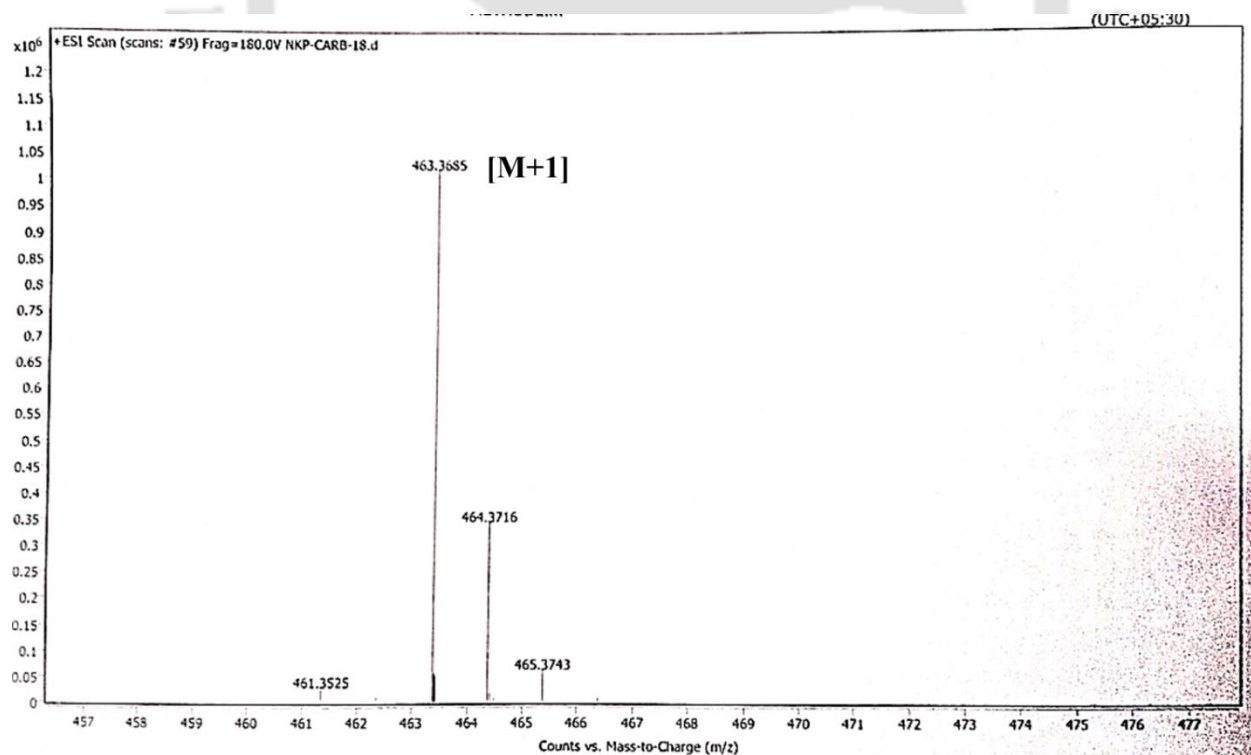
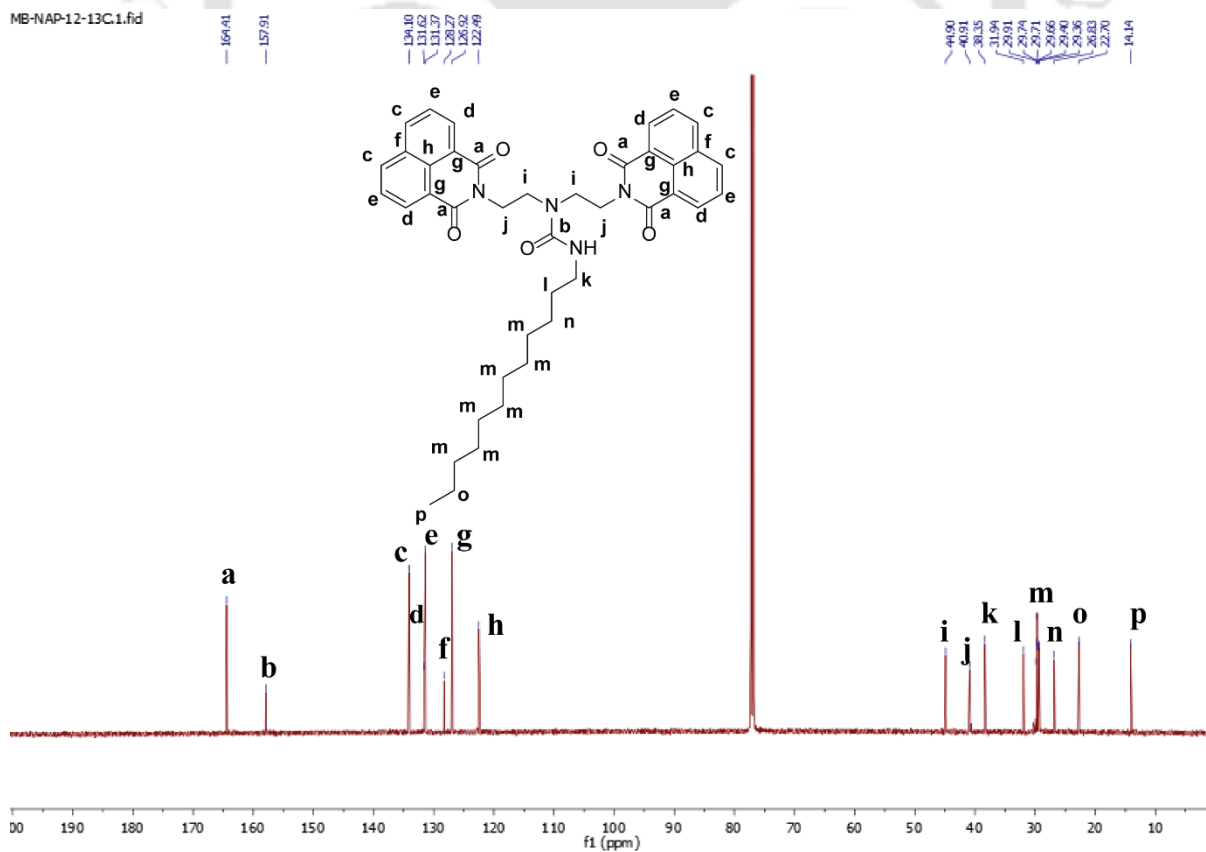
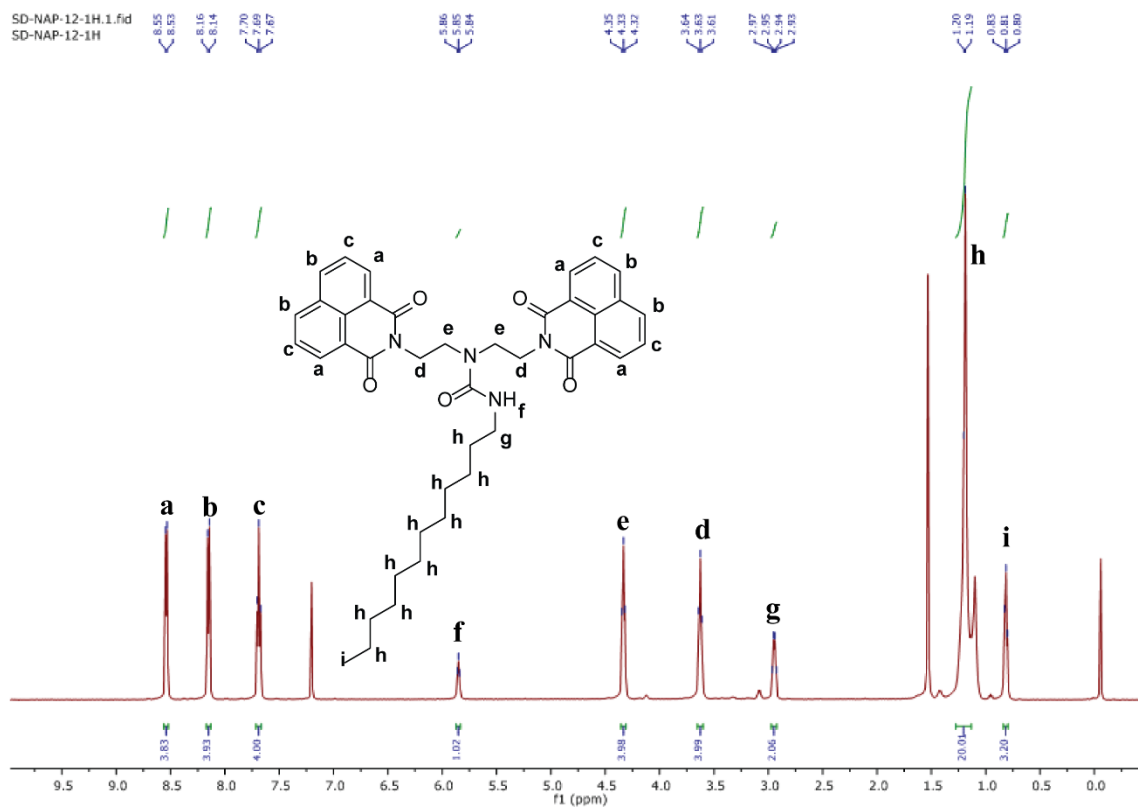
Figure A2.8: ^{13}C NMR of L3.

Figure A2.9: Mass spectrum of L3.



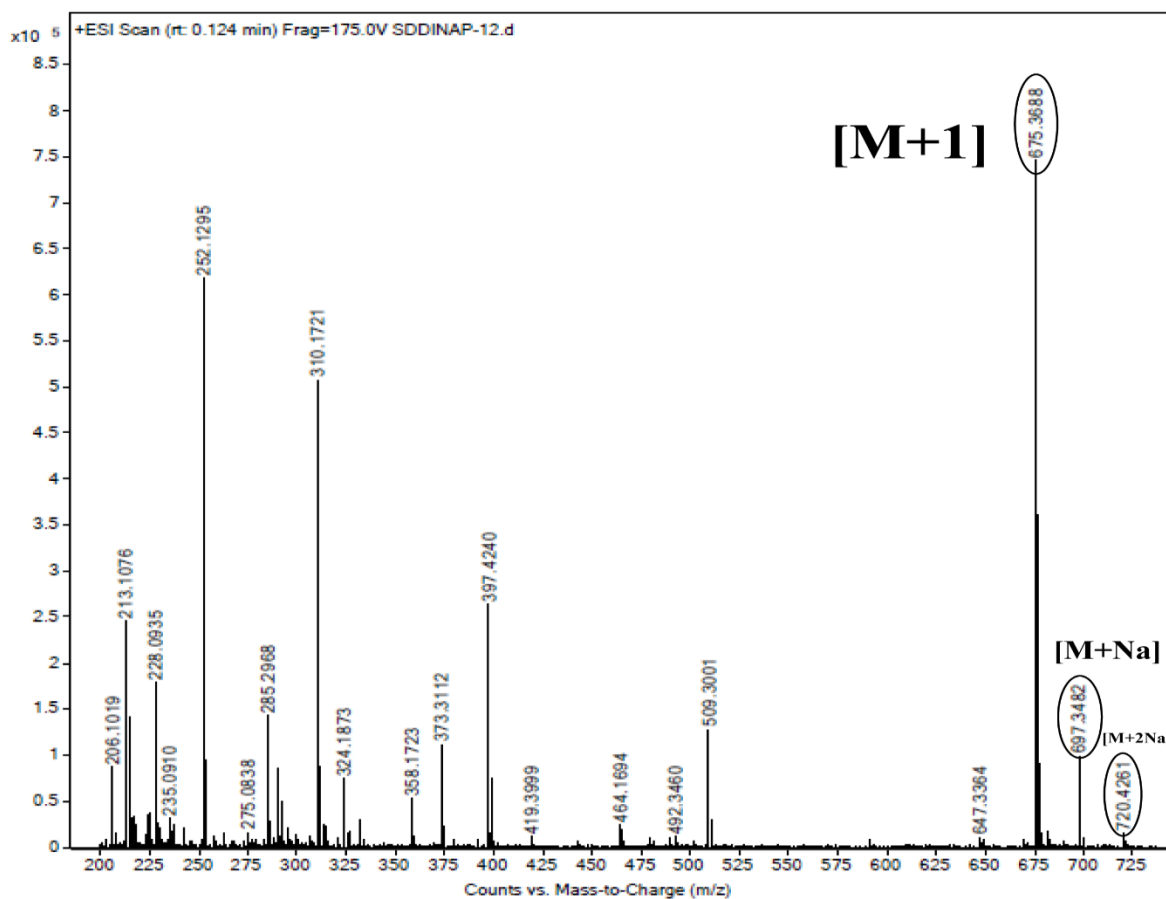
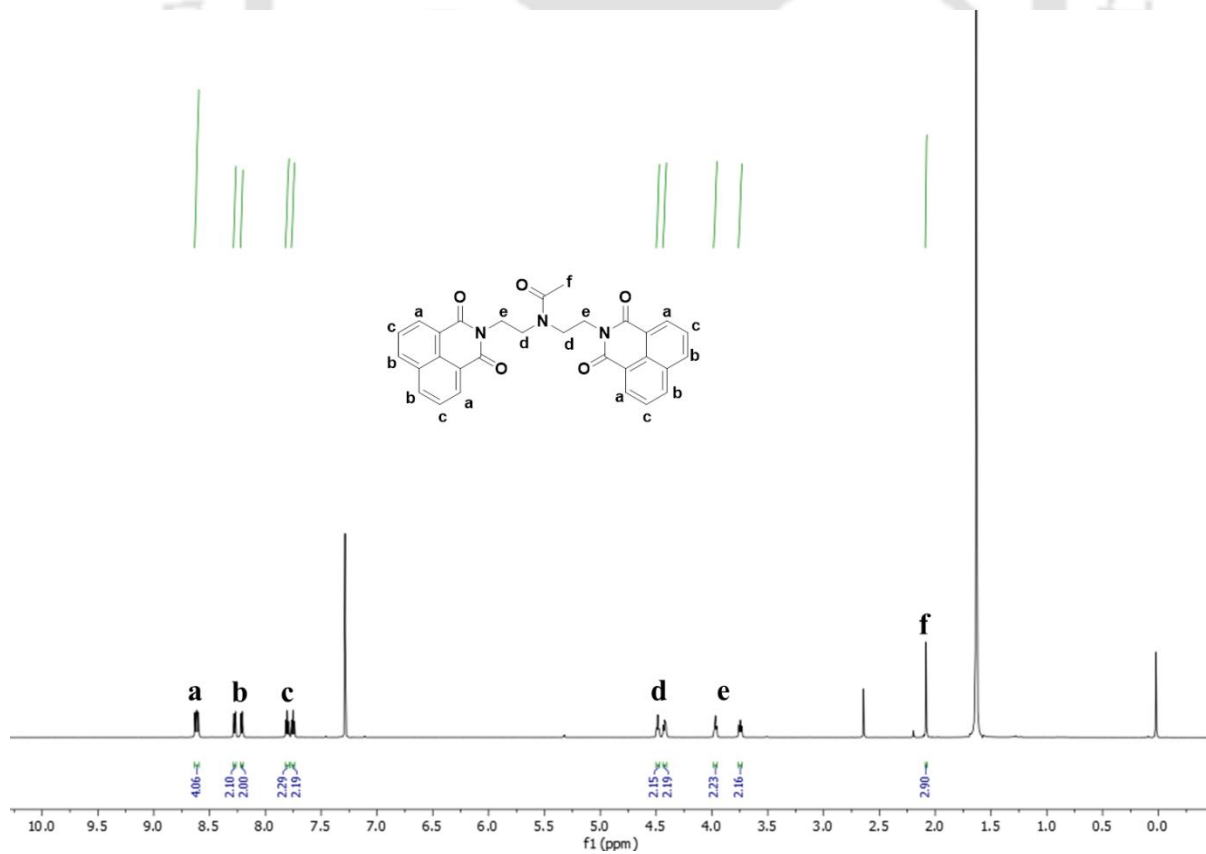
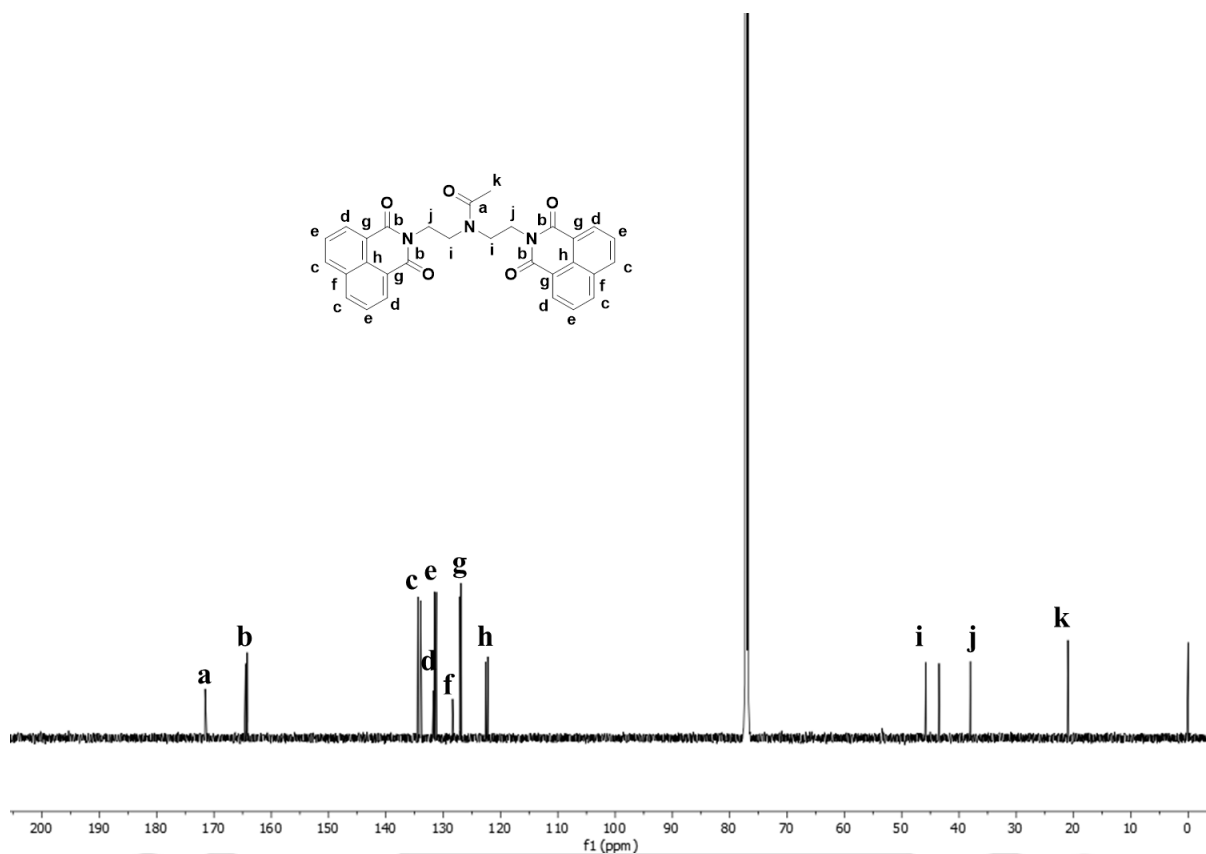
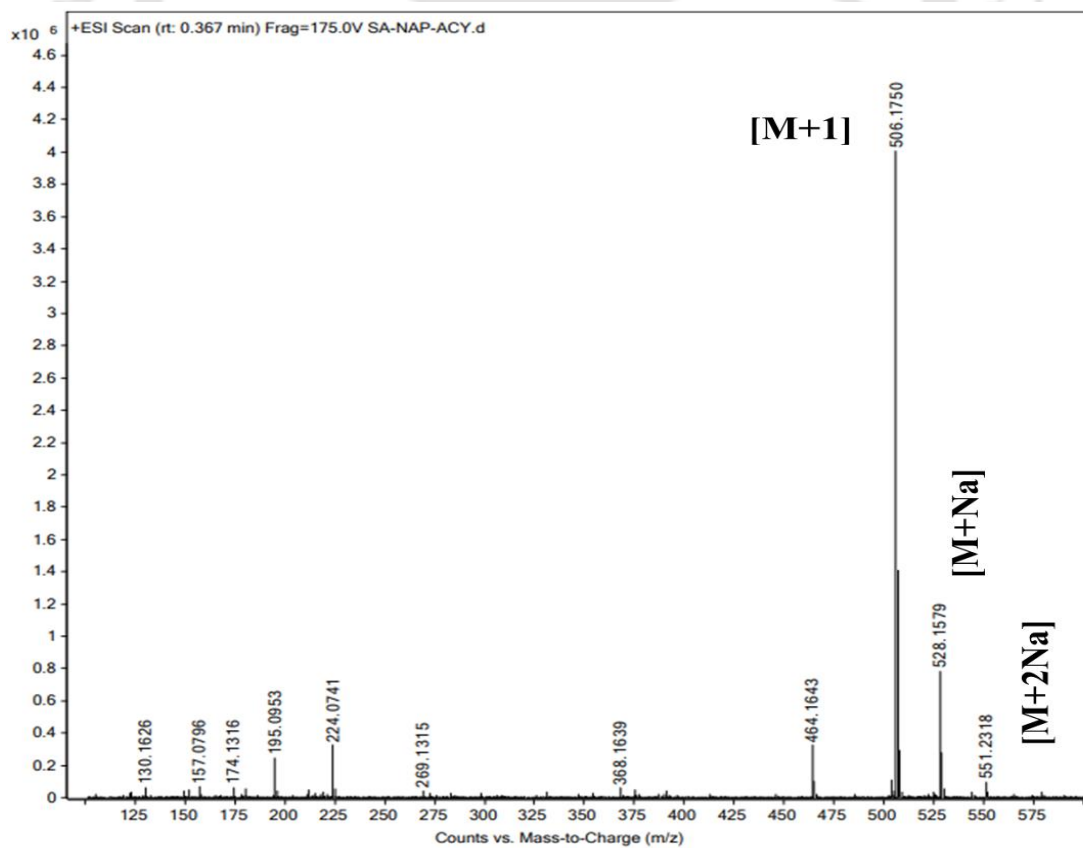


Figure A2.12: Mass spectrum of L4.

Figure A2.13: ¹H NMR spectrum of L5.

Figure A2.14: ^{13}C CMNR spectrum of L_5 .Figure A2.14: Mass spectrum of L_5 .

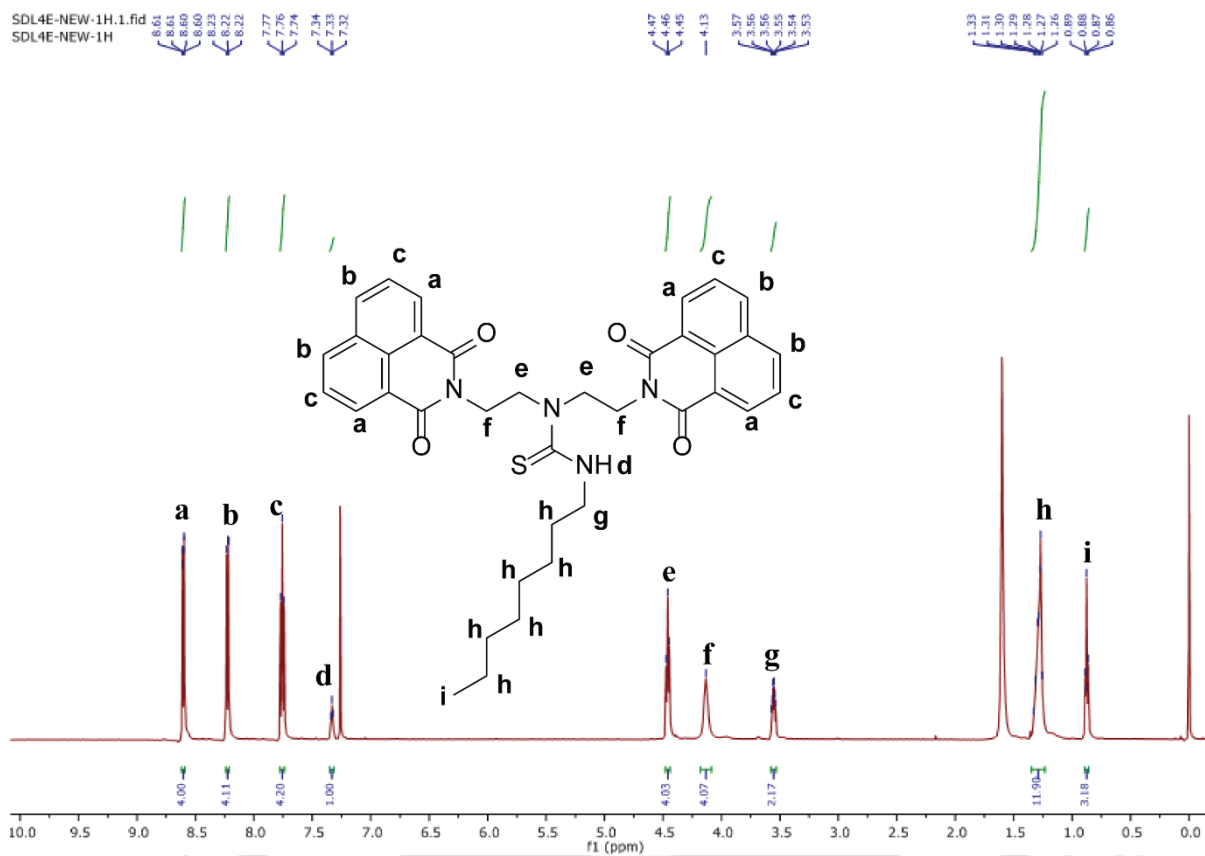
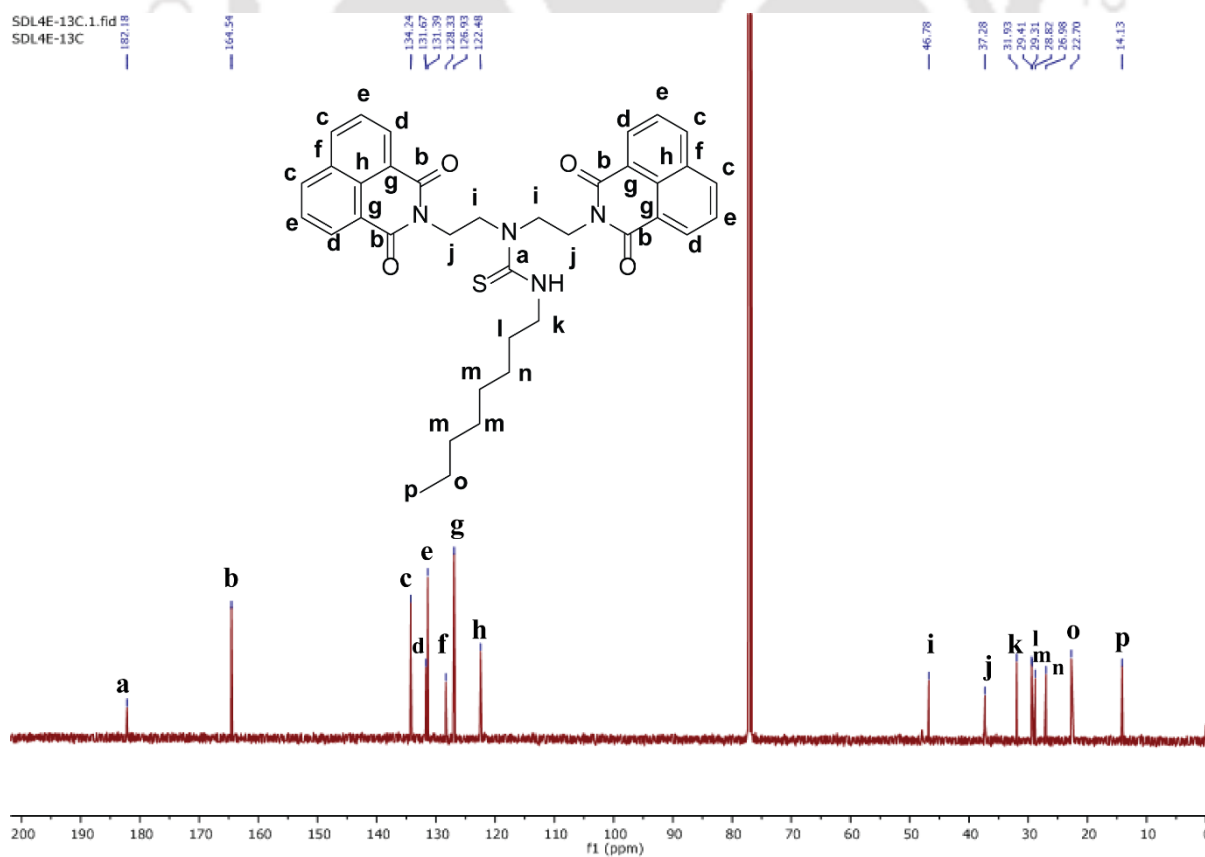
Figure A2.15: ^1H NMR spectrum of L6.

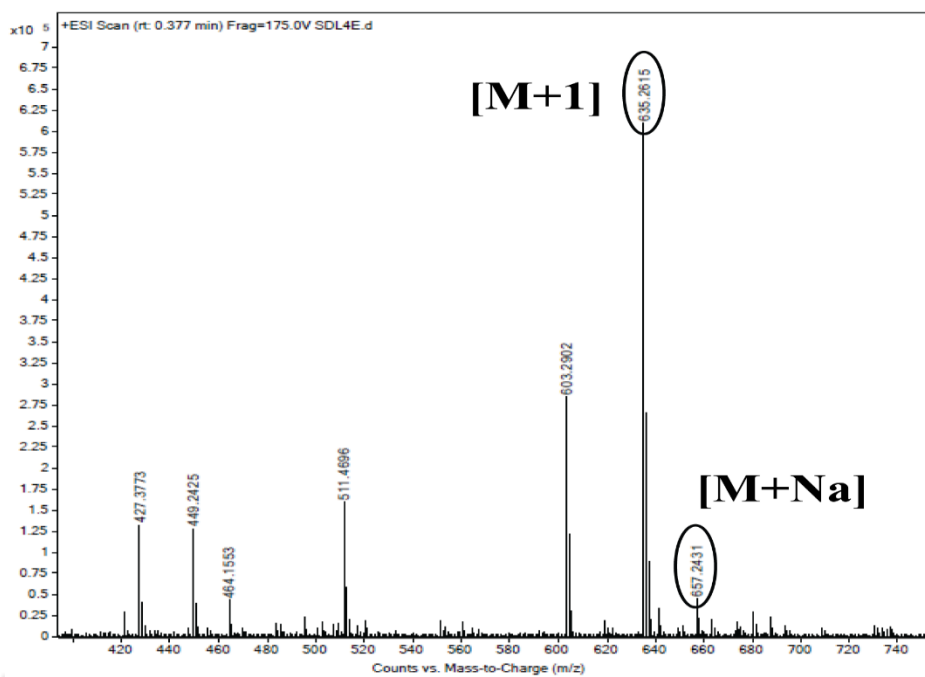
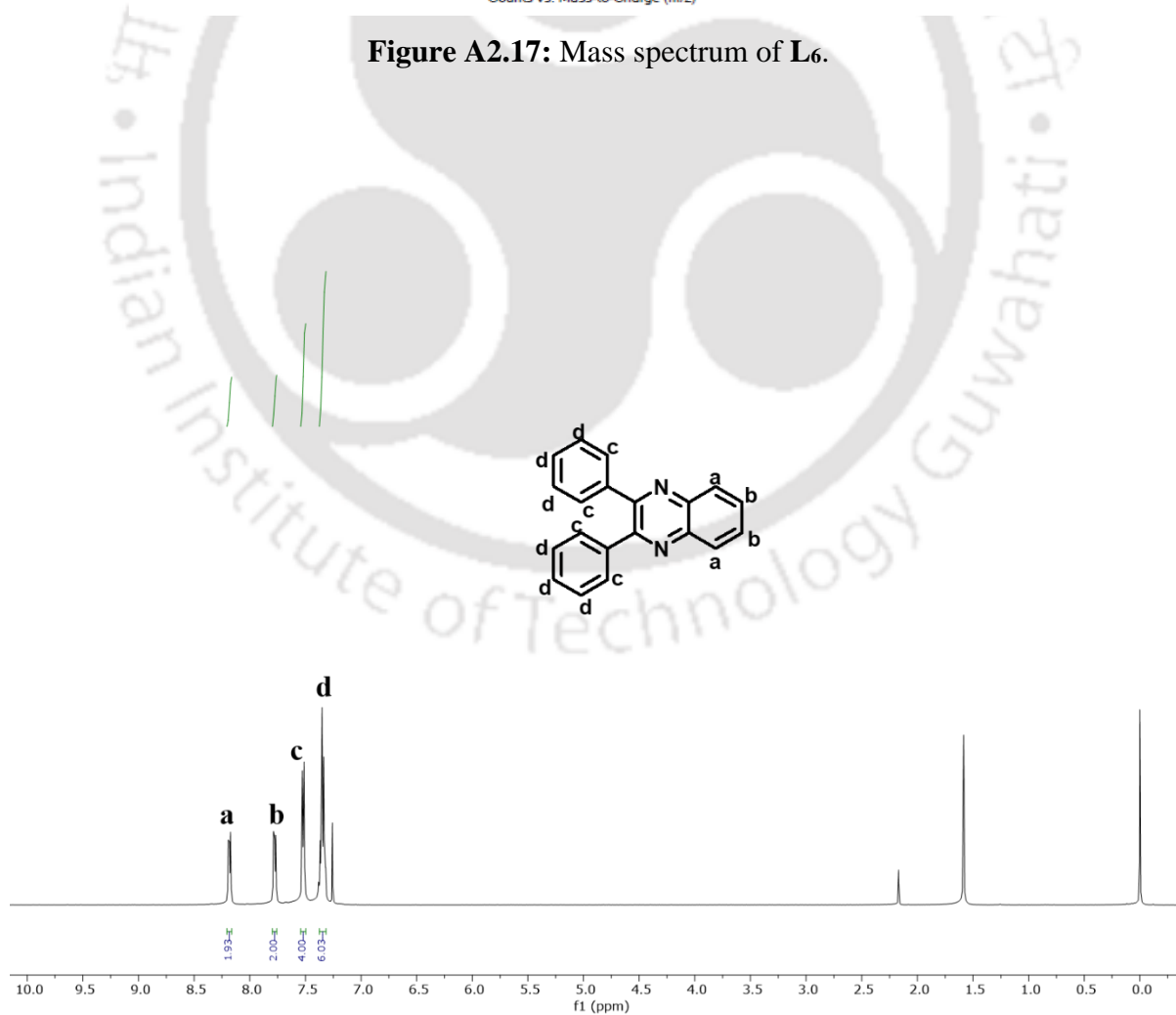
Figure A2.16: ^{13}C NMR spectrum of L6.

Figure A2.17: Mass spectrum of L6.

Figure A2.18: ^1H NMR of L7.

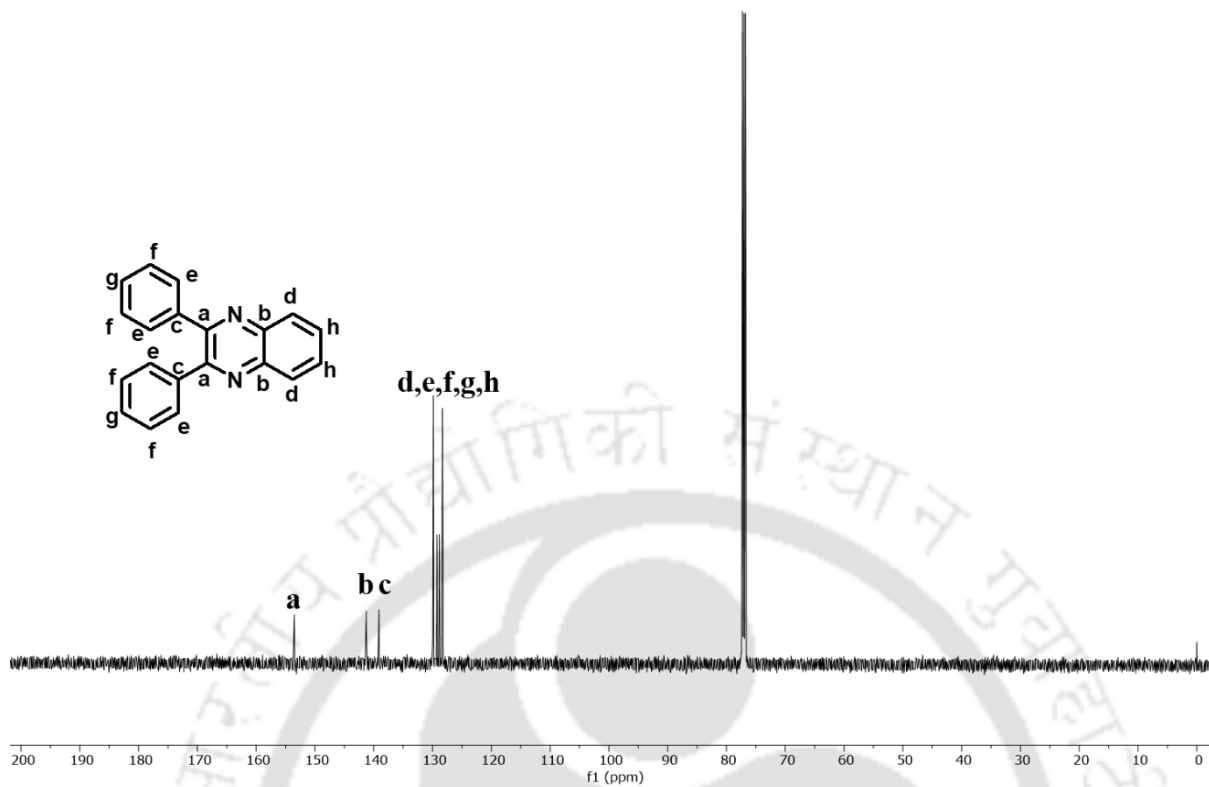
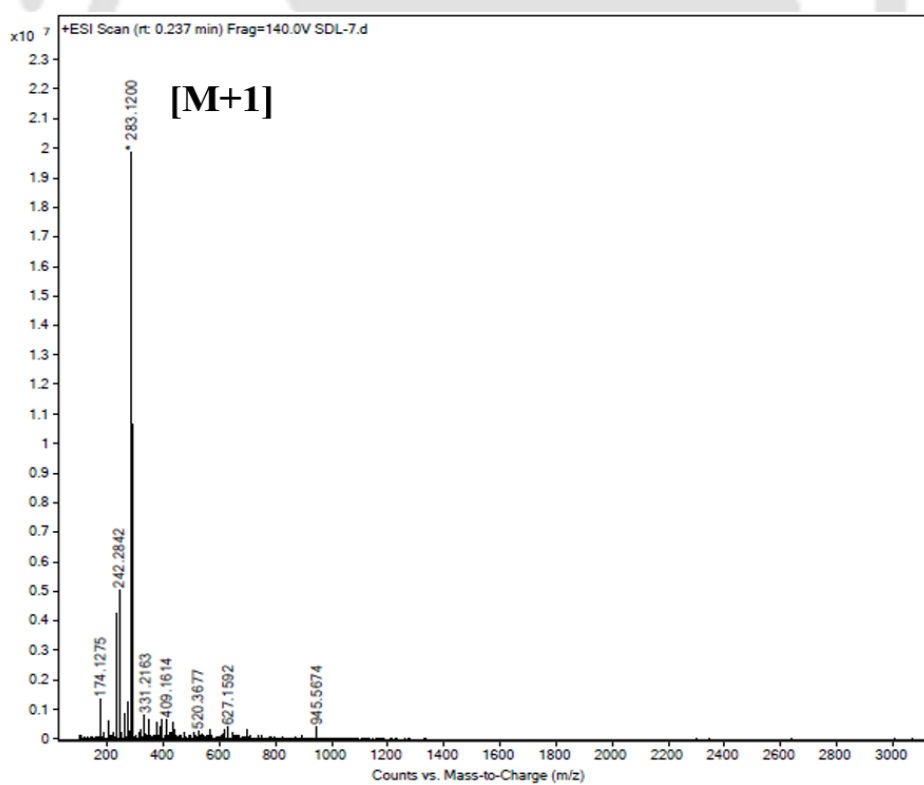
Figure A2.19: ^{13}C NMR of L7.

Figure A2.20: Mass spectrum of L7.

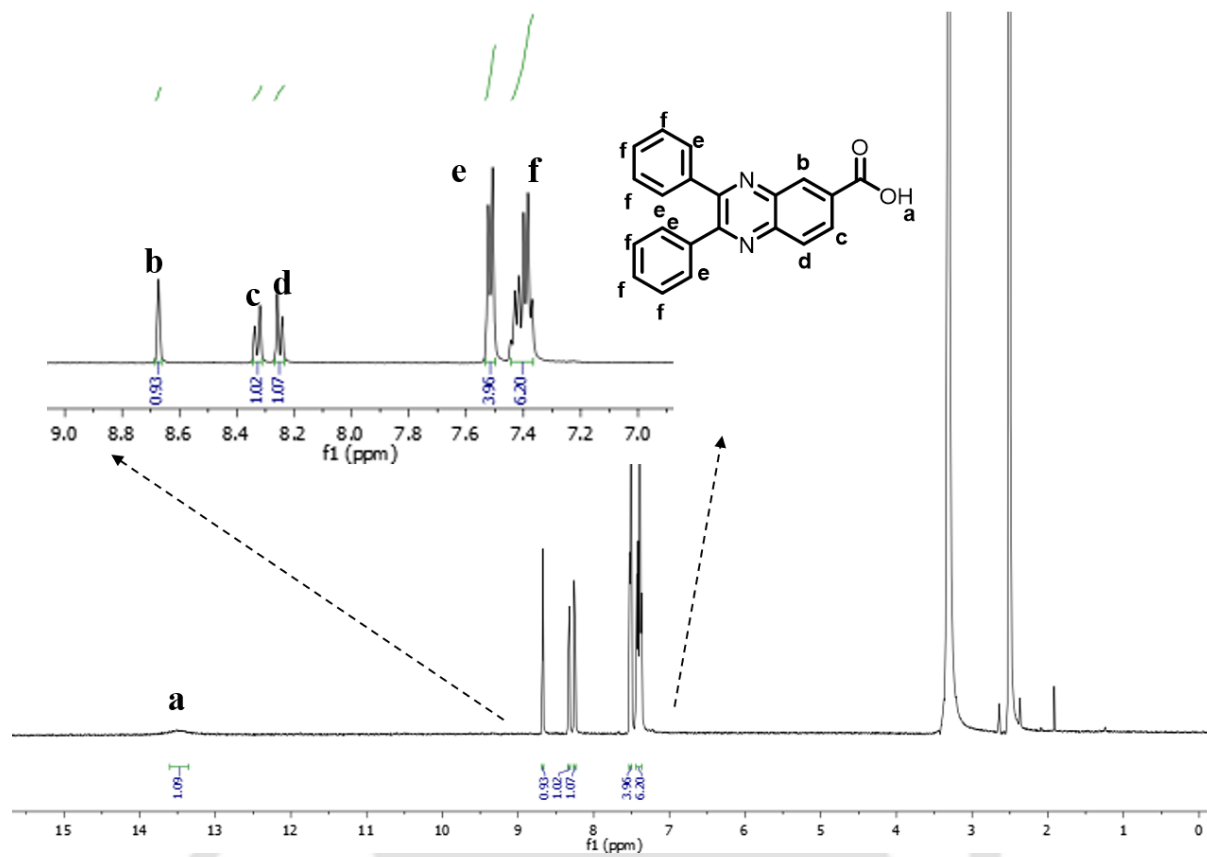


Figure A2.21: $^1\text{H NMR}$ of **L8**.

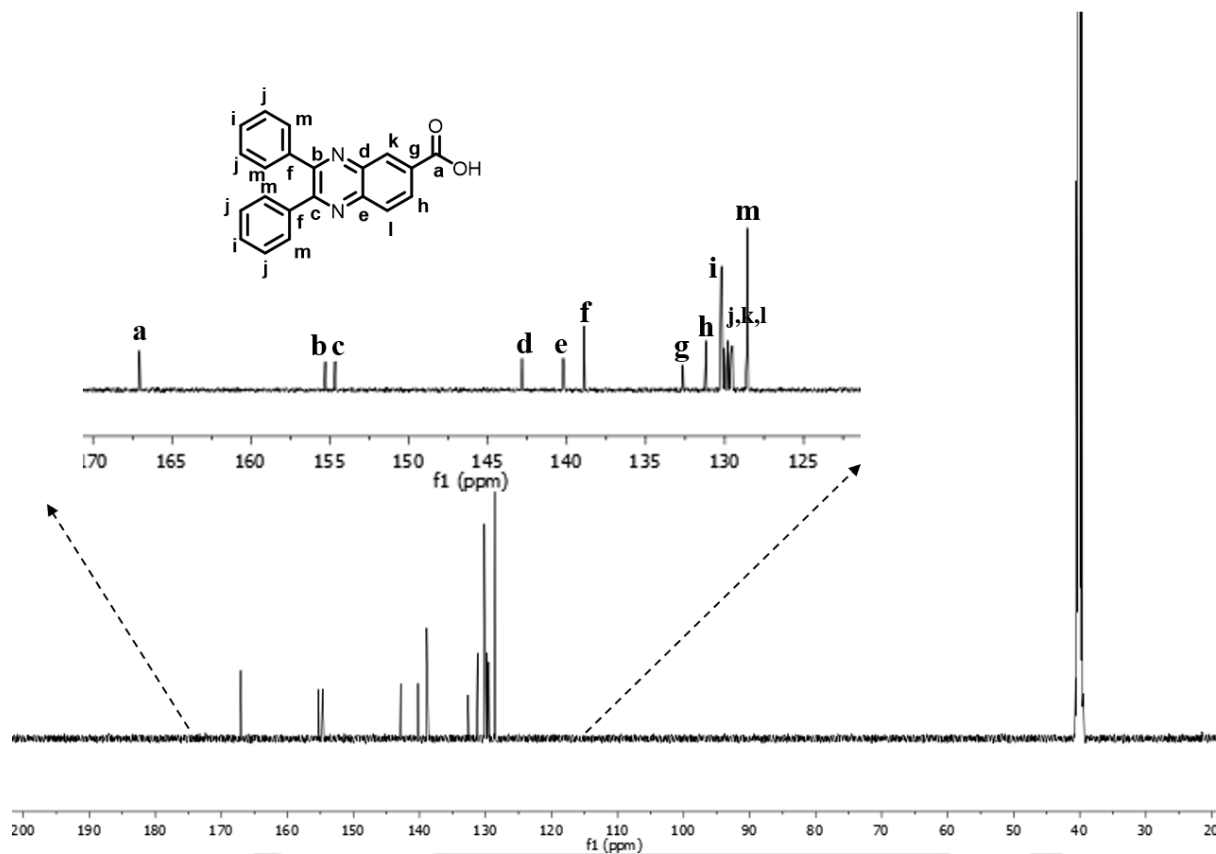
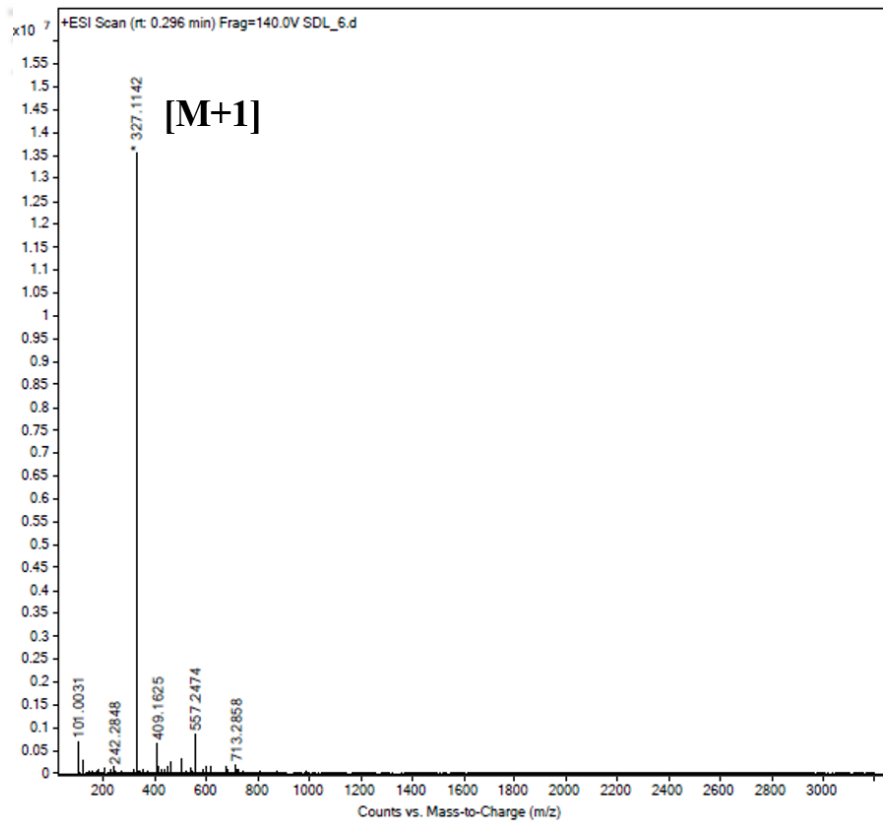
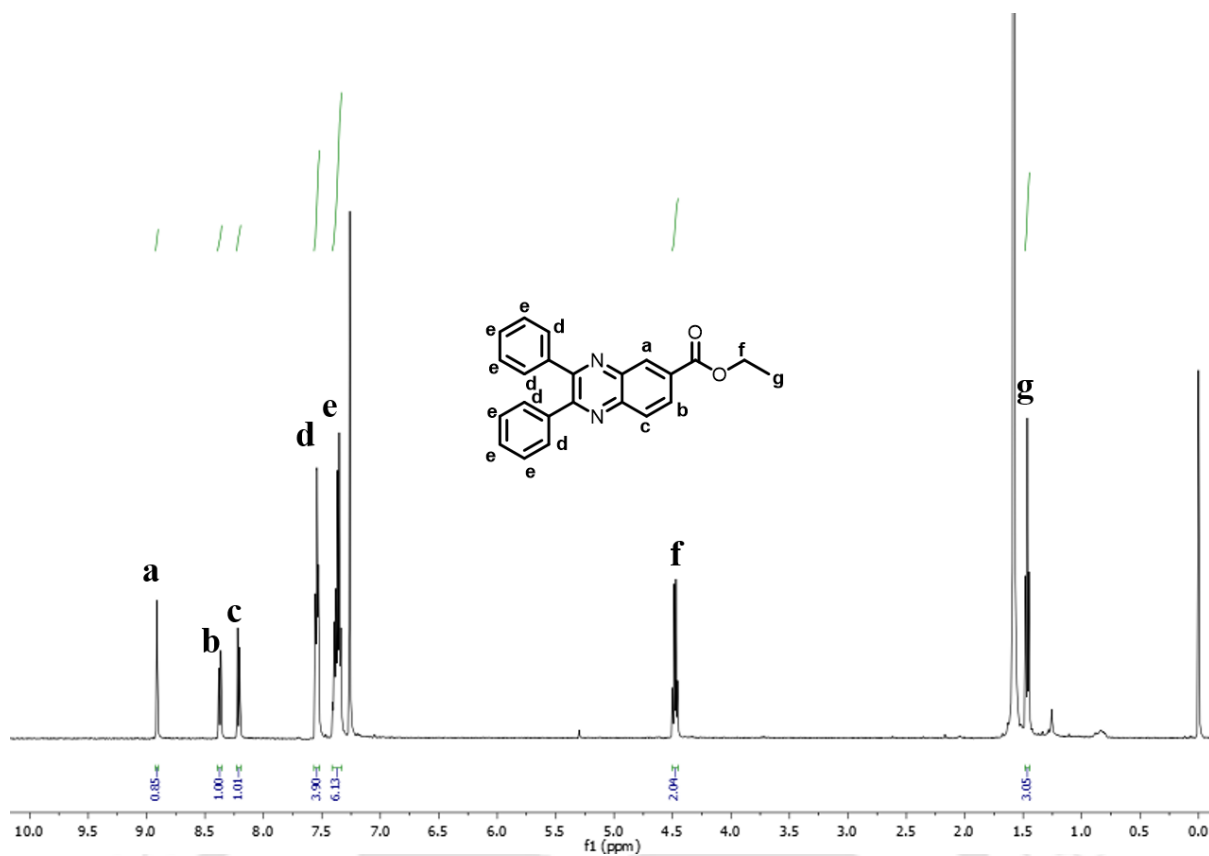
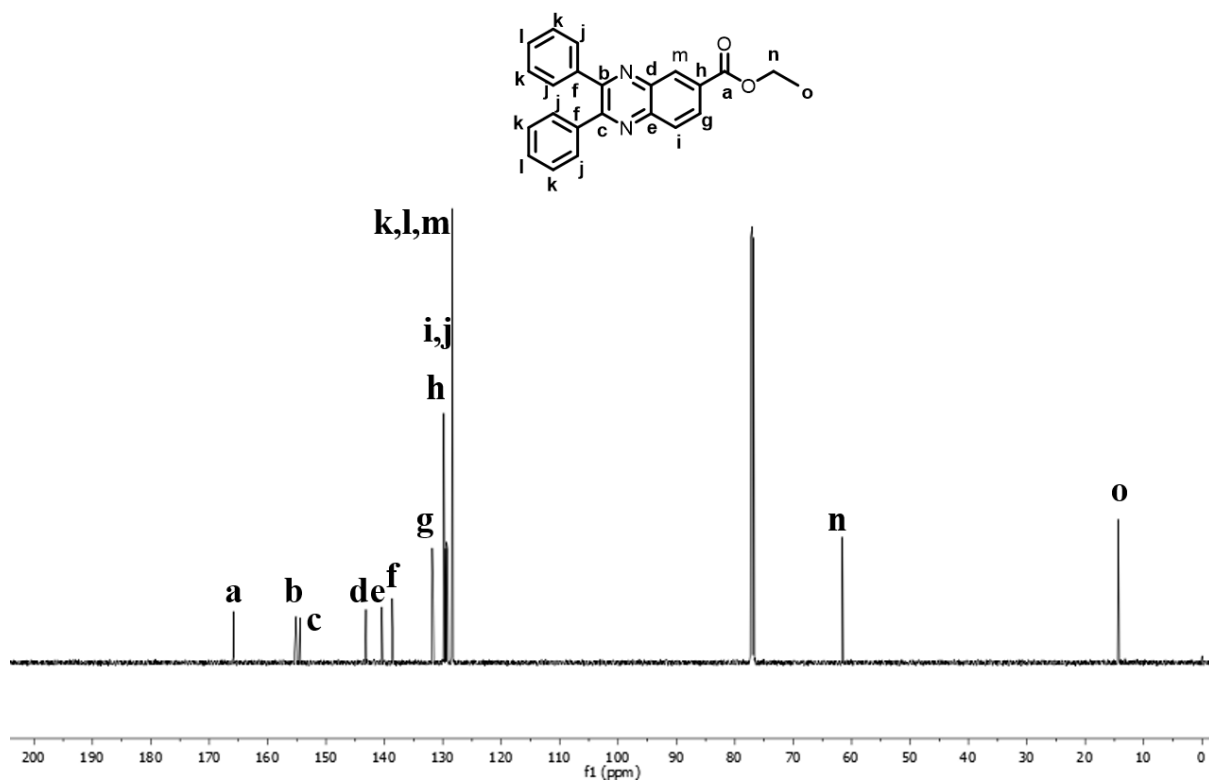
Figure A2.22: ^{13}C NMR of L8.

Figure A2.23: Mass spectrum of L8.

Figure A2.24: ^1H NMR of L9.Figure A2.25: ^{13}C NMR of L9.

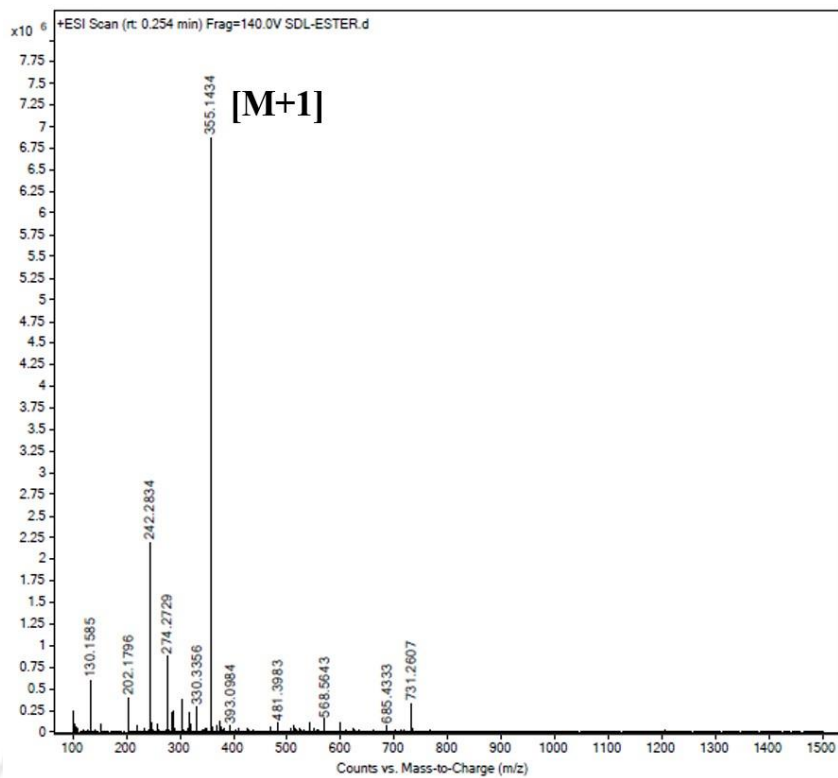


Figure A2.26: Mass spectrum of L9.

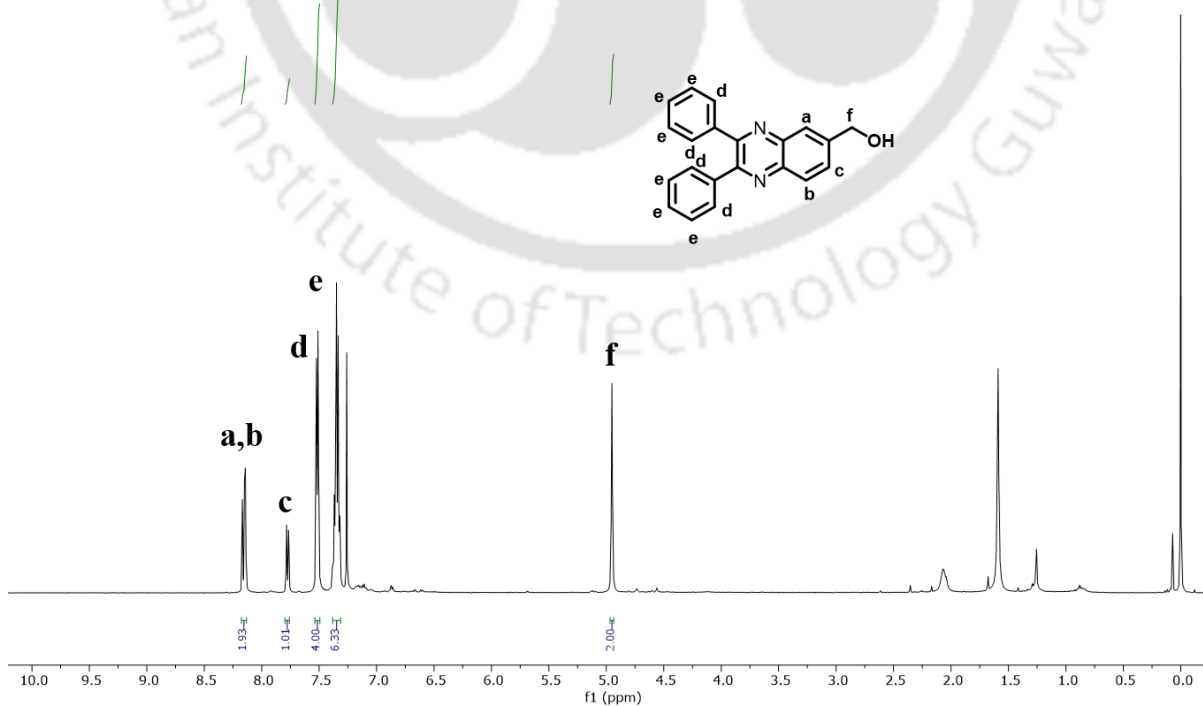


Figure A2.27: ¹H NMR of L10.

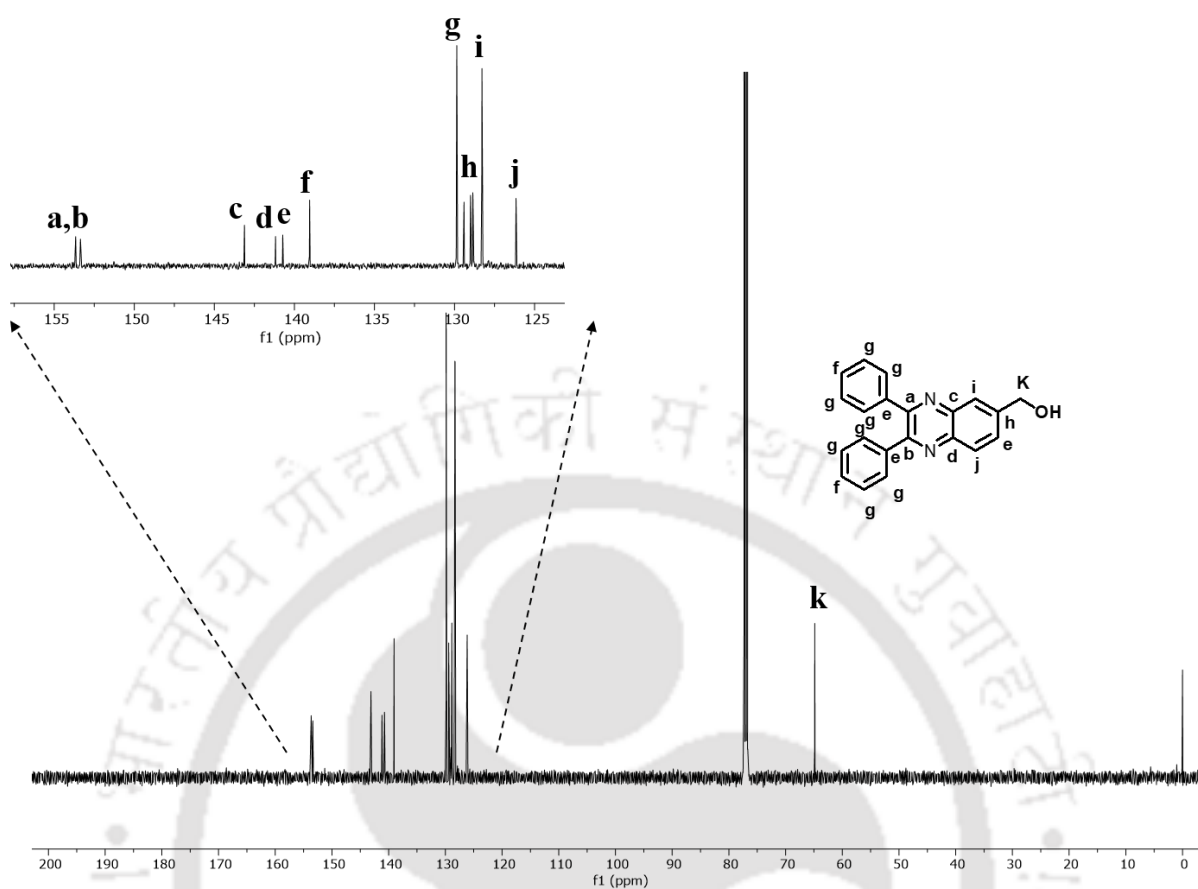
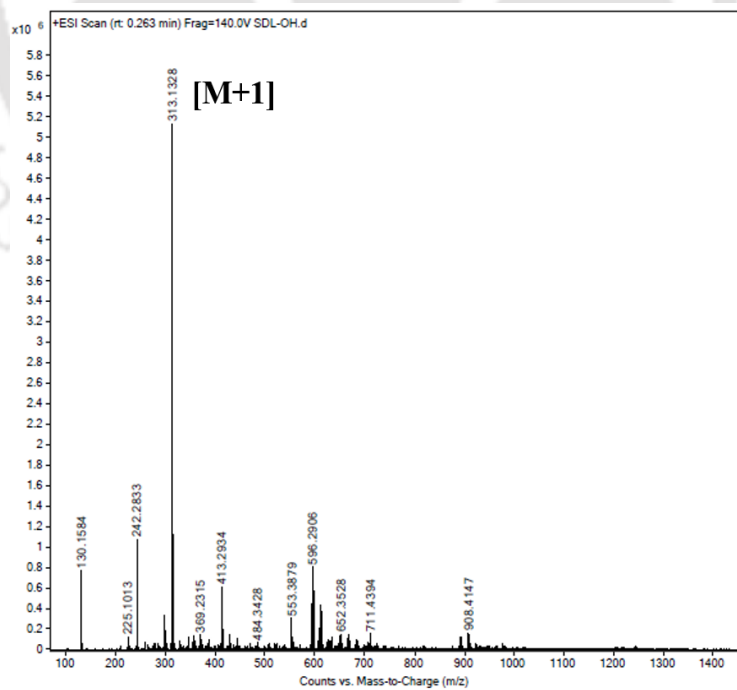
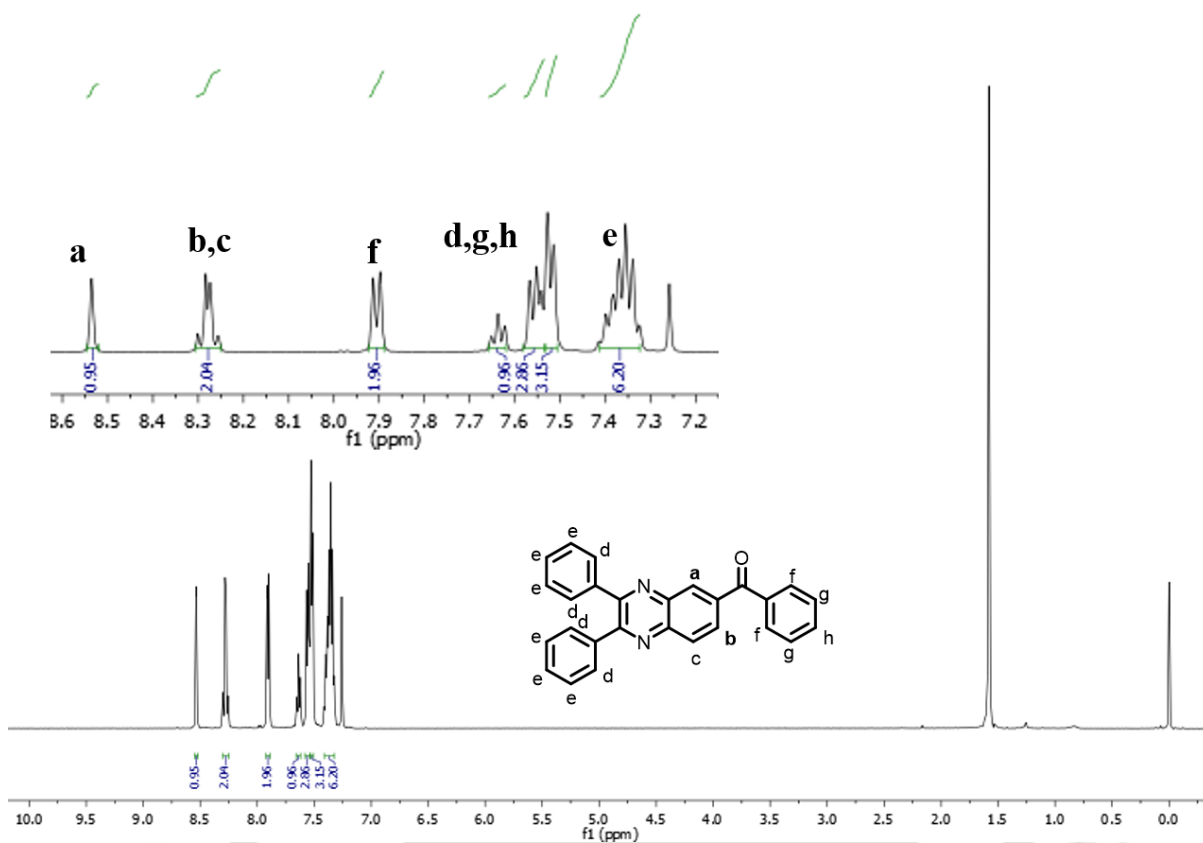
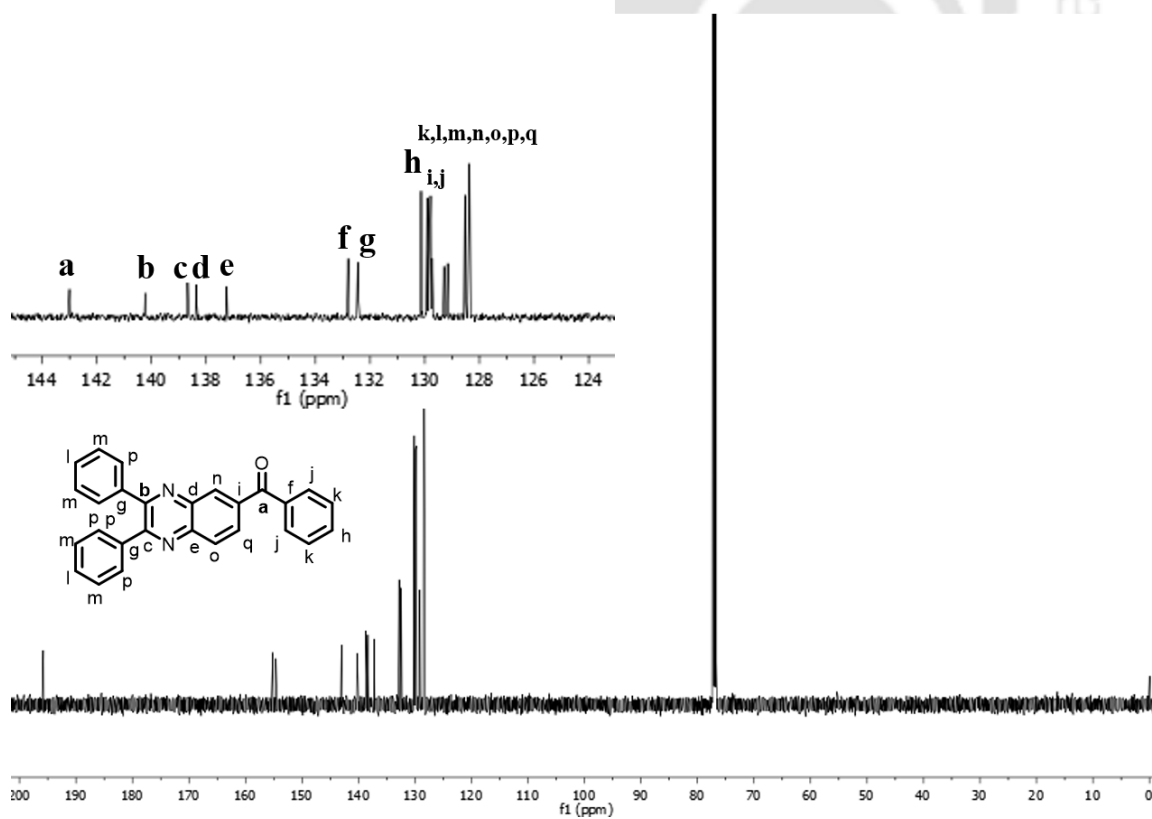
Figure A2.28: ^{13}C NMR of L10.

Figure A2.29: Mass spectrum of L10.

Figure A2.30: $^1\text{H NMR}$ of L11.Figure A2.31: $^{13}\text{C NMR}$ of L11.

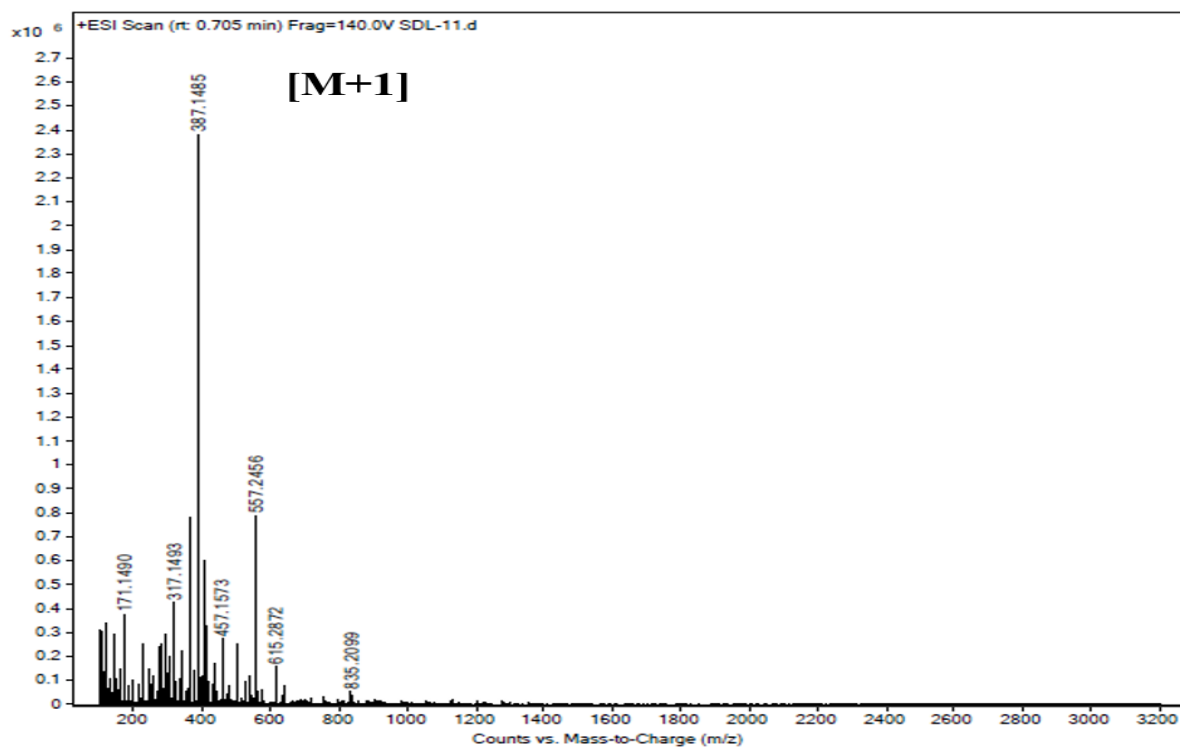
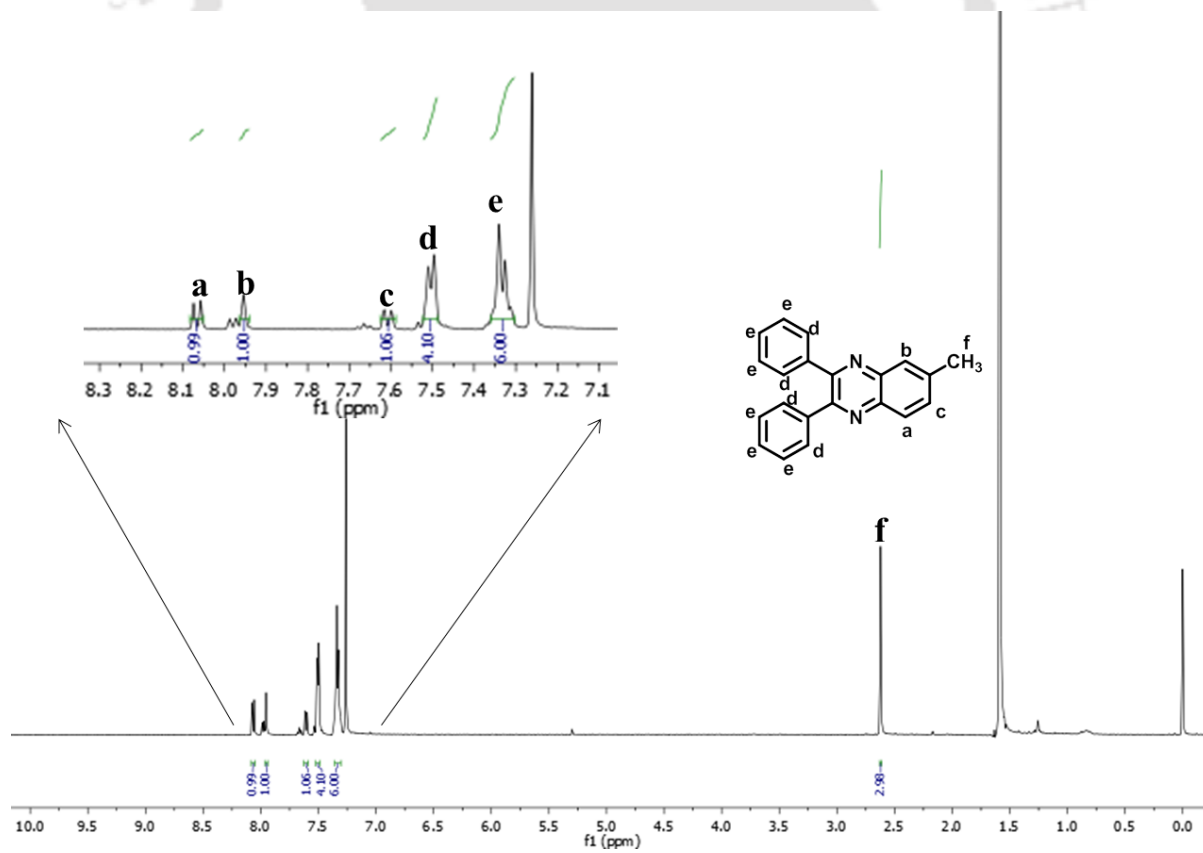


Figure A2.32: Mass spectrum of L11.

Figure A2.33: ¹H NMR of L12.

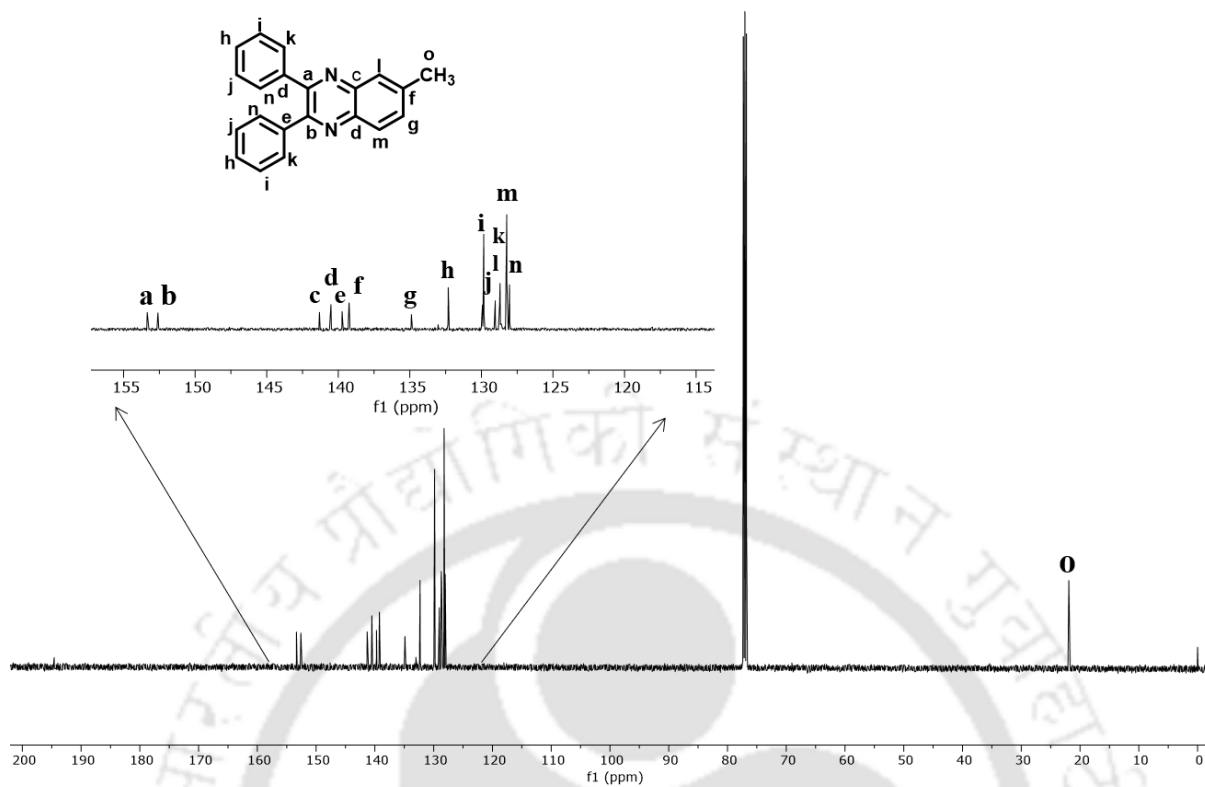
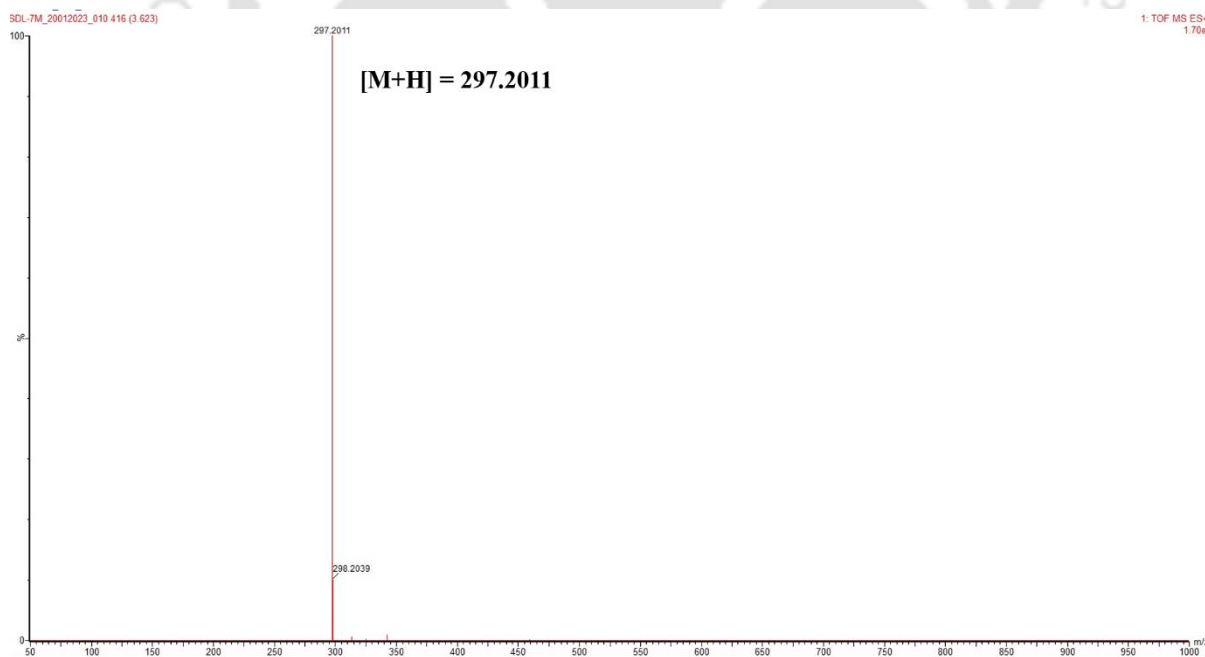
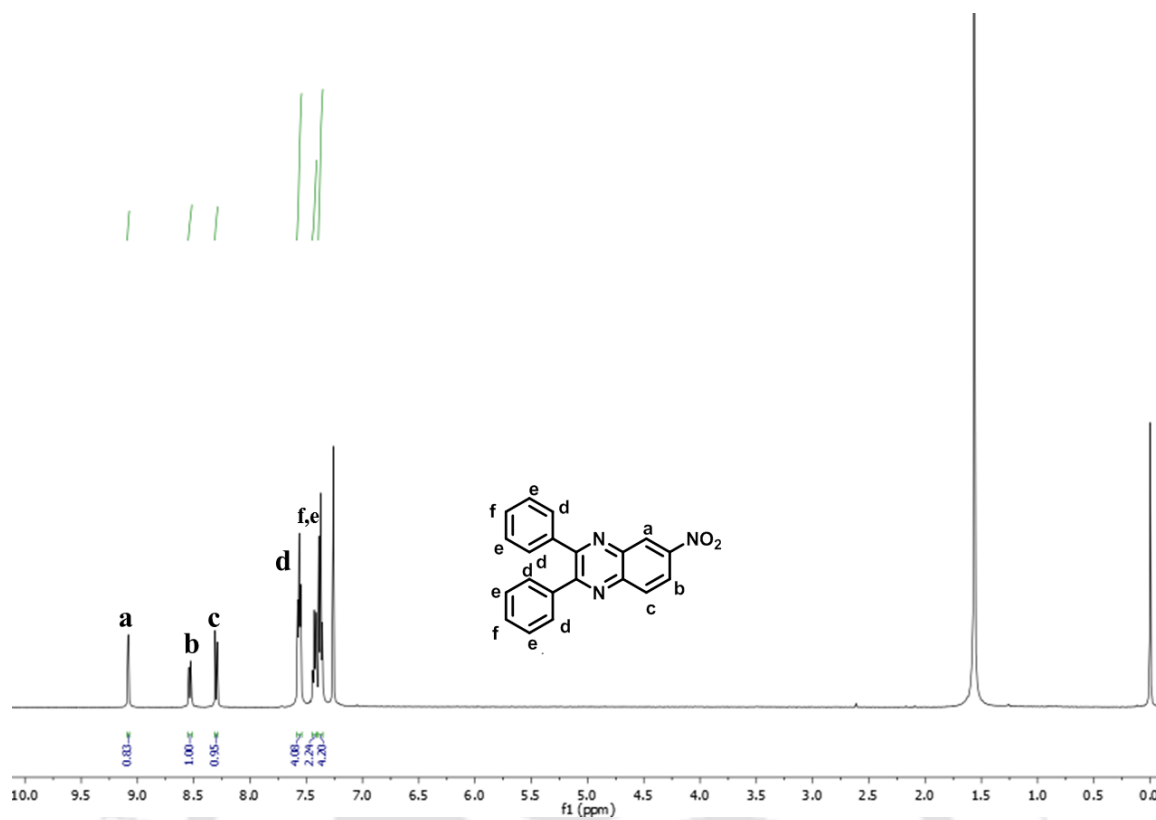
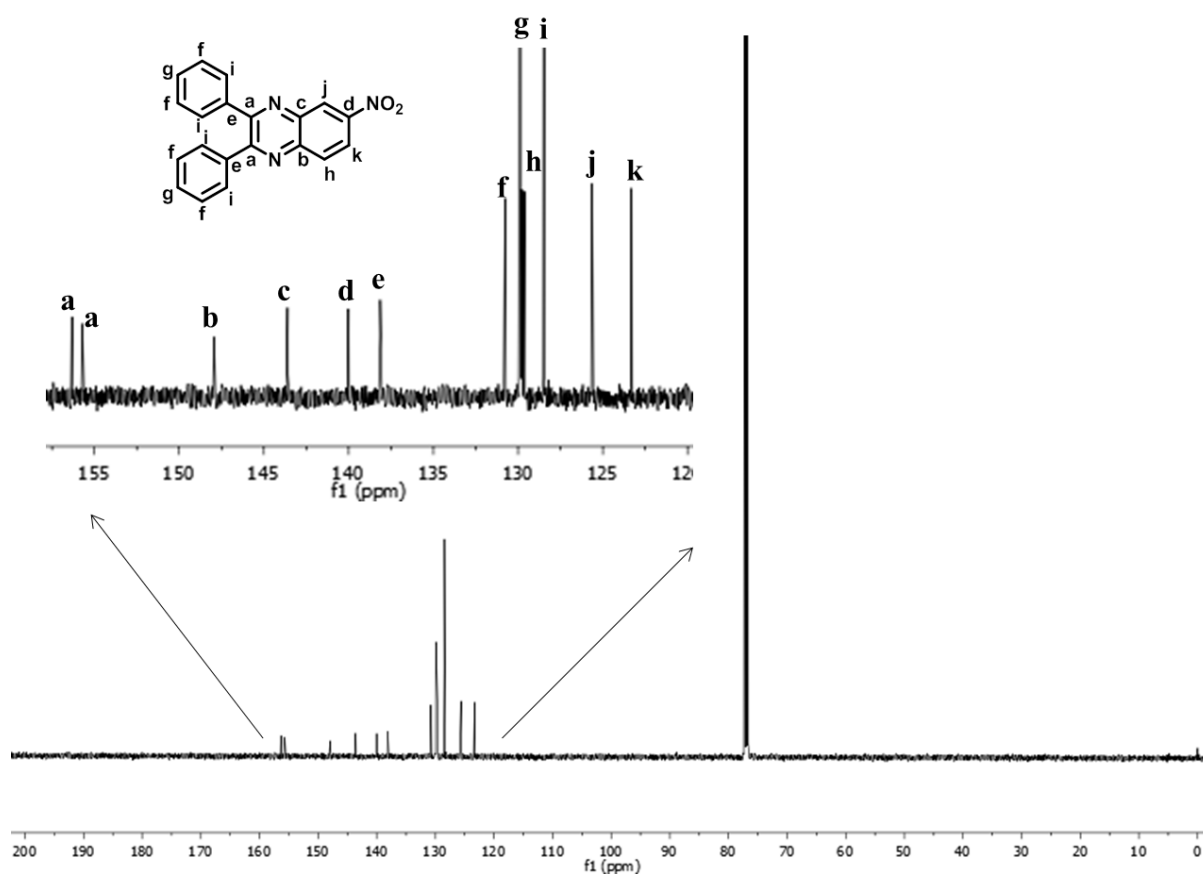
Figure A2.34: ^{13}C NMR of L12.

Figure A2.35: Mass Spectra of L12.

Figure A2.36: $^1\text{H NMR}$ of L13.Figure A2.37: $^{13}\text{C NMR}$ of L13.

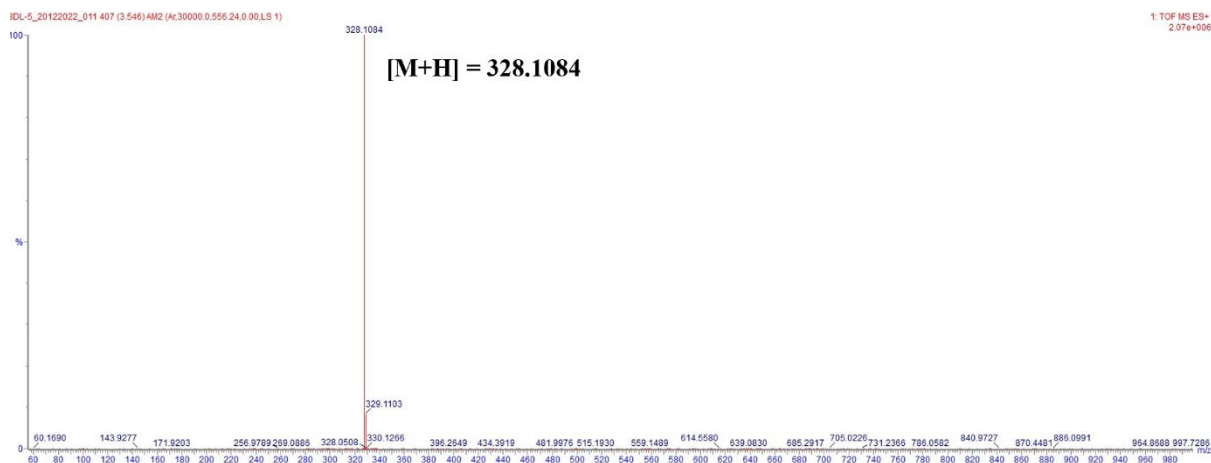
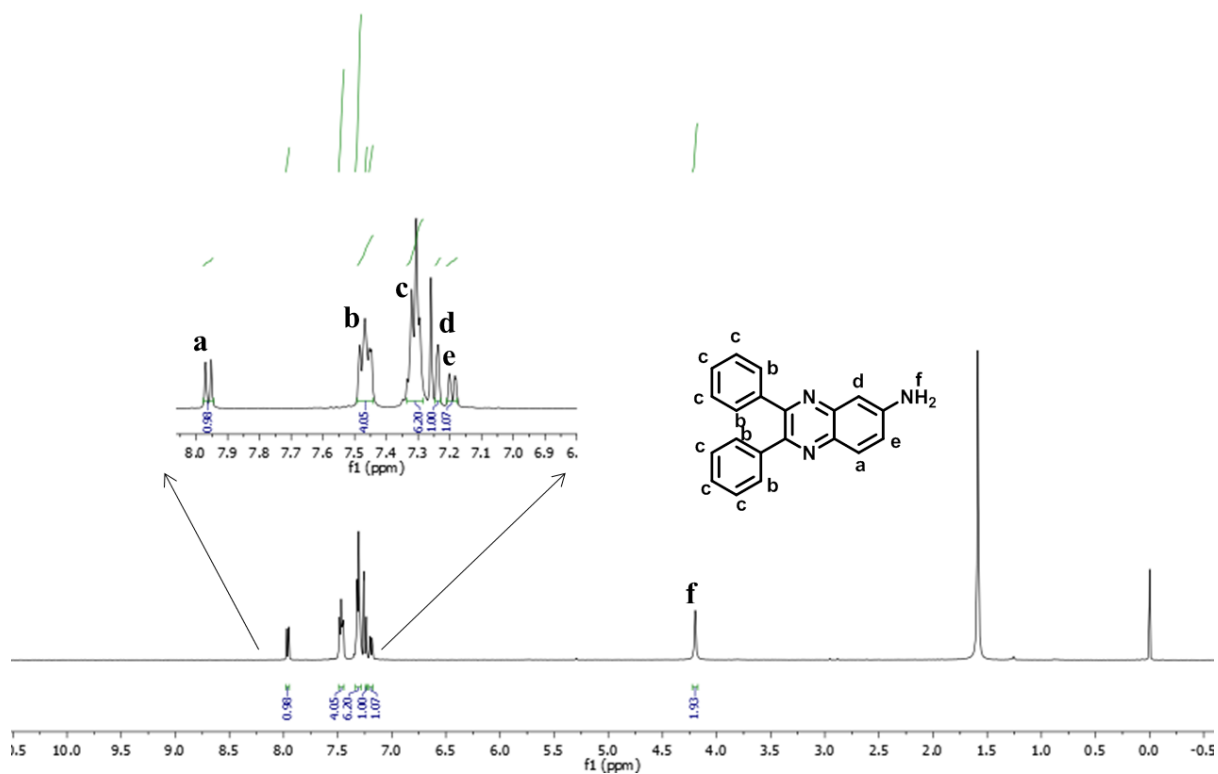


Figure A2.38: Mass Spectra of L13.

Figure A2.39: ¹H NMR of L14.

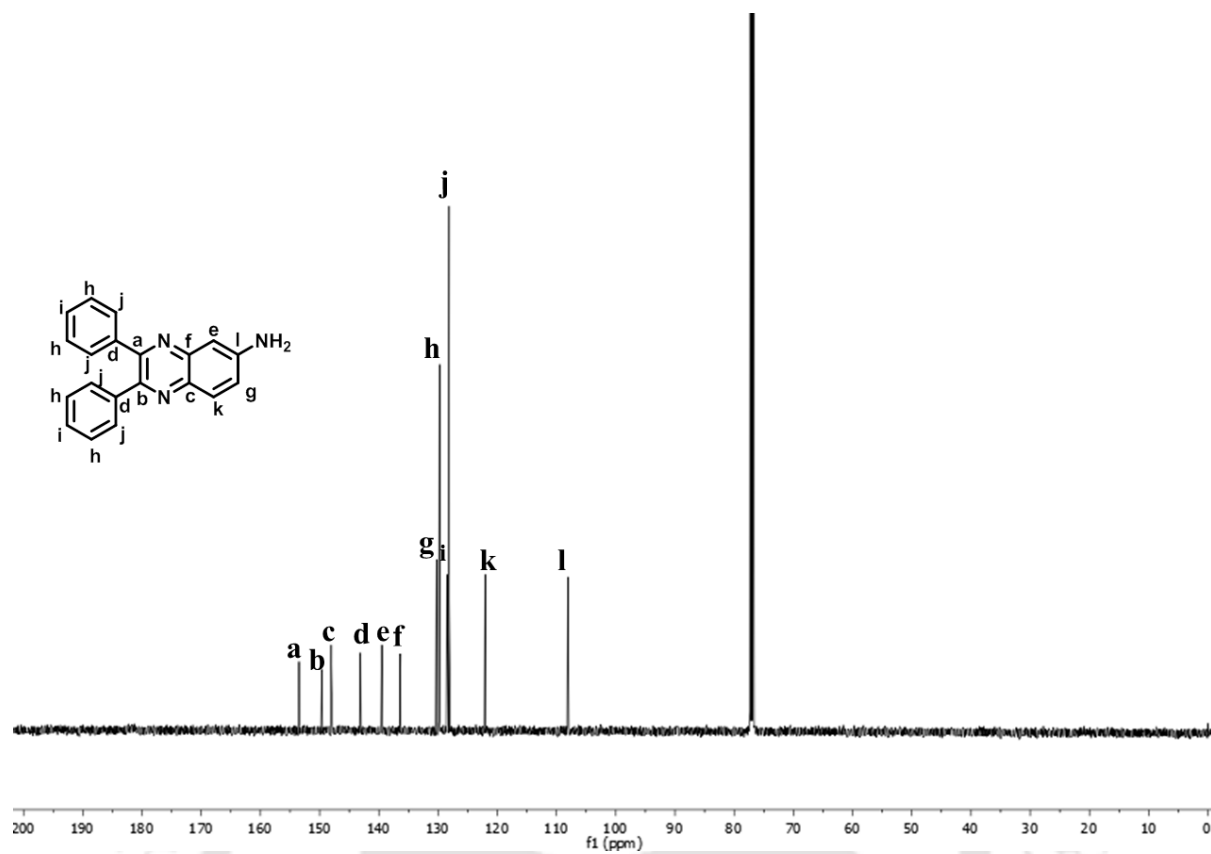
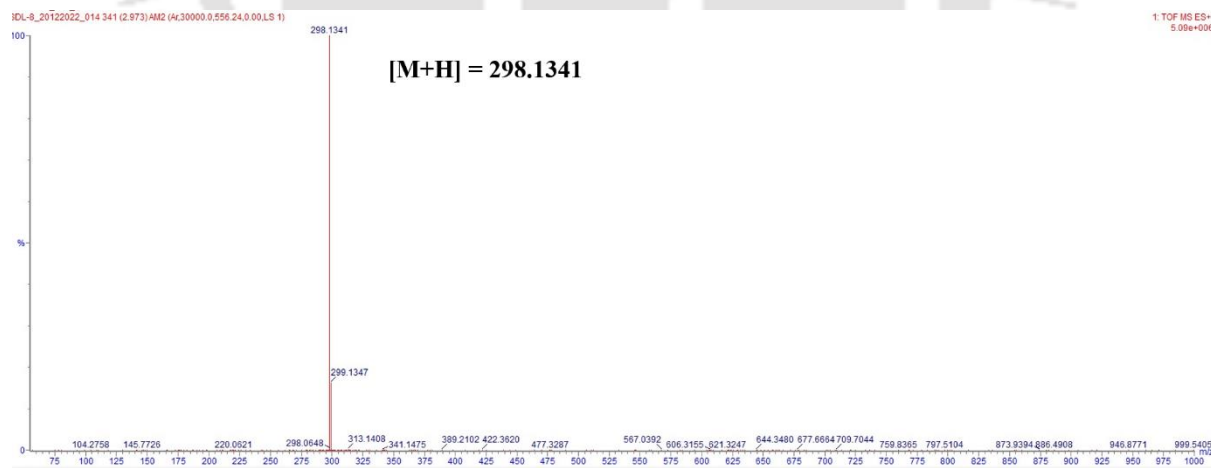
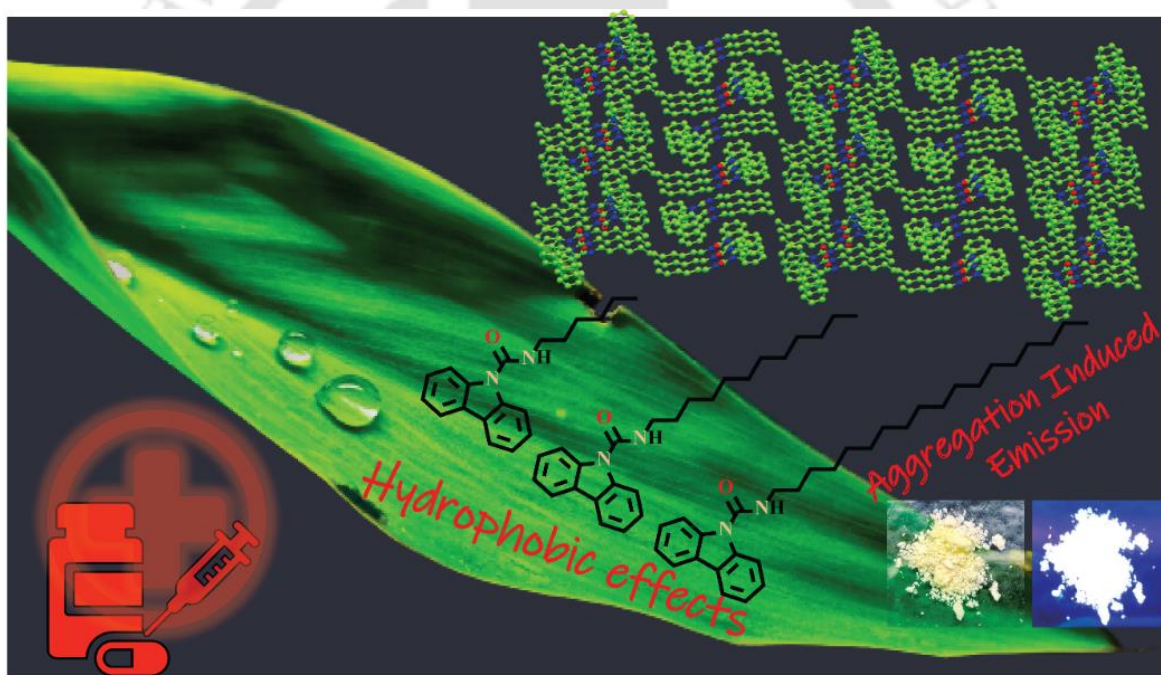
Figure A2.40: ^{13}C NMR of L14.

Figure A2.41: Mass Spectra of L14.



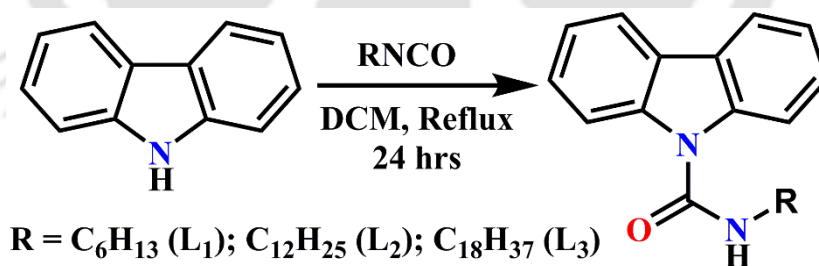
Carbazole-adhered Amphiphilic AIEgen: Detection of Nitro-Antibiotics and Hydrophobic Surfaces



3.1 Background and focus of the chapter

Nature has always been an inspiration for researchers to develop a rudimentary understanding about various phenomenon, diverse constituents involved, their features, textures, and designs which lead to unique technologies while imitating it. As an example, wettability is a particular facet of material surfaces which helps in water-repellent behaviours, e.g., lotus leaf, Yam leaf, rose petals, scales of fish, water strider, parts of cactus, furs of river otter and many more.^{3.1-3.2} Implementation of amphiphilic molecules in this application is an interesting task. Further molecular framework can be tuned with chemical synthesis achieving fluorescent hydrophobic surface and expanding the utility.

Nowadays, hundreds of antibiotics are prescribed for human beings, animals, agriculture, stockbreeding, breeding, and aquaculture, as a cure against several kinds of hostile bacteria. Unfortunately, the widespread use, and even overuse, of antibiotics has undesirable consequences for the environment and human health. In recent years, several types of fluorescent sensors have been developed for detecting different classes of antibiotics, including luminescent metal–organic frameworks, fluorescent organic polymers, and small-molecule fluorescent sensors.^{3.3-3.5} AIEgen being a promising candidate for chemosensing has been used for this purpose in this piece of work. Nitrofurazone (NFZ) and nitrofurantoin (NFT) are two very common antibiotics primarily used to treat skin infections and urinary tract and kidney infections, respectively. Prolonged exposure to these antibiotics can cause a variety of side effects such as vomiting, headache, nausea, loss of appetite, and dizziness. Hence, it is imperative to develop a proper method to prevent the environmental pollution caused by these antibiotics.^{3.6-3.10}



Scheme 3.1: Synthesis route of L_1 , L_2 , L_3 .

3.2 Crystallographic evidence

The suitable crystal for single-crystal X-ray analysis of the amphiphile, L_1 was obtained from the CHCl_3 -MeOH mixture, and it crystallized in the monoclinic space group $\text{P}21/n$ [CCDC number: 2235513]. The structural elucidation revealed the existence of four symmetrical probes in the asymmetric unit ($Z = 4$). L_1 forms a one-dimensional self-assembled architecture through hydrogen bonding interaction ($\text{N-H}\cdots\text{O}=\text{C}$). The intermolecular hydrogen bonding distance was measured to be 2.196 \AA (Figure 1(A)). Figure 1(C) depicts efficient head-to-tail packing and the

alkyl chains are in interdigitated orientation. Observation from the crystal structure reveals, there exists an $\pi\cdots\pi$ interaction between the aromatic motifs at a distance of 5.04 Å. Detailed hydrogen bonding interactions (distances and bond angles) of **L1** are provided as supporting information (Table S1). We suppose these typical supramolecular interactions are present in the other congeners. However, **L2** and **L3** did not crystallize even after several attempts.

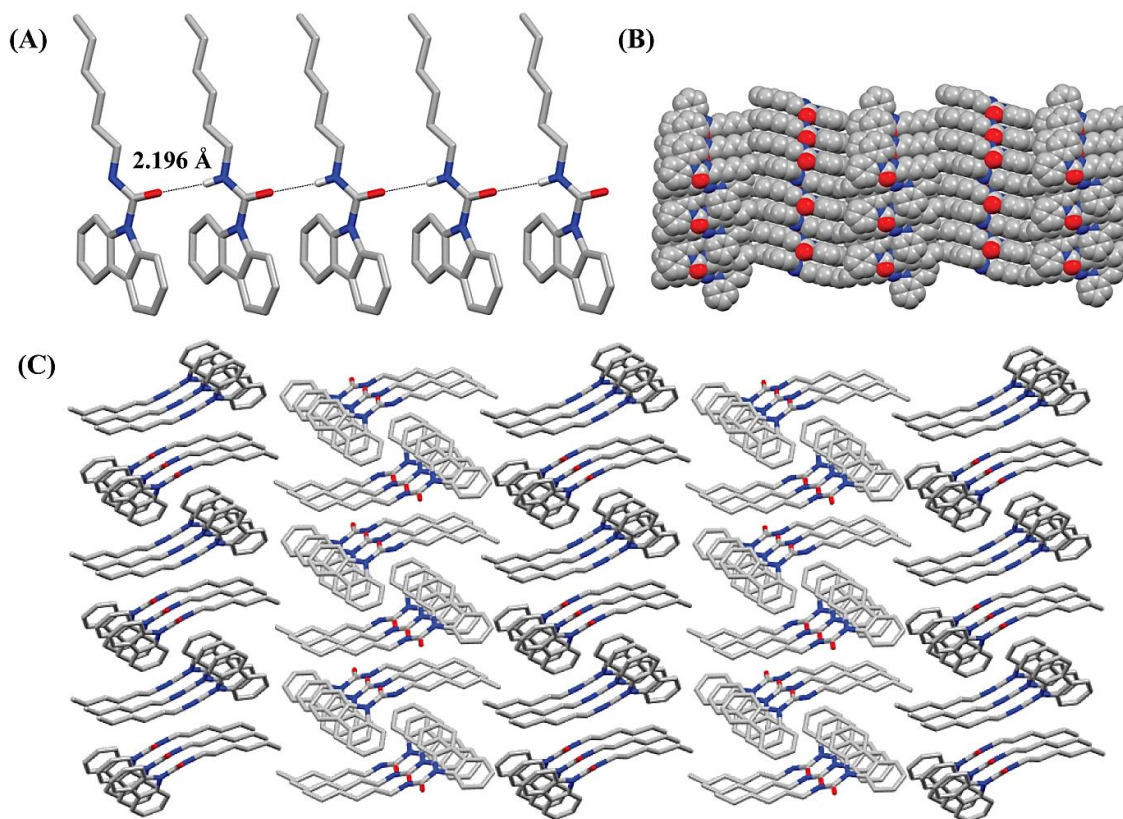


Figure 3.1: (A) Structure of **L1** showing intermolecular hydrogen bonding (B) Space-filled model view of **L1** (C) Packing diagram of **L1**, as seen along the crystallographic *b*-axis.

3.3 Photophysical studies

Preliminarily, the spectral properties of **L1**, **L2**, and **L3** were analyzed by absorption spectroscopy. All the compounds exhibited absorption maxima around 300 nm in both organic (THF) and aqueous media. A notable change in the UV-vis spectra recorded in aqueous media was observed. The tail region of the spectra rose above the baseline and higher than the spectra recorded in the organic medium (Figure 3.2(A), (B), (C)). The extent of the rise in the tail region varied in three cases. We have monitored it at 600 nm wavelength. From the plot, (Figure 3.2(D)) **L3** displayed the highest relative absorbance value of its other congeners. This experiment output explains the formation of aggregates in the water among the three cases. Light scattering occurs due to the presence of aggregated particles in the aqueous solution which is recorded in UV-vis spectra.

Concentration-dependent aggregation studies were carried out via emission spectroscopy. The output has been shown in (Figure 3.2(C)) where the relative intensity has been plotted concerning the concentration of the three congeners. L_2 and L_3 displayed almost similar traits in the enhancement of fluorescence intensity on increasing concentration in water.

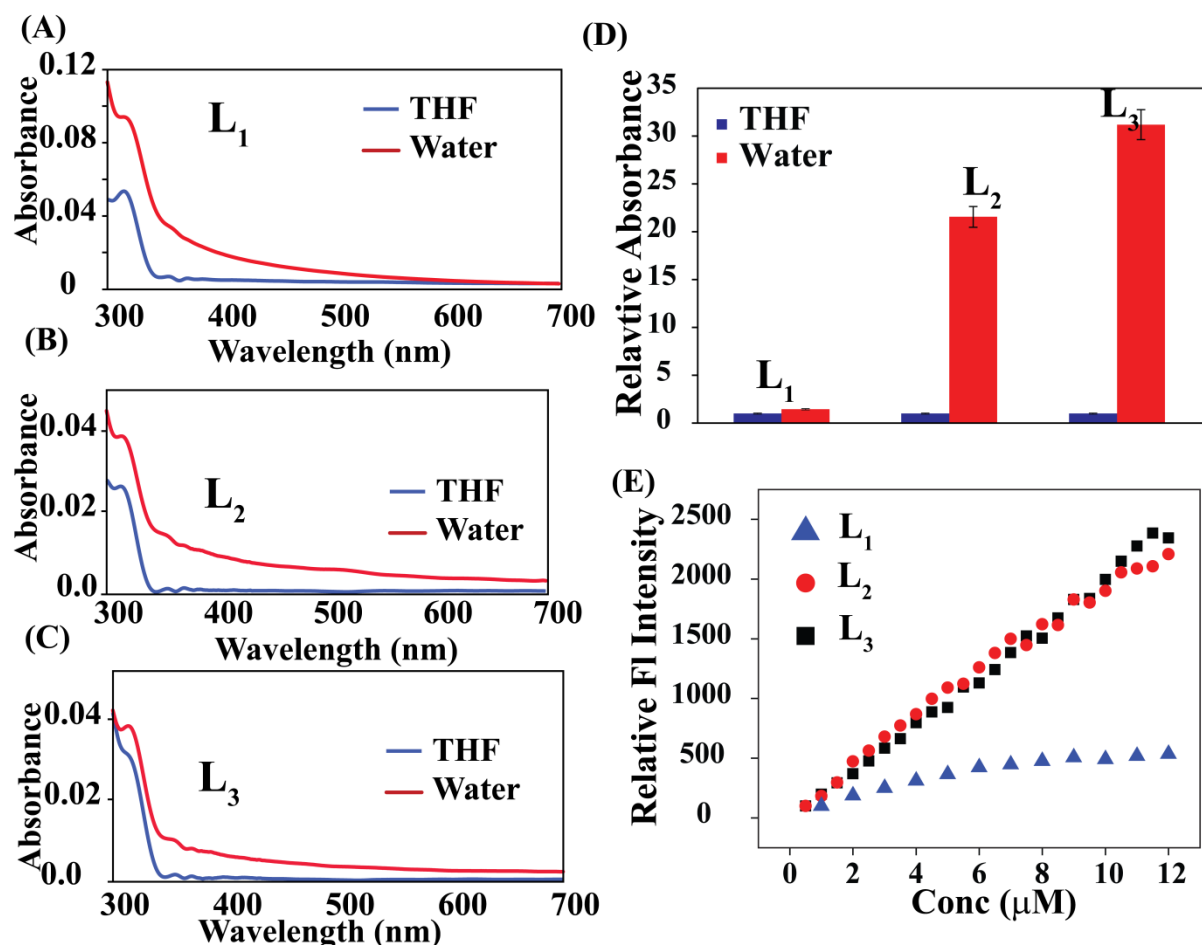


Figure 3.2: Absorbance spectrum of (A) L_1 , (B) L_2 , (C) L_3 in THF and Water. (D) The plot of Relative absorbance for L_1 , L_2 , L_3 . (E) The plot of relative emission intensity of L_1 , L_2 , and L_3 on increasing concentration in water.

Further dealing with emission spectroscopy, it was found that L_1 , L_2 , and L_3 exhibit aggregation-induced emission (AIE) properties to various extents. Maintaining an effective concentration of $10 \mu\text{M}$ of the three compounds solvent switching was adopted. It was noted that on increasing water percentage in organic medium (THF) there was an enhancement in emission intensity. This indicates the compounds were in a dispersed or monomeric state in organic media. In addition to poor solvent, water, solubility wanes and they start to aggregate. The hydrophobicity of these amphiphiles reduces solubility in water. Thus, these hydrophobic amphiphiles aggregate and cause emission intensity enhancement. In the case of

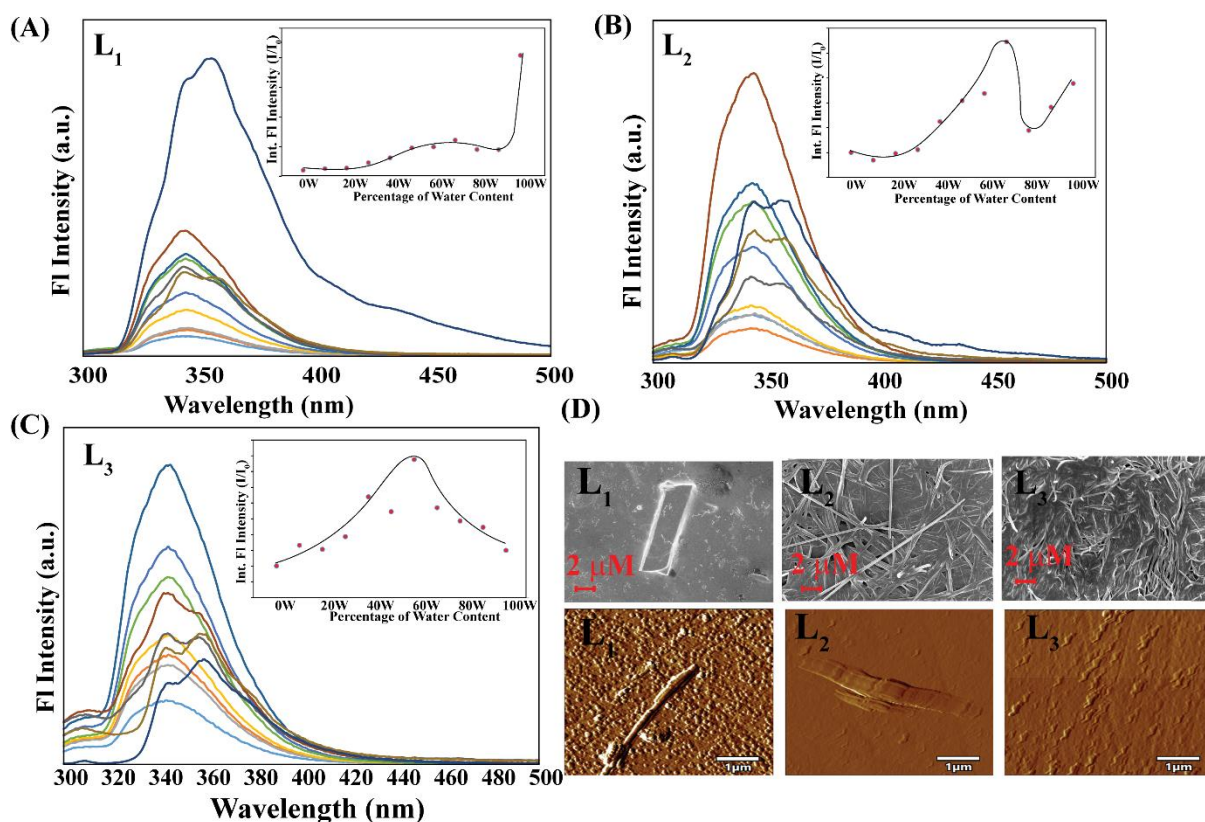


Figure 3.3: Emission spectroscopy plot with varying water percentage in THF (A) L_1 , (B) L_2 , and (C) L_3 (D) FESEM and AFM images of L_1 (in 100% water), L_2 (in 70% water), L_3 (in 70% water).

L_1 , the highest emission intensity was observed. The fluorescence intensity at 100% water is almost 16 times the original intensity in 100% THF. While in the case of L_2 and L_3 on increasing poor solvent content highest fluorescence emission intensity was noted at 70% water. The intensity at 70% water was approx. 6.04 and 2.85 times than the original intensity in THF regarding L_2 and L_3 respectively (Figure 3(A), (B), (C)). Water is an anti-solvent for the congeners, on increasing the water percentage in the mixed THF-Water system could alter their prevailing form from a solution in pure THF to aggregated species in higher water content mixtures. All the compounds in THF remain solvated and exhibited weak fluorescence intensity. The spectral profile changes slowly in THF-Water mixtures with lower water percentages because the solvent mixture's solvating power is still enough to dissolve the luminogens. Subsequently, the emission intensity of L_1 rises abruptly when $f_w > 90\%$, and at this stage, the luminogen aggregates. In the case of L_2 and L_3 when $f_w > 60\%$ the intensity rises indicating the formation of aggregate. L_2 and L_3 display a fall in emission intensity when $f_w > 80\%$ specifying the aggregated species exhibits a kind of insolubility in higher aqueous content. As obvious from the crystal structure, there remains a propensity of hydrogen bonding between urea NH and C=O and solvent molecules along with hydrophobic effects cause the amphiphiles to aggregate. Dynamic light scattering experiments were performed to determine the hydrodynamic size of L_1 , L_2 , and L_3 (Figure A3.1). The solid-

state fluorescence of the congeners is recorded along with the images held under bright light and UV 365 nm lamp (Figure A3.2(A) & (B)). Additionally, time resolved fluorescence spectroscopy was also studied to evaluate the fluorescence lifetime of the three amphiphiles while taking into account the working solvent where the emission was highest (A3.2 (B)).

To analyze the size and morphology of these congeners FESEM and AFM studies were inspected. **L1** showed the highest emission intensity at 100% water which manifested as rectangular block structures when studied under microscopy. Similarly, 7:3 water: THF was considered for **L2** and **L3** which revealed needle-like and worm-like morphology when examined under microscopy. Identical morphologies were reflected in FESEM and AFM as depicted in (Figure 3.3(D)). FESEM images of **L2** and **L3** in water are attached in A3.1 (D).

3.4 Hydrophobicity and water-repelling properties

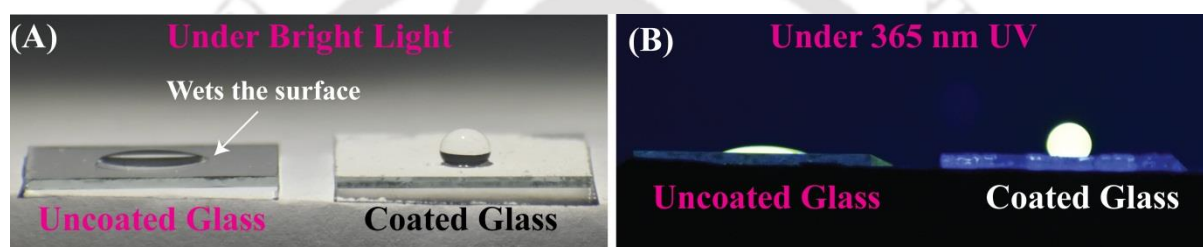


Figure 3.4: Photographs of uncoated and coated glass slides with **L3** depicting wettability: (A) Water droplet on glass slides, featured under bright light. (B) A droplet of water containing fluorescein on the glass slides featured under 365 nm UV-Lamp.

Hydrophobicity, along with hydrophobic materials paves a wide range of applications. It is crucial in applicability ranging from oil spills and their management to clothes and gadgets etc. Being hydrophobic, these compounds, **L1**, **L2**, and **L3** are coated on glass surfaces to form a hydrophobic and water-repelling surface. Compounds were dissolved in DCM and spread evenly on glass surfaces and dried at room temperature. Water droplets were sprinkled on both surfaces (coated and uncoated) and images were taken. The uncoated glass was wet by water droplets as it started to spread. While it formed a globular shape on the coated glass slide without wetting the surface. To visualize under a UV lamp, Fluorescein was dissolved in water and sprinkled on both surfaces (Figure 3.4). Similarly, **L1** and **L2** were coated on a glass slide and tested for their water-repelling properties (Figure A3.3). These coated surfaces remain intact after usage and can be reused (supplementary video). We have also measured the contact angle of the coated surface and water droplet (Figure A3.4).

3.5 Interactions with Nitro antibiotics

Chemosensing aggregated species viz; AIEgens is prevalent. In this work, we assorted five important nitro antibiotics and studied their interaction with L_1 , L_2 , and L_3 . All these nitro-

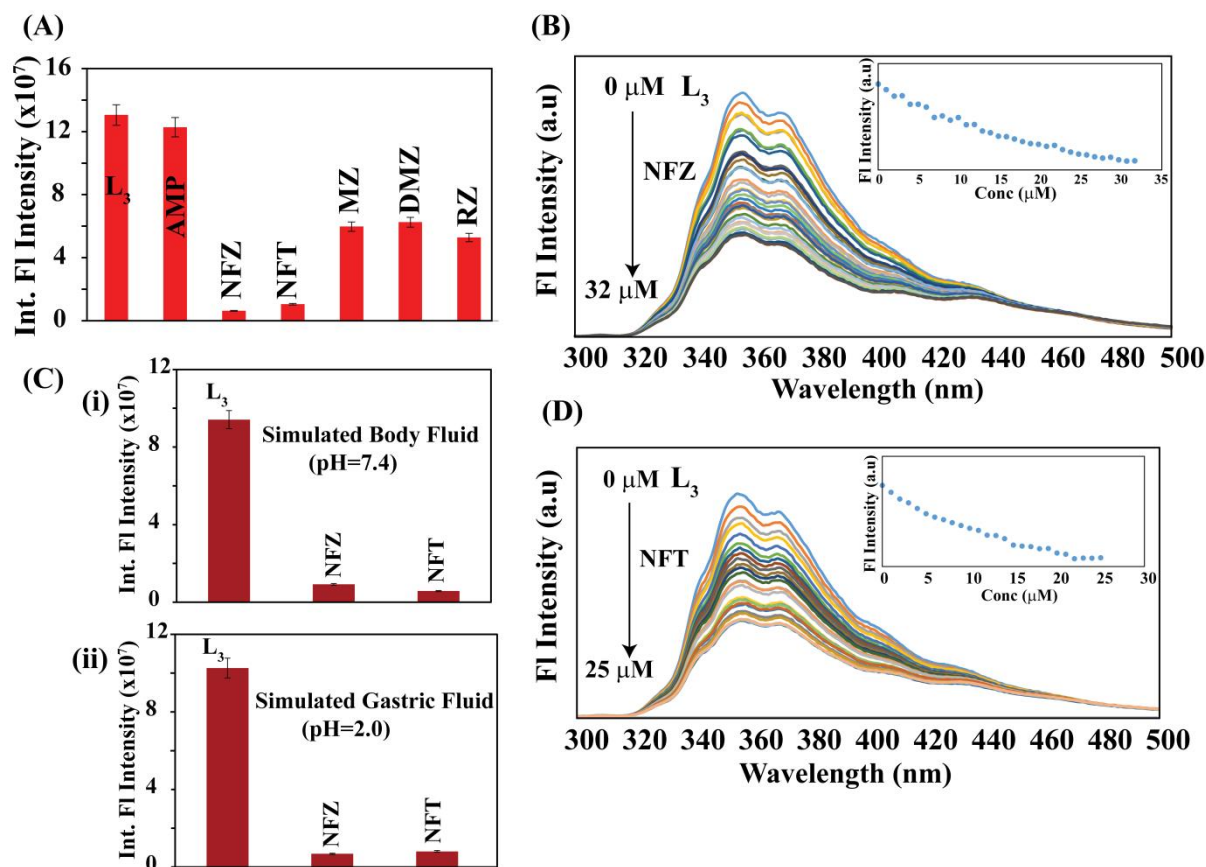


Figure 3.5: (A) Bar diagram representing emission intensity of L_3 before and after the addition of antibiotics in water; Ampicillin =AMP, Nitrofurazone = NFZ, Nitrofurantoin = NFT, Metronidazole =MZ, Dimetridazole = DMZ, Ronidazole = RZ. (B) Emission intensity profile depicting the titration of L_3 with NFZ (C) Bar diagram representing emission intensity of L_3 before and after addition of NFZ and NFT in (i) SBF & (ii) SGF. (D) Emission intensity profile depicting the titration of L_3 with NFT.

antibiotics displayed quenching in water to various extents. In the presence of nitro- antibiotics, we observed a sharp drop in emission intensity. Targeted nitro-compounds have been plotted against L_1 , L_2 , and L_3 's quenching effectiveness. The extent of quenching has been compared with the common antibiotic ampicillin (AMP) which showed almost negligible quenching. Nitrofurazone (NFZ) and nitrofurantoin (NFT) exhibited almost 90% quenching of high fluorescent intensity in water. Regarding metronidazole (MZ), dimetridazole (DMZ), and ronidazole (RZ) the extent of quenching is lesser than NFZ and NFT (Figure 3.5(A)). Differences in fluorescence intensity between these samples were significant based on a p value of < 0.001 in ANOVA followed by an all-pairwise comparison (Holm–Sidak method) (Table A3.2). Titration

was carried out in aqueous media with NFZ and NFT against the congeners. On titrating NFZ and NFT Limit of detection (LOD) was calculated to be 3.37 μM and 2.06 μM respectively (Figure 3.5B, D). To confirm the usability of the congeners, the chemosensing capacity was checked in Simulated Body and Gastric fluid. At first, the emission intensity of the AIEgens was measured in these simulated fluids. NFZ and NFT, which displayed maximum quenching in water were added in 100 equivalents to these fluids containing the AIEgens. A similar sharp decrease in fluorescence intensity was recorded. This experiment reveals that AIEgens are operative in extreme pH conditions ($\text{pH}_{\text{S.G.F}} = 2.0$) (Figure 3.5(C)). This ensures the applicability of the congeners in environmental as well as analytical fields. Similar experimentation regarding interactions of nitroantibiotics with L_1 & L_2 were carried out (Figure A3.5-A3.6).

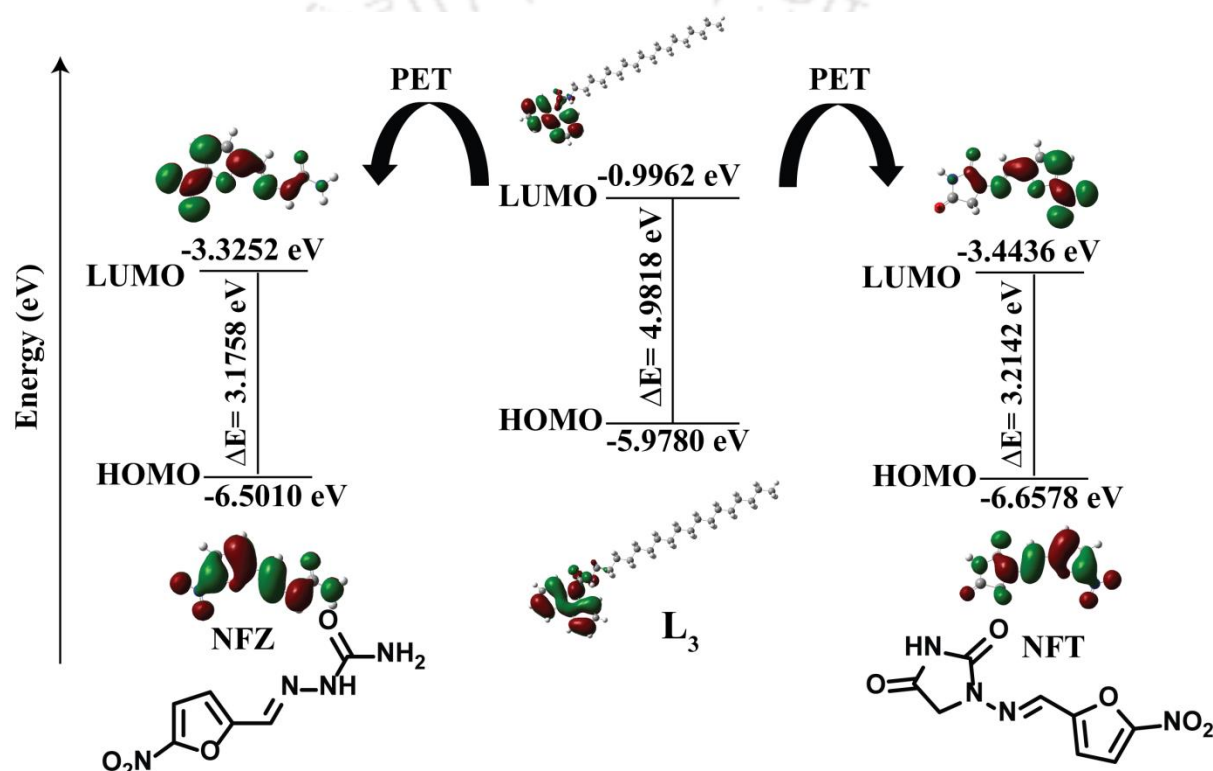


Figure 3.6: DFT images depicting Photo-induced electron transfer (PET) between Nitroantibiotics and L_3 .

The plausible reason for quenching is Photo-induced electron transfer (PET) which is operative. Fluorescence intensity is decreased as PET is on. To examine the emission intensity “turn-off” mechanism of AIEgen with nitro-antibiotics, density functional theory (DFT) calculations were calculated with the B3LYP/6-31G(d,p) method basis set using the Gaussian 09 program. CPCM solvent model has been implemented using water as a solvent during calculation. The energy levels depicted electron transfer occurs between the LUMO of the amphiphiles and the LUMO of the nitro-antibiotics. The LUMO of the nitro-antibiotics is situated lower than the LUMO of L_1 , L_2 ,

and L₃ (Figure 3.6). This occurrence can be attributed to the difference in the energy gap between the LUMOs of electron donor-acceptor levels. The Photoinduced electron transfer is higher when the gap is larger hence leading to higher quenching efficiency. The energy level differences regarding MZ, DMZ, and RZ are lower compared to NFZ and NFT. Therefore the extent of quenching is lower in these instances. Individual antibiotics along with their interaction between the LUMOs L₁, L₂, and L₃ have been plotted (Figure A3.7-A3.14). The energy differences of LUMO's corresponding to amphiphiles and nitro-antibiotics are listed in Table A3.3.

3.6 Conclusion

In an essence, applying microscopic and spectroscopic methods, we have conducted a comparative analysis of substituted urea-based amphiphiles with a change in chain lengths. Several facets of the compounds are addressed from aggregation studies to analytical applications. These hydrophobic AIEgens are coated to create water-repellent surfaces. To include the practicality of the AIE-gens, their interactions with nitro-antibiotics were examined in water as well as simulated biofluids. Our current work is intended to contribute to both photophysical research and analytical utility.

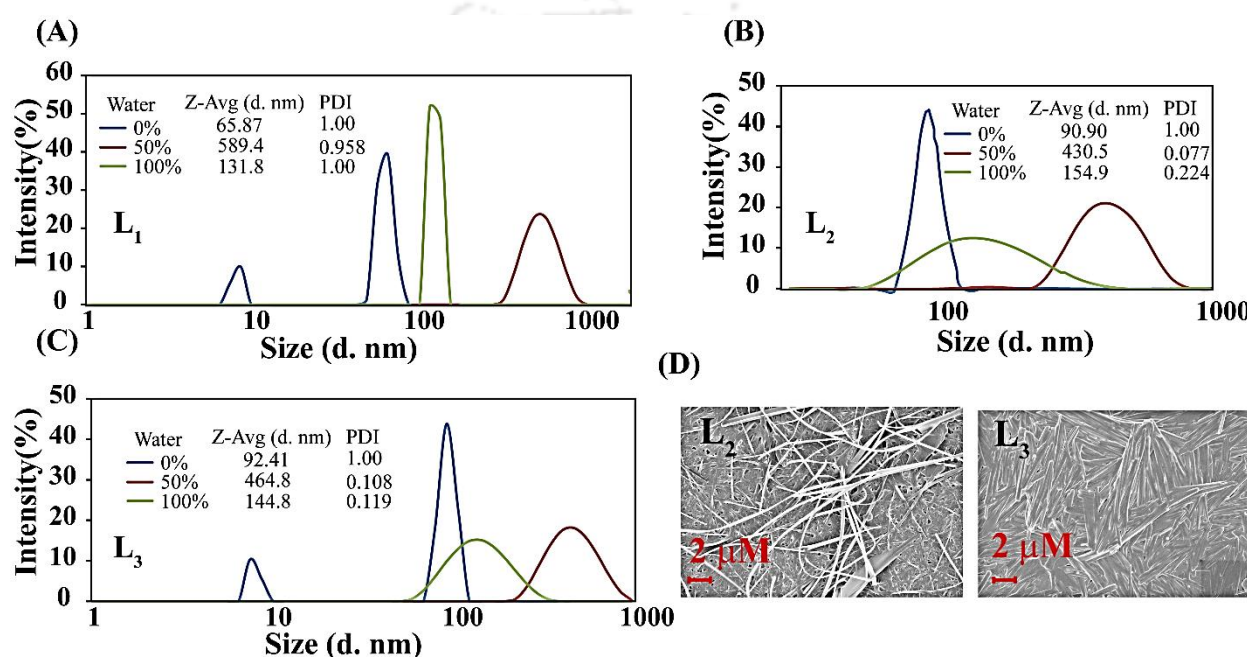
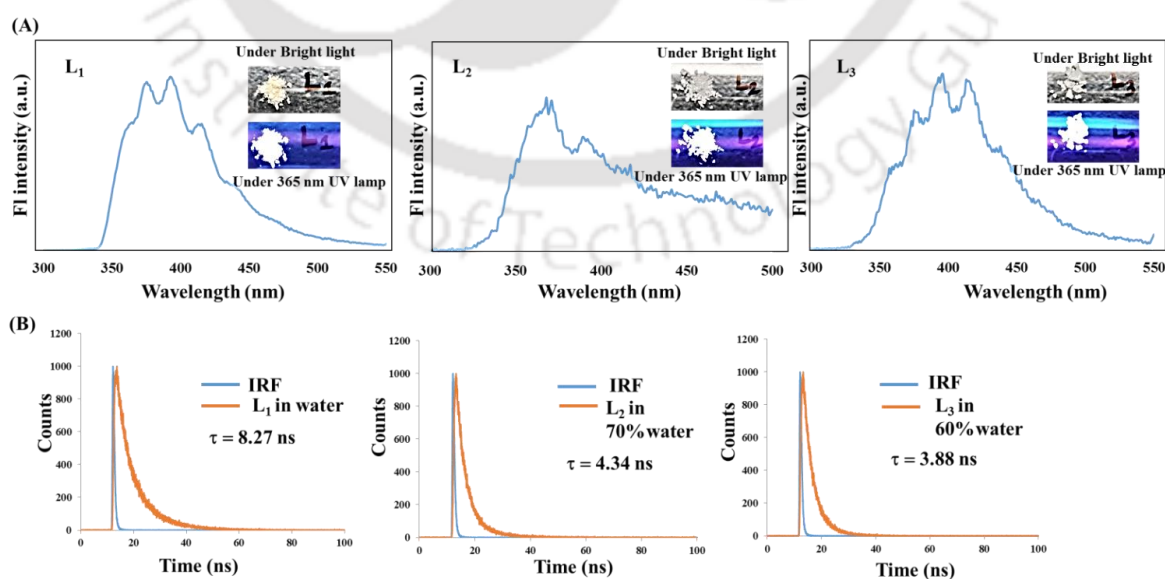
References

- 3.1. S. Parvate, P. Dixit, and S. Chattopadhyay, Superhydrophobic Surfaces: Insights from Theory and Experiment, *J. Phys. Chem. B*, 2020, **124**, 8, 1323–1360.
- 3.2. G. S. Watson, B. W. Cribb, and J. A. Watson, How Micro/Nanoarchitecture Facilitates Anti-Wetting: An Elegant Hierarchical Design on the Termite Wing, *ACS Nano*, 2010, **4**, 1, 129–136.
- 3.3. A. S. P. R. Lakshmi, D. Umadevi and S. Shanmugaraju, Discriminative fluorescent sensing of nitro-antibiotics at ppb level using N-phenyl-amino-1,8-naphthalimides chemosensors. *Results Chem.*, 2022, **4**, 100546.
- 3.4. S. Ghosh, F. Steinke, A. Rana, S. Biswas, A fluorescent zirconium organic framework displaying rapid and nanomolar level detection of Hg (II) and nitro antibiotics., *Inorg. Chem. Front.*, 2022, **9**, 859.
- 3.5. S. Sun, X. Y. Sun, Q. Sun, E. Q. Gao, highly efficient fluorescent chemosensor for nitro antibiotic detection based on luminescent coordination polymers with 2,6-di(4-carboxyphenyl) pyrazine., *CrystEngComm.*, 2021, **23**, 3167.
- 3.6. B. Sloan and N. Scheinfeld, The Use and Safety of Doxycycline Hyclate and Other Second-generation Tetracyclines., *Expert Opin. Drug Saf.* 2008, **7**, 571– 577.
- 3.7. A. K. Mittal, R. Bhardwaj, P. Mishra and S. K. Rajput, Antimicrobials Misuse/Overuse: Adverse Effect, Mechanism, Challenges and Strategies to Combat Resistance., *Biotechnol. J.*, 2020, **14**, 107–112.
- 3.8. C. Llor and L. Bjerrum, Antimicrobial Resistance: Risk Associated with Antibiotic Overuse and Initiatives to Reduce the Problem., *Ther. Adv. Drug Saf.*, 2014, **5**, 229– 241.
- 3.9. A. B. A. Boxall, D. W. Kolpin, B. Halling-Sørensen and J. Tolls, Are veterinary medicines causing environmental risks? *Environ. Sci. Technol.*, 2003, **37**, 286A– 294A.
- 3.10. T. P. V. Boeckel, S. Gandra, A. Ashok, Q. Caudron, B. T. Grenfell, S. A. Levin and R. Laxminarayan, Global Antibiotic Consumption 2000 to 2010: An Analysis of National Pharmaceutical Sales Data., *Lancet Infect. Dis.*, 2014, **14**, 742– 750.

Appendix - Chapter 3

Table A3.1: Hydrogen bonding distances (\AA) and Bond angles ($^\circ$) in L_1 :

D-H \cdots A	d(D \cdots H)/ \AA	d(H \cdots A)/ \AA	d(D \cdots A)/ \AA	\langle D-H \cdots A/ $^\circ$
N2-H2N \cdots O1	0.86	2.20	2.999(4)	155
C2-H2 \cdots O1	0.93	2.46	2.965(4)	114
C11-H11 \cdots N2	0.93	2.56	3.041(5)	113

**Figure A3.1:** DLS output of (A) L_1 , (B) L_2 & (C) L_2 (D) FESEM images of L_2 & L_3 in water.**Figure A3.2:** (A) Solid State Fluorescence of L_1 , L_2 & L_3 . (B) Fluorescence lifetime measurements of L_1 , L_2 & L_3 .

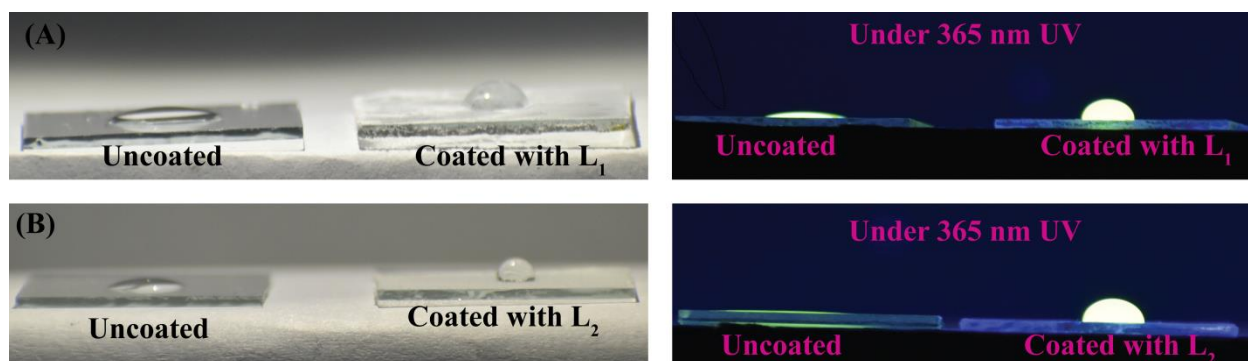


Figure A3.3: Photographs of uncoated and coated glass slides with (A) L₁ & (B) L₂ depicting wettability: Water droplet on glass slides, featured under bright light and Droplet of water containing fluorescein on the glass slides, featured under 365 nm UV-Lamp.

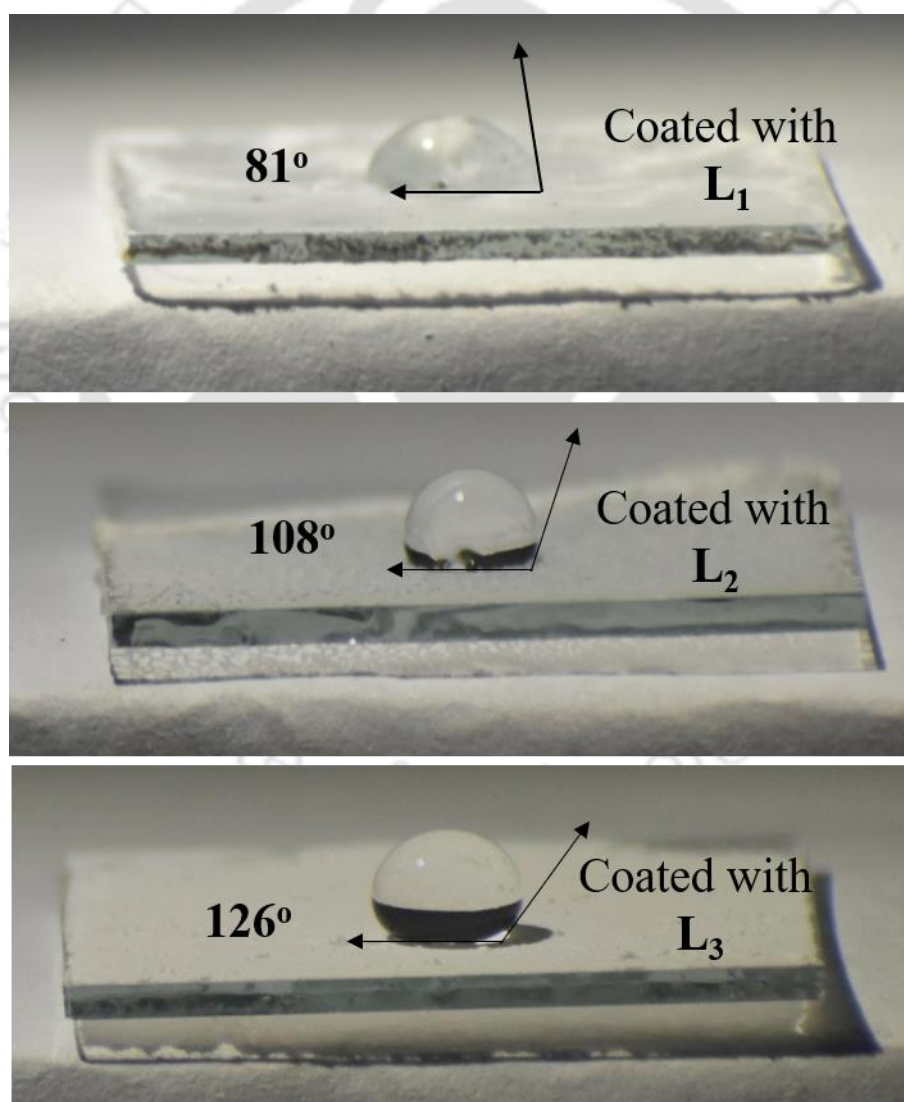


Figure A3.4: Photographs of coated glass slides along with measured contact angles.

Table A3.2.: Analysis of fluorescence quenching of with respect to various antibiotics.

Sl. No.	Statistical Analysis for Fluorescence quenching carbazole by antibiotics	
	Comparison Group	Significant Difference* (L ₁ / L ₂ / L ₃)
1.	Ampicillin versus Nitrofurantoin	Yes/ Yes /Yes
2.	Ampicillin versus Nitrofurazone	Yes/ Yes /Yes
3.	Ampicillin versus Metronidazole	Yes/ Yes/ Yes
4.	Ampicillin versus Dimetridazole	Yes/ Yes / Yes
5.	Ampicillin versus Ronidazole	Yes/ Yes /Yes

* Significant difference implies p value < 0.001 ($2.58026E-05$) based on analysis of variance (ANOVA) followed by all pair wise multiple comparisons (Holm-Sidak method) Fluorescence quenching.

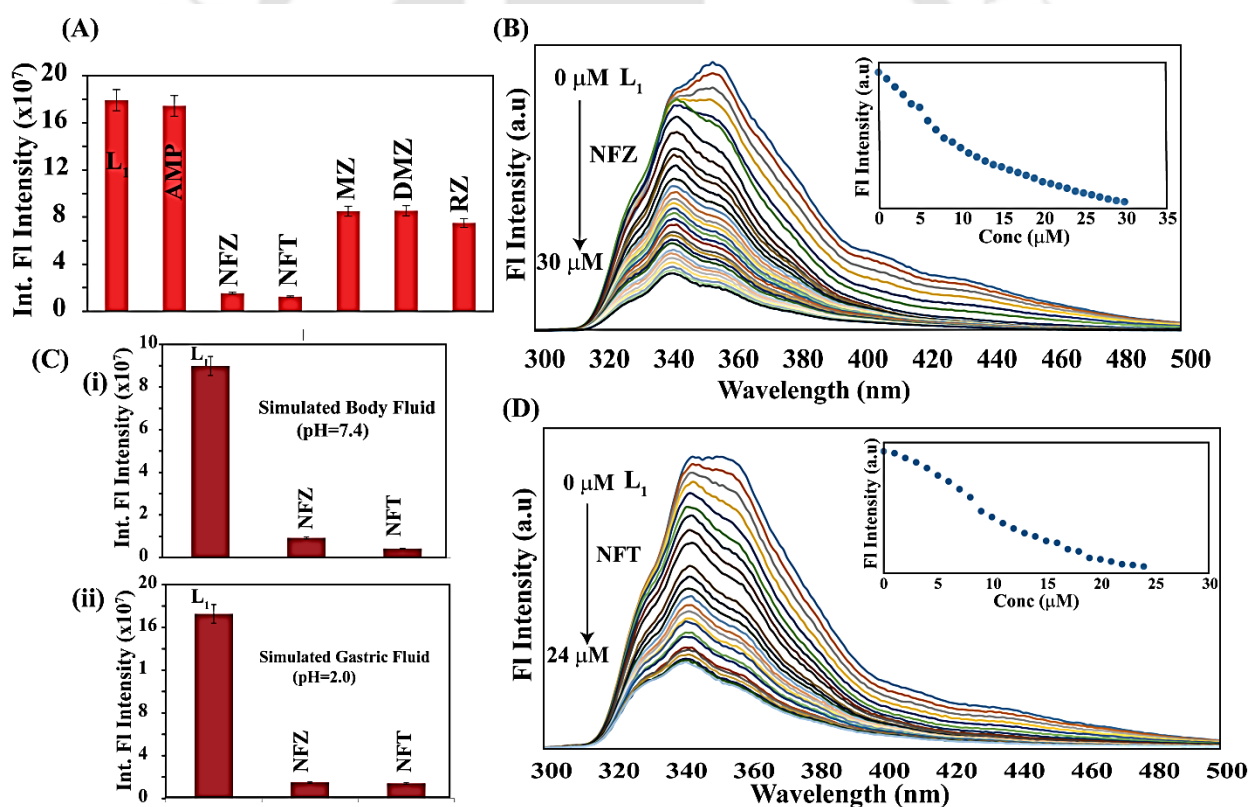


Figure A3.5: (A) Bar diagram representing emission intensity of L₁ before and after the addition of antibiotics in water. (B) Emission intensity profile depicting the titration of L₁ with NFZ (C) Bar diagram representing emission intensity of L₁ before and after addition of NFZ and NFT in (i) SBF & (ii) SGF. (D) Emission intensity profile depicting the titration of L₁ with NFT.

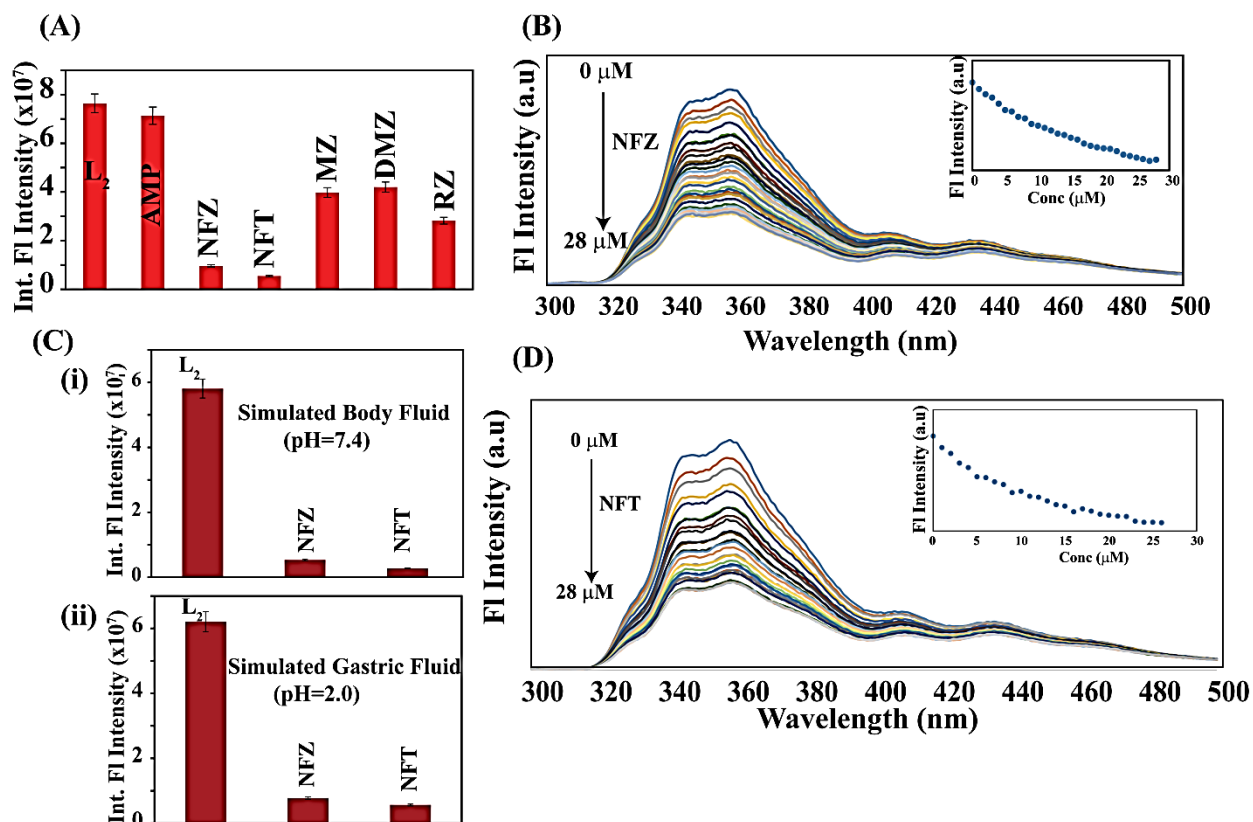


Figure A3.6: (A) Bar diagram representing emission intensity of L₂ before and after the addition of antibiotics in water. (B) Emission intensity profile depicting the titration of L₂ with NFZ (C) Bar diagram representing emission intensity of L₂ before and after addition of NFZ and NFT in (i) SBF & (ii) SGF. (D) Emission intensity profile depicting the titration of L₂ with NFT.

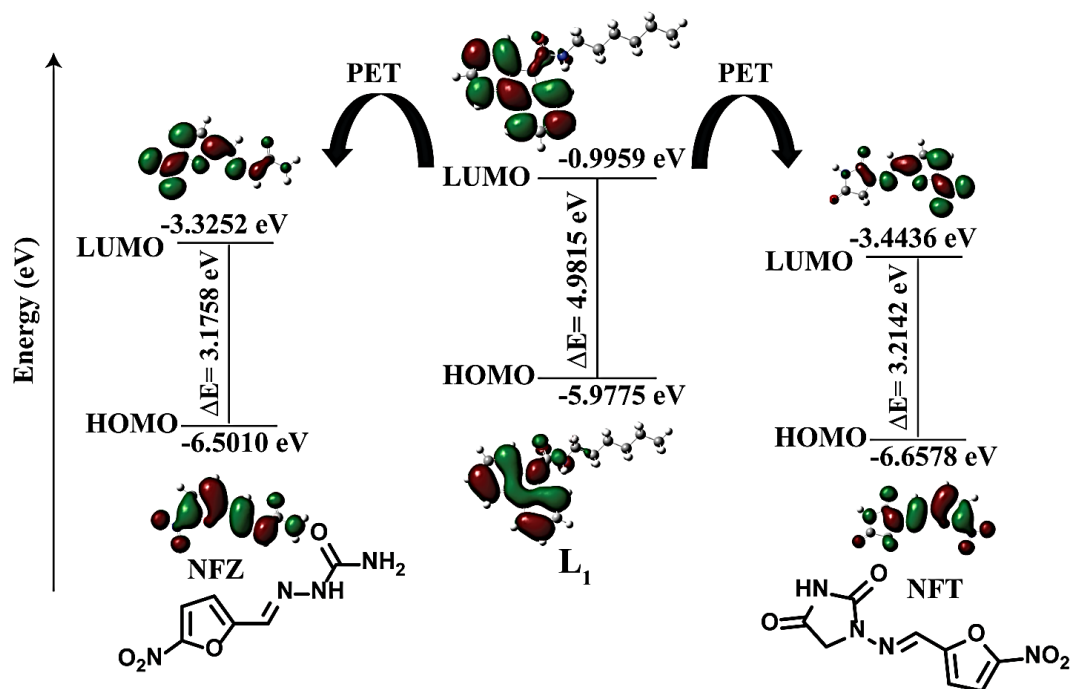


Figure A3.7: DFT images depicting Photo induced electron transfer (PET) between NFZ, NFT, and L₁.

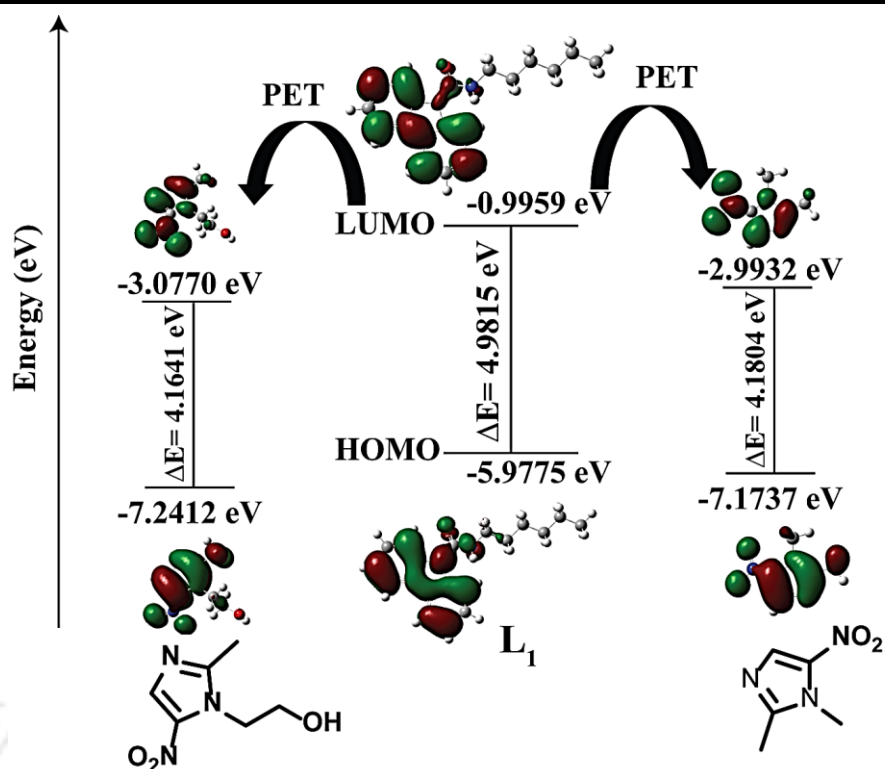


Figure A3.8: DFT images depicting Photoinduced electron transfer (PET) between metronidazole, dimetridazole, and L1.

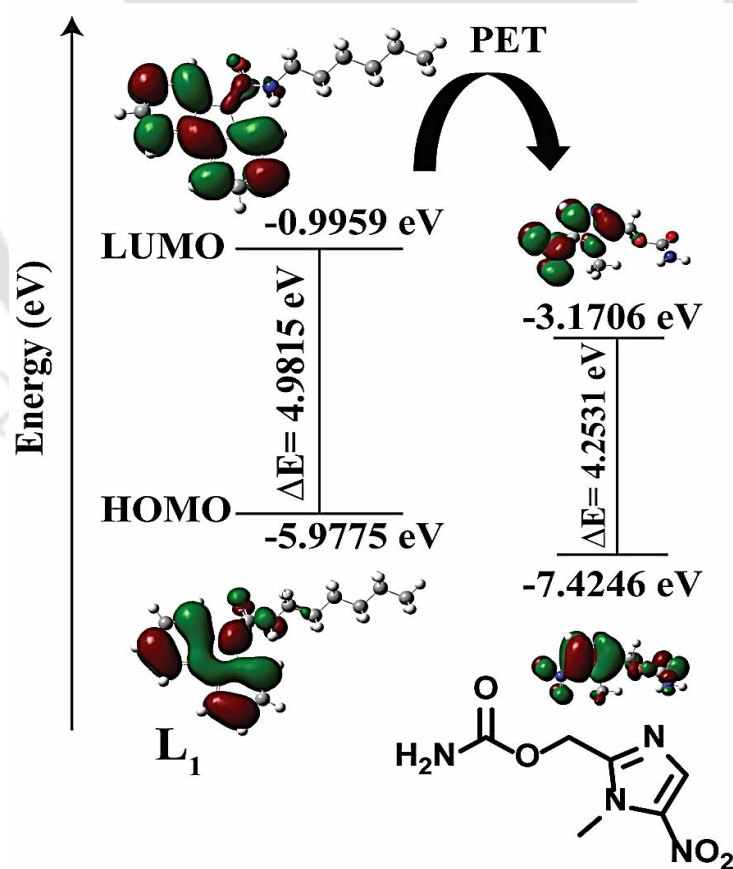


Figure A3.9: DFT images depicting Photoinduced electron transfer (PET) between ronidazole and L1.

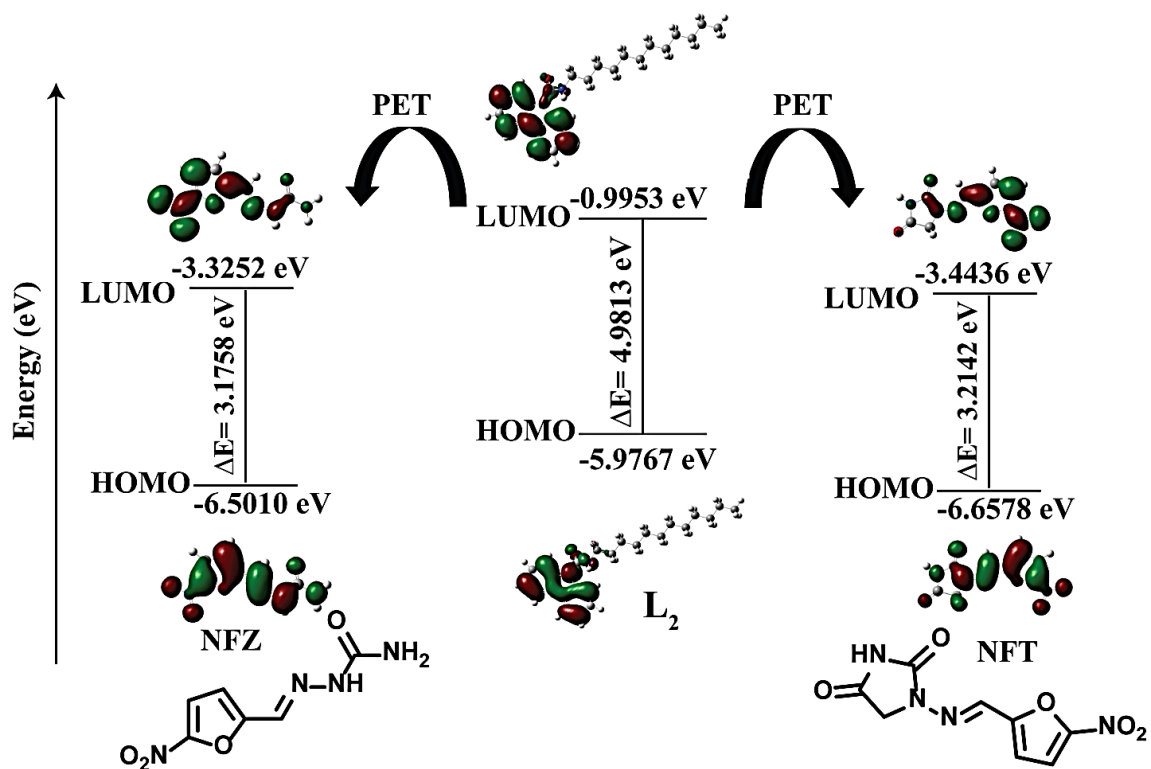


Figure A3.10: DFT images depicting Photoinduced electron transfer (PET) between NFZ, NFT, and L₂.

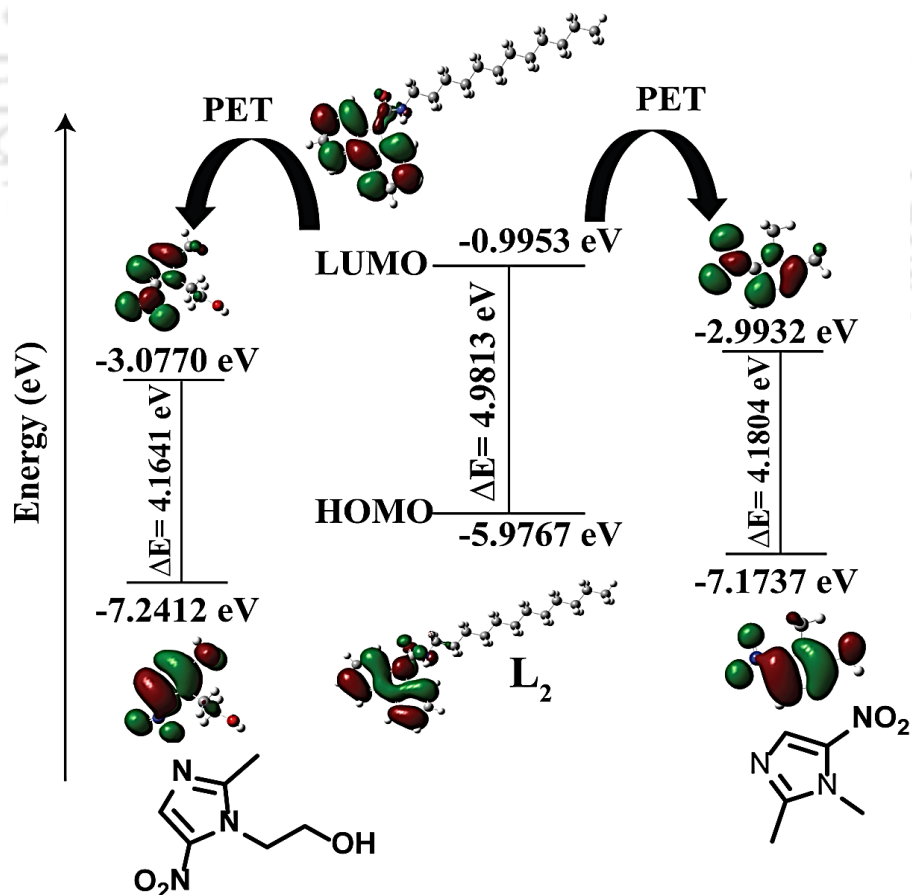


Figure A3.11: DFT images depicting Photoinduced electron transfer (PET) between metronidazole, dimetridazole, and L₂.

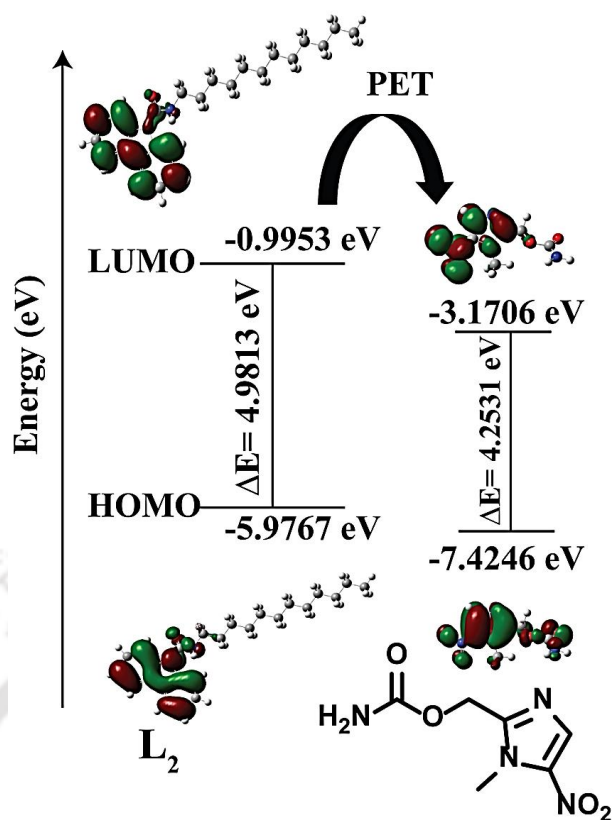


Figure A3.12: DFT images depicting Photoinduced electron transfer (PET) between ronidazole and L_1 .

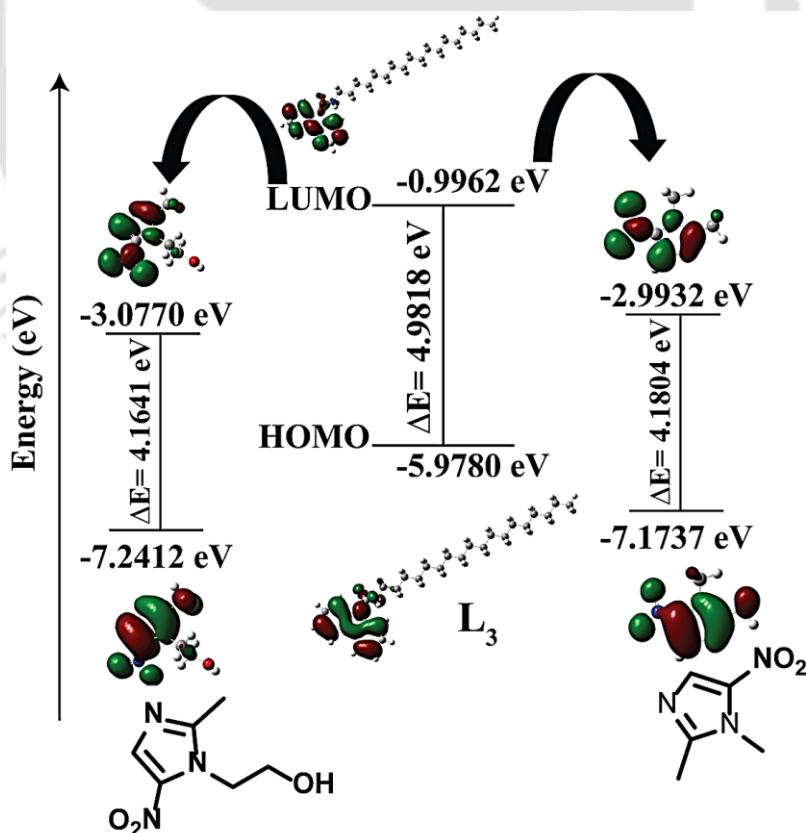


Figure A3.13: DFT images depicting Photoinduced electron transfer (PET) between metronidazole, dimetridazole, and L_3 .

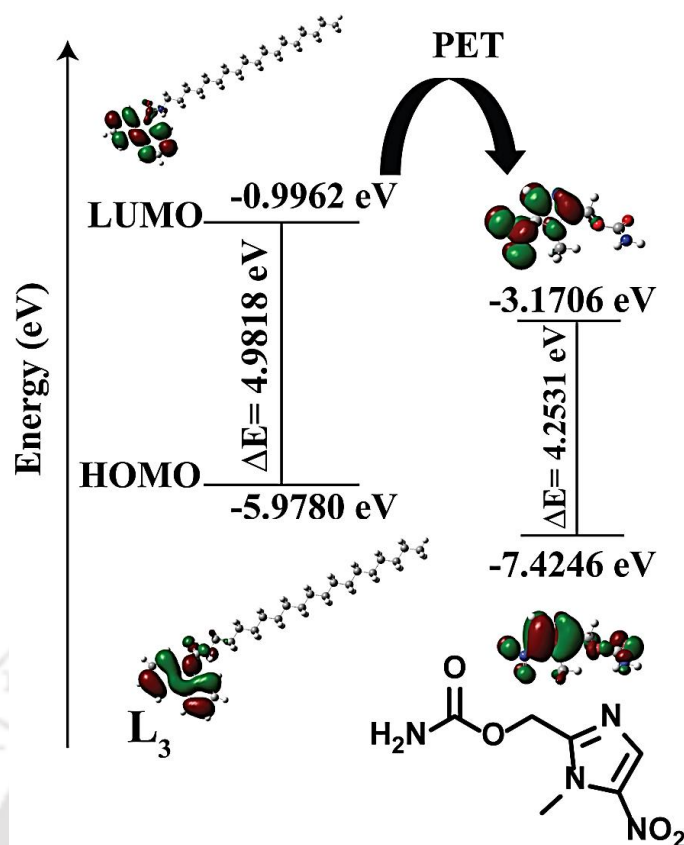


Figure A3.14: DFT images depicting Photoinduced electron transfer (PET) between ronidazole and L₃.

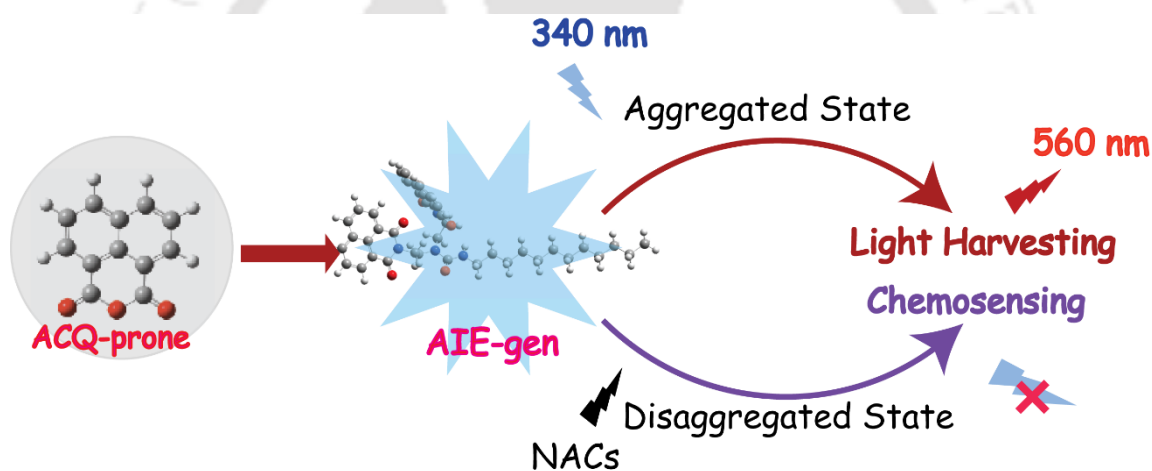
Table A3.3: Energy differences (eV) between the LUMOs of Nitroantibiotics and L₁, L₂, and L₃.

	Nitrofurazone	Nitrofuratoin	Metrodinazole	Dimetridazole	Ronidazole
L ₁	0.0856	0.08997	0.07648	0.0734	0.07992
L ₂	0.08562	0.08997	0.0765	0.07342	0.07994
L ₃	0.08559	0.08994	0.07647	0.07339	0.07991



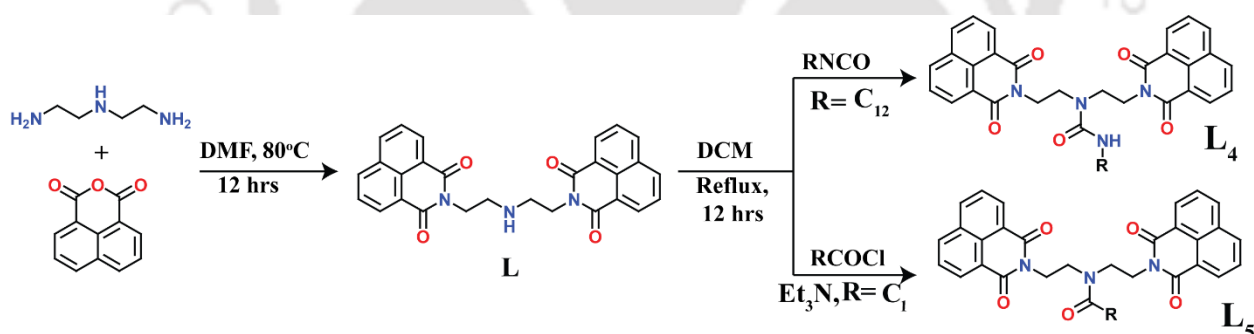
CHAPTER 4A

Insights into the Aggregation performance and Light-Harvesting facet of Naphthalimide-based Amphiphile and Non-amphiphile AIEgen



4A.1 Background and focus of the chapter

Photo physical application with AIEgens is diverse and expanding. From analytical tools to biochemical materials, they find applications. In nature, plants, bacteria, etc., are able to capture, transfer, and store solar energy using their highly effective light-harvesting systems. Light-harvesting molecular systems that can efficiently transport absorbed photons unidirectional over nanoscale distances are currently attracting a lot of attention.^{4A.1-4A.5} The phenomena of natural systems capturing sunlight and utilizing it have prompted research in a variety of disciplines.^{4A.6-4A.9} Several attempts are in progress in accomplishing effective energy transfer from donors to acceptors via the Forster resonance energy transfer (FRET) process. Despite all of this, the majority of the reported artificial light-harvesting systems have been known in organic solvents instead of the aqueous medium and only a limited of them are efficient aqueous light-harvesting systems that are precisely made to deal with this problem. Research is still limited in similar light-harvesting systems with AIE-genic compounds in an aqueous environment.^{4A.10-4A.13} Among various applications, AIEgen is applied in the detection of biologically relevant species, bioanalytes, toxic analytes, and so forth. Chemical explosives include nitroaromatic compounds (NACs), nitramines, peroxides, and nitrate esters. Picric acid (PA), a member of nitroaromatics, exhibits versatility in dual chemistry-a toxic substance with explosive properties, as well as an analytical reagent. Thus, it needs specific and sensitive detection and hence the major focus of our study.



Scheme 4.1: Synthetic route of **L₄** and **L₅**.

4A.2 Studies on Photophysical Behaviours

The photophysical features of the two compounds were examined in Dimethylformamide (DMF) /water solvent system. The absorbance spectra of **L₄** and **L₅** (10 μM) in pure DMF medium displayed an absorbance maximum around 340 nm (Fig. 4A.1(A) & 4A.1(B)), which led to a gradual drop along with a noticeable change in the baseline for both the cases. The upliftment of baseline in both cases suggested the formation of aggregates in water. In absorption spectra at 600 nm, **L₄** and **L₅** were compared (Fig. 4A.1 (C)) which revealed that **L₄** has the greater aggregating

aptitude in water. The aggregating capacity of **L**₄ was almost twice **L**₅. Interestingly, the spectral responses of **L**₄ and **L**₅ were plotted in the chromaticity diagram. As evident from the chromaticity diagram (Fig. 4A.1(D)), the absorption spectra **L**₄ and **L**₅ in 100 % water content were closer to the pure white light emission coordinates (0.33, 0.33). The respective coordinates of **L**₄ and **L**₅ were (0.26, 0.26) and (0.32, 0.33).

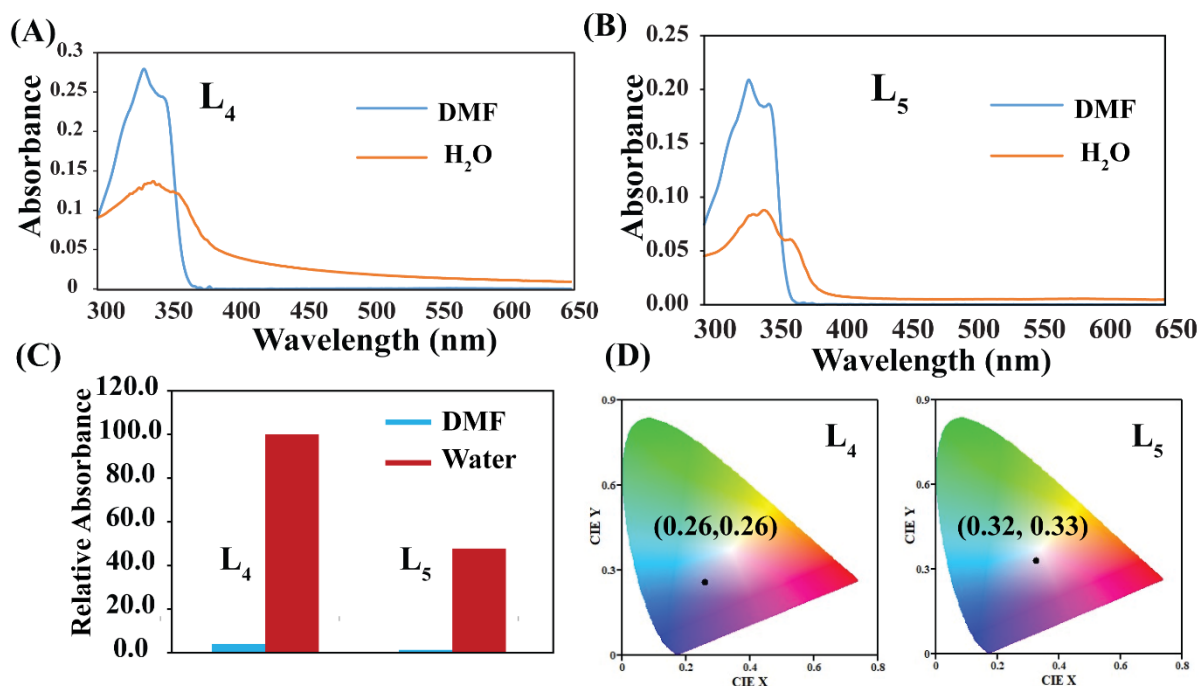


Figure 4A.1: (A) UV spectra of **L**₄ (10 μ M) in DMF and aqueous medium. (B) UV spectra of **L**₅ (10 μ M) in DMF and aqueous medium. (C) Bar diagram of absorbance at 600 nm comparing the aggregating capacity **L**₄ and **L**₅ in water. (D) Chromaticity diagram with respective coordinates for **L**₄ and **L**₅.

Both **L**₄ and **L**₅ were almost non-fluorescent in 100% DMF (dissolved form) with an emission band at 380 nm. The aggregating phenomena of **L**₄ and **L**₅ was studied via emission spectroscopy with the same solvent switching (Fig. 4A.2(A) & (B)). With increasing water fraction, **L**₄ and **L**₅ started to aggregate, and at 100 % water, it exhibited red-shifted maxima. The 80 nm shift from 380 nm to 460 nm suggested the formation of new aggregated particles (Fig. A4A.3(B), SI). An intense Aggregation induced emission (AIE) (25-fold greater than DMF solution) was perceptible in 100% water. Similarly, **L**₅ showed an AIE feature in aqueous media, when the water fraction was increased in DMF. Comparative AIE and aggregation ability have been depicted in Fig. A4A.3(A), SI. As water is an anti-solvent for the compounds, increasing the water percentage in the mixed DMF-Water system could change their prevailing form from a solution in pure DMF to aggregated particles in higher water content mixtures. Both compounds in DMF remain solvated and exhibit weak fluorescence intensity.

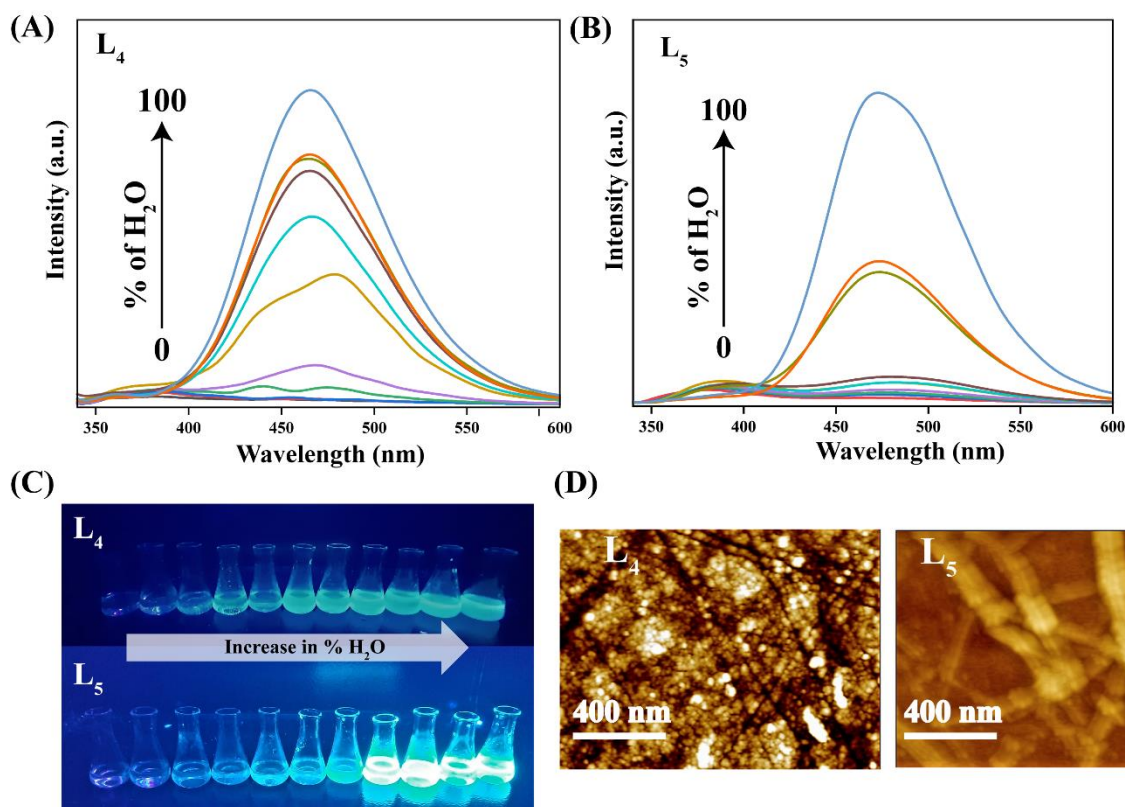


Figure 4A.2: (A) Emission spectra of **L₄** (10 μM) with varying water percentage in DMF. (B) Emission spectra of **L₅** (10 μM) with varying water percentage in DMF. (C) Images of **L₄** and **L₅** solution in varied DMF-water percentage held under 365 nm UV lamp (D) AFM images of **L₄** and **L₅** in aqueous solution.

The spectral profile changes negligibly in DMF-Water mixtures with less than 40% water percentage due to the solvent mixture's solvating power being still enough to dissolve the luminogens. Subsequently, the fluorescence intensity of **L₄** starts to rise when $fw > 50\%$, and at this stage, the luminogen begins to aggregate. In the case of **L₅**, when $fw > 80\%$ the intensity rises indicating the formation of aggregate. Corollary, **L₅** remained in the molecularly dispersed form up to 80% water, specifying its lower aggregation capacity. These outcomes suggest that a hydrophobic chain can certainly provide molecules with distinct emission characteristics and aggregation aptitude. Though **L₅** proves to be an AIE gen the propensity of aggregation is much greater in case of **L₄**.

Dynamic light scattering experiments (DLS) were conducted to measure the size or hydrodynamic radii of the formed aggregates. The size of **L₄** increased from 177.1 nm in pure DMF to 375.9 nm in 100 % water (Fig. A4A.1(A), SI). Thus, confirming the formation of larger aggregates in water.

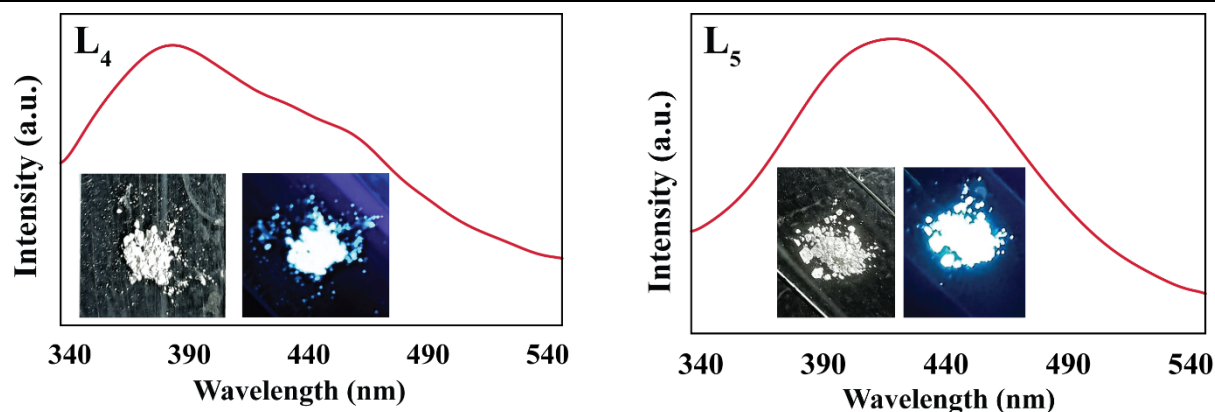


Figure 4A.3: Solid State emission spectra of (A) L_4 and (B) L_5 .

The photographs with increasing water content in DMF for both the compounds have been laid out in Fig. 4A.2(C). It can be observed that it bears coherence with the depicted AIE emission spectra. The solid-state emission was recorded for both the compounds (Fig. 4A.3(A) & (B)). The respective chromaticity diagram for a solution and solid-state are plotted in Fig. A4A.2, SI.

Being aggregating in nature and exhibiting AIE behaviour it was obvious to study the size and morphology of the compounds. Same solvent variation was adopted. FESEM images of both L_4 and L_5 were taken in DMF and increased water content is laid out in Fig. 4A.4(A)&(B). In the case of L_4 petals like morphology in DMF changed with incremental water addition to spike-like structures. The spikes are around 200 nm in length. These spikes are the highly emissive

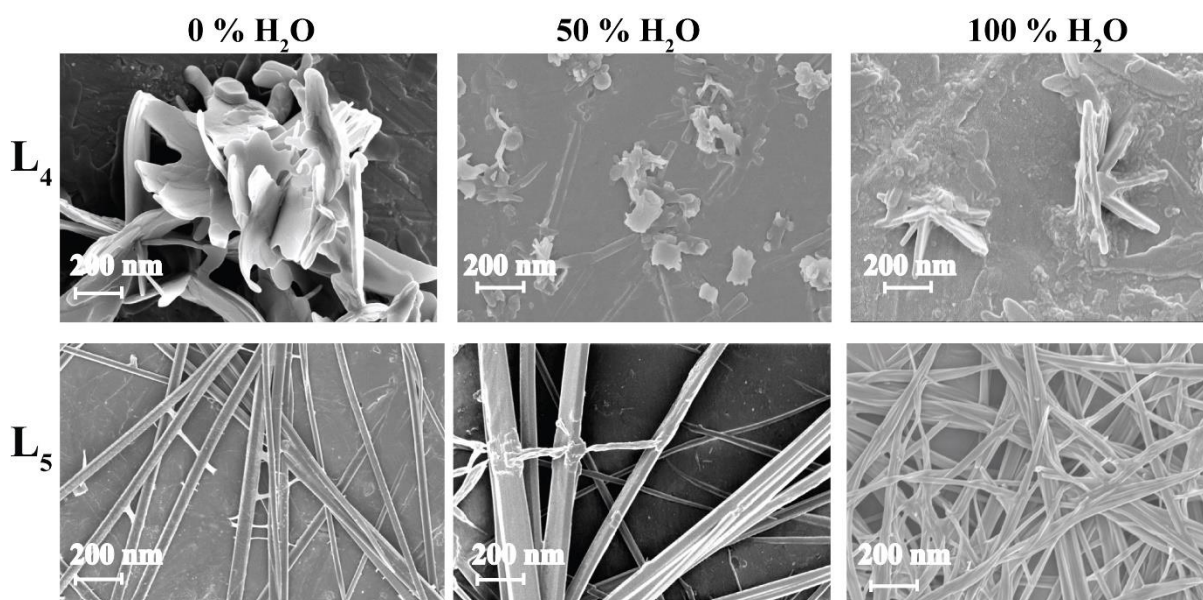


Figure 4A.4: (A) FESEM of L_4 with varying water percentage in DMF. (B) FESEM of L_5 with varying water percentage in DMF.

state. In contrast, L_5 did not show much morphological variance. The micro-length splints remained almost the same on solvent switching. The splints were of greater length and size than

those observed in **L4**. AFM analysis of **L4** and **L5** was done in an aqueous medium via the drop cast method. The same morphology was reflected in AFM images (Fig 4A.2(D)).

4A.3 Light Harvesting

The possibility of FRET between AIEgen **L4** and rhodamine B (RhB) has been studied. After aggregation **L4** shows an emission intensity that overlaps with the absorption range of two commercially available dyes. The fair spectral overlap between the emission of AIEgen and absorption of the dyes satisfies the prime criteria for energy transfers in Donor-Acceptor FRET systems (Fig A4A.4(A) & A4A.5(A), SI). Measured addition of RhB to the aqueous solution of the AIE gen (donor) caused quenching of the emission due to **L4** at 460 nm, while the emission intensity of RhB (acceptor) was spiked (570 nm) upon excitation at 340 nm (Fig. 4A.5(A).)

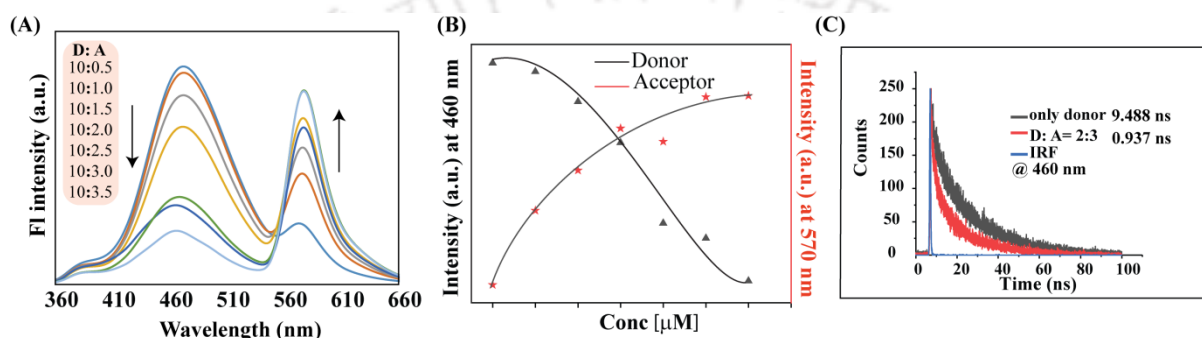


Figure 4A.5: (A) Emission spectra of titration by increasing acceptor (RhB) concentration in presence of donor (**L4**). (B) Line graph of emission intensity profile of **L4** (donor) and RhB (acceptor) (C) Fluorescence lifetime measurements **L4** in presence and absence of acceptor (RhB).

The graph has been plotted describing the rise and decrease in fluorescence intensity of acceptor and donor respectively (Fig. 4A.5(B)). The emission intensity of the acceptor in absence of a donor was less when excited at 340 nm. The fluorescence lifetime of the donor in the presence of the acceptor is the best way to assess the energy transfer process. Fluorescence lifetime decay curves for **L4** and RhB have been examined at 460 nm in this approach (Fig. 4A.5(C)). Notably, AIEgen **L4** ($\tau = 9.488$ ns) exhibited a higher fluorescence lifetime than **L4** in the presence of RhB ($t = 0.937$ ns) (Table A4A.1, SI). These findings suggested that energy is transferred from the AIEgen **L4** to RhB. As a result, it is safe to assume that AIEgen **L4** and RhB have an efficient FRET process in which AIEgen **L4** acts as the energy donor and RhB acts as the energy acceptor. Using a simple AIEgen molecule, ideal model for mimicking the natural light-harvesting process in an aqueous environment is obtained.

4A.4 Interactions with Nitroaromatics

To focus on versatility and the analytical utility of **L**₄ and **L**₅, interaction with nitro-aromatics was examined. The high emission intensity of **L**₄ and **L**₅ due to AIE was quenched to various extents by multiple nitro-aromatics. Comparing the quenching phenomenon, a few nitro-aromatics did not quench the intensity of **L**₅ (Fig. A4A.6(A), SI) while **L**₄ responded to all the targeted analytes via quenching. We assume the disaggregation mechanism of the aggregated states **L**₁ in presence of nitro-aromatics which led to a drastic fall in emission intensity. The quenching efficiency of **L**₄ has been plotted against targeted nitro-compounds (Fig. 4A.6(B)). On the addition of different NACs, noticeable quenching was detected in the case of nitrophenol solutions, while the others showed nominal changes.

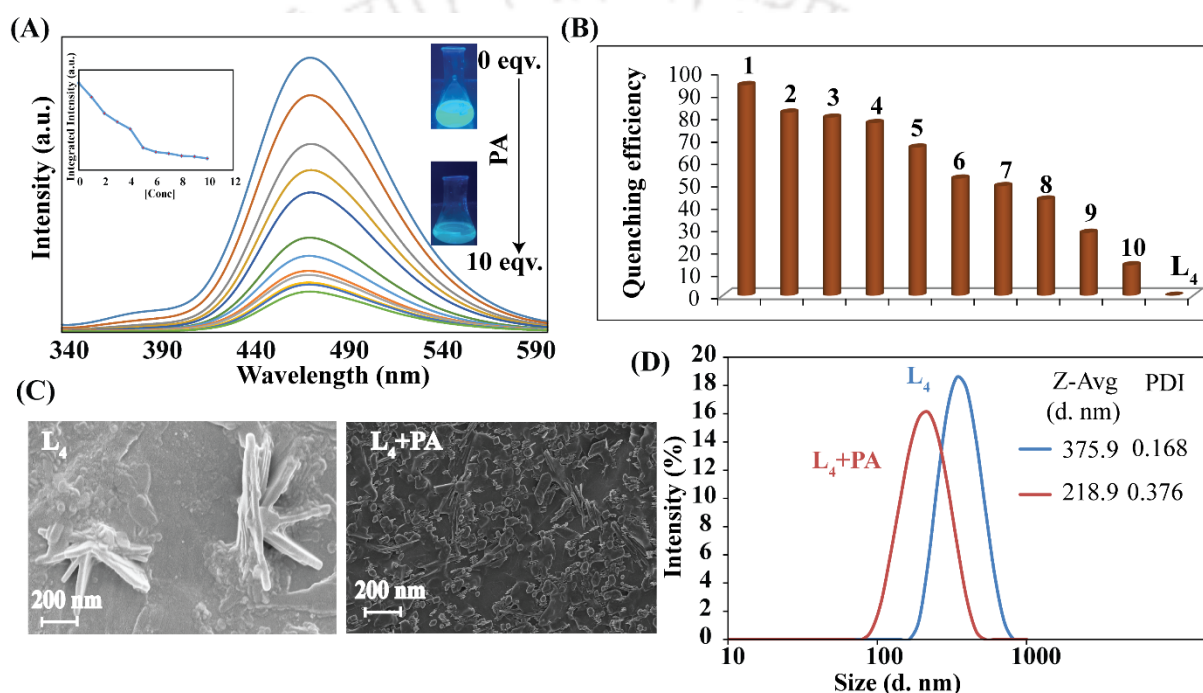


Figure 4A.6: (A) Emission spectra titration of **L**₁ by Picric Acid (B) Bar diagram of quenching efficiency of emission signal of **L**₁ (10 μM) by varying nitroaromatics (1= 2,4-dinitroaniline, 2= 2,4,6-trinitrophenol, 3= 4-nitrophenol, 4= 4-nitroaniline, 5= 2,4-dinitrophenol, 6= 2-nitrophenol, 7= 2,4-dinitrotoluene, 8= nitrobenzene, 9= 2,4-dinitrobenzoic acid, 10= nitromethane, in water. (C) FESEM images of **L**₁, **L**₁+ PA (D) DLS output of **L**₁, **L**₁+ PA, depicting the decrease in size and disaggregation process.

A significant quenching of emission (94%) was reported upon the addition of 10 Eq. of picric acid (PA), while for 4-nitro phenol and 2,4-dinitrophenol quenching efficiency was only ~79.5% and ~66%, respectively. Since picric acid remains in focus due to toxicity and constant disrepute, we carried out further analysis with PA only. FESEM analysis was done to determine the difference in morphology and disaggregation of aggregated **L**₄ in the presence and absence of PA. The spikes

like morphology in water were disrupted in addition to PA (Fig. 4A.6(C)) Further, DLS, experiments were performed to support the disaggregation process. In aqueous media hydrodynamic radii of both L_4 and L_4 + PA were measured. A fall in hydrodynamic radii from 375.9 nm to 218.9 nm was recorded (Fig. 4A.6(D)) Possibly, interaction with picric acid caused the disaggregation of the self-aggregated L_4 . The Limit of Detection (LOD) for picric acid was determined to be 5.12 μM .

For practical applicability, detection of picric acid in solid support was performed. Silica Gel Plates loaded with L_4 and picric acid was held under a 365 nm-UV lamp. A distinct black spot was obtained in presence of the analyte (Fig. 4A.7(A)). Similarly, regular filter papers were cut out and the same protocol was adopted. L_4 was coated on both the pieces of paper and to one of them Picric acid solution was added. Quenching of emission intensity of L_4 on the paper was visible (Fig. 4A.7(B)).

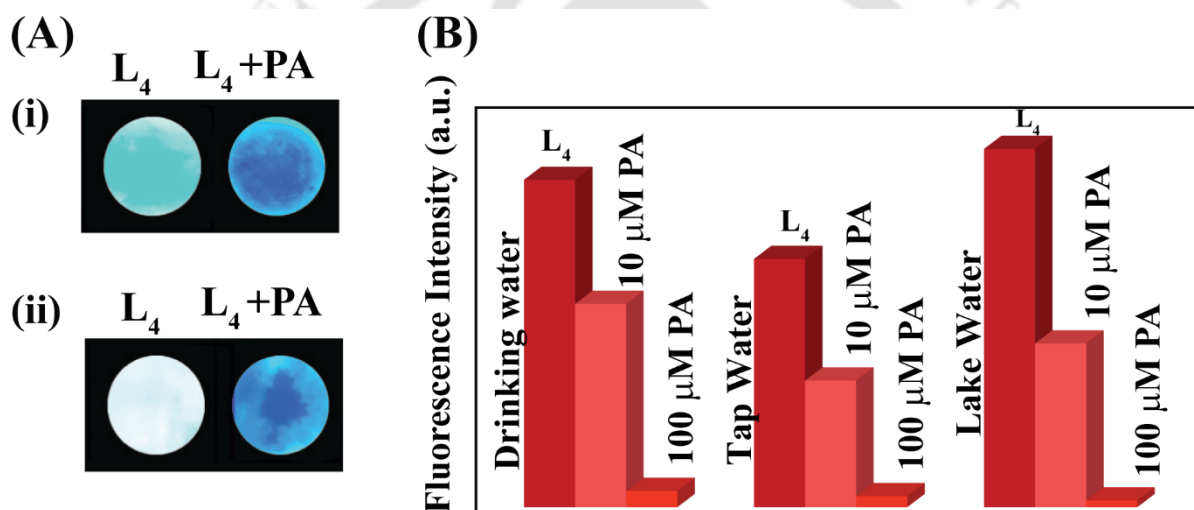


Figure 4A.7: (A) Detection of picric acid on (i) Silica gel plates (ii) Paper strips (B) Bar Diagram representing detection ability of L_4 in multiple water sample.

To validate the usability of L_4 the chemosensing capacity was checked in multiple water samples. Water from various sources was sorted. In drinking water, emission intensity was quenched to 62%, 51 % in Tap water, followed by 45% in lake water on the addition of 5 equivalents of PA. Consecutively, the addition of 50 equivalents of PA quenching to 4.9%, 4.4%, and 1.8% of initial fluorescence intensity was recorded (Fig. 4A.7(B)). This ensures the applicability of L_4 in environmental as well as analytical fields.

4A.5 Conclusion

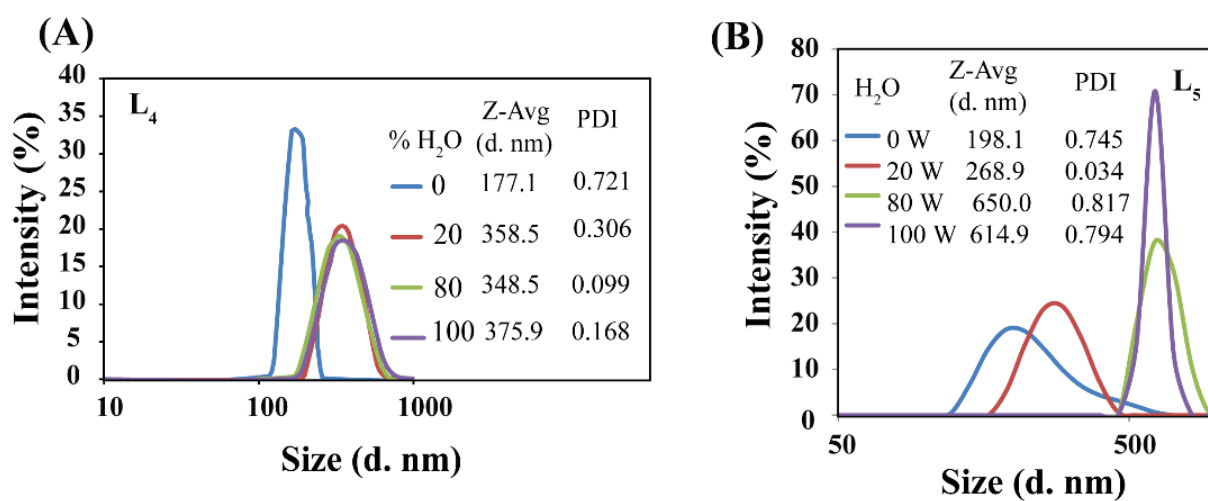
In a nutshell, we have carried out a comparative study between a synthesized amphiphile and non-amphiphile through microscopic and spectroscopic techniques. Various aspects of the compounds are dealt with from aggregation studies to realistic applications. The aggregated state

takes part in light-harvesting systems as a donor in an aqueous solution that mimics natural phenomena. A Light-harvesting system operated via FRET has been established between our proposed AIE-gen and commercial dye. To extend the versatility of AIE-gen, the interaction of AIE-gen with nitro-aromatics was examined. Detection of picric acid in solid support, environmentally relevant water samples is also detailed. We intend that our present work contributes to both photo-physical research and analytical applicability.

References

- 4A.1. V. B. Bojinov, A. I. Venkova and N. I. Georgiev, Synthesis and energy-transfer properties of fluorescence sensing bichromophoric system based on Rhodamine 6G and 1,8-naphthalimide., *Sens. Actuators B*, 2009, **143**, 42– 49.
- 4A.2. N. I. Georgiev, V. B. Bojinov and A. I. Venkova, Design, Synthesis and pH Sensing Properties of Novel PAMAM Light-Harvesting Dendrons Based on Rhodamine 6G and 1,8-naphthalimide., *J. Fluoresc.* 2013, **23**, 459– 471.
- 4A.3. N. I. Georgiev, R. Bryaskova, R. Tzoneva, I. Ugrinova, C. Detrembleur, S. Miloshev, A. M. Asiri, A. H. Qusti, V. B. Bojinov, A novel pH sensitive water soluble fluorescent nanomicellar sensor for potential biomedical applications., *Bioorg. Med. Chem.*, 2013, **21**, 6292– 6302.
- 4A.4. N. I. Georgiev, A. M. Asiri, A. H. Qusti, K. A. Alamry and V. B. Bojinov, A pH sensitive and selective ratiometric PAMAM wavelength-shifting bichromophoric system based on PET, FRET and ICT., *Dyes Pigm.* 2014, **102**, 35– 45.
- 4A.5. N. I. Georgiev, A. M. Asiri, K. A. Alamry, A. Y. Obaid and V. B. Bojinov, Selective ratiometric pH-sensing PAMAM light-harvesting dendrimer based on Rhodamine 6G and 1,8-naphthalimide., *J. Photochem. Photobiol.* 2014, **277**, 62– 74.
- 4A.6. K. A. Alamry, N. I. Georgiev, S. A. El-Daly, L. A. Taib and V. B. Bojinov, A highly selective ratiometric fluorescent pH probe based on a PAMAM wavelength-shifting bichromophoric system., *Spectrochim. Acta, Part A*, 2015, **135**, 792– 800.
- 4A.7. K. A. Alamry, N. I. Georgiev, S. A. El-Daly, L. A. Taib and V. B. Bojinov, A ratiometric rhodamine–naphthalimide pH selective probe built on the basis of a PAMAM light-harvesting architecture., *J. Lumin.*, 2015, **158**, 50– 59.
- 4A.8. N. I. Georgiev, M. D. Dimitrova, A. M. Asiri, K. A. Alamry, V. B. Bojinov, Synthesis, sensor activity and logic behaviour of a novel bichromophoric system based on rhodamine 6G and 1,8-naphthalimide., *Dyes Pigm.*, 2015, **115**, 172– 180.
- 4A.9. M. D. Dimitrova, N. I. Georgiev and V. B. Bojinov, Novel PAMAM Dendron as a Bichromophoric Probe Based on Rhodamine 6G and 1,8-Naphthalimide., *J. Fluoresc.*, 2016, **26**, 1091– 1100.
- 4A.10. J. Chai, Y. Wu, B. Yang and B. Liu, The photochromism, light harvesting and self-assembly activity of a multi-function Schiff-base compound based on the AIE effect., *J. Mater. Chem. C*, 2018, **6**, 4057– 4064.
- 4A.11. N. Melnychuk, S. Egloff, A. Runser, A. Reisch and A. S. Klymchenko, Light-Harvesting Nanoparticle Probes for FRET-Based Detection of Oligonucleotides with Single-Molecule Sensitivity., *Angew. Chem., Int. Ed.*, 2020, **59**, 6811– 6818.
- 4A.12. Q. Song, S. Goia, J. Yang, S. C. L. Hall, M. Staniforth, V. G. Stavros and S. Perrier, Efficient Artificial Light-Harvesting System Based on Supramolecular Peptide Nanotubes in Water., *J. Am. Chem. Soc.*, 2021, **143**, 382– 389.
- 4A.13. S. Wang, J.-H. Ye, Z. Han, Z. Fan, C. Wang, C. Mu, W. Zhang and W. He, Highly efficient FRET from aggregation-induced emission to BODIPY emission based on host–guest interaction for mimicking the light-harvesting system., *RSC Adv.*, 2017, **7**, 36021.

Appendix - Chapter 4A

Figure A4A.1: DLS output of (A) L_4 and (B) L_5 in varying DMF-Water percentage.

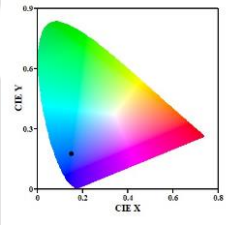
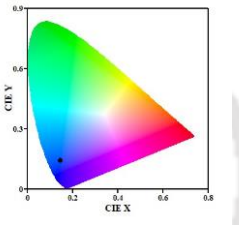
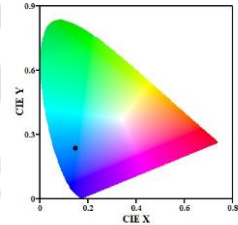
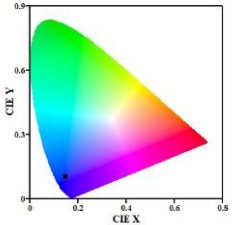
Compounds	Emission Intensity	Solid-State Intensity	Emission
L_4	 (0.15, 0.18)	 (0.14, 0.14)	
L_5	 (0.15, 0.24)	 (0.15, 0.10)	

Figure A4A.2: Chromaticity Diagram of L_4 and L_5 w.r.t solution state and solid state emission intensity along with their coordinates.

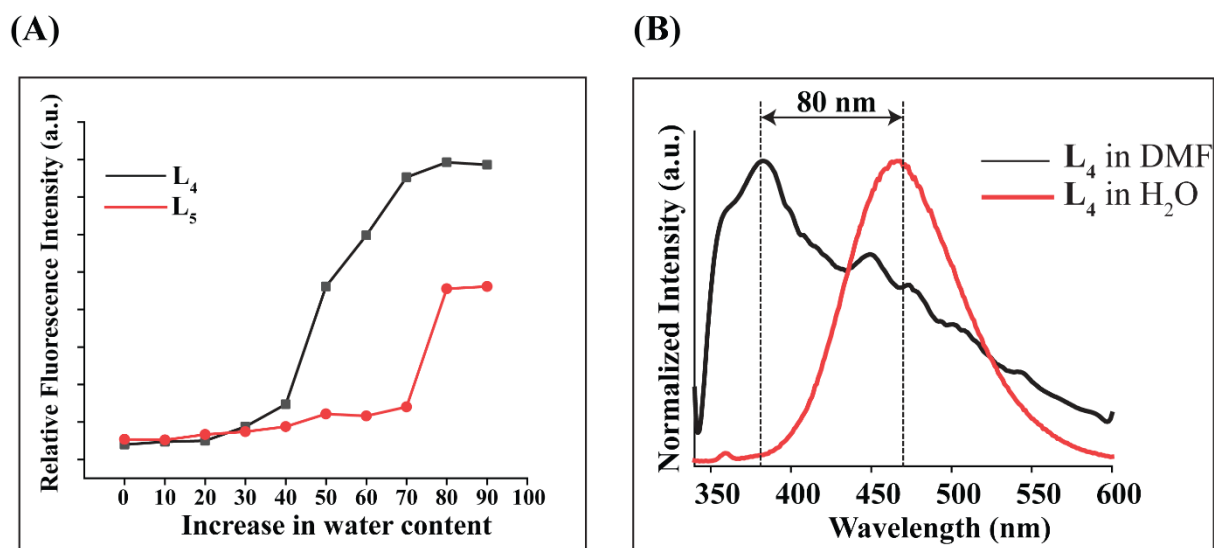


Figure A4A.3: (A) Line graph of emission profile comparing the aggregating aptitude of L₄ and L₅. (B) Normalized emission spectra depicting redshift of L₄.

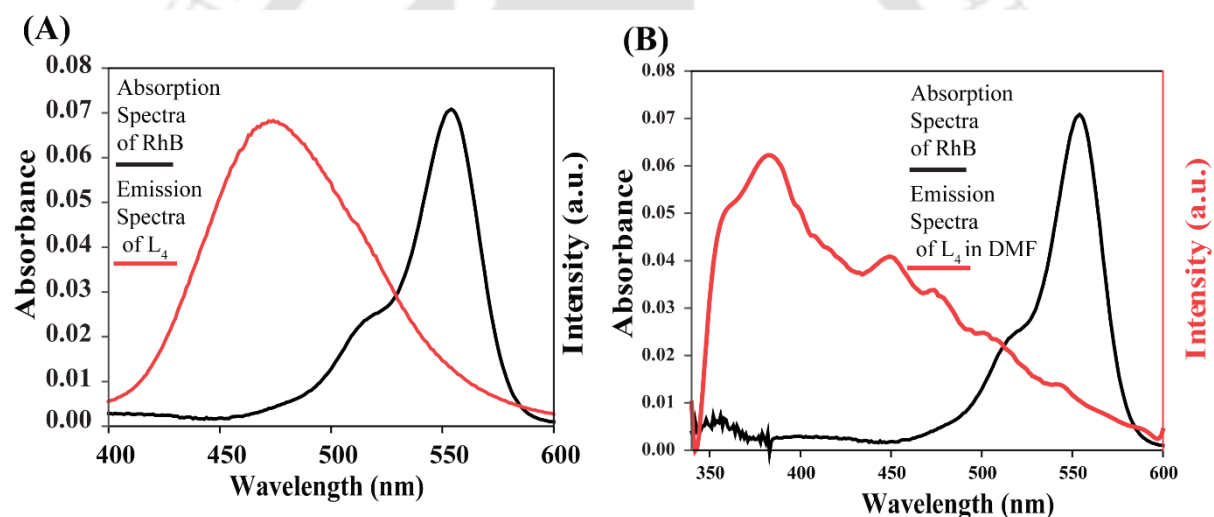


Figure A4A.4: (A) Absorption and emission spectra of Rhodamine B and L₄ respectively in water depicting spectral overlap (B) Absorption and emission spectra of Rhodamine B (in water) and L₄ (in DMF) respectively depicting poor spectral overlap.

Compounds	B ₁	B ₂	a ₁	a ₂	τ ₁	τ ₂	< τ > ns	χ ²
L ₄	0.0136	0.0260	0.07072	0.92928	2.940	20.197	9.488	1.110
L ₄ + RhB	0.0323	0.0164	0.18158	0.09669	2.054	15.536	0.937	1.069

Table A4A.1: Fluorescence lifetime values of L₄ (2μM) and L₄+ RhB in aqueous medium.

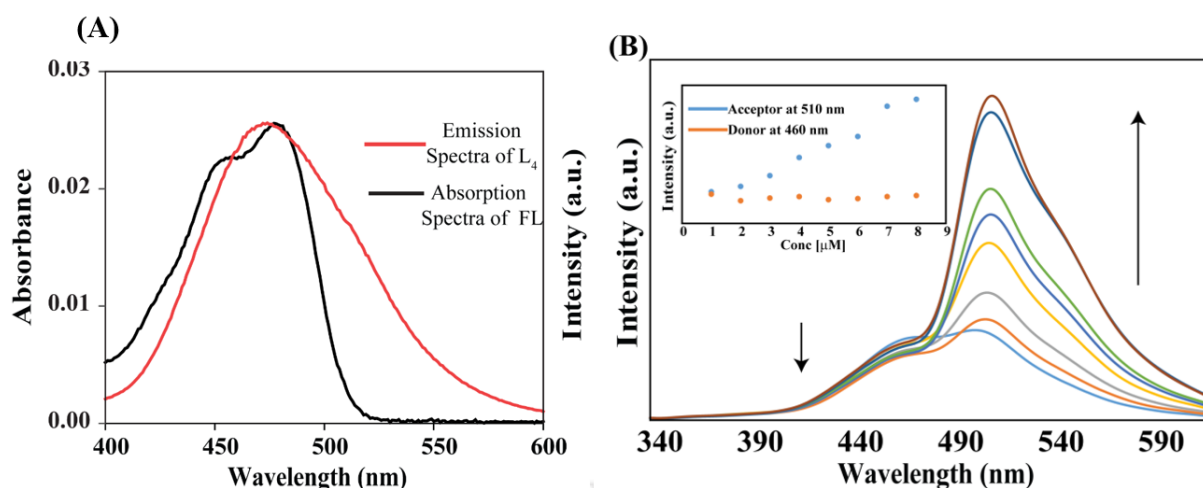


Figure A4A.5: (A) Spectral overlap between the emission profile of Donor (L_4) and absorbance range of Acceptor (Fluorescein) (B) Increasing emission intensity of acceptor in presence of donor with increasing concentration.

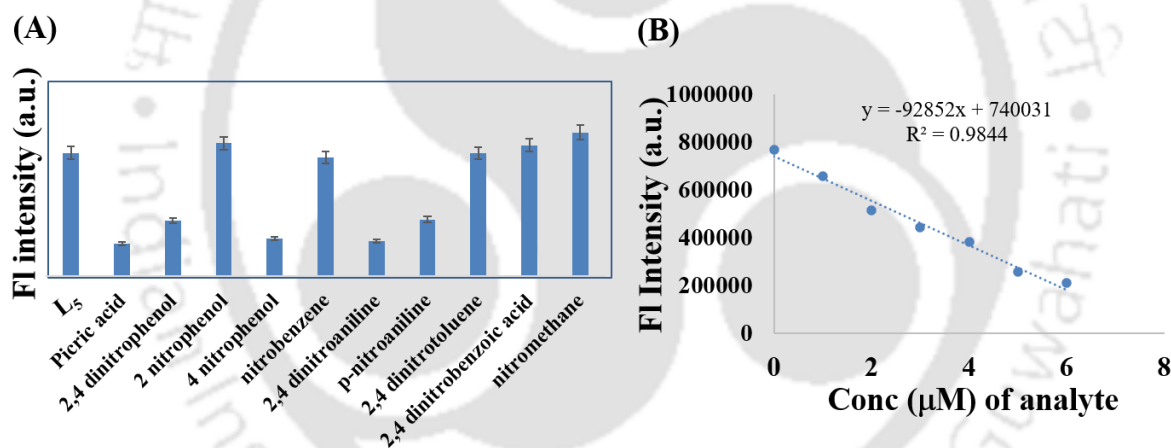
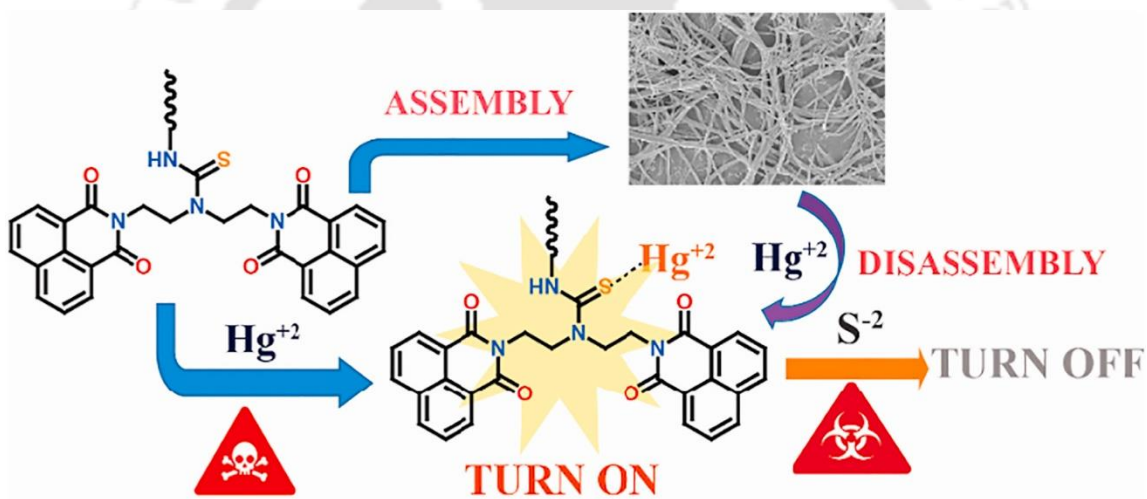


Figure A4A.6: (A) Bar Diagram of emission intensity of L_5 with other nitroaromatics. (B) Plot for determination of LOD.

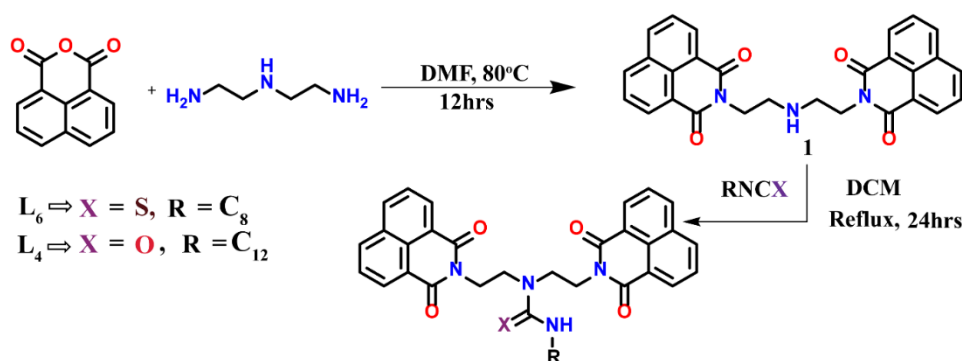
CHAPTER 4B

Turn-ON mercury detection in water by tripodal synthetic amphiphile chemosensors via self-assembly and desulfurization



4B.1 Background and focus of the chapter

With constant disrepute of toxicity, mercury remains the focal point of research, and its detection in the aqueous medium is a crucial task. It is invariably obnoxious to flora, fauna, and human life from water bodies to agricultural soil. Due to its severe toxicity and bioaccumulation, water-soluble Hg^{+2} is one of the most prevalent and known forms of mercury pollution. The Hg^{+2} binds the thiol residues of proteins, leading to difficulty in removal from living beings.^{4B.1-4B.6} Accumulation of mercury in water bodies through biomagnification impedes algal, plankton growth and hampers the reproductive life of fishes and other aquatic life. By inactivating sulfur, intracellular mercury can deactivate various enzymes, hormones, and cofactors resulting in many disorders in animals and humans. Human life is exposed to mercury by consuming mercury-laden fishes or crops grown in mercury-contaminated soil.^{4B.7-4B.11} Fluorometry shows high sensitivity, non-destructibility of samples, rapid detecting ability, renders accurate data on the localization and quantity of the targets of concern. Apart from classical chemosensors and probes, which can alter a chemical input into action, chemodosimeters have a wide range of uses as reagents for sensing numerous amounts of reactants in irreversible/reversible chemical processes. Utilizing chemical phenomena, multiple novel chemodosimeters have been helpful to develop in response to current needs for improved selectivity and sensitivity.^{4B.12-4B.13} Mercury is known to cause quenching of fluorescence in fluorophores. Quenching is undesirable on an excellent signal output during recognition and becomes challenging to separate spectrally similar complexes in the case of time-resolved fluorometry. Particularly for mercury, among other heavy metals, the availability of “Turn-On” fluorescent chemosensors is scarce. These heavy metal ions are prone to cause quenching of emission signal by spin-orbit coupling or electron transfer. Preferences are towards those sensors capable of fluorescent enhancement on cation binding because they offer lower detection limits and good spatial resolution through microscope imaging.^{4B.14-4B.15}



Scheme 4B.1. Synthetic route of L_6 and L_4 .

4B.2 Explore the self-aggregation potential

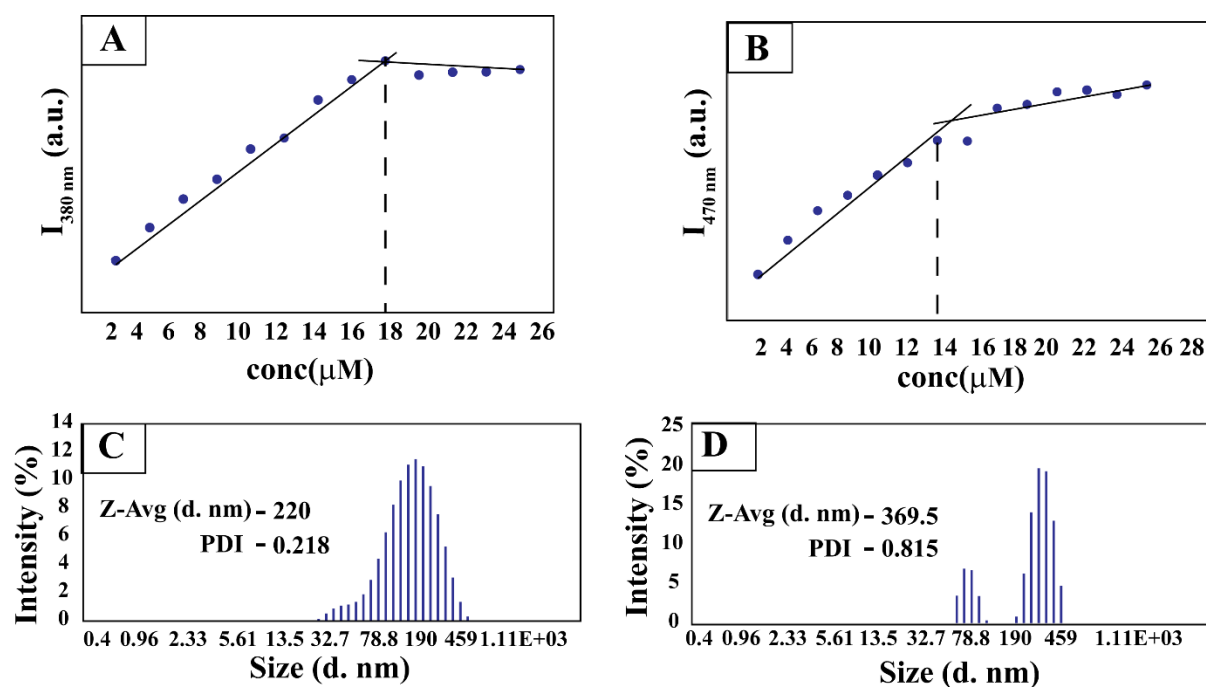


Figure 4B.1: Emission spectra of L_6 (A) & L_4 (B) for determining Critical Aggregation Constant (CAC); Corresponding DLS experiment of L_6 (A) & L_4 (B) to determine the particle size of aggregated particles.

L_6 and L_4 being amphiphilic potent enough to self-assemble in the aqueous medium. L_6 and L_4 were studied under emission spectroscopy. The excitation I_{max} was 320 nm for both L_6 and L_4 . The emission maxima for L_6 and L_4 were 400nm and 470 nm respectively in the aqueous medium. Determination of Critical Aggregation Constant (CAC) for L_6 and L_4 was done by fluorometry. The concentration of probes was increased from 2 μM to greater than 15 equivalents. The observed emission maxima intensity was plotted against concentration. The nature of obtained plot evidenced the CAC value of each probe. Each of the graphs displayed a systematic growth of FL intensity with an increase in concentration and eventually, the abrupt break in this trait evidenced the CAC of each probe at certain concentrations. For L_4 , the abrupt change occurred at 18 μM concentration while in the case of L_6 , the concentration was 14 μM (Figure 4B.1). These were considered as the CAC value of the probes. Measurement of the particle size at the inferred concentration i.e.; CAC was done by dynamic light scattering experiment at room temperature. The hydrodynamic diameter of self-assembled L_6 and L_4 in water was found to be 220 nm and 369.5 nm (Figure 4B.1). For further perceptive, examination of the morphology of the self-assembly of the probes was essential. Therefore, microscopic studies were conducted at two different concentrations; one way below the CAC and the other above the CAC value. In Field Emission Scanning Electron Microscope studies, the L_6 , showed

spherical shapes of diameter around 200nm, in the lower concentration. With increasing concentration, these spherical-shaped L_6 aggregated to form mesh-like ribbons of greater length. For more validation of microscopy studies, Atomic Force Microscopy was conducted using a similar concentration. Interestingly, the exact morphology was reflected in the same. Under scan area of $5 \times 5 \mu\text{m}$, at lower CAC value spherical shapes and higher CAC value the ribbon-shaped aggregates were visible (Figure 4B.2).

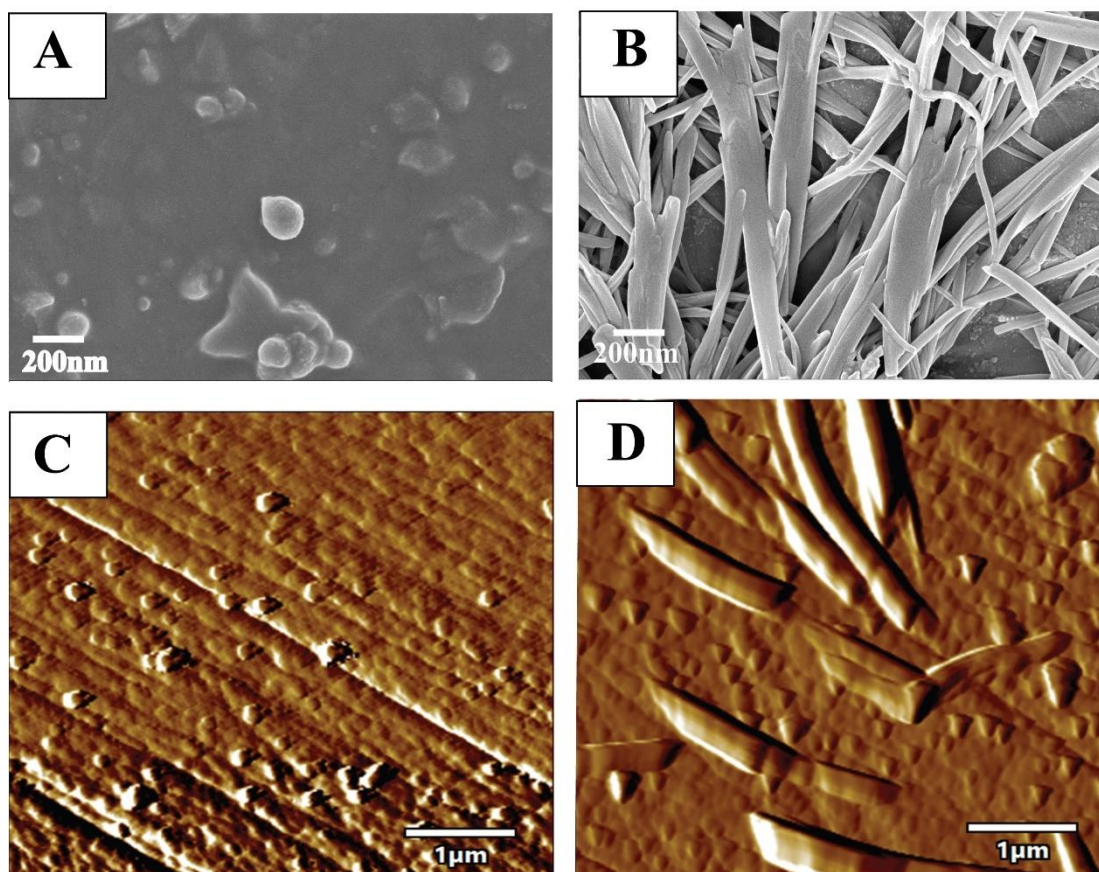


Figure 4B.2: FESEM images of L_6 concentration below(A) and above CAC (B). AFM images of L_6 concentration below(C) and above CAC (D).

4B.3 Response of metal ions on the probe: Selective interaction with mercury

To begin with photophysical studies; UVvis studies were conducted on both the probes in the aqueous medium. L_6 and L_4 depicted well-defined absorbance maxima nearby about 345nm and 340 nm in water respectively and along with a rise in the baseline. To go through the colorimetric analysis of the probes with metal ions, an array of cations was tried in the aqueous medium. Methanolic or aqueous solution of nitrate, acetate, and chloride salts of metals namely; Al^{+3} , Cr^{+3} , Mn^{+2} , Fe^{+2} , Co^{+2} , Ni^{+2} , Cu^{+2} , Zn^{+2} , Pb^{+2} , Hg^{+2} , Cd^{+2} , Ag^{+} , Ca^{+2} and Mg^{+2} were tested. All metal ions failed to show a substantial change in absorption spectra for L_6

except Hg^{+2} , where the absorbance value 0.088 increased to 0.175 (at 345 nm). In the case of L_4 , there was no noticeable spectral change with all the tested cations (Figure 4B.3(A)).

Indecisive results from UVvis studies provided us an impetus to study the fluorometric responses of the probes towards metal ions. The probes L_6 and L_4 exhibited a weak emission peak at 380 nm and 470 nm in the HEPES buffer (0.1M, pH 7.4) medium. Adding metal ions to the buffer solution of the probes changed the emission spectrum L_6 distinctly. Methanolic or aqueous solution of diverse cations was employed to examine the selective quality of the probes. For L_6 , a selective “turn-on” emission signal was noticed particularly for Hg^{+2} ion among all other the tried cations. An intense and new strong emission signal at 475nm, with amplification of intensity up to 15 times, was perceived along with the existing emission peak at 380 nm. To gain definite insights into the sensing occurrence, titration experiments with increasing concentration Hg^{+2} ions were conducted in HEPES buffer (0.1M, pH 7.4) medium. A serial addition of Hg^{+2} ions to L_6 caused an orderly rise of the fluorescence emission intensity at 475 nm retaining until 15 aliquots of Hg^{+2} ions were added (Figure 4B.3(D)). The perceived

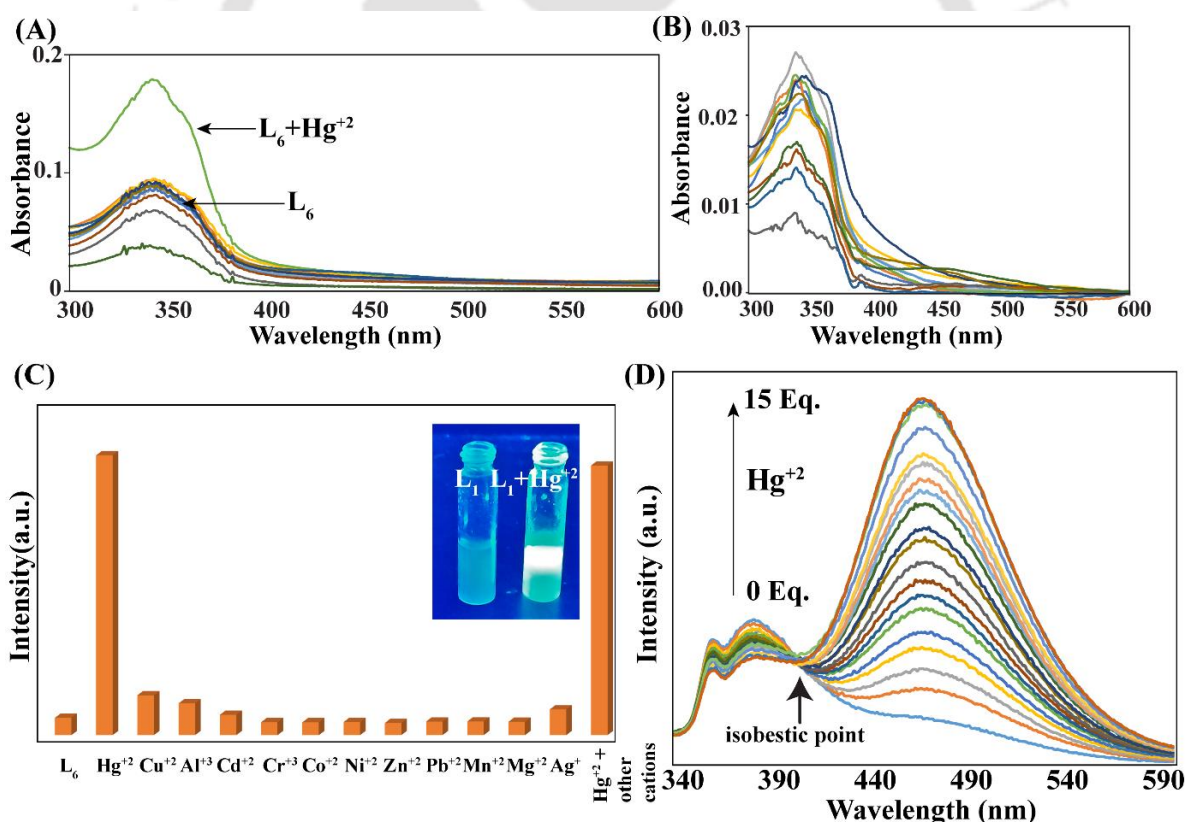


Figure 4B.3: (A) UV-vis Spectra of L_6 (2 μM) in aqueous media with various metal ions. (B) UV-vis Spectra of L_4 (2 μM) in aqueous media with various metal ions. (C) Bar diagram depicting emission intensity and interaction of L_6 with metal ions (D) Fluorescence titration profile of L_6 upon gradual addition Hg^{+2} ions in HEPES buffer media (0.1 M, pH=7.4).

results can be attributed to the ON-OFF; Photo-induced electron transfer (PET) mechanism. The weak emission L_6 was due to the occurrence of PET from thiourea N-substituted parts of L_6 , to the electron-deficient naphthalimide fluorophores. From the HOMO LUMO plot (Figure A), it is assumed that PET is operative between the suggested parts of L_6 . The incoming mercury binds to the sulfur atom in virtue of soft-soft interaction thus blocking the operative PET. Owing to the termination of the PET process, there arose a substantial Turn-ON or enhancement of fluorescence intensity than the former emissive status of L_6 via this proposed binding process. The control probe, L_4 devoid of sulfur displayed no emission enhancement with Hg^{+2} as well as poor selectivity towards all employed cations (Figure A4B.1). An additional feature was drawn concerning timescapes, how the L_6-Hg^{+2} fluorescence intensity decayed with time (Figure A4B.7(B)). The total time taken for a considerable decline of fluorescence intensity was approx. 4.5hrs.

Analysing carefully, the Benesi-Hildebrand (B-H) plot, the binding constant related with the generation of an L_6-Hg^{+2} complex was found to be $3.6 \times 10^4 M^{-1}$, stating strong chelation between the L_6 and Hg^{+2} ion (Figure A4B.5(A)). Following equation (1), the detection limit (LOD) was calculated to be $0.375 \mu M$, far below the EPA (U.S. Environmental Protection Agency) permissible Hg^{+2} limit in safe drinking water (Figure A4B.5(C)). After a detailed titration experiment, for deriving Job's plot estimated formation of a 1:1 complex between L_6 and Hg^{+2} ion (Figure A4B.5(B)). Hence, on basis of photophysical analyses, it may be addressed that the probe L_6 is capable to detect Hg^{+2} ions via a selective fluorometric response amongst all other reliable metal ions.

4B.4 Analyte and the self-aggregated state

It was interesting to comprehend, how the targeted analyte ie; Hg^{+2} responded towards the self-assembled states. The FESEM images L_6 revealing its ribbon-shaped morphology was completely disrupted in presence of Hg^{+2} ions. DLS experiments were carried out to measure the particle size of assembled and disassembled states. A fall from 220 nm to 113.4 nm size was noted by DLS particle size measurement. Hence, it evidenced the disassembly of self-aggregated states in presence of Hg^{+2} (Figure 4B.4). The disaggregation did not compromise the sensing potentiality of the L_6 . A "Turn-ON" was achieved by the probe (30mM; concentration much greater than CAC) upon addition of 10 equivalents of Hg^{+2} ions and nearly 7.30 times amplification of emission intensity was noted (Figure A4B.7(C)).

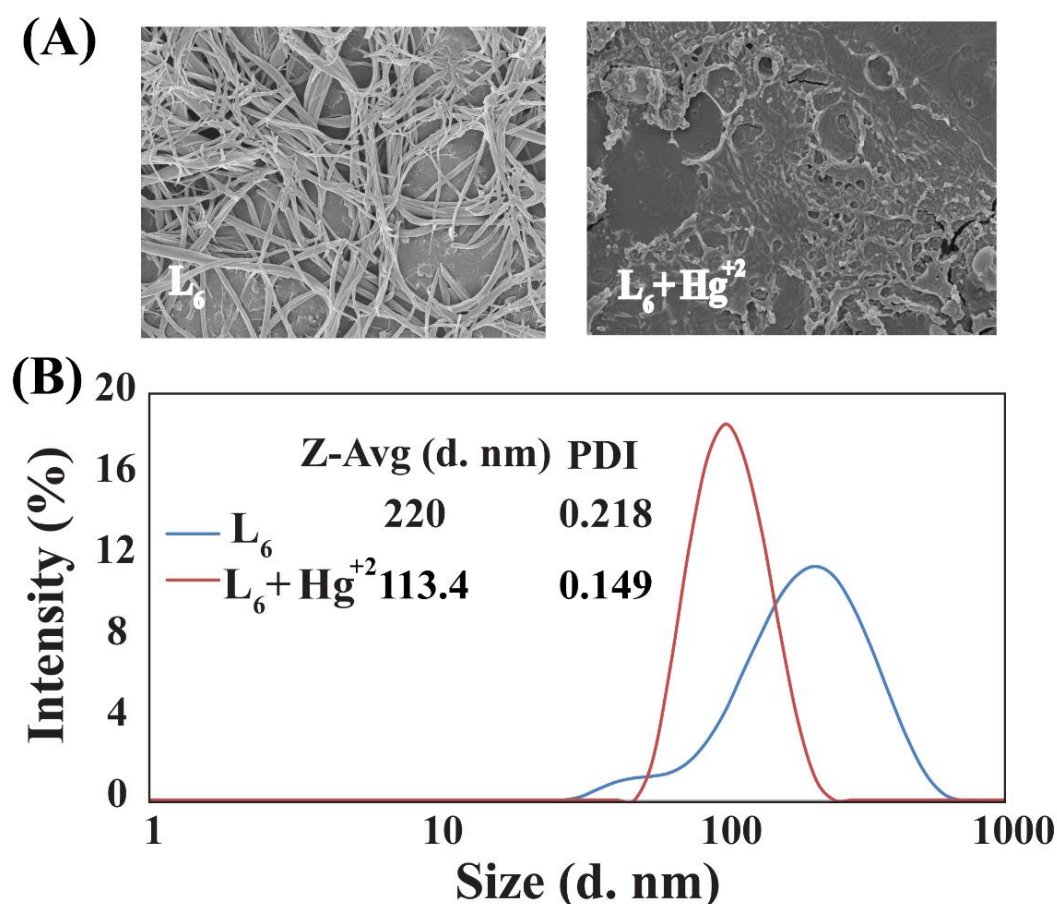


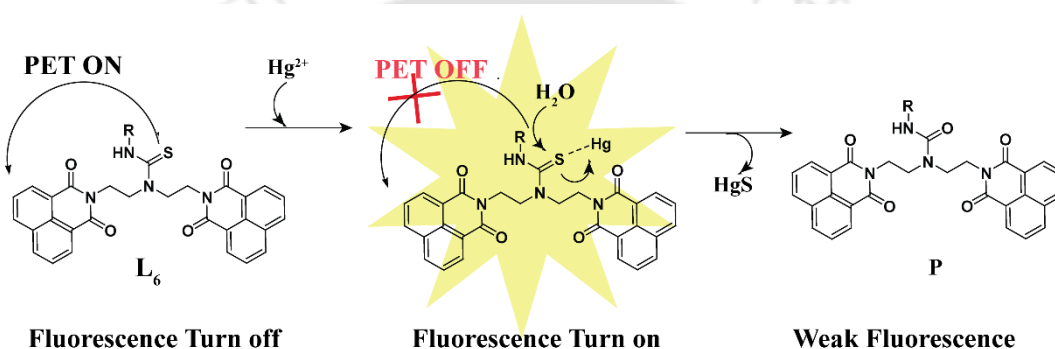
Figure 4B.4: (A) FESEM images of aggregated L_6 in the absence and presence of Hg^{+2} . (B) DLS experiment depicting the size variation and interaction of aggregated L_6 and Hg^{+2} .

4B.5 Probing the mechanism of sensing

A plausible mechanism is sketched out, stating desulfurization. In accordance with the HSAB principle, the Hg^{+2} binds to the sulfur atom due to soft-soft interaction. Carbon attached to the sulfur atom becomes prone to the nucleophilic attack of water molecules existing in the system. The Hg^{+2} is precipitated as HgS along with the formation of a new $C=O$ bond in place of $C=S$. To corroborate the stated proposal, L_6 was subjected to desulfurization under reaction conditions. L_6 was dissolved in DCM and the equivalent amount of methanolic Hg -salt was added to it. The reaction was refluxed in DCM for 4 hrs. Gradually, white precipitate separated. After filtration, the residue was washed with DCM and cold ether. Then the residue was taken for EDX analysis. The filtrate; the organic layer was washed twice with deionized water and taken for HRMS analysis. From, Mass spectrum a peak at 619.2998[M+1] indicated the formation of P (Figure A4B.3), while the EDX spectrum (Figure A4B.4) showed the atomic percentage of Hg and S 4.2% and 3.1% respectively, revealing the precipitation of HgS . Hence corroborating our supposition, the substituted thiourea ($>C=S$) component of L_1 , solely directs

the sensing potentiality and the control **L**₄ bearing substituted urea (>C=O) failed to do so (Scheme 4B.2).

For further detailing, spectral outcomes were compared among **L**₆, **L**₄, and **P**, along with the effect of Hg⁺² on them. Fluorescence emission intensity was measured in each case and plotted, to infer the spectral observations in the experimentation. A stock solution of **P** was prepared with a similar concentration that of **L**₆ and **L**₄ so that the effective concentration remains the same in all the cases. After excitation at 320 nm, **P** displayed emission maxima around 470 nm quite similar to **L**₄ (Figure A4B.7(A)). The fall in emission intensity of **L**₁+Hg⁺² with time has already been put up and the final state of the decline is quite similar to emission spectra of **P**. This indicating desulfurization and formation of **P**.



Scheme 4B.2: Plausible reaction mechanism of **L**₆ and Hg⁺²

4B.6 Investigation in real sample

To realize the ability of **L**₆ in the real spectrum, the detection of mercury in different water sources was carried out. The probe **L**₆ was utilized in detecting Hg⁺² in real water samples which includes Milli-Q[®], drinking, tap, and river water samples. Milli Q, Drinking, Tap, and river water were collected from the laboratory, water filters, and regular usable taps at IIT Guwahati, and river Brahmaputra (near the campus of IIT Guwahati, Assam, India), respectively. A known concentration of Hg⁺² (50 μM) was spiked into the experimental medium (ie; collected water sample) and **L**₆ (2mM) was added. The associated change emission intensity at 475 nm was tabulated. Significantly probe **L**₆ exhibited the ability to identify mercury in environmental water samples based on distinctive fluorescence responses at 475 nm (Figure 4B.5(C)). The percentage of recovery amount of the provided samples of the relevant metal ion is estimated by assuming 100% recovery in standard MilliQ water, which was taken for the experiment's standard medium, and the results are presented in tabular form (Table A4B.1).

Visual Detection of Hg^{+2} was done under a 365nm -UV lamp for various soil samples. Focus on the collection of multiple soil samples lies in the fact; several staple crops in alluvial soil, cotton in black soil, lentils in red soil, etc are widely cultivated. Another feature of detection can be comprehended, how the probe acts under several like soil nutrients, varying mineral acids, typical organic substrates, varying metallic content, etc. which these soil samples comprise. Agriculturally important 5 soil samples were sorted; namely Black, Loamy, Red, Alluvial, and Sandy soil. Each of them was loaded with mercury and held under the lamp with/without the addition of L_6 . The fluorescent change was prominent with the specimen being loaded with L_6 and mercury (Figure 4B.5(D)).

To denote a realistic outlook, paper strip tests were performed. The model paper strips were readily cut out from usual filter papers and arranged, by dipping them in the probe solution L_6 and drying it in the air for few hours. Afterward, different concentrations of mercury were loaded on them. One of them was loaded with 1 Eq. of Hg^{+2} while excess Hg^{+2} was added to the other strip. Prominent fluorescence variations were perceptible in the strips under the 365nm-UV lamp (Figure 4B.5(B)).

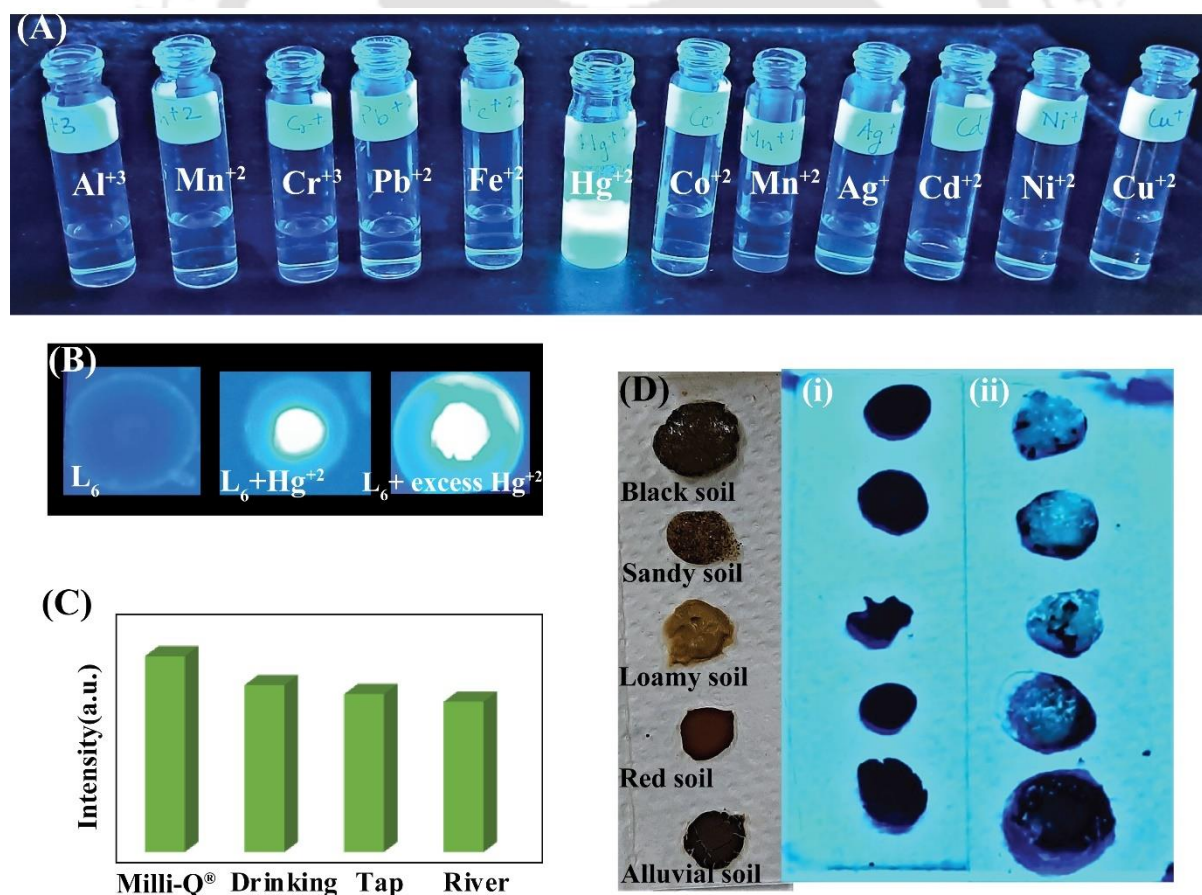


Figure 4B.5: (A) L_6 with various cations along with Hg^{+2} in glass vials under 365nm UV light. (B) (Under $\lambda = 365 \text{ nm}$ UV light) Change of Fluorescence on Paper strips in the absence,

presence, and excess Hg^{+2} . (C) Bar diagram profile of emission intensity in the detection of Hg^{+2} in the collected water samples from different sources (D) Detection of Hg^{+2} in multiple soil samples through fluorescence change (UV light $\lambda = 365 \text{ nm}$) (i) in presence of L_6 but devoid of mercury (ii) in presence of $\text{L}_6 + \text{Hg}^{+2}$.

4B.7 Effects of anion towards Hg (II)-ensemble

As of late, metal ensemble-based anion sensors have been significantly accepted in the research community. A feasible utility of the probe via the Hg (II)-ensemble was sought out in anion sensing. Sulfide is an important species in the anion family that is generated as a by-product of the Kraft process for the manufacturing of wood pulp. It is noxious and recognized by its typical rotten egg-like odor and is found in large amounts in oil wells and hot springs and wastewater. By microbial reduction, certain anaerobic bacteria can convert sulfate to sulfide, and they can also be produced from sulfur-containing amino acids in the biosystem. Excessive sulfide anions, on the other hand, can induce a range of side effects, including respiratory problems, unconsciousness, and mucous membrane irritation. The sulfide ion releases H_2S on hydrolysis, which is considerably more hazardous than S^{2-} . As a result of a keen interest in sulfide, it is imperative to produce a unique chemosensor for detecting sulfide efficiently and precisely.

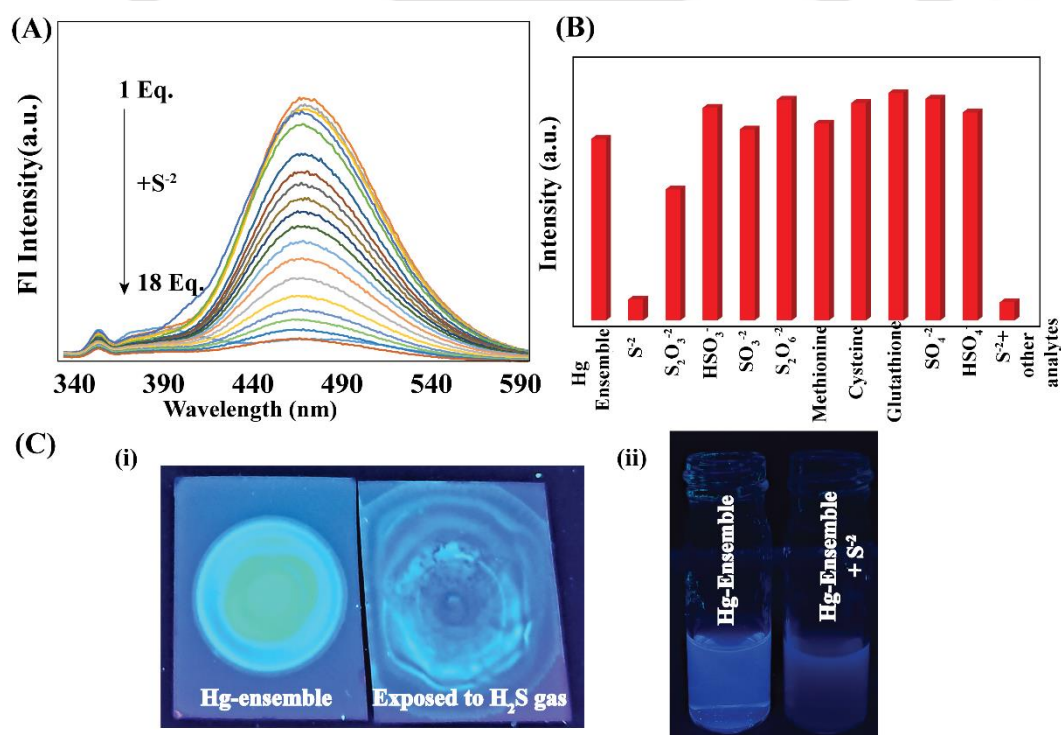


Figure 4B.6: (A) Titration profile of Emission spectra of Hg-ensemble with S^{2-} anion in aqueous media. (B) Bar diagram of emission intensity of Hg-ensemble responding towards other competitive sulfur-containing anions and thiol-based bio-analytes. (C) (i) Paper strip (ii)

vial experiment under 365nm UV showing the effectiveness of Hg-ensemble in H₂S gas detection.

It was exciting to exploit the application of the Hg (II)-ensemble for anion sensing in aqueous media. The high emission intensity of the Hg(II)-ensemble gained at 475nm was noticeably quenched by the addition of S²⁻ anion (Figure A4B.5(B)). The Hg(II)-ensemble binds to S²⁻ ion in aqueous media, thus turning out to be an H₂S sensor. To verify, the selectivity of Hg (II)-ensemble multiple sulphur oxo anions and thiol-based bio-analytes were tested. Selective ‘Turn-off’ was achieved only in the case of S²⁻ (Figure 4B.6(B)). Further to assess, systematic titration was carried out in the aqueous medium with S²⁻ against the ensemble which prompted gradual quenching of emission intensity (Figure 4B.6(A)). Using equation (1), the lower detection limit was determined to be about 0.5 ppm (Figure A4B.5(C)), far below the permissible level prescribed by EPA. To denote the viability of the ensemble in a real scenario, an easily arrangeable model paper strip was introduced for rapid H₂S gas detection. Two paper strips were cut out of regular filter paper, soaked in the ensemble, and was exposed to H₂S gas. A strong ‘turn-on’ emission was observed for the ensemble which faded on contact to H₂S gas, under the UV lamp light ($\lambda = 365 \text{ nm}$), indicating the efficiency of the method (Figure 4B.6(C)). Thus, we assert the potential ability of the ensemble to detect H₂S gas in the environment with excellency and selectivity.

4B.8 Conclusion

In conclusion, a tripodal amphiphilic receptor detects Hg²⁺ ions in aqueous media with precise selectivity. Not only is the fluorescent “Turn-On” chemo sensor apt enough to sense mercury in various water, soil samples, but it also self-aggregates in the aqueous medium. Microscopy studies and DLS details the self-aggregated morphology and hydrodynamic size of the reported probe. Furthermore, the mercury ensemble can sense noxious gas hydrogen sulphide viz; sulphide anions in water. The presented layout of sensing techniques is of high analytical utility for both the targeted cation; Hg²⁺ and anion; S²⁻. Also, the proposed paper strip-based chemo sensor is a promising fluorometric technique for mercury and H₂S monitoring in water samples, with quick and selective sensing capacities. Rapid response can render real-time detection.

References

- 4B.1. J.D. Dai, Yang, Y. Wang and Yang, Y.W.; Recent Progress in Functional Materials for Selective Detection and Removal of Mercury (II) Ions, *Adv. Funct. Mater.*, 2021, **31**, 2006168.

- 4B.2. B.W. Liu, Y. Chen, B.E. Songa and Y. Liu, Amphiphilic porphyrin assembly as a highly selective chemosensor for organic mercury in water, *Chem. Commun.*, 2011,**47**, 4418-4420.
- 4B.3. Z. Wang, Z. Yang, T. Gao, J. He, L. Gong, Y. Lu, Y. Xiong, and W. Xu, An Hg²⁺-selective chemosensor based on the selfassembly of a novel amphiphilic block copolymer bearing rhodamine 6G derivative moieties in purely aqueous media, *Anal. Methods*, 2015, **7**, 2738.
- 4B.4. J. Hu, L. Dai and S. Liu, Analyte-Reactive Amphiphilic Thermoresponsive Diblock Copolymer Micelles-Based Multifunctional Ratiometric Fluorescent Chemosensors, *Macromolecules*, 2011, **44**, 4699–4710.
- 4B.7. V. Poornima, V. Alexandar, S. Iswariya, P. T. Perumal and T.S. Uma, Gold nanoparticle-based nanosystems for the colorimetric detection of Hg²⁺ ion contamination in the environment, *RSC Adv.*, 2016, **6**, 46711.
- 4B.8 C. Kar, M. D. Adhikari, A. Ramesh and G. Das, Selective sensing and efficient separation of Hg²⁺ from aqueous medium with a pyrene based amphiphilic ligand, *RSC Advances*, 2012, **2**, 9201–9206.
- 4B.9. R. Li, H. Wu, J. Ding, W. Fu, L. Gan, and Y. Li, Mercury pollution in vegetables, grains and soils from areas surrounding coal-fired power plants, DOI: 10.1038/srep46545.
- 4B.10. I. Kim, N.E. Lee, Y.J. Jeong, Y.H. Chung, Choand Eunji Lee, B.K.; Micellar and vesicular nanoassemblies of triazole-based amphiphilic probes triggered by mercury (II) ions in a 100% aqueous medium, *Chem. Commun.*, 2014,**50**, 14006-14009.
- 4B.11. G. Sivaraman, T. Anand and D. Chellappa, Development of a pyrene based “turn on” fluorescent chemosensor for Hg²⁺. *RSC Advances*, 2012, **2**, 10605–10609.
- 4B.12. A. Singh, P. Raj and N. Singh, Benzimidazolium-Based Self-Assembled Fluorescent Aggregates for Sensing and Catalytic Degradation of Diethylchlorophosphate, *ACS Appl. Mater. Interfaces*, 2016, **8**, 28641–28651.
- 4B.13. L. Chen, S. J. Park, D. Wu, H. M. Kim and Yoon, J., A two-photon fluorescent probe for colorimetric and ratiometric monitoring of mercury in live cells and tissues, *Chem. Commun.*, 2019, **55**, 1766.
- 4B.14. B. Roy, S. Halder, A. Guha and S. Bandyopadhyay, Highly selective sub-ppm naked-eye detection of hydrazine with conjugated-1,3-diketo probes: imaging hydrazine in *Drosophila* larvae, *Anal Chem.*, 2017, **89**, 10625-10636.
- 4B.15. Y. Liu, T. Shen, J. Li, H. Gong, C. Chen, X. Chen and C. Cai, Ratiometric fluorescence sensor for the MicroRNA determination by catalyzed hairpin assembly, *ACS Sens.*, 2017, **2**, 1430-1434.

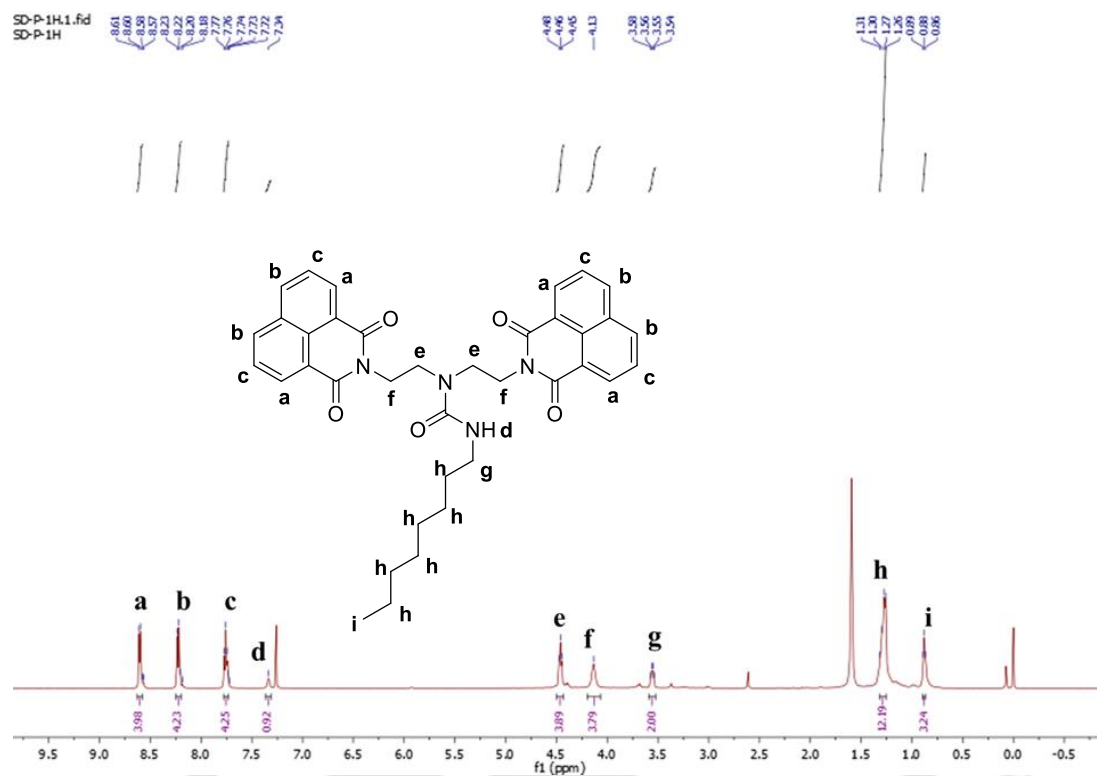


Figure A4B.3: $^1\text{H NMR}$ spectrum of P.

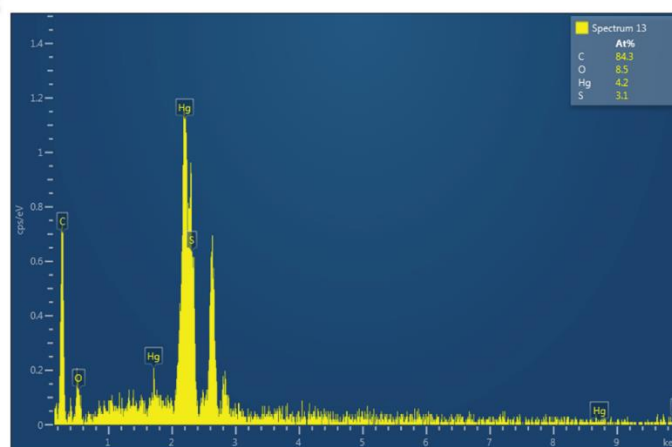
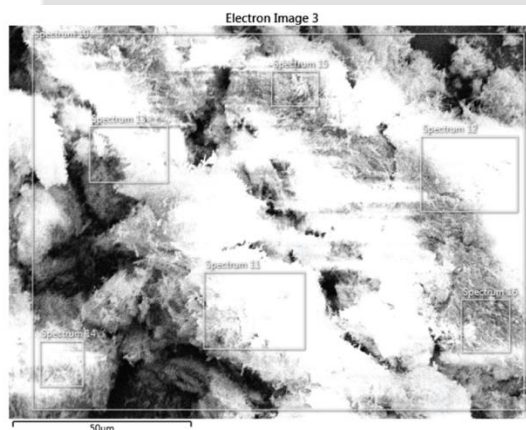


Figure A4B.4: EDX spectrum of the residue viz. HgS from synthesis of P.

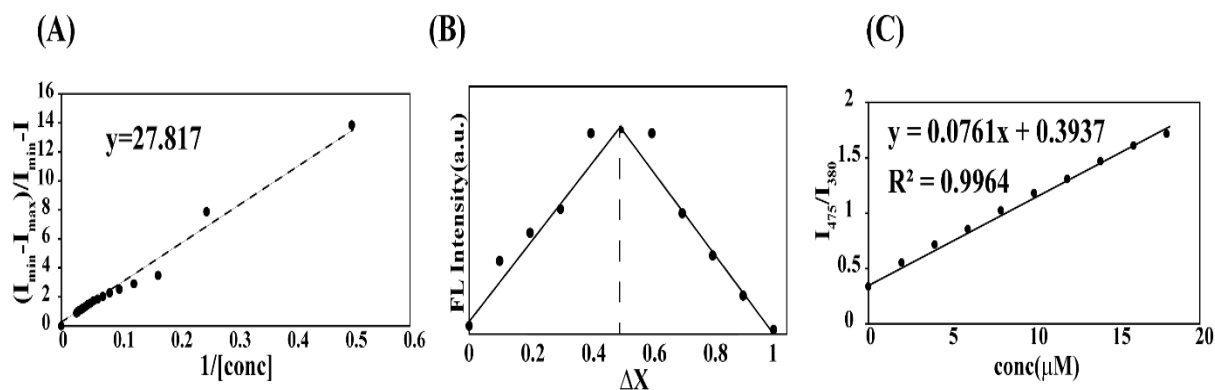


Figure A4B.5: (A) Benesi–Hildebrand plot for determination binding constant of L_6 and Hg^{+2} (B) Job's plot for L_6 - Hg^{+2} complexation from fluorescence emission spectrum (C) Fluorescence intensity ratio of 475nm and 380nm versus Hg^{2+} ion concentrations for lowest detection limits (LOD) calculation.

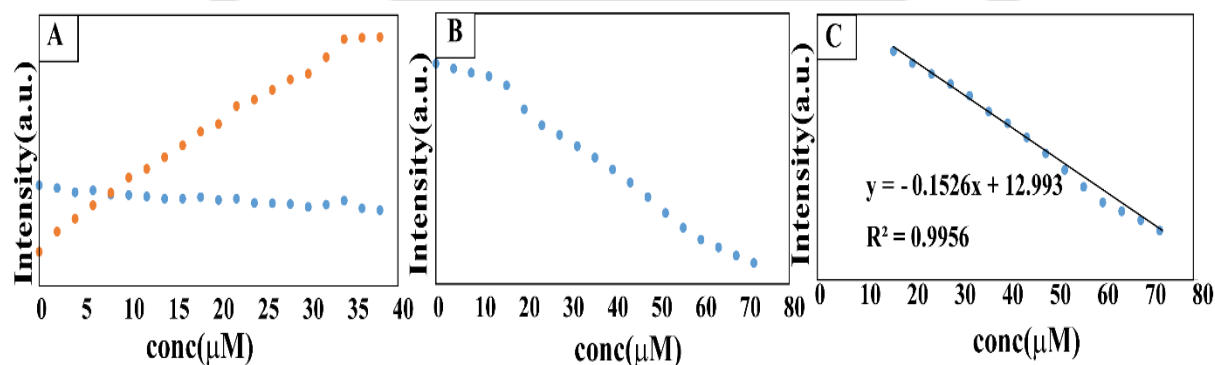


Figure A4B.6: (A) Plot of emission spectra at 475nm and 380nm of L_6 with the gradual addition of Hg^{+2} ions. (B) Fall in emission intensity of $\text{L}_6 + \text{Hg}^{+2}$ ensemble on incremental addition of S^{-2} anions. (C) Fluorescence intensity ratio of 475nm and 380nm versus S^{-2} anion concentrations for lowest detection limits (LOD) calculation.

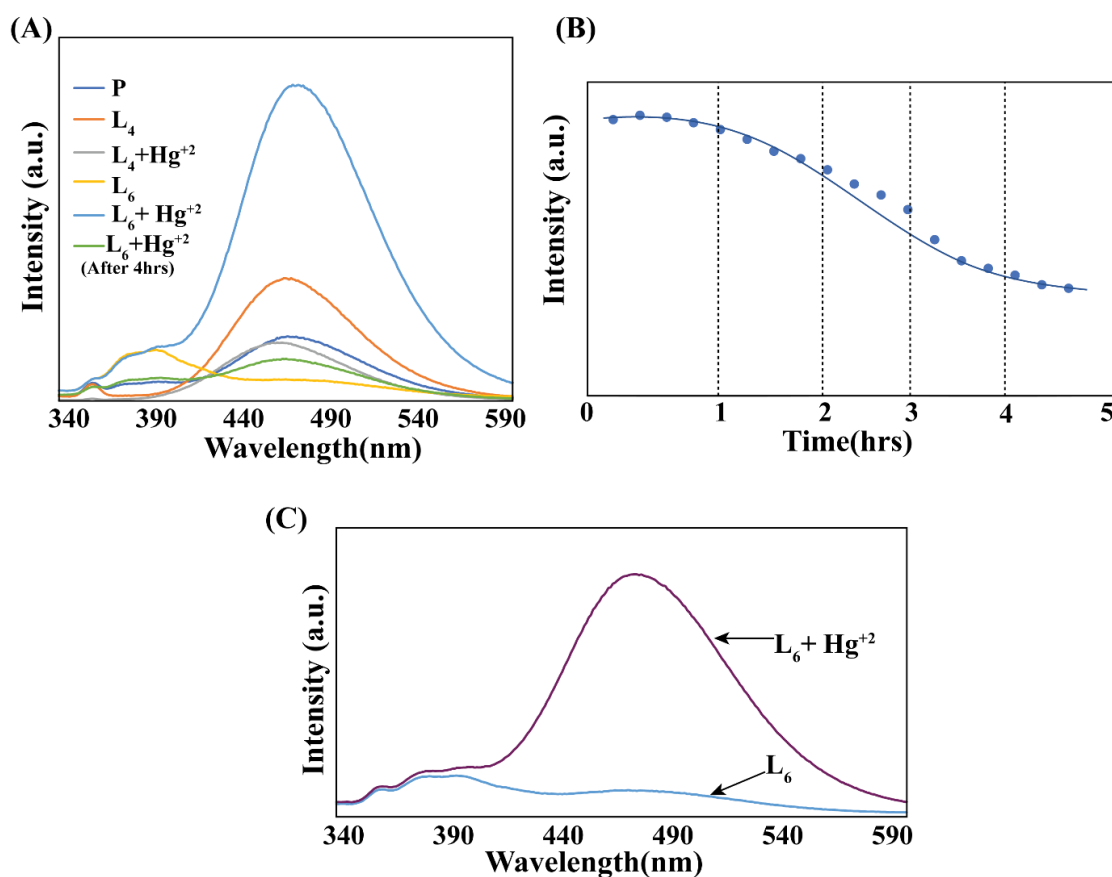


Figure A4B.7: (A) Emission intensity plot of P, L₆, L₄, L₆+Hg²⁺, L₄+Hg²⁺, L₆+Hg²⁺ (after 4hrs). (B) Fall in emission intensity of L₆+Hg²⁺ ensemble in due course time. (C) Depiction of “Turn-On” by self-assembled L₆ (30µM) and addition of Hg²⁺.

Table A4B.1: Quantitative recovery percentage of Hg²⁺ ions from various spiked water samples.

Sl no.	Water Sample	Spiked Hg ²⁺ (µM)	Recovery (%)
1.	Milli-Q [®]	50	100
2.	Drinking	50	85.27
3.	Tap	50	80.67
4.	River	50	76.78

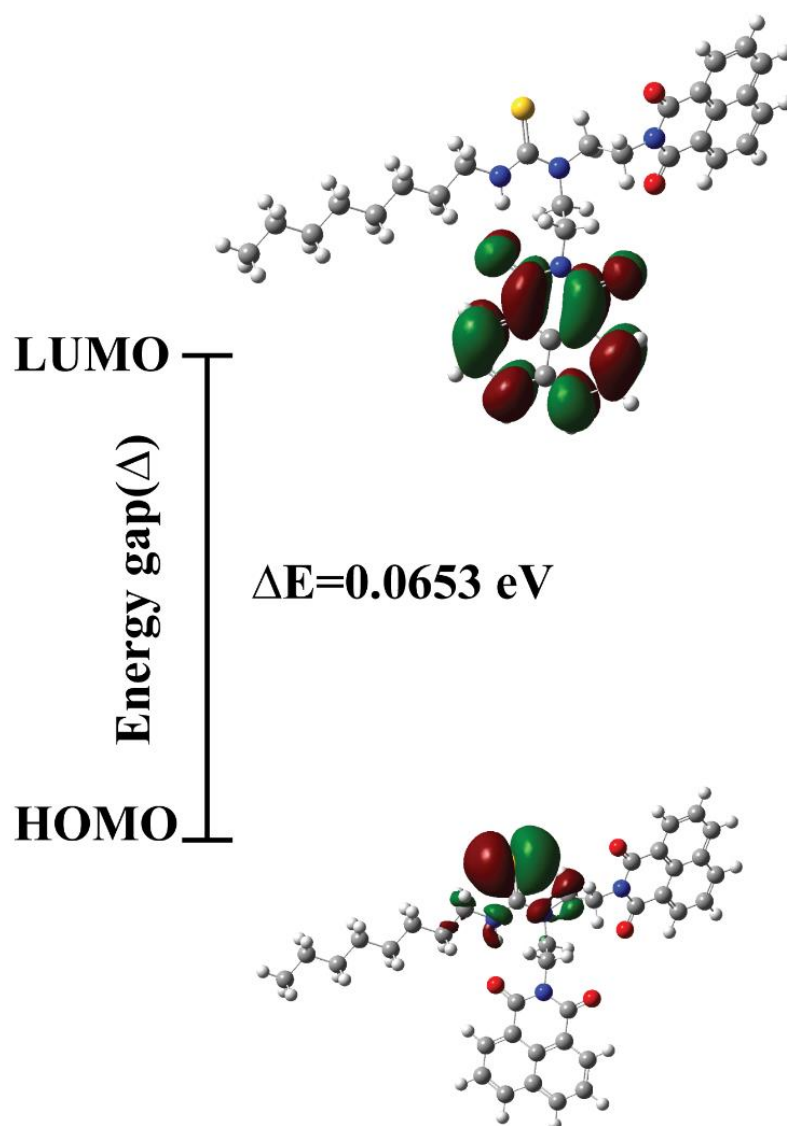


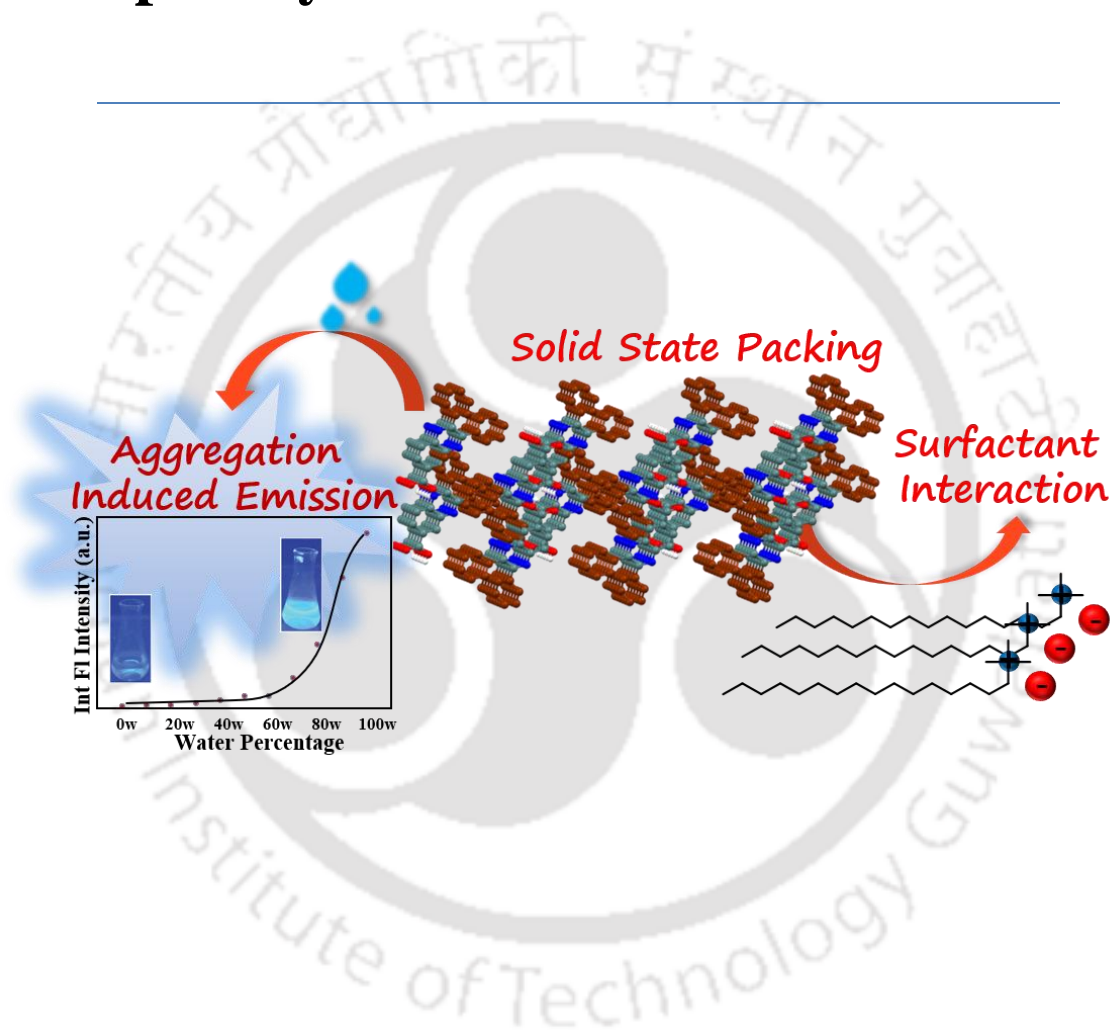
Figure A4B.8: HOMO-LUMO plot of L₆.

Table 2. The comparison of our chemosensor with other reported probes in mercury sensing available in recent literatures.

Sl No.	References	Fluorescence mechanism	Solvent System	LOD (μM)
1.	This work	enhancement	Aqueous HEPES buffer (0.1M, pH 7.4)	0.375
2.	B. K. Rani, S. A. John, <i>J. Hazard. Mater.</i> , 343(2018), pp. 98–106, 10.1016/j.jhazmat.2017.09.028	quenching	$\text{CH}_3\text{CN}:\text{H}_2\text{O}$ (1:1, v/v; pH 7.2)	0.00035
3.	F. Song, C. Yang, X. Shao, L. Du, J. Zhu, C. Kan, <i>Dyes Pigm.</i> , 165(2019), pp. 444–450, 10.1016/j.dyepig.2019.02.054.	enhancement	$\text{EtOH}:\text{H}_2\text{O}$ (1:1, v/v)	0.077
4.	S. Liu, S. Tan, H. Hu, Z. Chen, S. Pu, <i>J. Photochem. Photobiol. A.</i> , 418(2021), 113439, 10.1016/j.jphotochem.2021.113439.	quenching	CH_3CN	4.53
5.	M. Sethupathi, G. Muthusankar, V. Thamilarasan, N. Sengottuvelan, G. Gopu, N.M. Vinita, P. Kumar, F. Perdih, <i>J. Photochem. Photobiol. B, Biol.</i> , 203(2020), 111739, 10.1016/j.jphotobiol.2019.111739.	quenching	$\text{CH}_3\text{CN}/\text{HEPES}$ buffer (2:8, v/v)	0.001
6.	M. Tripathy, U. Subuddhi, S. Patel, <i>Dyes Pigm.</i> , 174(2020), 108054, 10.1016/j.dyepig.2019.108054.	enhancement	Methanol- H_2O (4:1 v/v)	7.5
7.	H. Mohammad, A. S. M. Islam, C. Prodhan, M. Ali, <i>New J. Chem.</i> , 43(2019), 5297, 10.1039/C8NJ05418E.	enhancement	10 mM HEPES buffer at pH 7.2	1.24
8.	E. G. C. Ergun, <i>New J. Chem.</i> , 45(2021), 4202, 10.1039/D1NJ00085C.	quenching	Water	40.00
9.	J. R. Lavado, A. Lorente, E. Flores, A. Ochoa, F. Godoy, P. Jaque, C. Saitz, <i>RSC Adv.</i> , 10(2020), 21963, 10.1039/D0RA04092D.	enhancement	$\text{CH}_3\text{CN}/\text{DMSO}$ (99 : 1)	0.00811
10.	S. Xue, P. Wang, K. Chen, <i>Spectrochim. Acta A Mol. Biomol. Spectrosc.</i> , 226 (2020), 117616, 10.1016/j.saa.2019.117616.	quenching	HEPES buffer (20.0 mM, pH 7.4)	0.00759

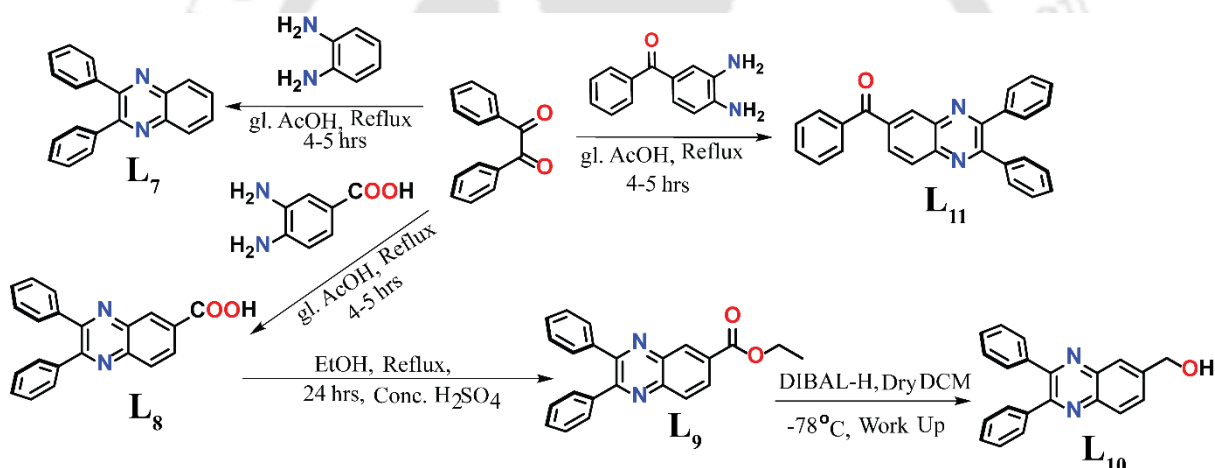
CHAPTER 5

Disaggregation of Quinoxaline derived AIEgen by Surfactants: Aggregation Propensity in Solid and Solution States



5.1 Background and focus of the chapter

Application of AIEgen in pollution control, handling and monitoring and dealing with complex organics is necessary and important. Large-scale environmental and public health issues are being created by the growing release of unwanted pollutants such as surfactants, personal care products, medicines, and colours into wastewater as a result of industrial development and population expansion. Several of them contain complex organics, which are challenging to remove using traditional management methods. Surfactants or surface-active agents, which are frequently utilised in industrial and household activities due to their amphiphilic features such as foaming, dispersion and solubilisation effects, have become a significant environmental problem.^{5.1-5.2} Rapid and sensitive surfactant detection is gaining importance, as surfactants not only pollute water but also have an impact on human health. Surfactants are one of the most challenging rising toxins that are continually released into the environment by wastewater treatment facilities.^{5.3-5.4} Surfactants are molecules that minimize interfacial energy and make other pollutants more soluble in water.^{5.5}



Scheme 5.1: Synthetic route for **L7**, **L8**, **L9**, **L10**, and **L11**.

5.2 Crystallographic description

Suitable crystals were obtained by slow evaporation technique from CHCl_3 -MeOH solvent layering and DMSO for **L8** only. **L7** crystallized into orthorhombic, space group $Pca2_1$ and the structural analysis stated the existence of eight probes in the asymmetric unit ($Z = 8$). **L7** assembles in a one-dimensional interdigitated fashion and $\pi-\pi$ interaction was prevalent which was measured to be 3.283 Å, (Figure A5.1 (A & B), A5.2A, SI). **L8** crystallized in Triclinic, space group $P\bar{1}$. The structural study specified the existence of two centrosymmetric probes in the asymmetric unit ($Z = 2$). Both H-bonding and $\pi-\pi$ interaction is present in the solid state. The H-bonding existed between the electronegative carboxylic acid oxygen and hydrogen and it was

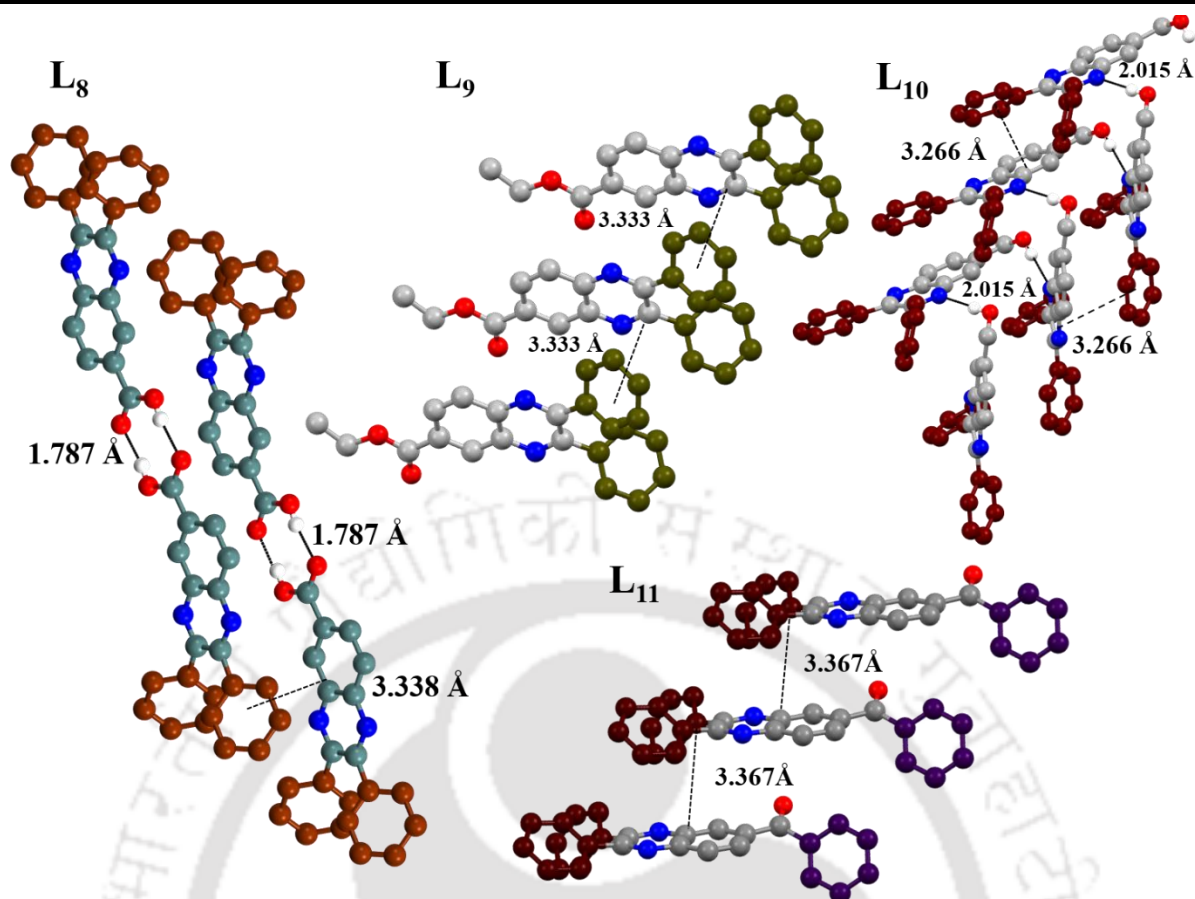


Figure 5.1: Representation of Non-Covalent interaction in solid state **L₈**, **L₉**, **L₁₀**, and **L₁₁**.

measured to be 1.787 Å. The π — π interaction was found to be 3.338 Å. The packing of **L₈** in a solid state was 1D and seemed to stair-like arrangement when viewed from the b-axis (Figure 1, 2(A), S12B, SI). **L₉** crystallized in Monoclinic, space group: P 21/n while the structural analysis detailed the existence of four probes in the asymmetric unit ($Z = 4$). In the solid-state packing, there existed only π — π interaction which is 3.333 Å in size. **L₉** assembled in 1-D manner and wave-like or open book assemblies in the solid state (a-axis), (Figure 5.1, 5.2(C), A5.3C, SI). **L₁₀** crystallized in monoclinic, space group P 21/n and there are four probes in the asymmetric unit ($Z = 4$). Two types of interactions are visible in **L₁₀**. The H-bond and π — π interaction were measured to be 2.015 Å and 3.266 Å respectively. Interestingly, when viewed from the c-axis, **L₁₀** is oriented almost in a double helical structure similar to the DNA helix, (Figure 5.1, 5.2(B), A5.2D, SI). **L₁₁** crystallized in monoclinic, space group P 21/n. The only interaction found to be π — π interaction, measured to be 3.367 Å. **L₁₁** is also assembled in 1-D and wave-like or open-book alignment (a-axis), (Figure 5.1, 5.2(D), A5.2E, SI).

5.3 Photophysical studies

These synthesized compounds are studied under absorption spectroscopy. The compounds displayed absorption maxima around 350 nm to 380 nm using water as solvent (Figure A5.A).

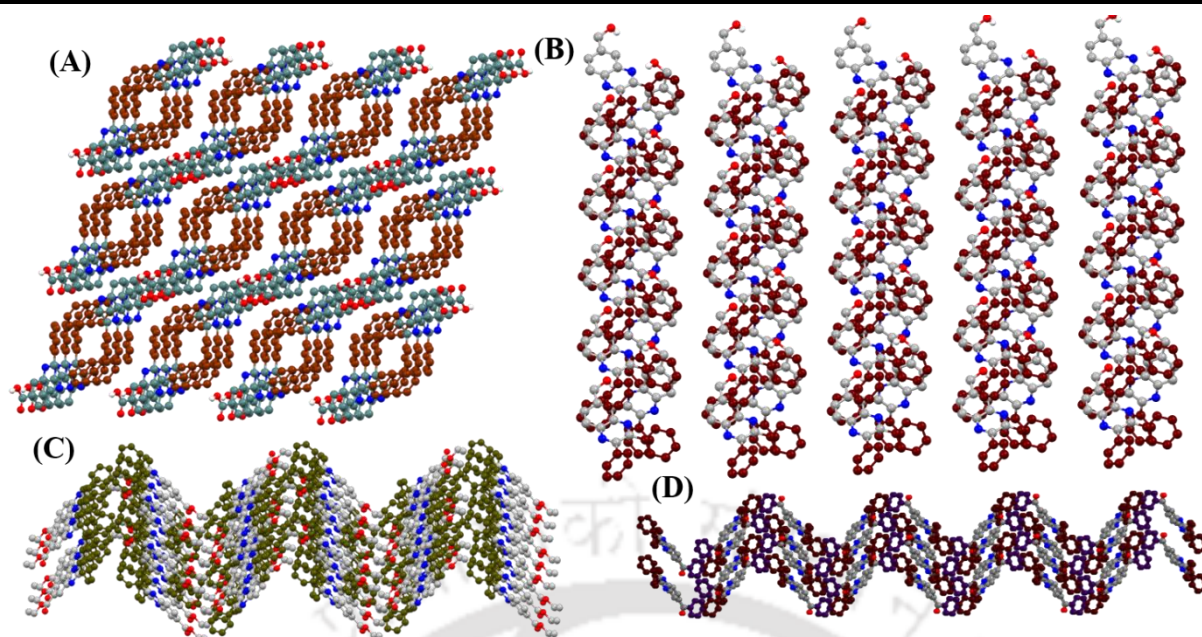


Figure 5.2: Representation of packing arrangement of (A) **L₈** viewed from the b-axis (B) **L₁₀** viewed from the a-axis (C) **L₉** viewed from the c-axis (D) **L₁₁** viewed from the a-axis.

The compounds are excited at 350 nm in emission spectroscopy in water to compare the results (Figure A5.B). As per our proposition, they were subjected to aggregation studies under emission spectroscopy. A miscible binary solvent mixture was selected i.e.; THF-water. Here, THF acts as a good solvent whereas water acts as an anti or poor solvent. An AIEgen (aggregation-induced emission-gen) remains solvated and displays poor spectra in the organic or good solvent while it becomes emissive with the gradual addition of an anti-solvent. This notion is reflected in our synthesized congeners. **L₇**, **L₈**, **L₉**, **L₁₀**, and **L₁₁** remained solvated and exhibited poor spectra in THF while the emission intensity rose at various stages and extents individually, on the addition of water. **L₇**, **L₈**, **L₉**, and **L₁₀** showed a rise in fluorescence intensity after the addition of 60% of water and a steep increase in emission intensity after 80% of water. The emission intensity of **L₇**, **L₈**, **L₉**, and **L₁₀** rises abruptly when $f_w > 80\%$, and at this point, the luminogen aggregates. All of them displayed the highest emission intensity in 100% water. Thus, we confirm them as AIEgens. In the case of **L₅** scenario is somewhat different. **L₁₁** displays a fall in emission intensity when $f_w > 80\%$, indicating that the aggregated species exhibits a kind of insolubility in higher aqueous content (Figure 5.3 & Figure A5.5(A)). Probing further into the size and morphology of the aggregates dynamic light scattering experiments and Field Emission Scanning Electron microscopy were carried out. FESEM analysis of the aggregates in water showed varied morphology and size in each case. **L₈** aggregated into grain-like particles ranging from 233.5 nm

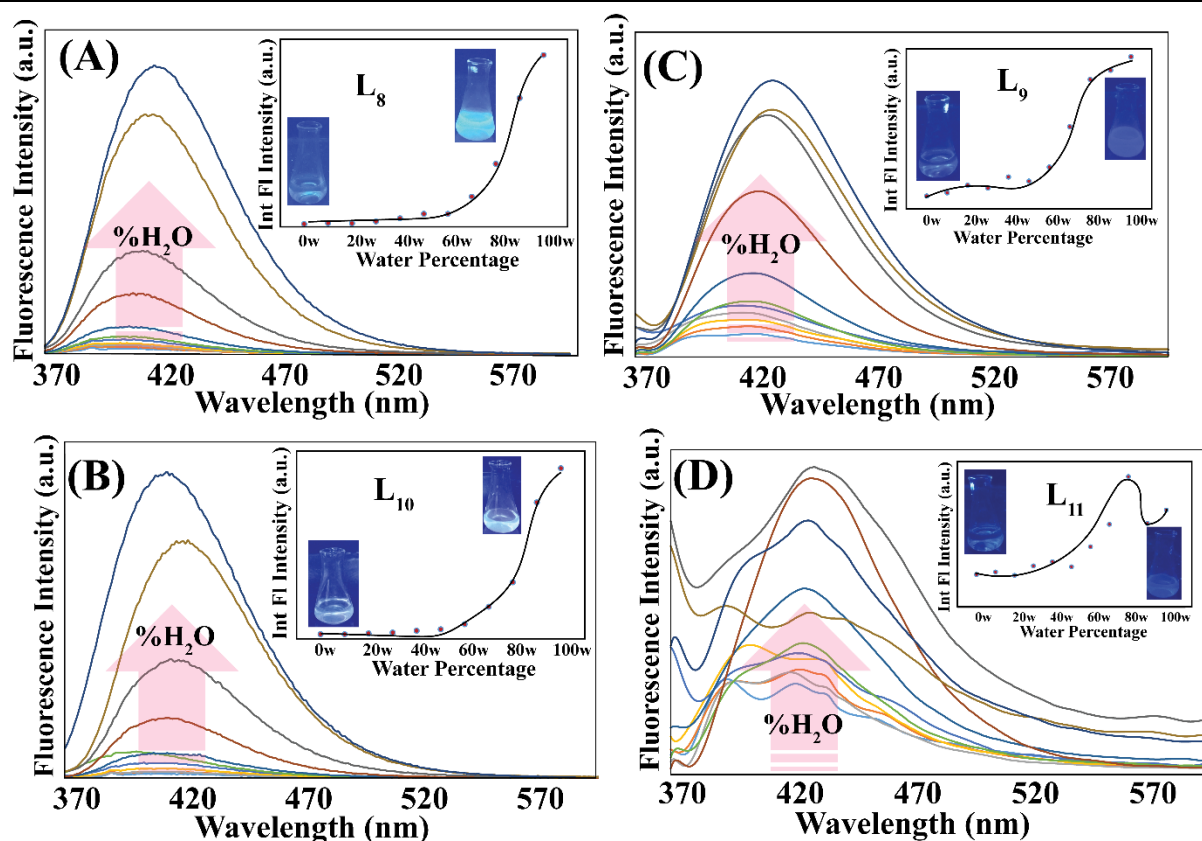


Figure 5.3: Emission spectra of (A) **L**₈, (B) **L**₉, (C) **L**₁₀, and (D) **L**₁₁ with varying water percentages in THF medium. (Inset: Spectral profile depicting the emission intensity variation with water, glass vials containing respective compounds in 0% & 100% water)

to 724.4 nm while the ester derivative, **L**₉ resulted in splint-like shapes (13.23 μm \times 1.527 μm). In the case of **L**₁₀, the long flakes (5.705 μm \times 1.020 μm) accumulated to form a spindle whereas **L**₁₁ aggregated into cilia shapes (1.838 μm \times 382 nm), (Figure 5.4 & A5.5B). The DLS output reveals the hydrodynamic radii of the aggregates in 100% water i.e.; **L**₇-172.1, **L**₈-352.8, **L**₉-312.4, **L**₁₀-236.7, and **L**₁₁-238.2(d. nm) (Figure A5.7(A)).

5.4 Surfactant Interaction

Rapid and sensitive surfactant detection is gaining importance, as surfactants not only pollute water but also have an impact on human health. Surfactants are one of the most challenging rising toxins that are continually released into the environment by wastewater treatment facilities³⁰⁻³². Surfactants are molecules that minimize interfacial energy and make other pollutants more soluble in water³³.

Here, we have targeted to analyze the disaggregation process in presence of surfactant. This interaction leads to chemo sensing of the molecule. **L**₈, bearing a carboxylic acid group (-COOH) holds a probability of existing as an anionic species in water so ensuring a chance to interact with

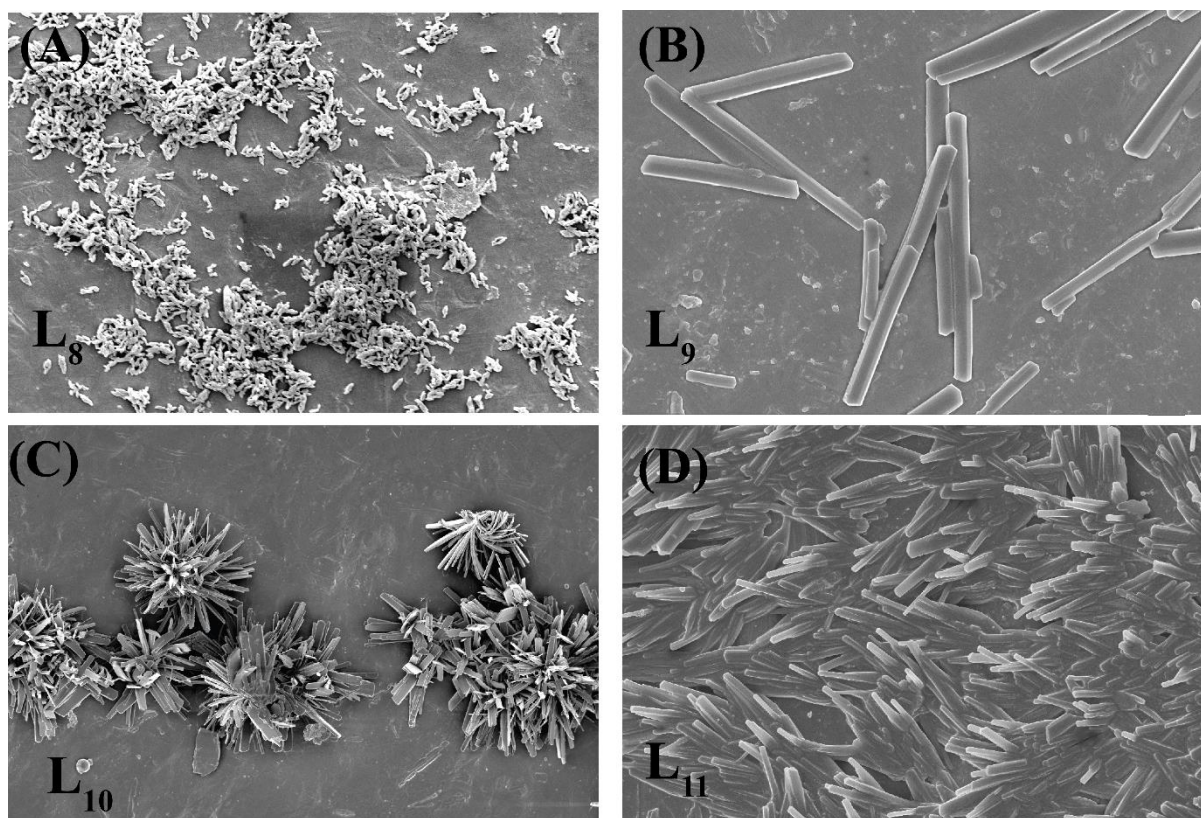


Figure 5.4: FESEM images of (A) L_8 , (B) L_9 , (C) L_{10} , and (D) L_{11} in water.

cationic surfactant viz; Cetyltrimethylammonium ammonium bromide (CTAB). Based on our scheme, we tested all the congeners with CTAB through emission spectroscopy (Figure 5.5A). Interestingly, L_8 only responded to CTAB via fluorescence quenching. The quenching can be attributed to the disaggregation of the aggregated AIEgen. For affirmation, we tried an anionic amphiphile (Sodium dodecyl sulfate), a neutral amphiphile (Triton X-100), and Tetrabutylammonium bromide (TBABr). These control analytes did not show any change in fluorescent intensity (Figure 5.5 B). Furthermore, we can affirm both the length and charge of the tried amphiphile are essential for the disaggregation process. We performed titration of L_8 with CTAB in water and monitored at 426 nm (Figure S5.17(A)). From the titration, we were able to deduce the Limit of Detection (LOD) by applying $3\sigma/k$ (where k is obtained from Figure A5.8(B)). The L.O.D. was determined to be $0.219 \mu\text{M/mL}$ (Figure A5.8(B)). We measured the hydrodynamic radii of the aggregated particles before and after the addition of anionic surfactant. There was a fall in the radii from 352.8 to 75.98 d. nm upon the addition of CTAB (Figure A5.7, (A)). FESEM image analysis shows the complete disintegrated rice-grain shapes. Upon the addition of CTAB, we did not notice any defined morphology in the images (Figure 5.5D). All this experimentation hints towards the disaggregation of AIEgen which can be further utilized in chemo sensing of surfactant.

Detection ability of in real water sample is important. Effluents from multiple sources were taken: Domestic wastewater, wastewater from Petroleum refinery and Brewing industry. These samples were filtered to remove any suspended particles or solids and used directly without any other further chemical treatment. L_8 ($10\ \mu\text{M}$) added to the collected water effluent and fluorescence emission intensity was recorded before and after addition of increasing concentration of CTAB ($50\ \mu\text{g/ml}$, $100\ \mu\text{g/ml}$, $150\ \mu\text{g/ml}$) (Figure 5.5(C)). Fluorescence quenching in all the cases ascertained the sensing process via disaggregation in all extreme and actual conditions.

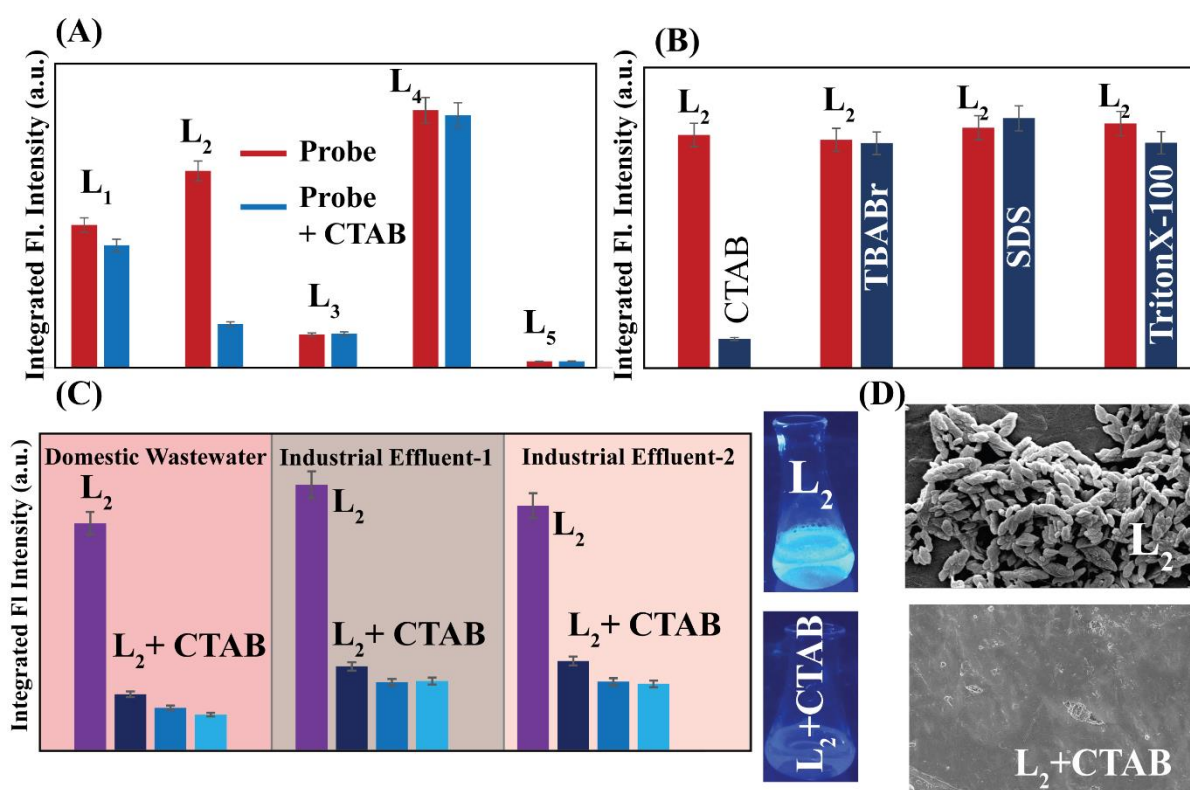
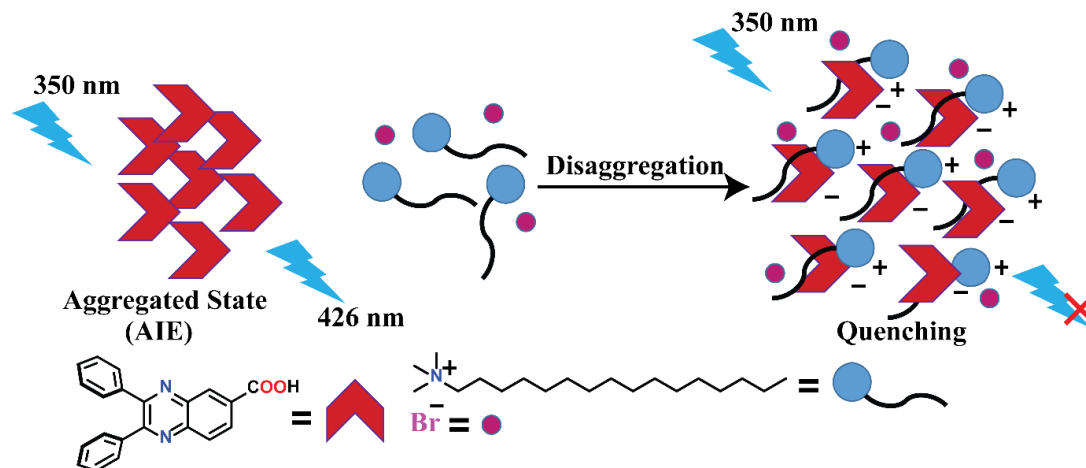


Figure 5.5: (A) Bar diagram representing integrated fluorescence intensity with probe ($10\ \mu\text{M}$) and CTAB ($50\ \mu\text{g/mL}$) in water. (B) Bar diagram representing integrated fluorescence intensity with probe ($10\ \mu\text{M}$) and other competitive analytes. (C) Bar diagram representing quenching of fluorescence intensity after addition of CTAB solution to L_8 in various effluents, Glass vials containing an aqueous solution of L_8 in the absence and presence of CTAB (D) FESEM image of L_8 before and after the addition of CTAB.

The proposed L_8 is used for specificity and high sensitivity in monitoring CTAB in freshwater samples. A standard addition method was used to detect CTAB in Milli-Q[®] water, drinking water, tap water, Lake water, and Brahmaputra River water to further examine the probe's applicability. Water sample tests were carried out with the CTAB concentration of $50\ \mu\text{g/mL}$ spiked in each sample along with L_8 ($10\ \mu\text{M}$). In the above-stated water samples, 77.04, 77.59, 81.15, 83.89, and 80.78 % respectively fluorescence quenching of L_8 was observed with the addition of targeted

cationic amphiphile (Figure S16B, SI). These experiments help in the detection of CTAB in environmental water samples, shown to be reliable and practicable.

We tried to visualize the disaggregation process in presence of CTAB. As CTAB approaches the aggregated state, due to inherent length and charge it interacts with each anionic carboxylic acid group. Thus, electrostatic interaction overpowers and causes disaggregation (Scheme 2).



Scheme 2: Plausible mechanism of disaggregation process.

5.5 Conclusion

To round up, we have synthesized propellor-shaped quinoxaline motifs with a change in the functional group. A comprehensive and comparative aggregation study from the solid to solution phase has been demonstrated. These congeners displayed aggregation-induced emission in water, on solvent switching. Further, **L8** selectively interacts with a cationic amphiphile CTAB through quenching of fluorescence and disaggregation. This prospect brings analytical and environmental importance to our piece of work.

References

- 5.1. B. Mondal, A. Adak and P. Datta, Effect of operating conditions and interfering substances on photochemical degradation of a cationic surfactant, *Environ Technol.*, 2018, **39**, 2771-2780.
- 5.2. S. Koner, A. Pal and A. Adak, Utilization of silica gel waste for adsorption of cationic surfactant and adsolubilization of organics from textile wastewater: a case study. *Desalination*. 2011, **276**,142–147.
- 5.3. Bioconcentration of Several Series of Cationic Surfactants in Rainbow Trout, Amelie Kierkegaard, Marcus Sundbom, Bo Yuan, James M. Armitage, Jon A. Arnot, Steven T. J. Droge, and Michael S. McLachlan, *Environ. Sci. Technol.*, 2021, **55**, 8888–8897.
- 5.4. Metal–Organic Framework as a Chemosensor Based on Luminescence Properties for Monitoring Cetyltrimethylammonium Bromide and Its Application in Smartphones, Zhe Sun, Yu Ling, Shi Gang Liu, Yu Zhu Yang, Xiao Hu Wang, Yu Zhu Fan, Nian Bing Li, and Hong Qun Luo, *Inorg. Chem.*, 2019, **58**, 8388–8395.
- 5.5. Environmental behaviour and ecotoxicity of cationic surfactants towards marine organisms, O. Kaczerewska, R. Martins, J. Figueiredo, S. Loureiro and J. Tedim, *J. Hazard. Mater.*, 2020, **392**, 122299.

Appendix - Chapter 5

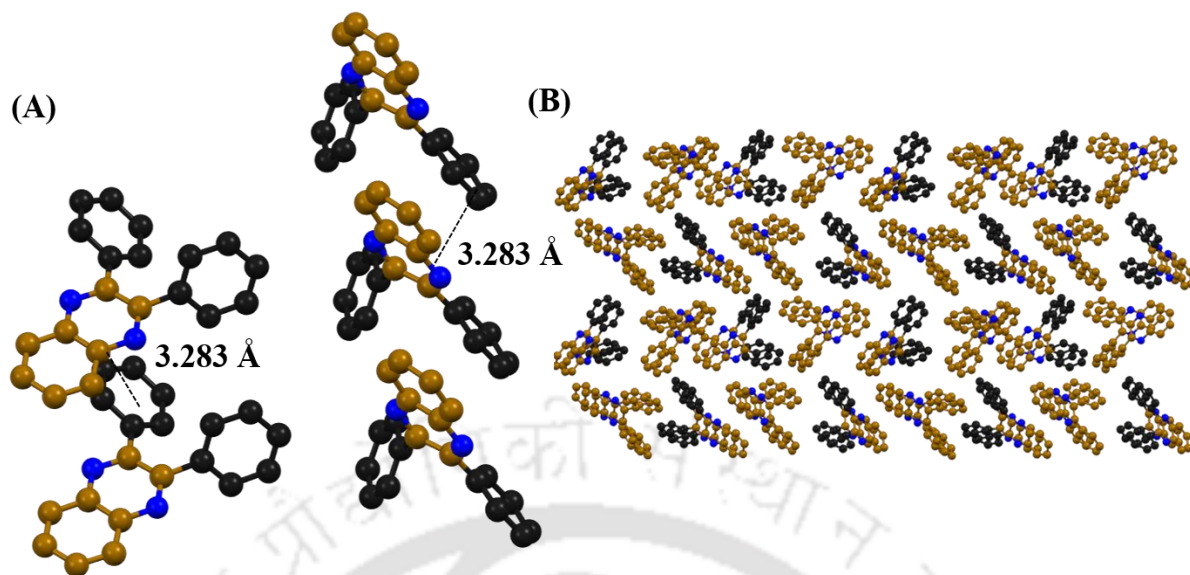


Figure A5.1: (A) Ligand-ligand interaction (B) Packing arrangement of **L7** in solid state.

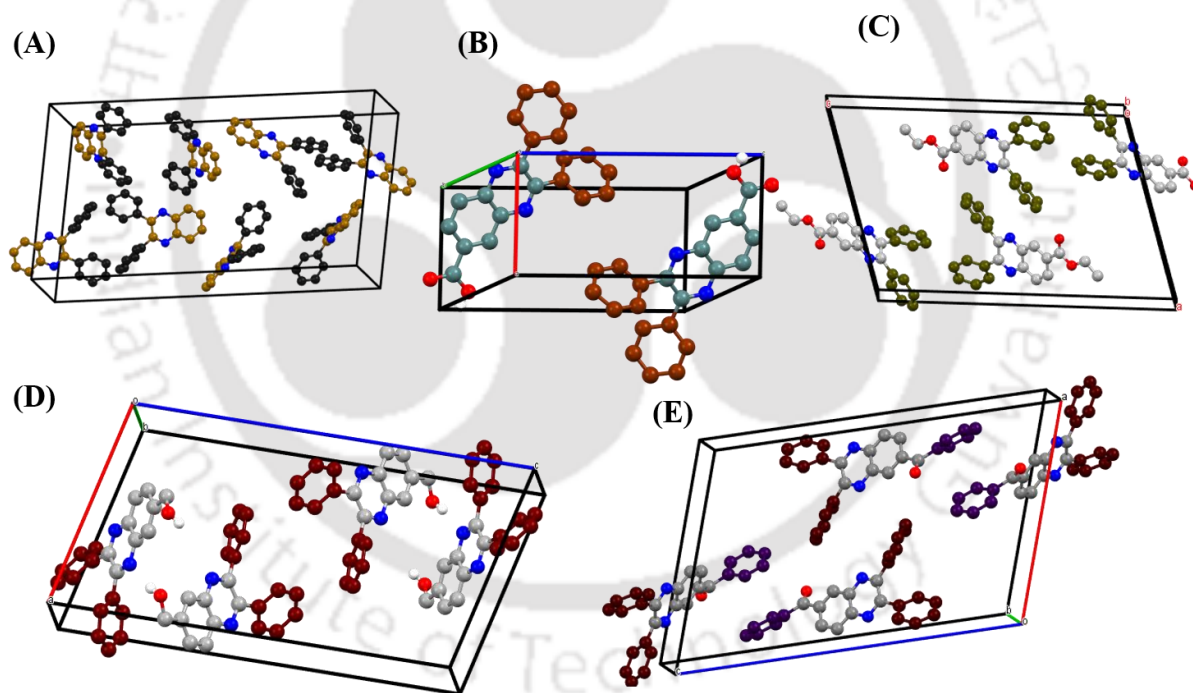


Figure A5.2: Unit packing diagram (Z values) for **L7**, **L8**, **L9**, **L10** & **L11**.

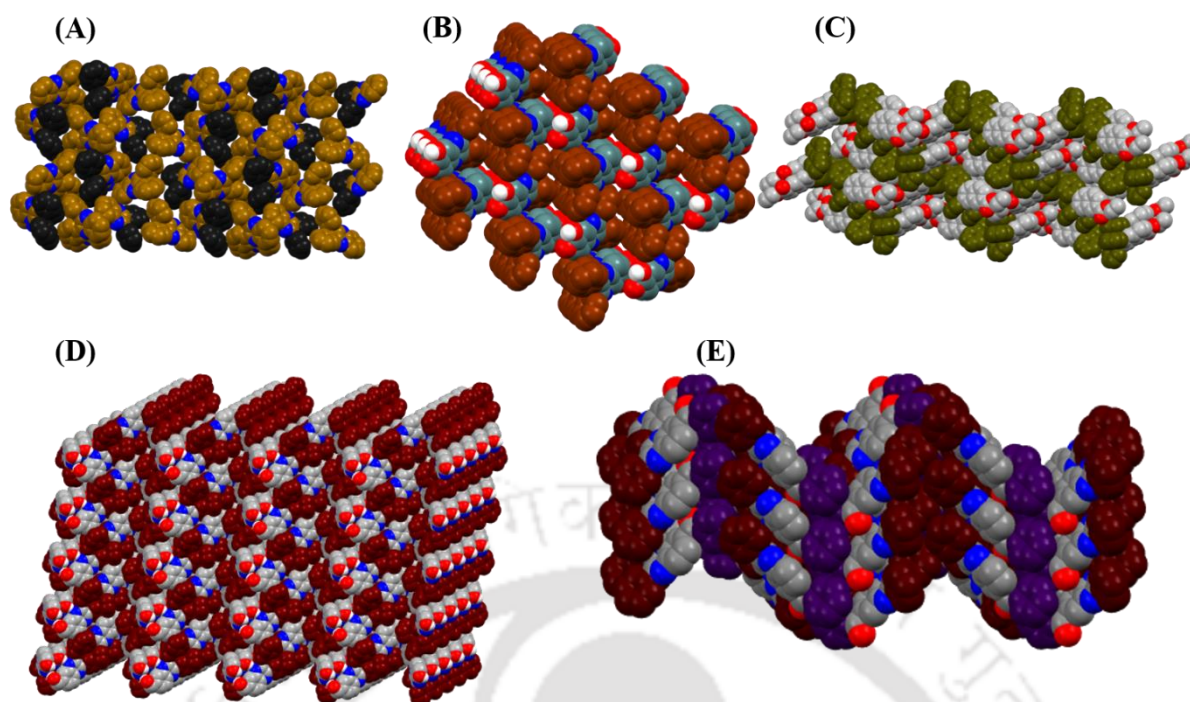


Figure A5.3: Space fill diagram for (A) L_7 , (B) L_8 , (C) L_9 , (D) L_{10} & (E) L_{11} .

Table A5.1: Hydrogen bonding distances (\AA) and Bond angles ($^\circ$) in L_8 & L_{10} .

Compound	D-H \cdots A	d(D \cdots H)/ \AA	d(H \cdots A)/ \AA	d(D \cdots A)/ \AA	\angle D-H \cdots A/ $^\circ$	Symmetry codes
L_8	O24--H24 \cdots O25	0.82	1.79	2.593 (4)	167	2-x, 2-y,-z
	C7--H7N \cdots O24	0.93	2.42	2.736 (5)	167	
L_{10}	O24—H15 \cdots N1	0.82	2.01	2.825(3)	170	3/2-x, -1/2+y,1/2-z
	C20—H11 \cdots O24	0.93	2.53	2.853(3)	100	

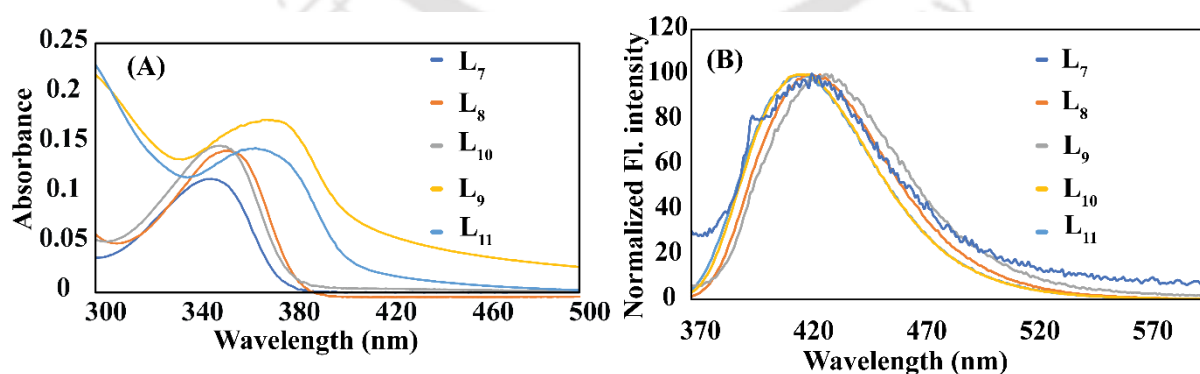


Figure A5.4: (A) UV-vis spectra of L_7 , L_8 , L_9 , L_{10} & L_{11} in water. (B) Emission spectra of L_7 , L_8 , L_9 , L_{10} & L_{11} congeners in water.

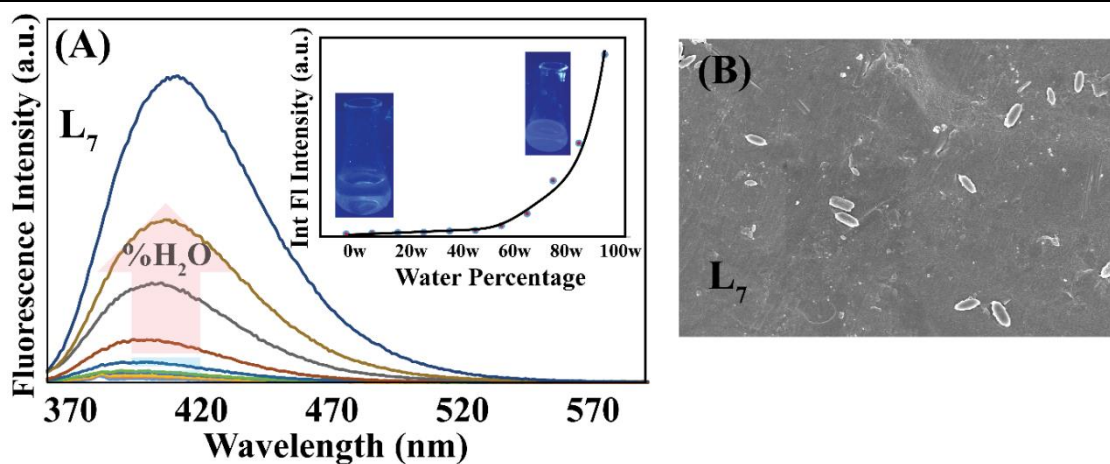


Figure A5.5: (A) Emission spectra of L₇ depicting AIEgenic behaviour. (B) FESEM image of L₇ in water.

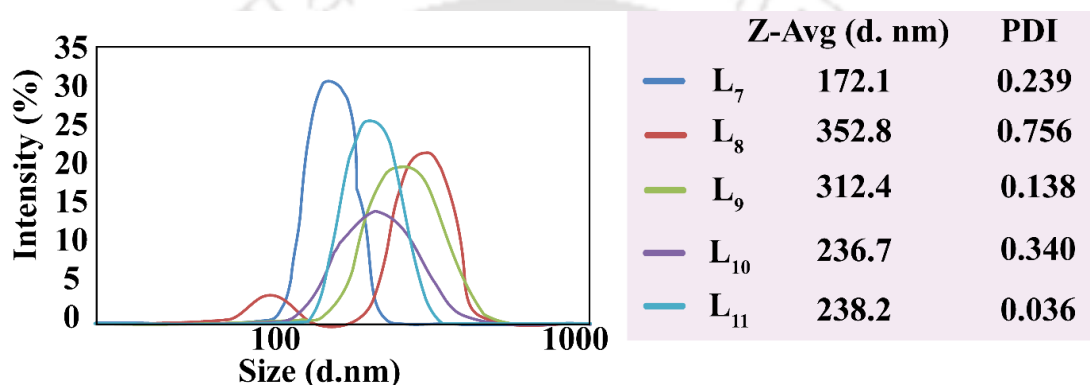


Figure A5.6: DLS output of L₇, L₈, L₉, L₁₀ & L₁₁.

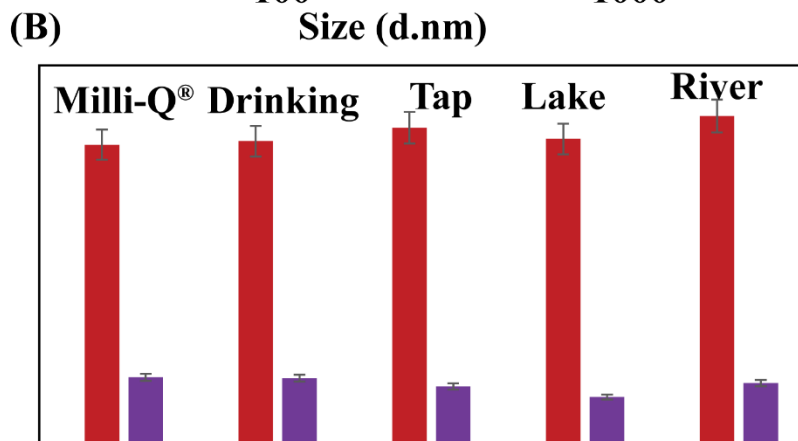
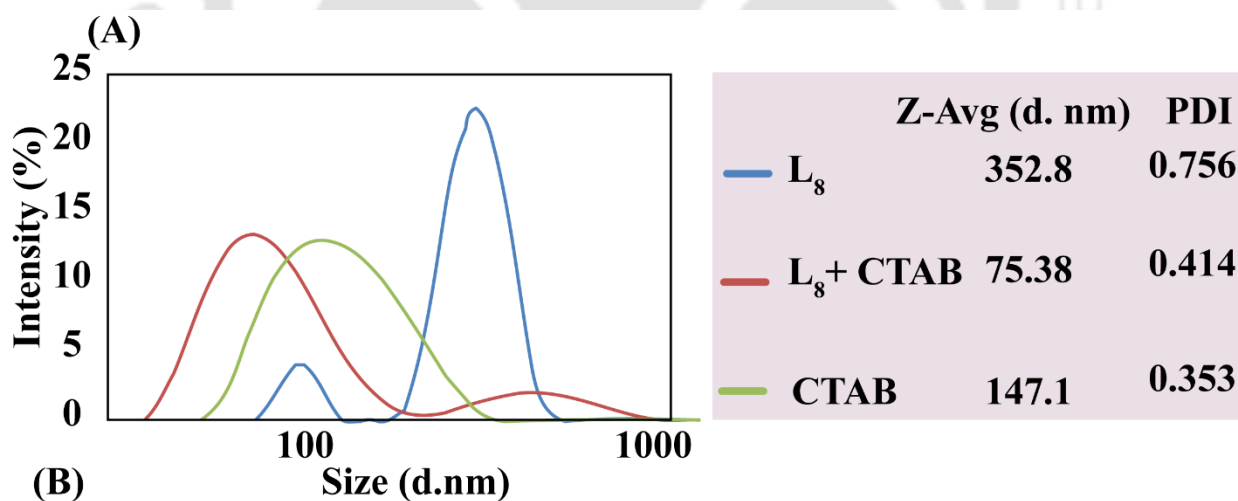


Figure A5.7: (A) DLS output of L_8 in presence and absence of CTAB. (B) Real water samples as a medium for chemo sensing of CTAB with L_8 .

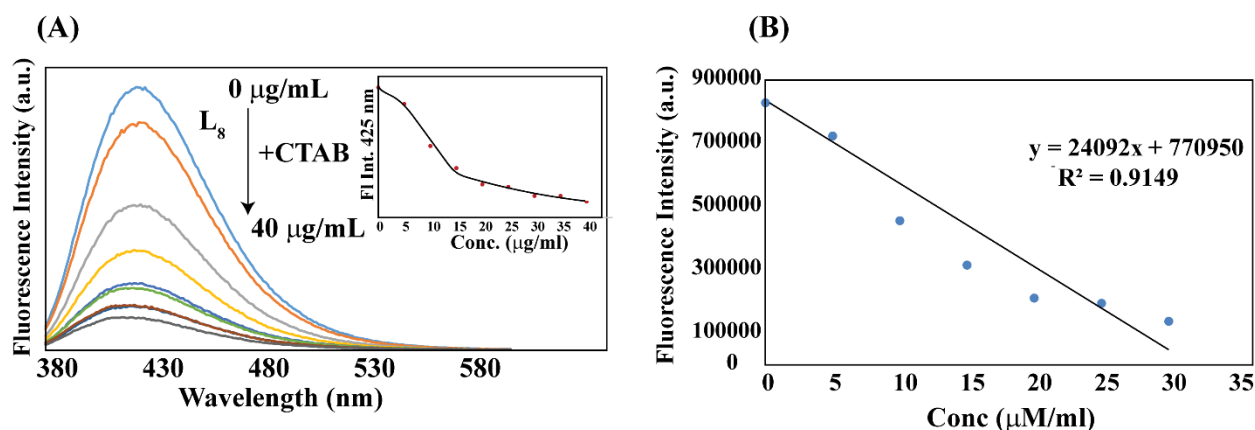


Figure A5.8: (A) Emission spectra of titration with the gradual addition of CTAB, (inset: Graph depicting fall in fluorescence intensity w.r.t increase in CTAB concentration (B) Plot from the titration and determination of slope for L.O.D. calculation.

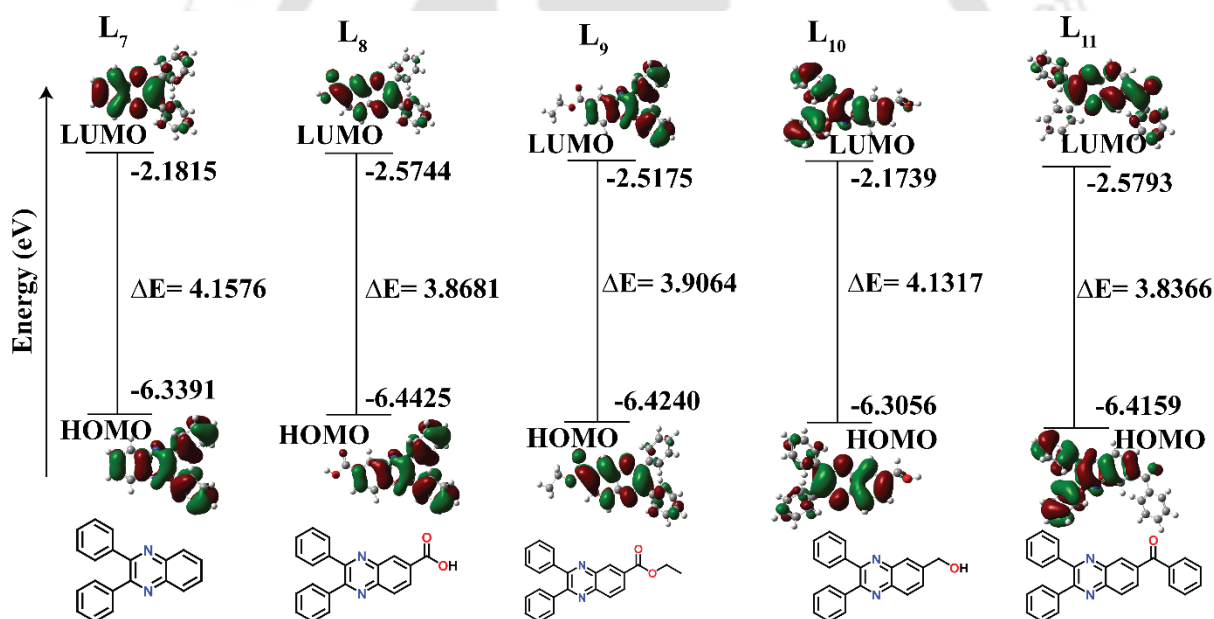
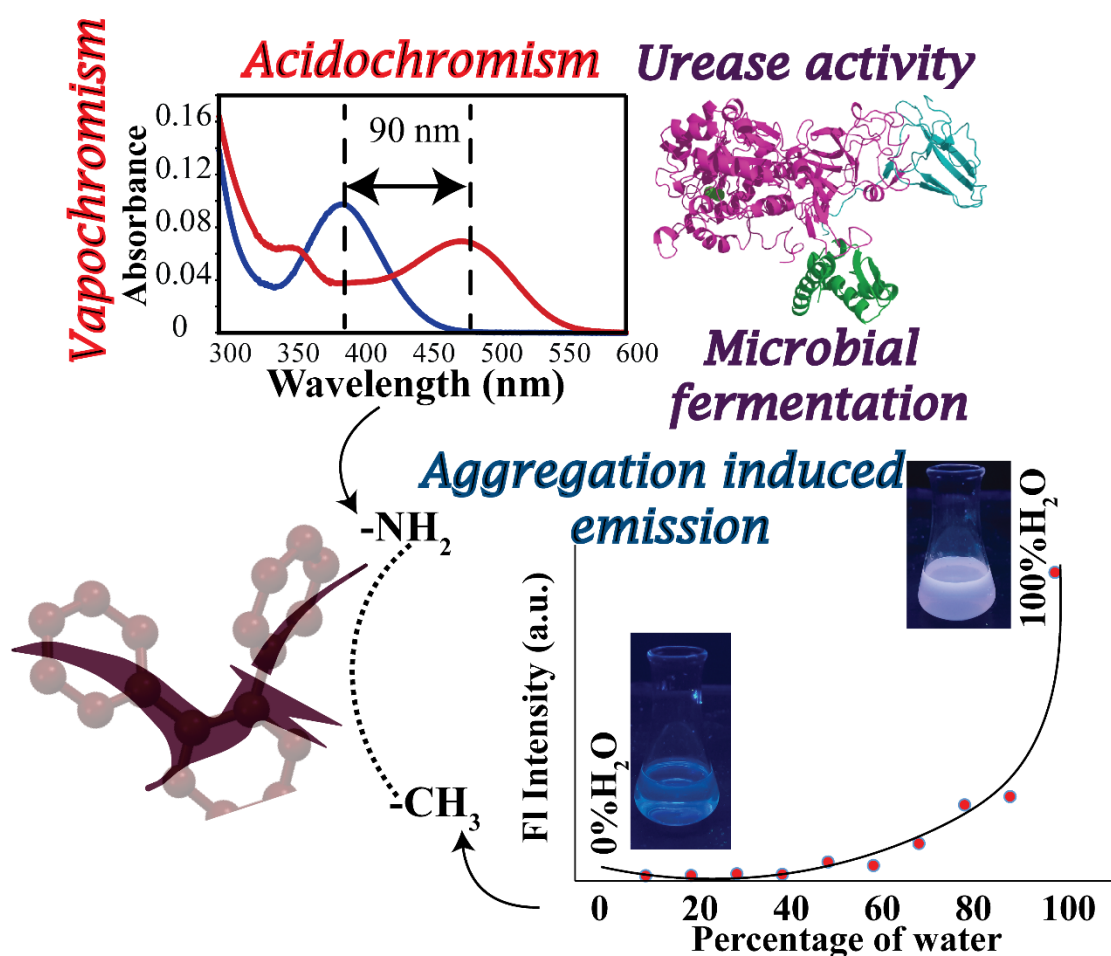


Figure A5.9: Output of DFT calculation on L_7 , L_8 , L_9 , L_{10} & L_{11} , Density functional theory (DFT) calculations were calculated with the B3LYP/6-31G(d,p) method basis set using the Gaussian 09 program. The CPCM solvent model has been implemented using water as a solvent during calculation.

CHAPTER 6

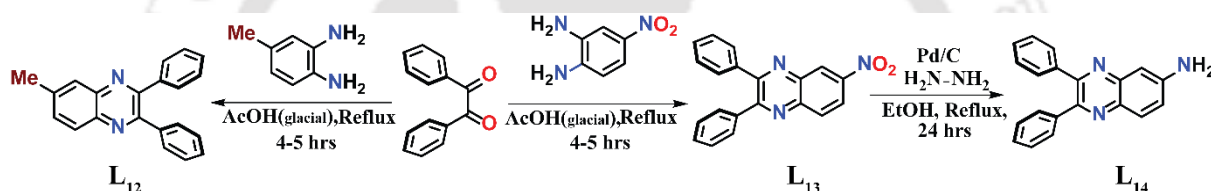
The aggregation and optical properties of a Quinoxaline scaffold as an acidochromic and solvatochromic urease tracker



6.1 Background and focus of the chapter

The foundation of material design has always been the interplay between composition, structure, and properties.^{6.1-6.3} Intermolecular interactions are critical for many photophysical properties of chromophores. Realizing this interaction enables one to grasp the relationship between structure and features and makes major advancements possible in areas like luminescence, and sensing and allows the creation of advanced materials.^{6.4-6.7}

Stimuli-responsive materials are abundant in living systems and play a crucial role in the survival of life and the maintenance of biological function. Scientists have created a variety of stimuli-responsive molecular frameworks to mimic nature. These smart molecular frameworks can change their chemical and/or physical characteristics in response to single or multiple external stimuli such as temperature, pH, mechanical force, light irradiation, and specific analytes (ions, gases, bioactive molecules, etc.). These findings lead to the development of efficient advanced materials. Tracking pH is crucial for environmental monitoring, cell metabolism, and chemical process control.^{6.8-6.9}



Scheme 1: Synthesis route for L₁₂, L₁₃, and L₁₄.

6.2 Crystallographic evidence

The suitable crystal for single-crystal X-ray analysis of the quinoxaline derivative, L₁₂ was gotten from the CHCl₃-MeOH mixture, and it crystallized in the monoclinic space group P 21/c. The structural examination revealed the existence of four symmetrical probes in the asymmetric unit ($Z = 4$). Observation from the crystal structure reveals (Figure 6.1), there occur several CH $\cdots\pi$ interactions (measured distances ranging from 2.84-2.85 Å) between phenyl rings, aromatic hydrogen as well as methyl hydrogen. Figure 6.1(C) depicts well-organized zig-zag packing and the adhered phenyl ring are in propellor orientation.

6.3 Photophysical studies

The experimentation on the photophysical properties of L₁₂, L₁₃, and L₁₄ regarding absorption studies was carried out in various solvents. In THF, L₁₂, L₁₃, and L₁₄ showed a peak at 358 nm, 365 nm and 404 nm respectively. Among all the compounds the photophysical properties of L₁₄ were found to be strongly influenced by solvent polarity. L₃ exhibited solvatochromism, unlike the other two congeners. Both absorption and emission spectral studies were probed to understand

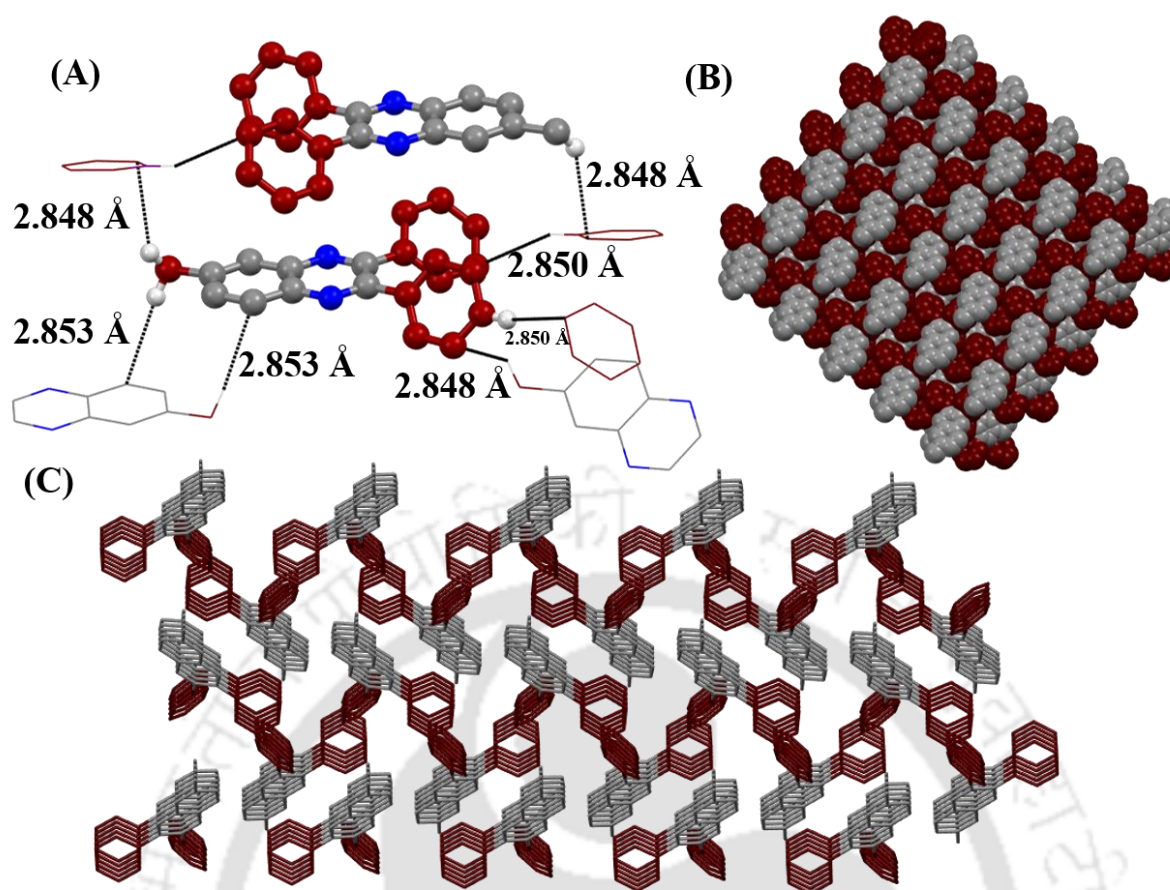


Figure 6.1: (A) Non-covalent interactions between ligand **L12** (B) Space-filled model view of **L12** (C) Packing diagram of **L12**, as seen along the crystallographic a-axis.

solvatochromism. Interestingly, a positive solvatochromic behaviour of **L14** was noted from the UV-vis spectra. In Toluene, **L14** displayed absorbance maxima at 393 nm, which steadily shifted to 415 nm in DMSO, a high-polarity solvent. To deal with solvatochromism regarding emission spectra, we obtained similar shifts in wavelength. **L14** showed an emission maximum of around 469 nm in Toluene, and it slowly shifted to 506 nm in a high-polarity solvent, DMSO. On contrary, **L12** and **L13** displayed no solvatochromic behaviour. We perceive that the $-\text{NH}_2$ functional group in **L14**'s molecular framework is responsible for the solvatochromic shifts. The labile lone pair of $-\text{NH}_2$ interacts with the solvent's polarity, leading to changes in energy levels and spectral shifts. Another result is to be noted, where emission spectral outcome of **L12**, **L13**, and **L14** was excited in water as solvent and there was almost 52 nm shift between **L1** and **L3** (Figure A6.1(A)). **L13** was non-emissive. **L13** displayed no optical response and poor spectra so it was left out. This arises due to the presence of electron-withdrawing $-\text{NO}_2$ group with activates the PET process in molecular framework and fluorescence is quenched. Therefore, we did not proceed further with **L13** which has poor optical characteristics. This suggests optical property tuning of molecular framework with modulation in functional group.

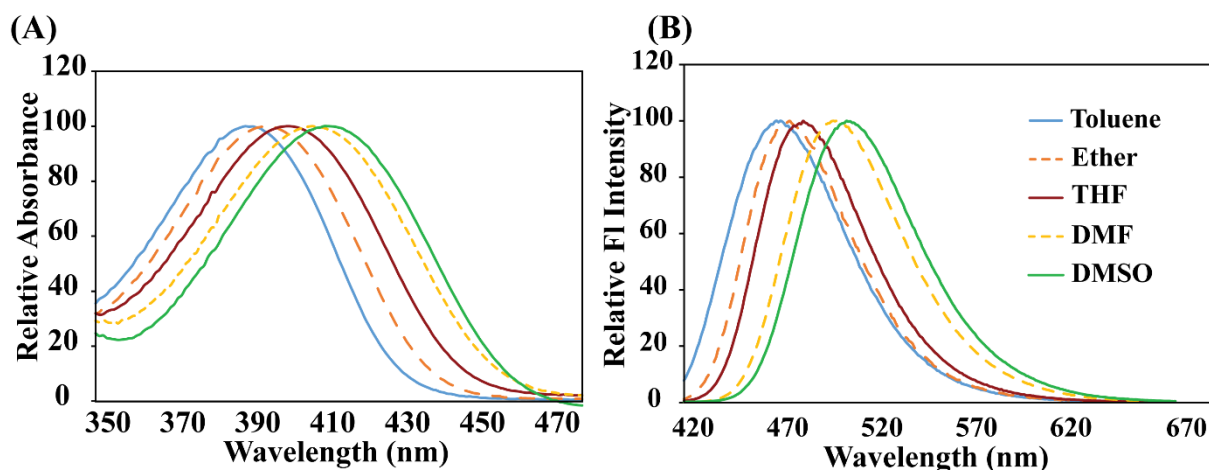


Figure 6.2: (A) Absorption Spectra of **L14** (10 μM) in various solvent. (B) Emission Spectra of **L14** (10 μM) in various solvent.

We supposed that the V-shaped or propellor shaped alignment in the molecular framework edges in aggregation. Thus, probing aggregation features through emission spectroscopy was important. **L12** and **L14** were subjected to solvent switching and monitored under fluorescent spectroscopy. Between **L12** and **L14**, the scenario is quite different. Both of them exhibited an appreciable optical response to solvent variation. A miscible solvent system THF-Water mixture was chosen for the emission studies. **L12** revealed low emission intensity at lower water percentages while emission

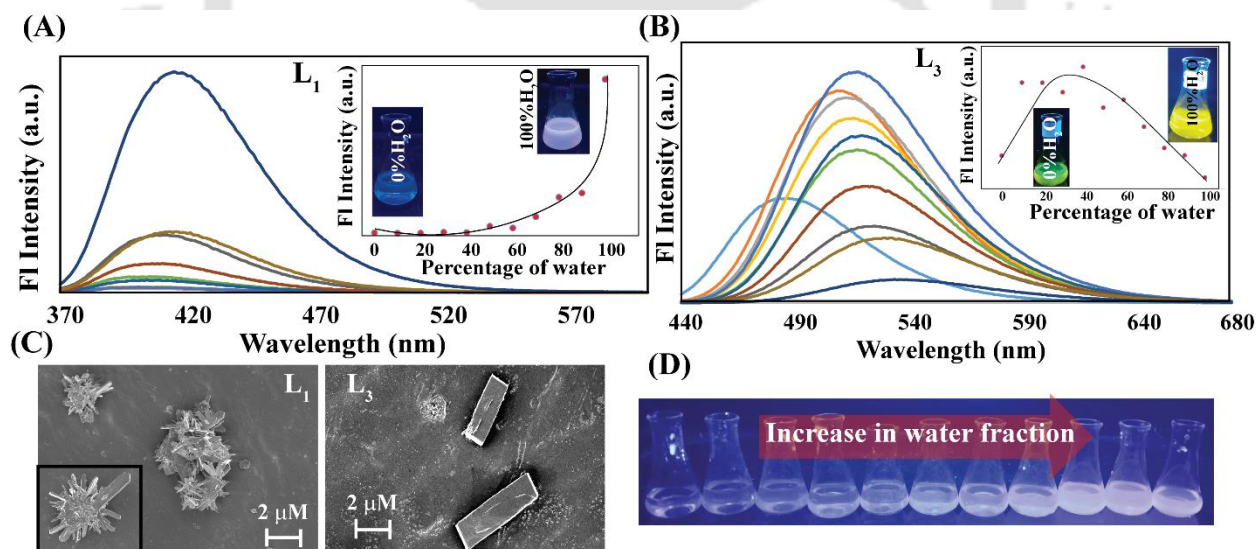


Figure 6.3: (A) Emission spectroscopy plot with varying water percentage in THF of **L12**. (B) Emission spectroscopy plot with varying water percentage in THF of **L14**. (C) FESEM images of **L12** and **L14** in water. (D) Glass vial held under 365 nm UV lamp containing solution of **L12** in varying water fraction in THF.

intensity was highest at 100% water. As water is an anti-solvent for the compounds, increasing the water fraction in the mixed THF/water system can alter their existing form from a solution in

100% THF to aggregated species in higher water content mixtures. **L**₁₄ in THF remain solvated and exhibited low fluorescence intensity. The spectral pattern changes slowly in THF/water mixtures with less than 80% water percentage because the solvent mixture's solvating power is still enough to dissolve the luminogens. Subsequently, the fluorescence intensity of **L**₁₄ starts to rise when $f_w > 80\%$, and at this point, the luminogen begins to aggregate. These emissive aggregates in water corroborate aggregation-induced emission phenomena in **L**₁₂, stating **L**₁₂ as AIEgen. In the case of **L**₁₄ on increasing water fraction the highest emission intensity was obtained at 40% of the Water-THF mixture and the intensity fell at a higher percentage of water ($f_w > 50\%$). This quenching of emission intensity indicates that at higher water fraction **L**₁₄ aggregates and 'the concentration quenching effect'²⁹⁻³⁰ comes into play.

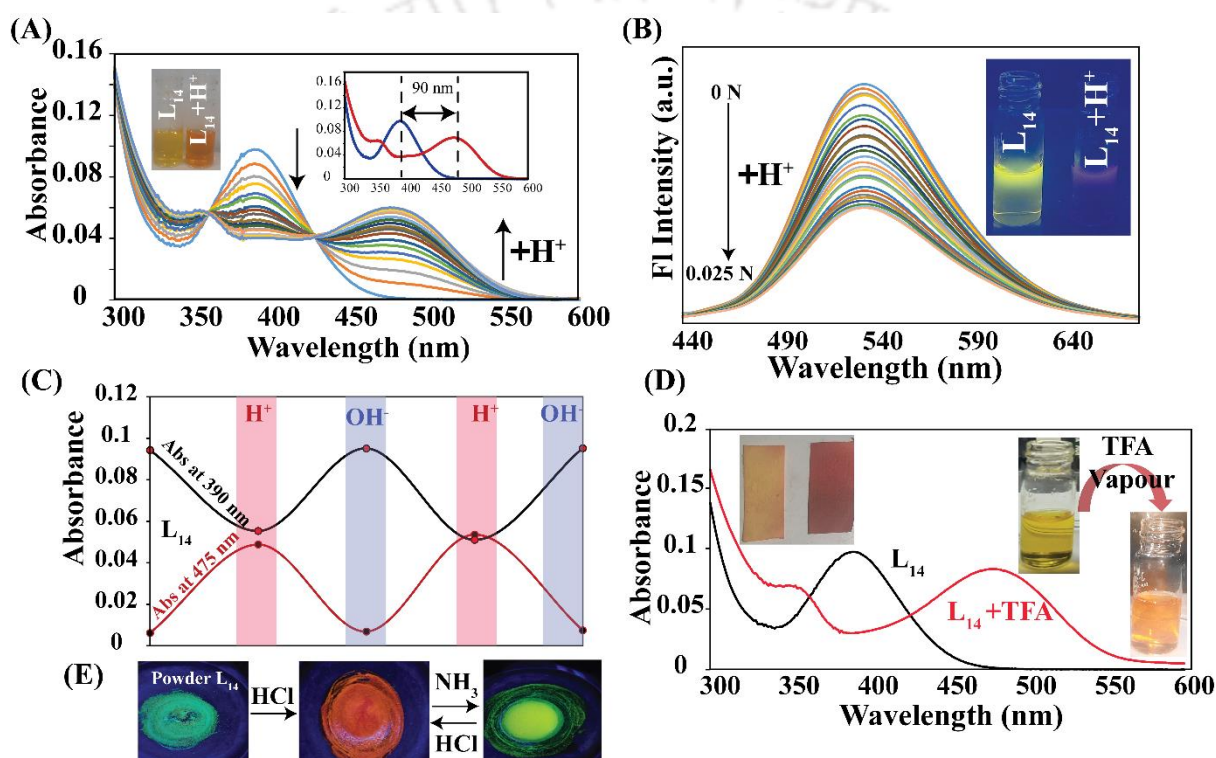


Figure 6.4: (A) Absorption spectra depicting titration profile of **L**₁₄ (10 μ M) with gradual addition of acid (inset: glass vial containing solution of **L**₁₄ (10 μ M) and after addition H^+ , Graph showing the extent of red shift in UV spectrum)). (B) Emission Spectra depicting titration profile of **L**₁₄ (10 μ M) with gradual addition of acid (inset: glass vial containing solution of **L**₁₄ and after addition H^+ held under 365 nm UV lamp) (C) Output of UV spectra showing fall and growth of peak at 390 nm and 475 nm respectively. (D) UV-vis spectra showing the change after addition of Trifluoroacetic acid (TFA) (inset: Paper strip dipped in and glass vials containing **L**₁₄ solution and exposed to TFA vapours).

Measurement of particle size in aggregation studies is imperative. Dynamic light scattering experiments were carried out for **L**₁₂ and **L**₁₄. **L**₁₂ displayed 273.4 d.nm and **L**₁₄ 84.15 d.nm in

100% water. The variance in DLS particle size for **L12** and **L14** is consistent with the aggregation behaviour from emission spectroscopy (Figure A6.2(A)). Dealing with morphological and size of the aggregated particles, FESEM and AFM analysis was performed. The analysis and the images were taken in drop cast aqueous solution of **L12** and **L14**. **L12** showed spiked spheres while **L14** displayed rectangular block-shaped structures under electron microscopy. The images of **L14** aggregates were confirmed as well as reflected under AFM analysis.

6.4 pH Sensitivity and other applications

To measure the pH sensitivity of **L12** and **L14** they were tested under extreme pH conditions. Under absorption spectroscopy, **L12** exhibited no significant spectral change under pH fluctuation (Figure A6.1 (B)). On contrary, **L14** exhibited a newly generated peak at 475 nm along with decreased absorbance at 390 nm. We hypothesise this pH sensitivity is due to the presence of the $-\text{NH}_2$ functional group in **L14**'s molecular framework. Under emission spectroscopy, **L14** showed quenching when acid was added to the solution. **L14** and acidified **L14** were studied under IR spectroscopy ((Figure A6.3 (A))). There we observed a shift in NH peaks after addition of acid to it.

This property of **L14** requires further consideration and extended applications. Titration of **L14** against acid was performed and monitored under absorption as well as emission spectroscopy. On gradual addition of acid, a new peaked appeared at 475 nm and the peak at 390 nm gradually diminished (Figure 6.4(A)). Similarly, when monitored under fluorescence spectroscopy, the gradual addition of acid leads to quenching of the emission intensity at 538 nm (Figure 6.4(B)). This acid-chromic feature of the probe was further utilized in important applications.

The reversibility of this probe was also checked by acid-alkali fluctuation. Figure 6.4(C) graph denotes the on-off nature of the two peaks at 390 nm and 475 nm corresponding to acid and alkali. On acidifying (addition of HCl) the peak at 390 nm vanishes and the peak at 475 nm emerges. In addition to alkali (NH_4OH), the peak at 390 nm re-appears and the peak at 475 nm diminishes. This was repeated up to 3 cycles. An image of acid-alkali sensitivity is attached in (Figure 6.4(E)). Powder **L3** was ground with acid (HCl) and subsequently with alkali (NH_4OH) and held under a UV-365 nm lamp to snap the images.

Vapo-chromism is a significant analytical tool. We propose our probe to be vapo-chromic. The Trifluoroacetic acid vapours are infused in a closed vessel containing a solution of **L14**. The colour of the solution changed to red indicating vapo-chromism. Further, this experiment was on a solid support via a paper strip test. A regular filter paper was cut and dipped in the solution of **L14** and dried well. TFA vapours were held near the test paper. On exposure, the colour changed to red. It

was imperative to note the spectroscopic view of this experimentation. In the UV-vis spectrum, a similar peak appeared at 475 nm on the addition of TFA to a solution L_{14} (Figure 6.4(D)).

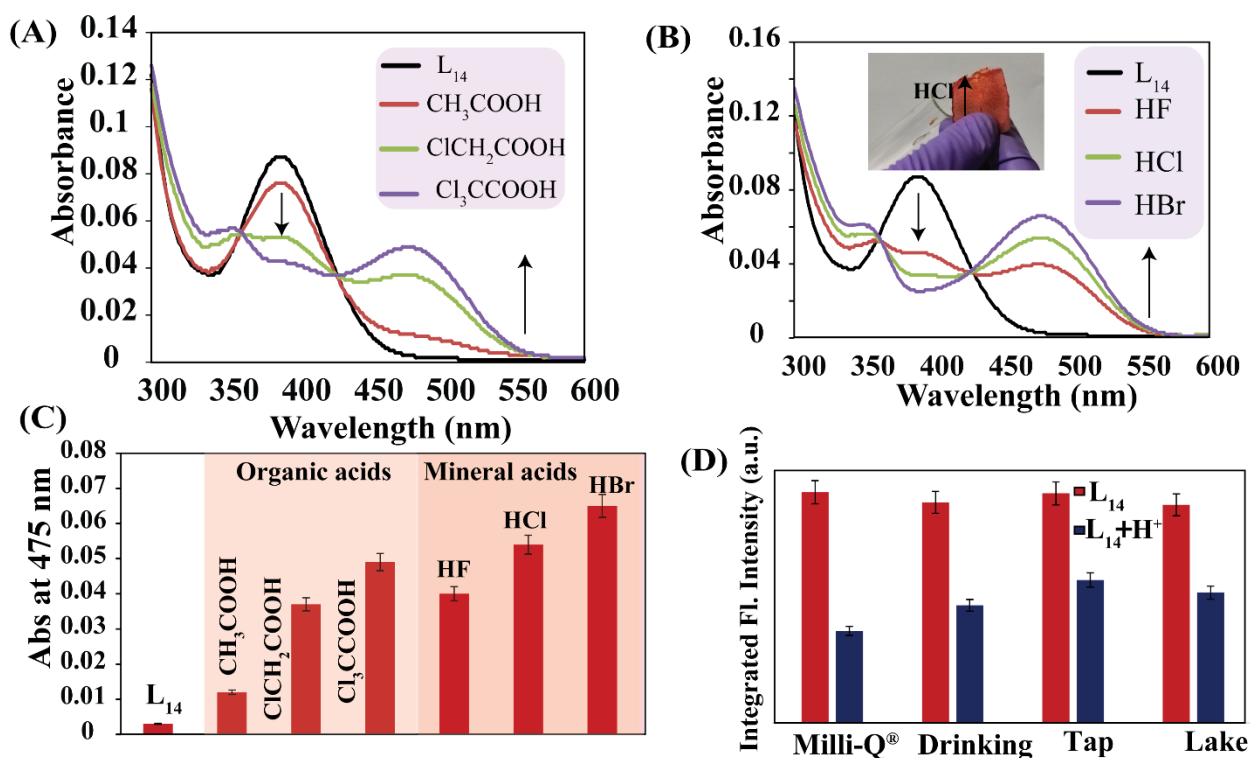


Figure 6.5: (A) UV-vis spectra demonstrating the change of spectral profile on addition of acetic and chlorinated acetic acids to solution of L_{14} (10 μ M). (B) UV-vis spectra demonstrating the change of spectral profile on addition of halogen acids to solution of L_{14} (10 μ M). (C) Bar diagram of the output from UV-vis spectra of above experiments. (D) Bar diagram of the output from emission spectra showing intensity quenching of L_{14} (10 μ M) in various acidified water samples.

L_{14} can distinguish the extent of ionization i.e.; the acidity of the medium ranging from weaker to stronger acids. To demonstrate two sets of acids are considered mineral acids and organic acids. L_{14} was tested with acetic acid, chloroacetic acid and trichloroacetic acid. As we know, by increasing the number of chlorine atoms the dissociated carboxylate ion stabilizes via the -ve inductive effect thus increasing the dissociation of H^+ eventually increasing the acidity of the media. In absorption spectroscopy, the peak at 475 nm showed varied growth in absorbance value under these acidic conditions. The rate of growth of the peak at 475 nm is at par with the induced acidity of the organic acids (Figure 6.5(A)). Fluorescence studies were also run which resulted in varied quenching in sync with the acidity of the media ((Figure A6.3 (B) & (C)). In the case of mineral acids, halogen acids were sorted. Moving down the periodic table in the halogen group (HF to HI) the strength of the halogen acids increases. This was reflected in the increment of absorbance at 475 nm peak with increase in halogen acidity (Figure 6.5(B)). As the acidity of the

media increases the absorbance also increases. This entire experimentation outcome with organic acids and mineral acids in form of bar diagram (absorbance values vs acids) are plotted (Figure 5(C)). In this context we also experimented how this probe behaves before HCl vapours. Barium chloride salt was taken in a test tube and conc. H_2SO_4 was added to it. The paper soaked in **L14** solution was held near it. The colour changed from yellowish green to red (Figure 6.5(B)), proving its vapochromic property.

L14 was subjected to real water sample analysis. Water from four different sources was sorted: Milli-Q[®], Drinking, Tap and lake water. This was analysed under emission spectroscopy. Firstly, the intensity of the probe was measured in each media and the intensity was again measured after the addition of 5 equivalents of acid (HCl) to it. The spectral output in form of a bar diagram has been represented. Integrated Fluorescence intensity has been plotted against the types of media to represent the quenching process. In all three cases, quenching of the emission intensity reveals the efficiency of the probe to detect acidity even in presence of impurities and contaminated water samples (Figure 6.5(D)).

6.5 Urease Activity and Microbial Fermentation

The hydrolysis of urea into ammonia and carbon dioxide is carried out by the Nickel-dependent urease enzyme. Ureases are found in a wide range of bacteria, algae, fungi, plants, and invertebrates, along with in soils as a soil enzyme. The hydrolysis of urea occurs in two stages. Ammonia and carbamic acid are generated in the first stage. The carbamate hydrolyses spontaneously and rapidly to ammonia and carbonic acid. Urease activity raises the pH of its environment by producing ammonia, which is alkaline³¹⁻³².

Experimentation on reversibility earlier, reveals the sensitivity of protonated **L14** towards alkali. Hence the protonated **L14** was utilized in tracking urease activity. As per our proposition, the released ammonia from urease hydrolysis would increase the pH of the media leading to deprotonation of protonated **L14**. This entire experiment was monitored under absorption spectroscopy. A solution of 0.5 N urea was considered as the working solvent. By adding acid, protonated **L14** was produced, and an obvious peak at 475 nm appeared, diminishing the absorbance maxima at 390 nm. The Urease enzyme was gradually added to this solution at a concentration of 0.09 mg/mL. After every addition, the UV spectra were recorded. The spectral profile is plotted (Figure 6.6(A)). The growth and fall of absorbance regarding peak at 390 nm and 475 nm respectively are also outlined (Figure 6.6(B)). This spectral output demonstrates the urease activity which is in sync with our scheme. This was further verified in emission spectroscopy. The quenching of fluorescence due to acidification of **L14** was recovered on gradual addition of urease enzyme. Urease enzyme was added at a rate of 10 $\mu\text{g/ml}$ to a solution containing 0.5 N urea and

protonated L_{14} . The regain of fluorescence intensity was recorded and plotted (Figure 6.6(C)). Furthermore, fluorescence microscopy was used to track the enzyme activity. L_{14} emitted as green and red fluorescence which subsequently quenched in presence of acid. Now, the in presence or gradual addition of urea and urease the fluorescence intensity was recovered. All the images were snapped and arranged (Figure 6.6(D)).

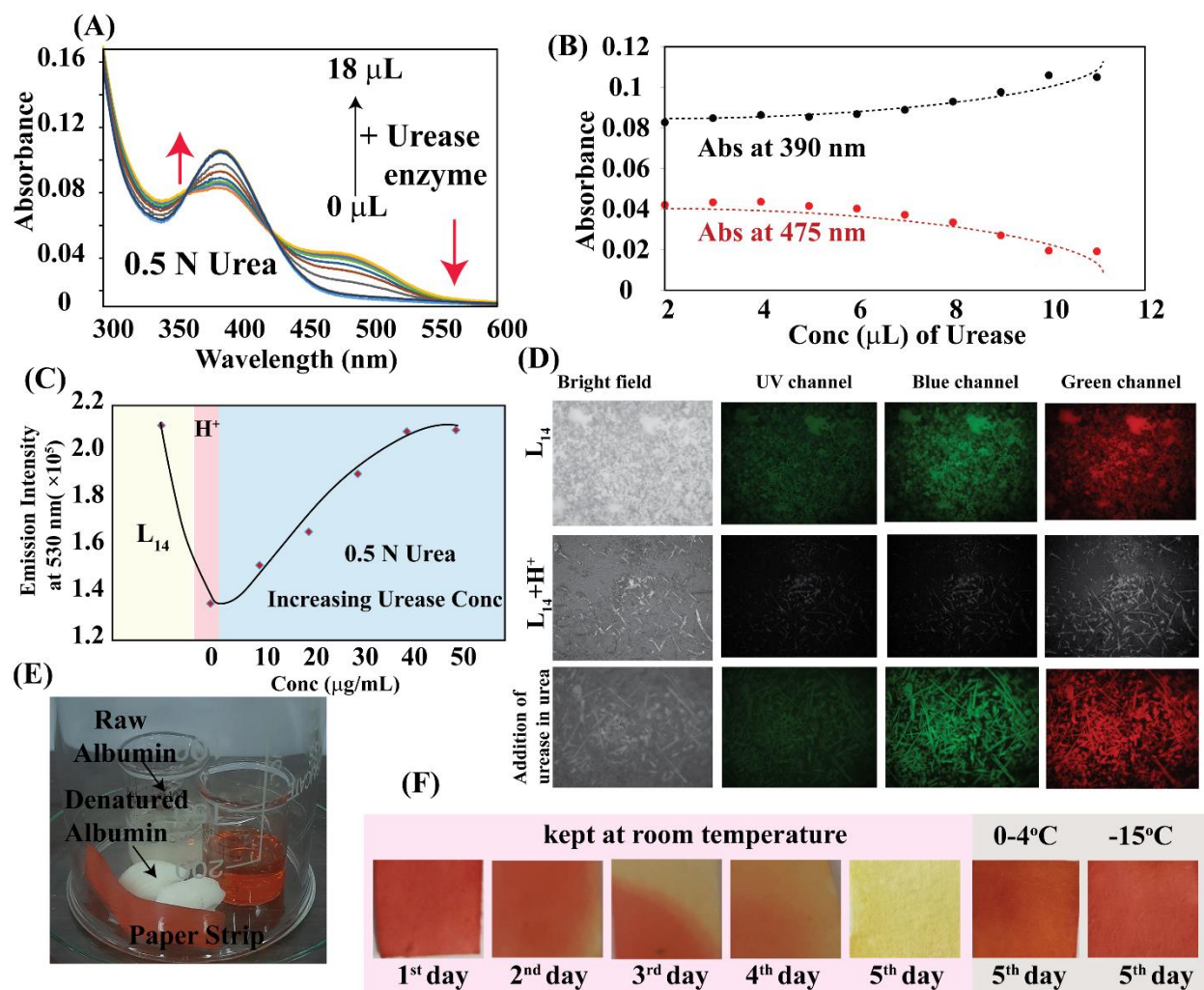


Figure 6.6: (A) Absorption spectra of titration showing gradual addition of urease in 0.5 N urea solution and protonated L_{14} . (B) Graphical output of 6(A) showing the fall and growth of absorbance values of peaks at 475 nm and 390 nm respectively. (C) Fluorescence titration showing gradual addition of urease in 0.5 N urea solution and protonated L_{14} . (D) Fluorescence microscopy images of L_{14} , protonated L_{14} , and after urea-urease addition. (E) Photograph of experimental setup. (F) Snapshots paper strips soaked in L_{14} solution and stowed with food samples at different temperatures.

The proposed scheme was utilised to monitor the formation of biogenic amines and assess the freshness of food after these encouraging results. The prepared protonated L_{14} -loaded paper strips were then used as an indicator to monitor food freshness under optimal conditions (Figure 6.6(E)).

3 sets were prepared where raw and boiled egg albumin was taken for our experimentation. One of them was kept at room temperature for several days while the other two sets were stowed in the refrigerator at 0-4°C and a freezer below 0°C. Significant changes were observed in the colour of the paper strips (Figure 6.6(F)). Protein samples kept at room temperature showed signs of fermentation manifested in the colour change of paper strips. Individual images were snapped each day to monitor the fermentation by our probe. Samples stowed at low temperatures negligibly showed signs of fermentation as detected by our prepared paper strips. All these snapshots are attached. This experimentation shows that our probe bears analytical utility by tracking the onset of microbial fermentation.

6.6 Conclusion

In a nutshell, we have synthesized quinoxaline-derived motifs with functional group tuning. The dependence of aggregation not only lies with the propellor structure but also the functional group attached to it. This tuning leads to an alteration in optical features as well as aggregational properties characterized by spectroscopy and microscopy. Aggregation-induced emission was displayed by **L1**. Solvatochromic, Vapochromic and Acidochromic properties of **L14** are demonstrated. Further, to delve, pH labile- **L14** have applied in several applications; sensitivity towards organic acids to minerals acids based on acidity. Utilizing this pH-lability we have tracked urease activity along with microbial fermentation. We affirm that this piece of work adds to future research on photophysical and aggregation studies along with applications in analytical and agricultural fields.

References

- 6.1. A. M. Kaczmarek and P.V. D. Voort, Chemical sensors based on nano-sized lanthanide-grafted periodic mesoporous organosilica hybrid materials, *J. Mater. Chem. C*, 2019, **7**, 8109.
- 6.2. K. Malhotra, D. Hrovat, B. Kumar, G. Qu, J. V. Houten, R. Ahmed, Paul A. E. Piunno, P. T. Gunning, and U. J. Krull, Lanthanide-Doped Upconversion Nanoparticles: Exploring A Treasure Trove of NIR-Mediated Emerging Applications, *ACS Appl. Mater. Interfaces*, 2023, **15**, 2499–2528.
- 6.3. 6.3. A. D. Cabral, N. Rafiei, E. D. de Araujo, T. B. Radu, K. Toutah, D. Nino, B. I. M. Evans, J. N. Milstein, D. Kraskouskaya, and Patrick T. Gunning, Sensitive Detection of Broad-Spectrum Bacteria with Small-Molecule Fluorescent Excimer Chemosensors, *ACS Sens.*, 2020, **5**, 2753–2762.
- 6.4. R. Haldar, M. Jakoby, M. Kozłowska, M. R. Khan, H. Chen, Y. Pramudya, B. S. Richards, Lars Heinke, W. Wenzel, F. Odobel, S. D., I. A. Howard, U. Lemmer, and C. Woll, Tuning Optical Properties by Controlled Aggregation: Electroluminescence Assisted by Thermally-Activated Delayed Fluorescence from Thin Films of Crystalline Chromophores, *Chem. Eur. J.*, 2020, **26**, 17016 – 17020.
- 6.5. Y. Ni, Y. Han, E. A. Kataev and M. A. Olson, Three-state fluorescence hydrochromism of a fluorophore–spacer–receptor system with variations in relative humidity, *Chem. Commun.*, 2022, **58**, 13463.

- 6.6. T. Kim, J. Y. Park, J. Hwang, G. Seo, Y. Kim, Supramolecular Two-Dimensional Systems and Their Biological Applications, *Adv.Mater.*, 2020, **32**, 2002405.
- 6.7. M. Yang, X. Li and J. Yoon, Activatable supramolecular photosensitizers: advanced design strategies, *Mater. Chem. Front.*, 2021, **5**, 1683-1693.
- 6.8. A. B. Cook and P. Decuzzi, Harnessing Endogenous Stimuli for Responsive Materials in Theranostics, *ACS Nano.*, 2021, **15**, 2068–2098.
- 6.9. M. Däntl, A. J. S. and Bettina V. Lotsch, Stimuli-responsive one-dimensional photonic crystals: design, fabrication and sensing, *Mater. Adv.*, 2022, **3**,7406.



Appendix - Chapter 6

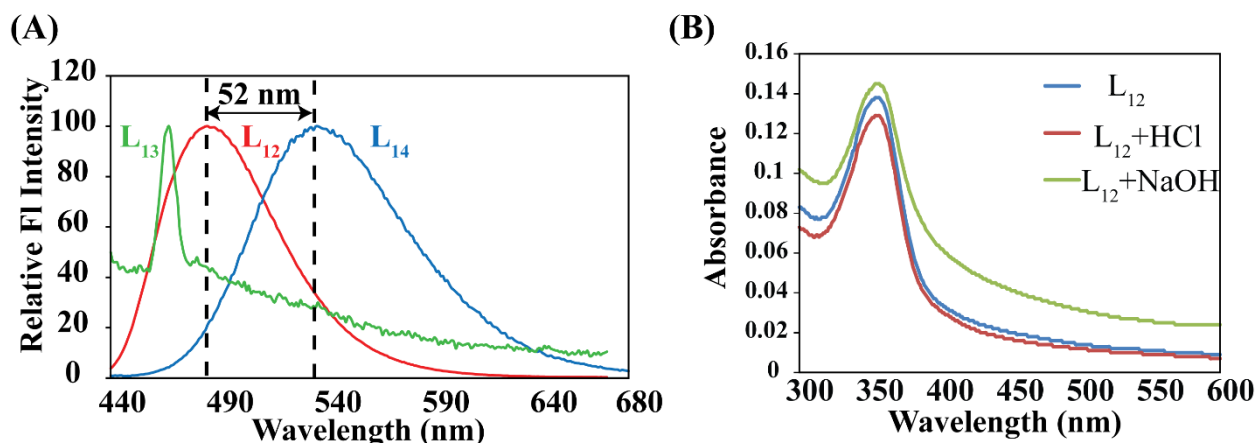


Figure A6.1: (A) Plot of emission intensity of L₁₂, L₁₃ and L₁₄ (10 μM) in water. (B) Absorption spectra of L₁₂ (10 μM) in presence of Strong acid and alkali.

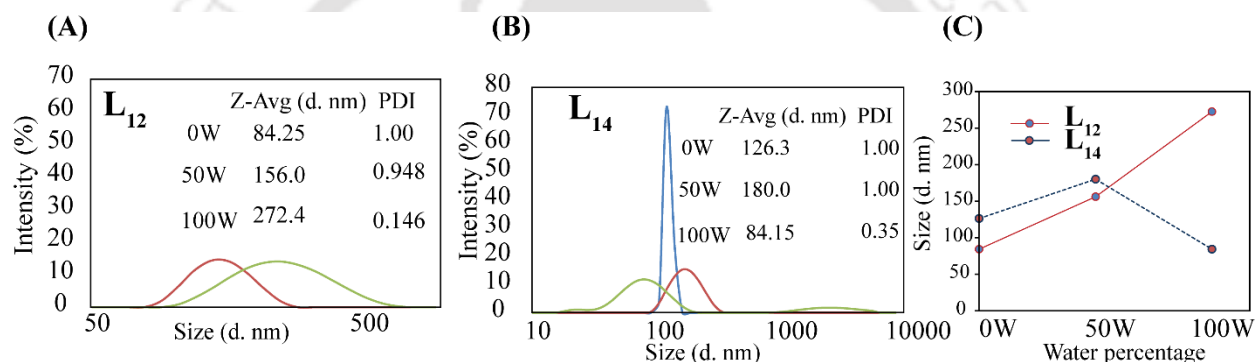


Figure A6.2: (A) DLS output L₁₂ (10 μM) in THF-water mixture. (B) DLS output L₁₄ (10 μM) in THF-water mixture. (C) Portray line graph of (A) and (B) showing growth and fall of particle sizes.

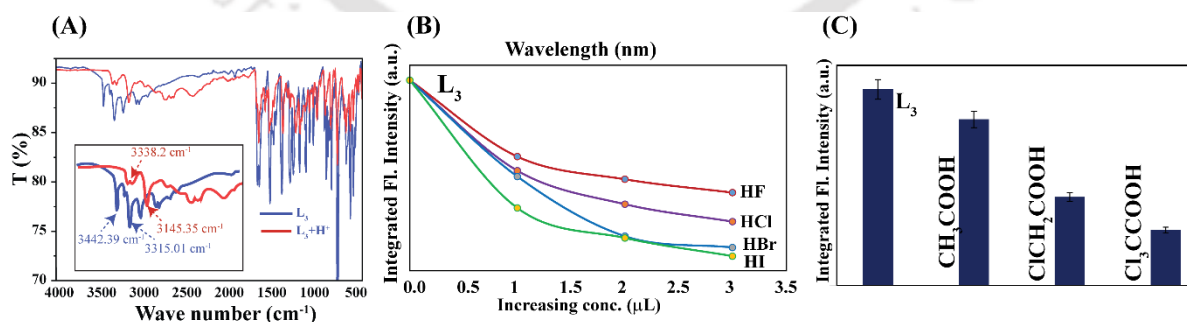


Figure A6.3: (A) IR spectra of L₁₄ and L₁₄+H⁺, showing the shifts in -NH stretching frequency. (B) Line graph from Emission spectra demonstrating the quenching in intensity on addition of halogen acids to solution of L₁₄ (10 μM). (C) Bar diagram from Emission spectra demonstrating quenching in intensity on addition of acetic and chlorinated acetic acids to solution of L₁₄ (10 μM).

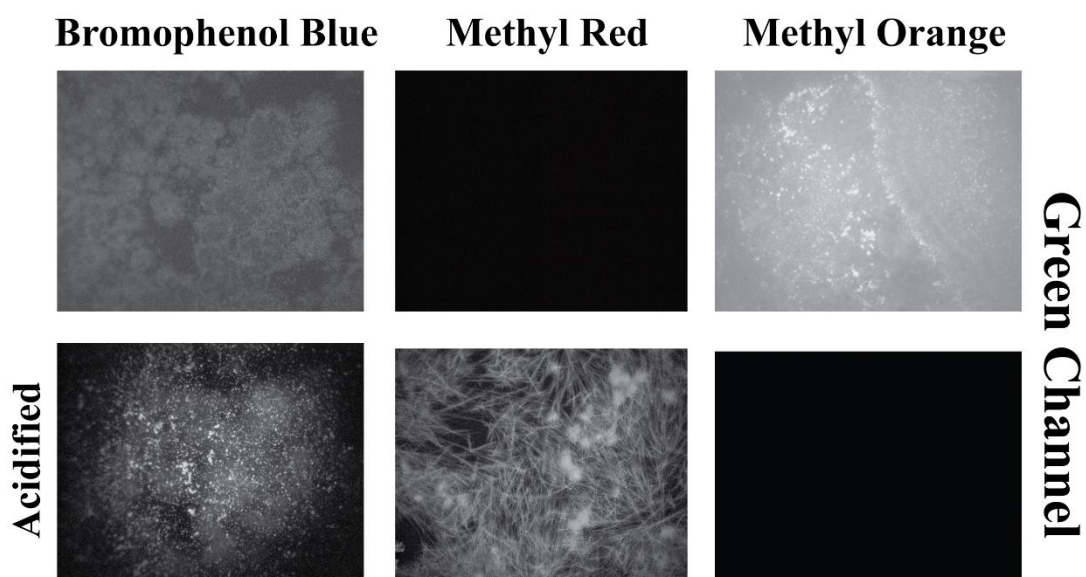


Figure A6.4: Fluorescence Microscopy images of commonly available acid-base indicators.

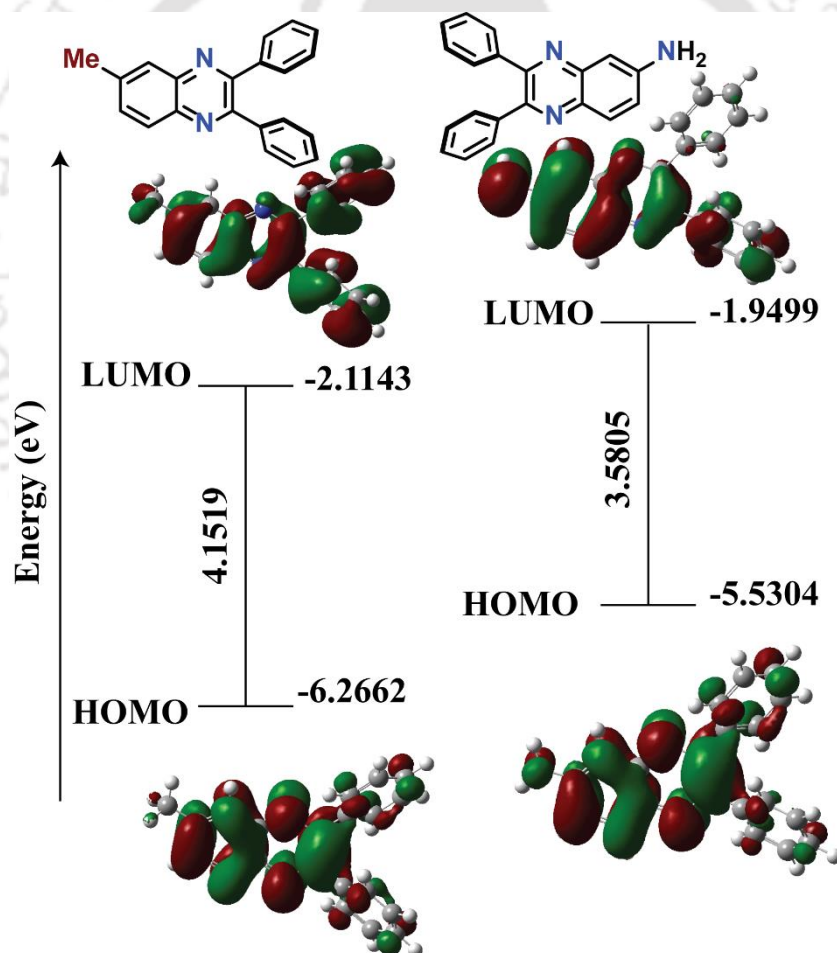


Figure A6.5: Output of DFT calculation on L12 and L14, Density functional theory (DFT) calculations were calculated with the B3LYP/6-31G(d,p) method basis set using the Gaussian 09 program. The CPCM solvent model has been implemented using water as a solvent during calculation.



Conclusion and Future Perspective

At the fag end, it can be concluded that this thesis elucidates the significant consequences in comprehension of aggregation perspective of flexible and rigid frameworks and their response towards environmentally and biologically relevant analytes. The results during the research period offer some decent findings in the aspect of small molecule aggregation and suitable routes in morphological changes concerning design, synthesis, and characterization of amphiphiles and non-amphiphiles with contrasting aggregation outlook in developing supramolecular structures for advanced application in related fields.

During this insightful chemical journey, we designed **L₁-L₃** which shows a comparative aggregation aptitude with chain length variation in amphiphiles. The entire photophysical study on aggregation mechanism is dealt with. Then, these synthesized amphiphiles are used in forming hydrophobic surfaces due to their inherent property of hydrophobicity. Furthermore, the concept of Photoinduced Electron Transfer or PET is applied in the detection of nitro antibiotics via fluorescence quenching. This chemo sensing was probed in biofluids viz; simulated gastric and body fluid. Next, a layout is drawn where a comparative study between an amphiphile and a non-amphiphile is presented. The compounds designed and synthesized were substituted urea and amide (**L₄ & L₅**). Studies on aggregation-induced emission are shown by a binary solvent system DMF-Water. Morphological variance is depicted on solvent switching by electronic microscopy imaging. Both solid and solution state emissive property is depicted. A typical photophysical prospect is shown in this piece of work i.e., light harvesting. Förster resonance energy transfer or FRET mechanism provides the basis for this light-harvesting phenomenon between the amphiphile and a commercial dye; Rhodamine. Once more, PET is applied to detect nitro explosives in aqueous media is demonstrated. This detection proceeds via disaggregation of the aggregated state. In the allied chapter, functionalization of amphiphile was done: a comparative outline on substituted urea and thiourea (**L₄ & L₆**). Apart from detailing aggregational features through spectroscopy and microscopy, an edge on the chemo-sensing property was found. The thiourea selectively recognizes Hg (II) ions in an aqueous solution due to the soft-soft interaction between the sulfur atom and the heavy metal. Turn-On or fluorescence emission enhancement is achieved even in the presence of heavy metal during the detection process. The toxic metal ion interaction causes disaggregation of the amphiphile demonstrated through DLS and FESEM

experiments. The chemo-sensing experiments were done with various real samples. Moreover, The Hg(II)-amphiphile ensemble detects sulfide ions in the water among all other sulfur-containing anions and amino acids.

After detailing the aspects of aggregation and chemosensing the thesis provides an outline of the rigid molecular framework. The quinoxaline motif was chosen as the rigid template. Possible functionalization was done on the molecular framework and photophysical studies regarding the aggregation behavior were conducted. **L7-L11** proved to be AIEgen and the emission changes were shown by solvent switching of a binary solvent system (THF-Water). Both Microscopy and spectroscopic studies were carried out. Not only aggregational features were shown in the solution phase but also solid-state studies i.e., crystalline packing were laid out. Among all of them, the carboxylic acid group variant selectively interacted with a common surfactant: Cetyltrimethyl Ammonium Bromide (CTAB). This is due to the electrostatic interaction overpowering the non-covalent interaction via disaggregation of the emissive aggregated state. The detection was not limited to aqueous solution but was tested with real water samples. Domestic wastewater and factory effluents were chosen as media to confirm the detection ability.

The last chapter, **L12-L14** shows a variation in optical and analytical prospects upon functionalization of the quinoxaline scaffold. **L12 & L14** Differed in aggregation aptitude. **L14** showed solvatochromism and acidochromism. Now, this acid sensitivity or stimuli responsiveness is probed tracking urease enzyme activity and monitoring the freshness of food samples. The metalloenzyme activity is tracked via absorption, emission spectroscopy, and fluorescence microscopy.

In essence, we propose that this thesis will provide a significant contribution to the communities of analytical chemistry and supramolecular chemistry for improving understanding and advancement in the specific field of research. This thesis is intended to spark an additional investigation into intriguing photophysical properties as well as materials and sensing ability using this kind of small molecule moiety with an aggregative nature.

Curriculum Vitae

SAGNIK DE



Date of Birth: 06/01/1994

Nationality: Indian

Phone No.: +9330545739

Email id: sagnik18@iitg.ac.in

Address: Indian Institute of Technology Guwahati, Assam, India

Academic Summary

2018-2023: Ph.D. in the Department of Chemistry **Indian Institute of Technology Guwahati**, India.

- Thesis title: “**Aggregation aptitude in rigid and flexible molecular systems: Comparative Photophysical and analytical Studies**”.
- Supervisor: **Prof. Gopal Das**

2015-2017: Master of Science in Chemistry from **University of Calcutta**, Kolkata, West Bengal, India.

- Dissertation: “PtBr₂ catalysed ring expansion of cyclopropane in synthesis of functionalized dihydropyrroles”.
- Supervisor: **Prof. Dilip Kumar Maity**
- Percentage: 75.00%

2012-2015: Bachelor of Science (Hons.) in Chemistry from S.A. Jaipuria College, **University of Calcutta**, Kolkata, West Bengal, India.

- Percentage: 73.12%

2010 & 2012: ICSE (92.2%) and ISC (86.25%) from **Methodist School**, Dankuni, West Bengal, India.

Professional Experience

- **Guest Lecturer** at Calcutta Women’s College, Kolkata: Teaching chemistry to undergraduate students including theoretical and practical classes (2017-2018).
- **FESEM** operator (Make: Zeiss, Model: Gemini 300) at IIT Guwahati (2021-2023).

Achievements

- Awarded S.A. Jaipuria Memorial Award for securing the first position in (Hons. Chemistry).

TH-3237_18612030 Graduate Aptitude test in Engineering (**GATE**) (2018 and 2019).

Teaching Experience

- **Teaching assistantship** at IIT Guwahati: Chemistry Practical Courses for undergraduate students.
- Co-guided two M.Sc. final year project students (2021 & 2022)

Research Interests

Supramolecular chemistry involving chemistry of Tailor-made Amphiphiles, Photophysical studies probe-analyte interaction, Macromolecules and advanced Materials.

List of Publications

In journals:

1. Carbazole-Derived Amphiphile-Based AIEgen: Detection of Nitro-Antibiotics and Water-Repelling Surfaces, **Sagnik De**, Oiyao Appun Pegu, and Gopal Das, *Langmuir* **2023**, **39**, **6**, **2444–2449**.
2. Exploring the Aggregation and Light-Harvesting Aptitude of Naphthalimide-Based Amphiphile and Non-amphiphile AIEgen, **Sagnik De** and Gopal Das, *Langmuir*, **2022**, **38**, **19**, **6158–6163**.
3. Self-assembly and desulfurization mediated Turn-ON mercury sensing in aqueous media by tripodal synthetic amphiphile chemosensors, **Sagnik De** and Gopal Das, *Dyes Pigm.* **2021**, **195**, **109659**.
4. Surfactant induced disaggregation of Quinoxaline AIEgen scaffold: Aggregation aptitude in solid and solution state, **Sagnik De** and Gopal Das, (*Soft Matter*, **2023**,**19**, **6116-6121**).
5. Acidochromic and solvatochromic urease tracker: The aggregation and optical feature of a Quinoxaline scaffold, **Sagnik De** and Gopal Das, *J. Photochem. Photobiol. A*, **2023**, **443**, **114884**.
6. Insights into the self-aggregating properties of a solvatochromic probe and interaction with β -lactoglobulin, **Sagnik De** and Gopal Das, *New J. Chem.*, **2022**,**46**, **18048-18054**.
7. Inhibition of Staphylococcal Nuclease by Benzimidazole-based Ligand: Implications in DNA-Mediated Entrapment and Uptake of MRSA by Macrophage-like Cells, B. Konwar; Sagnik De; G. Das; A. Ramesh. (**Manuscript Submitted**).
8. Amphiphilic polyphenol incorporated hydrogel derived from mucoadhesive of *Dillenia indica*: Potential Antioxidant and Adsorbent. Debolina Ghosh, Sagnik De, Deepmoni Deka and Gopal Das, *Int. J. Biol. Macromol.*, **254**, **127759**, **2023**.

9. Naphthyl-functionalized Ninhydrin-derived Receptor for 'CHEF'-based Sequential Sensing of Al(III) and PPI: Prospective Chemosensing Applications under Physiological Conditions. Aresh Das, **Sagnik De** and Gopal Das, *J. Photochem. Photobiol. A*, 2021, 418, 113442.
10. A series of benzothiazole-based Schiff bases for the colorimetric sensing of fluoride and acetate ions: acetate-induced turn-on fluorescence for selectivity, Nilotpal Borah, **Sagnik De**, Abhijit Gogoi, and Gopal Das, *New J. Chem.*, 2020, 44, 18703-18713.
11. Probing the solvent-tunable aggregation aptitude of neutral naphthyl bis-urea series and their interactions with nitro-aromatics, Senjuti Halder, Biswajit Nayak, **Sagnik De** and Gopal Das, *J. Mol. Liq.*, 2021, 329, 115601.
12. Binding consistency of anions by the effect of aromatic meta-substitution of bis-urea receptors: entrapment of hexafluorosilicate clusters, Biswajit Nayak, Senjuti Halder, **Sagnik De** and Gopal Das, *Crys. Eng. Comm.*, 2019, 21, 7172.

Conferences/Workshop attended

1. Interdisciplinary Symposium on Materials Chemistry (ICMS-2020), BARC, Mumbai.
2. Poster presentation at 20th National Conference on Surfactants, Emulsions and Biocolloids, IIT Guwahati.
3. Advances in Chemical and Material Sciences-ACMS-2022, HIT Kolkata.
4. Research & Industrial Conclave integration 2022, IIT Guwahati.
5. Frontiers in Chemical Sciences – 2022, IIT Guwahati.
6. Chemical Research Society of India-NSC-28,(CRSI-2022) IIT Guwahati.
7. Modern Trends in Inorganic Chemistry-2022. Department of Chemistry, Institute of Science, Banaras Hindu University, Varanasi.